Data-driven computational modelling for some of the implications of dopamine in the brain : From subcellular signalling to area networks

Alexandre Foncelle

N°d'ordre NNT : 2018LYSEI028

THESE de DOCTORAT DE L'UNIVERSITE DE LYON
opérée au sein de
(INSA LYON)

Ecole Doctorale N° 512
Mathématiques et Informatique (InfoMaths)

Discipline de doctorat : Informatique et applications

Soutenue publiquement le 5/04/2018, par :
Alexandre Foncelle

Data-driven computational modelling for some of the implications of dopamine in the brain: from subcellular signalling to area networks.

Devant le jury composé de :

Tsaneva-Atanasova, Krasimira Professor University of Exeter Rapporteure
Faure, Philippe Directeur de recherche Université Pierre et Marie Curie Rapporteur
Soula, Hédi Professeur Université Pierre et Marie Curie Examinateur
Beslon, Guillaume Professeur INRIA Examinateur
Berry, Hugues Directeur de recherche INRIA Directeur de thèse

Département FEDORA – INSA Lyon - Ecoles Doctorales – Quinquennal 2016-2020

SIGLE	ÉCOLE DOCTORALE	NOM ET COORDONNEES DU RESPONSABLE
CHIMIE	**CHIMIE DE LYON** **http://www.edchimie-lyon.fr** Sec. : Renée EL MELHEM Bât. Blaise PASCAL, 3e étage **secretariat@edchimie-lyon.fr** INSA : R. GOURDON	M. Stéphane DANIELE Institut de recherches sur la catalyse et l'environnement de Lyon IRCELYON-UMR 5256 Équipe CDFA 2 Avenue Albert EINSTEIN 69 626 Villeurbanne CEDEX **directeur@edchimie-lyon.fr**
E.E.A.	**ÉLECTRONIQUE, ÉLECTROTECHNIQUE, AUTOMATIQUE** **http://edeea.ec-lyon.fr** Sec. : M.C. HAVGOUDOUKIAN **ecole-doctorale.eea@ec-lyon.fr**	M. Gérard SCORLETTI École Centrale de Lyon 36 Avenue Guy DE COLLONGUE 69 134 Écully Tél : 04.72.18.60.97 Fax 04.78.43.37.17 **gerard.scorletti@ec-lyon.fr**
E2M2	**ÉVOLUTION, ÉCOSYSTÈME, MICROBIOLOGIE, MODÉLISATION** **http://e2m2.universite-lyon.fr** Sec. : Sylvie ROBERJOT Bât. Atrium, UCB Lyon 1 Tél : 04.72.44.83.62 INSA : H. CHARLES **secretariat.e2m2@univ-lyon1.fr**	M. Fabrice CORDEY CNRS UMR 5276 Lab. de géologie de Lyon Université Claude Bernard Lyon 1 Bât. Géode 2 Rue Raphaël DUBOIS 69 622 Villeurbanne CEDEX Tél : 06.07.53.89.13 **cordey@univ-lyon1.fr**
EDISS	**INTERDISCIPLINAIRE SCIENCES-SANTÉ** **http://www.ediss-lyon.fr** Sec. : Sylvie ROBERJOT Bât. Atrium, UCB Lyon 1 Tél : 04.72.44.83.62 INSA : M. LAGARDE **secretariat.ediss@univ-lyon1.fr**	Mme Emmanuelle CANET-SOULAS INSERM U1060, CarMeN lab, Univ. Lyon 1 Bâtiment IMBL 11 Avenue Jean CAPELLE INSA de Lyon 69 621 Villeurbanne Tél : 04.72.68.49.09 Fax : 04.72.68.49.16 **emmanuelle.canet@univ-lyon1.fr**
INFOMATHS	**INFORMATIQUE ET MATHÉMATIQUES** **http://edinfomaths.universite-lyon.fr** Sec. : Renée EL MELHEM Bât. Blaise PASCAL, 3e étage Tél : 04.72.43.80.46 Fax : 04.72.43.16.87 **infomaths@univ-lyon1.fr**	M. Luca ZAMBONI Bât. Braconnier 43 Boulevard du 11 novembre 1918 69 622 Villeurbanne CEDEX Tél : 04.26.23.45.52 **zamboni@maths.univ-lyon1.fr**
Matériaux	**MATÉRIAUX DE LYON** **http://ed34.universite-lyon.fr** Sec. : Marion COMBE Tél : 04.72.43.71.70 Fax : 04.72.43.87.12 Bât. Direction **ed.materiaux@insa-lyon.fr**	M. Jean-Yves BUFFIÈRE INSA de Lyon MATEIS - Bât. Saint-Exupéry 7 Avenue Jean CAPELLE 69 621 Villeurbanne CEDEX Tél : 04.72.43.71.70 Fax : 04.72.43.85.28 **jean-yves.buffiere@insa-lyon.fr**
MEGA	**MÉCANIQUE, ÉNERGÉTIQUE, GÉNIE CIVIL, ACOUSTIQUE** **http://edmega.universite-lyon.fr** Sec. : Marion COMBE Tél : 04.72.43.71.70 Fax : 04.72.43.87.12 Bât. Direction **mega@insa-lyon.fr**	M. Philippe BOISSE INSA de Lyon Laboratoire LAMCOS Bâtiment Jacquard 25 bis Avenue Jean CAPELLE 69 621 Villeurbanne CEDEX Tél : 04.72.43.71.70 Fax : 04.72.43.72.37 **philippe.boisse@insa-lyon.fr**
ScSo	**ScSo*** **http://ed483.univ-lyon2.fr** Sec. : Viviane POLSINELLI Brigitte DUBOIS INSA : J.Y. TOUSSAINT Tél : 04.78.69.72.76 **viviane.polsinelli@univ-lyon2.fr**	M. Christian MONTES Université Lyon 2 86 Rue Pasteur 69 365 Lyon CEDEX 07 **christian.montes@univ-lyon2.fr**

*ScSo : Histoire, Géographie, Aménagement, Urbanisme, Archéologie, Science politique, Sociologie, Anthropologie

Résumé

Au cours de l'histoire, le cerveau a été étudié sous différents aspects. Du 5ème au 17ème siècle, le cerveau fut comparé aux modèles hydrauliques, où les liquides étaient considérés comme le support des pensées. Puis, durant le 18ème siècle, le cerveau fut associé aux modèles électriques, on venait de découvrir la sensibilité des muscles et des nerfs aux décharges électriques (Mein, 1988). De nos jours, le fonctionnement du cerveau est comparé aux calculs en parallèle, aux statistiques bayésiennes et aux dynamiques de réseau de neurones.

Ce très bref historique montre que nos représentations du cerveau dépendent largement de ce qui peut être mesuré et des similitudes que l'on peut trouver avec des concepts déjà connus. Ces moyens de représentation simplifient notre compréhension du cerveau, c'est un objet très complexe comme l'illustre la diversité de sa composition, par exemple, la multitude de molécules, de cellules, de tissus et la variété de leurs interactions et leurs effets multiéchelle.

Dans le cerveau, il est difficile de mettre au point des expériences avec un niveau de contrôle approprié à cause du haut niveau de connectivité. Pour traiter ce problème, les modèles mathématiques sont utilisés pour représenter le cerveau d'une façon plus compréhensible. En effet, les modèles mathématiques peuvent être plus pratiques que les expériences pour tester des hypothèses et chercher à extraire l'essence même du principe étudié, en le simplifiant. De plus, la modélisation computationnelle forme une branche spécifique de la modélisation mathématique, permettant de résoudre de gros calculs numériques.

Dans cette thèse, j'ai utilisé la modélisation computationnelle à travers différentes approches pour étudier certaines régions cérébrales. Nous avons collaboré avec des neurobiologistes en appliquant nos modèles à des données expérimentales pour contribuer à mieux comprendre l'action de la dopamine, un neuromodulateur. J'ai étudié la diversité de l'action de la dopamine à trois échelles: la région cérébrale, le niveau cellulaire et le niveau moléculaire. La dopamine a un gros impact sur le cerveau et elle est principalement connue pour son implication dans le système de récompense. En effet, c'est une molécule associée à la prédiction de récompense et de punition. Peu de régions produisent de la dopamine et ces régions sont altérées par la maladie de Parkinson ou perturbées par la dépression. Pour la maladie de Parkinson, j'ai conçu un modèle de type taux de décharge pour reproduire l'activité neuronale des ganglions de la base. Ce modèle montre des réponses neuronales significativement différentes, entre la condition témoin et la condition parkinsonienne. Par ailleurs, avec un modèle de type Hodgin-Huxley prenant en compte la dynamique de l'ion potassium, j'ai pu appuyer l'hypothèse que la région cérébrale appelée l'habenula, lorsqu'elle est hyperactive, induirait la dépression. Cette dépression serait due à un déséquilibre de la concentration en potassium à cause d'une dysfonction de l'astrocyte (surexpression des canaux Kir4.1). Enfin, la dopamine est aussi impliquée dans la plasticité synaptique, un phénomène à la base de la mémoire. Je l'ai étudié avec un troisième modèle, prenant en compte plusieurs résultats expérimentaux relatifs à la plasticité en fonction du timing des potentiels d'action et de sa modulation.

La maladie de Parkinson Dans le contexte de la maladie de Parkinson, nous avons collaboré avec des expérimentateurs (l'équipe de Laurent Venance au Collège de France, Paris) pour étudier les ganglions de la base, une région du cerveau connue pour être altérée chez les malades parkinsoniens. La maladie de Parkinson est caractérisée, aux premiers stades, par des symptômes moteurs, comme des tremblements et une rigidité des muscles, puis des difficultés à un plus haut niveau cognitif, comme la planification ou la résolution de problèmes, enfin, si elle n'est pas traitée, de l'apathie et de l'anxiété. C'est une maladie neurodégénérative, ce qui signifie que des neurones spécifiques deviennent dysfonctionnels, en particulier les neurones des ganglions de la base, la région cérébrale impliquée dans le contrôle de la motricité et les fonctions exécutives. La principale caractéristique de la maladie de Parkinson est un manque de dopamine, qui peut être contrebalancé en prenant un substitut.

Pour mieux comprendre cette maladie et détecter ses premiers stades directement à partir de l'activité du cerveau, le but de ce projet était d'examiner les différences entre l'activité des ganglions de la base des rats témoins et celle des rats Parkinsoniens. Le cortex cérébral est constitué de la partie externe du cerveau et est impliqué dans les fonctions cognitives de haut niveau, comme l'attention, le langage ou la perception. Il impacte aussi différentes sous-régions (les noyaux) des ganglions de la base et à travers différentes voies neuronales.

Ainsi, en stimulant le cortex des rats et en enregistrant la réponse neurale de la substantia nigra pars reticulata, un noyau des ganglions de la base, on peut obtenir les caractéristiques des voies entre le cortex et les ganglions de la base et les comparer entre les conditions témoins et Parkinsoniennes. En effet, les réponses neuronales de ce noyau présentent un intérêt tout particulier puisque c'est le noyau de sortie de l'activité des ganglions de la base, ainsi il rend compte de toutes les informations reçues et traitées par les ganglions de la base. Cette information transite ensuite vers le cervelet et la moelle épinière, puis stimule les muscles. Ces enregistrements semblent donc une cible pertinente pour comparer l'activité du cerveau entre les deux conditions.

Après avoir prétraité les données enregistrées à partir de rats anesthésiés, nous avons créé un modèle computationnel que nous avons ajusté sur chaque enregistrement, pour caractériser chacun d'eux rigoureusement. Nous pouvions ensuite comparer les paramètres du modèle à chaque condition (témoin ou Parkinsonienne). Avec des analyses statistiques, nous avons pu montrer qu'il n'y avait pas de différence significative entre les réponses neuronales des rats témoins et Parkinsoniens. Néanmoins, il y avait différentes proportions de types de réponses neuronales entre les deux conditions, suggérant que les voies entre le cortex et les ganglions de la base ne sont pas modulées dans la maladie de Parkinson, mais que la proportion de voies actives est différente. Ces résultats fournissent une nouvelle voie d'exploration pour la maladie de Parkinson et suggèrent qu'elle pourrait être détectée à partir de l'activité d'un groupe de neurones des ganglions de la base.

La dépression Dans cette partie, nous explorons les origines de la mise en place de la dépression en collaboration avec des expérimentateurs (l'équipe de Hu's de l'université Zhejiang, Hangzhou, Chine). La dépression provoque une grande variété de symptômes comme une baisse de moral, une perte de motivation, des sentiments de désespoir et une inaptitude à ressentir le plaisir (anhedonia). Une des causes serait des déficits dans la région cérébrale de l'habenula. En effet, en condition témoin, l'habenula inhibe les neurones dopaminergiques de l'aire ventrale tegmentale, impliqués dans le système de récompense. Au contraire, dans les cas de dépression, l'habenula devient hyperactif et inhibe donc plus ces neurones dopaminergiques. Néanmoins, les causes de cette hyperactivité sont toujours inconnues.

Notre but est de déterminer l'origine de l'hyperactivité de l'habenula des rats. L'habenula

est constitué d'une population hétérogène de neurones, qui peuvent être catégorisés en fonction de leur type de décharge: neurones silencieux, neurones à potentiel d'action simple (neurones spiking) et neurones à potentiel d'action en rafale (neurones bursting). Les neurones silencieux ne présentent pas d'activité de décharge en tranche et au repos, et représentent la majorité de la population de neurone de l'habenula. Les neurones spiking déchargent des potentiels d'action un par un, tandis que les neurones bursting déchargent des groupes de potentiel d'action à haute fréquence. Les expériences sur les rats ont mis en évidence qu'en condition de dépression la proportion de neurones bursting dans l'habenula est plus forte que dans la condition témoin ce qui permet de faire l'hypothèse que les neurones bursting sont responsables de l'hyperactivité de l'habenula.

Nous avons conçu un modèle computationnel de la voie joignant l'habenula au neurone dopaminergique de l'aire ventrale tegmentale, soutenant l'idée que l'augmentation de la proportion de neurones bursting inhibe mieux le neurone dopaminergique. En comparant l'effet de différentes fréquences dans les modes spiking et bursting, le modèle suggère aussi que l'effet de l'hyperactivité de l'habenula est seulement dû à une augmentation de la quantité de potentiel d'action plutôt qu'à la spécificité du mode de décharge des neurones bursting.

Par ailleurs, les expériences dans l'habenula montrent que les neurones peuvent passer d'un mode de décharge spiking à bursting quand le voltage membranaire est plus négatif, c'est-à-dire qu'il s'hyperpolarise. Les responsables de cette hyperpolarisation seraient des canaux potassiums spécifiques, localisés sur la membrane des astrocytes. Les astrocytes représentent un autre type de cellule du cerveau, qui ne décharge pas, entourant les neurones. L'astrocyte possède des canaux qui retirent le potassium lâché par le neurone quand il décharge, ce sont des canaux rectifiant le potassium entrant (Kir). Le fait qu'ils laissent le potassium entrer ou sortir dépend principalement du déséquilibre de concentration en potassium entre l'intérieur et l'extérieur de l'astrocyte. Ce déséquilibre est appelé le gradient électrochimique du potassium. Pour soutenir cette hypothèse, nous avons implémenté un autre modèle, avec trois compartiments, le neurone, l'astrocyte avec des canaux Kir et l'espace entre le neurone et l'astrocyte, l'espace extracellulaire. Conformément aux expériences, lorsque les canaux Kir étaient surexprimés à la surface de l'astrocyte, la concentration de potassium dans l'espace extracellulaire diminuait suffisamment pour hyperpolariser à la fois le neurone et l'astrocyte. Ce résultat suggère que, puisque les neurones bursting sont plus hyperpolarisés que les neurones spiking, la surexpression des canaux Kir transformerait les neurones spiking en neurones bursting, conduisant à l'hyperactivité de l'habenula en condition de dépression. Ainsi, ces canaux Kir pourraient être la cible de nouveaux médicaments pour traiter la dépression.

Synaptic plasticity Dans cette étude, nous avons encore collaboré avec l'équipe de Laurent Venance (au Collège de France), mais aussi avec des modélisateurs (l'équipe de Kim Blackwell à l'université de George Mason, Fairfax, VA, USA) pour concevoir un modèle qui prend en compte la plasticité synaptique au niveau moléculaire. La plasticité synaptique est la capacité des synapses à ajuster leur efficacité en fonction des évènements. C'est un phénomène à la base de la mémoire et de l'apprentissage. Néanmoins, l'ensemble de la machinerie moléculaire de la plasticité synaptique est très peu comprise, en particulier à cause des nombreux acteurs qui y sont impliqués, mais aussi à cause de la grande diversité des règles de plasticité. En effet, ces règles dépendent de la région cérébrale, du type de neurone formant les synapses et aussi des caractéristiques de stimuli. Pour réduire notre étude, nous nous sommes focalisés sur les protocoles de plasticité en fonction du timing des potentiels d'action (STDP) en combinant notre modèle avec d'autres modèles publiés. Ces modèles présentaient les modulations de la STDP soit par des molécules endocannabinoïdes soit par des molécules de dopamine, mais pas les deux à la fois. Notre

travail fut d'unifier leurs propriétés sur la STDP en un seul modèle computationnel.

La STDP est obtenue avec un protocole expérimental spécifique, où les neurones pre- et post-synaptique déchargent à des timings précis. La règle classique, appelée la règle Hebbienne spécifie que les neurones déchargeant dans l'ordre pre- puis post-synaptique voient l'efficacité de leurs synapses accrue alors que l'ordre inverse diminue l'efficacité de la synapse. Cependant, en fonction du type de la synapse (excitatrice ou inhibitrice), la région cérébrale ou les molécules de neuromodulation impliquée, cette règle peut être modifiée. Tout d'abord, le but était d'ajuster le modèle aux données expérimentales de STDP avec une trace claire de calcium. Nous avons fusionné deux modèles computationnels et préservé les caractéristiques de chacun d'eux. Un problème majeur était de trouver un équilibre entre chaque voie moléculaire pour préserver les dynamiques d'intérêt tout en restant dans une gamme réaliste de valeur de paramètre. Nous avons obtenu un modèle reproduisant avec succès certains des résultats expérimentaux de plasticité, en fonction du timing de stimulation et de la présence de dopamine. Ce modèle peut maintenant être spécifiquement ajusté sur des enregistrements expérimentaux de fluctuations de calcium. Ces enregistrements n'existent pas encore et seraient une très grande avancée pour comprendre la plasticité synaptique.

Abstract

In the brain, the high connectivity level makes it difficult to set up experiments with an appropriate level of control. To address that issue, mathematical models are used to represent the brain in a more comprehensive way. Easier than experiments to test hypotheses, mathematical models can extend them closer to reality and aim to extract the studied principle essence, by simplifying it. Computational modelling is a specific branch of mathematical modelling allowing to solve large numerical calculations. In this thesis, I used computational modelling to study brain parts through different approaches, all in collaboration with neurobiologists and applied to experimental data. A common framework is given by the goal of contributing to a picture of the action of the neuromodulator dopamine. I studied the diversity of dopamine's action at three different scales: the brain region, the cellular level and the molecular level. Dopamine has a large impact on the brain and it is mainly known for its rewarding dimension, it is, indeed, the molecule associated with reward prediction and punishment. Few regions in the brain produce dopamine and these regions are impaired in Parkinson's disease or disrupted in major depressive disorders. Concerning Parkinson's disease, I designed a firing-rate model to fit experimental basal ganglia neural activity, which disclosed significant changes of the neural response between control and Parkinsonian condition. Furthermore, with a Hodgkin-Huxley model accounting for the dynamics of the potassium ion, I could support the hypothesis that the brain region called lateral habenula hyper-activates and induces major depressive disorders because of unbalanced potassium concentration due to astrocyte dysfunction (Kir4.1 channels overexpression). Dopamine is also involved in synaptic plasticity, a phenomenon at the basis of memory that I explored with a third model accounting for several experimental results pertaining to spike-timing-dependent plasticity and its modulation.

Contents

1. Introduction

The stance of the neurosceptic is described by the science philosopher Denis Forest as "someone wondering about the validity, the utility or the innocuousness of the neuroscientific knowledge" (Forest, 2014). Before introducing how I used computational modelling in my work on neuroscientific projects, I would like to share my neurosceptic point of view concerning the current context of research.

This context, through the access to conferences, journals and grant applications, presents a bias in favor of positive and newsy results. Indeed, since the current system of research is also a means for its agents to fulfill their needs of financial security and appreciation, then, the validity, the utility or the innocuousness of the knowledge can become secondary. Therefore, scientific publications tend to overstate their results to become more attractive.

In addition, there is a democratization of scientific equipment, indeed, devices such as MRI imaging or EEG headsets, identifying which brain regions are activated during a task, become more precise, less costly and easier to use, leading to a craze for what neuroscience could teach us in various domains (Legrenzi and Umiltà, 2011). However, I think some results are oversold and can be misleading by rushing to hasty conclusions. To counterbalance this tendency, I think knowledge requires some "wisdom" (Aberkane, 2016), i.e. by placing a greater emphasis on its incertitudes and on the consequences of its implementations. Hence, I am worrying about the way this knowledge race can disseminate its conclusions because, for me, it lacks coherency, long-term efficiency and security on its applications.

I believe this "wisdom" can spread inside and outside of the scientific field in various ways of communication (e.g. ethics committee or popularizing science) and I simply want to engage the reader on what philosophical perspectives can bring to this issue with the following illustration.

The philosopher Denis Forest highlights that neuroscientific literature has a tendency to make a mereologic error, meaning to confer attributes, which are logically applying to the whole animal, only to one part. Hence, here, to restrict abilities of the individual only to its brain.

The example of the philosopher Ludwig Wittgenstein states that only a human can see or can be blind, and hence this human is the one seeing, not its occipital cortex, also, the human is answering its mail, not its brain. This mereologic error in certain neuroscientific speeches can have large consequences, such as suggesting that the brain is the mind. Even if most neuroscientists would probably agree that this simplification is not valid, scientific literature still contributes to propagate it. Thus, whereas this old body-mind duality is actually rather refuted by neuroscience, this mereologic error would propose a falsely new duality, the body-brain one, which is unfounded (Forest, 2014). Without necessarily changing the way to write, I think it is important to be very aware of this kind of bias and their consequences by developing our philosophical awareness.

1.1 Neuroscience and computational modelling

Through history, the brain has been studied from many aspects. From the 5th to the 17th century, the brain was compared to hydraulic models, where liquids were believed to be the support of thoughts. Then, during the 18th century, it has been associated with electrical models, since muscles and nerves were shown to be sensitive to electrical discharges (Mein, 1988). Nowadays, the brain operation is compared to parallelized calculations, Bayesian statistics and neural networks dynamics.

This very brief history shows that our representations of the brain depend largely on what can be measured and on similarities with already known concepts. These means of representation aim to simplify our understanding because the brain is a very complex object, as illustrated by the diversity of its composition, such as the plethora of molecules, cells and tissues and also by the variety of their interactions and their multi-scale effects.

In the brain, the high connectivity level makes it difficult to set up experiments with an appropriate level of control. To address that issue, mathematical models are used to represent the brain in a more comprehensive way. Mathematical models can be more convenient than experiments to test hypotheses and aim to extract the studied principle essence, by simplifying it. Computational modelling is a specific branch of mathematical modelling allowing to solve large numerical calculations.

In this thesis, I used computational modelling to study brain parts through different approaches, all in collaboration with neurobiologists and applied to experimental data. A common framework is given by the goal of contributing to a picture of the action of the neuromodulator dopamine. I studied the diversity of dopamine action at three different scales: the brain region, the cellular level and the molecular level. Dopamine has a large impact on the brain and it is mainly known for its rewarding dimension. It is, indeed, the molecule associated with reward prediction and punishment. Few regions in the brain produce dopamine and these regions are impaired in Parkinson's disease or disrupted in major depressive disorders. Concerning Parkinson's disease, I designed a firing-rate model to fit experimental basal ganglia neural activity, which disclosed significant changes of the neural response between control and Parkinsonian condition. Furthermore, with a Hodgkin-Huxley model accounting for the dynamics of the potassium ion, I could support the hypothesis that the brain region called lateral habenula hyper-activates and induces major depressive disorders because of unbalanced potassium concentration due to astrocyte dysfunction (Kir4.1 channel overexpression). Dopamine is also involved in synaptic plasticity, a phenomenon at the basis of memory that I explored with a third model accounting for several experimental results pertaining to spike-timing-dependent plasticity and its modulation.

1.2 Parkinson's disease

In the context of Parkinson's disease, we collaborated with experimentalists (Laurent Venance team from Collège de France, Paris) to explore the basal ganglia, a brain region known to be impaired in Parkinsonian patients. Parkinson's disease is widespread in the world and it is characterized by motor symptoms in early stages, such as tremor and muscle rigidity, then difficulties at higher cognitive level, such as planning and solving problem and finally, if not treated, apathy and anxiety. It is a neurodegenerative disease, meaning that specific neurons become dysfunctional, targeting especially neurons of the basal ganglia, a brain region involved in motricity control and executive functions. The main characteristic of Parkinson's disease is a lack of dopamine, it can be partially counterbalanced by the intake of a substitute.

In order to better understand this disease and to detect its early stages directly from the activity of the brain, the aim of this project was to investigate differences between basal ganglia activity of control and Parkinsonian rats. The cerebral cortex consists of an outer zone of neural tissue involved in high cognitive functions, such as attention, language or perception. It also impacts different subregions (or nuclei) of the basal ganglia and through different neural pathways.

Hence, by stimulating the cortex of rats and recording the neural response of the substantia nigra pars reticulata, one nucleus of the basal ganglia, the characteristics of the pathways between the cortex and the basal ganglia could be captured and compared between both control and Parkinsonian conditions. Indeed, the neural response of this specific nucleus is of peculiar interest because it is the output nucleus of the basal ganglia, so it accounts for all the information received and processed by the basal ganglia. Next, this information transits to the brainstem and spinal centers which then stimulate muscles. Therefore, these recordings seem to be a pertinent target to compare brain activity between both conditions.

After we treated the recorded data from anesthetized rats, we created a computational model that we fitted on each recording, in order to characterize each of them rigorously. We could then compare the parameters of the model associated to each class (control or Parkinson). With statistical analysis, we could show that there was no significative difference of response between control and Parkinsonian rats. However, there were different proportions of neural response type between both conditions, suggesting that pathways between the cortex and the basal ganglia are not modulated in Parkinson's disease but that the proportion of operating pathways is different. This result suggests that Parkinson's disease could be detected through a set of basal ganglia's neurons activity.

1.3 Major depressive disorder

In this section, we explore the origins of major depressive disorder, in collaboration with experimentalists (Hu's team from Zhejiang University, Hangzhou, China). Major depressive disorder causes a large variety of symptoms such as low mood, loss of motivation, feelings of despair and inaptitude to feel pleasure (anhedonia). Impairments in the habenula brain region would be one of the causes. Indeed, in control condition, the habenula inhibits dopaminergic neurons of the ventral tegmental area, involved in the reward system. On the contrary, in depression cases, the habenula becomes hyperactive and hence, inhibits more these dopaminergic neurons. However, the reasons behind this hyperactivity are still unknown.

The goal was to get some insight into the source of rats' habenula hyperactivity. The habenula comprises a heterogeneous population of neurons which can be categorized according to their firing pattern: silent neurons, spiking neurons and bursting neurons. Silent neurons show no firing activity in slices, at rest, and represent the majority of habenula's neurons population. Spiking neurons fire single spikes whereas bursting neurons fire groups of spikes at high frequency. Experiments on rats brought to light that in depression conditions the proportion of bursting neurons in the habenula is higher than in control condition, leading to the hypothesis that bursting neurons are responsible for the hyperactivity of the habenula. We designed a computational model of the pathway from the habenula to the dopaminergic neuron that supports the idea that increasing the proportion of bursting neurons do inhibit better dopaminergic neurons. By comparing the effect of different frequencies in spiking and bursting mode, the model also suggests that the effect of habenula hyperactivity is only due to an increased quantity of spikes rather than a specific pattern of bursting mode.

Furthermore, experiments in the habenula show that neurons can shift from spike firing to burst firing when their membrane voltage is more negative, namely hyperpolarized. The responsible for this hyperpolarization would be specific potassium channels located on the membrane of astrocytes. The astrocytes represent another type of cell in the brain, not firing, that are surrounding neurons. The astrocyte possesses channels clearing the potassium expelled by the neuron when it is firing, they are inwardly rectifying K+ (Kir) channels. Namely, the fact that they let potassium enter or exit depends mainly on the potassic concentration imbalance between the inside and the outside of the astrocyte. This imbalance is called the electrochemical gradient of K+. To support this hypothesis, we implemented another computational model with three compartments, the neuron, the astrocyte with Kir channels and the space between the neuron and the astrocyte, the extracellular space. In accordance with experiments, when Kir channels were overexpressed on the surface of the astrocyte, the concentration of K+ in the extracellular space diminished enough to hyperpolarize both the neuron and the astrocyte. This result suggests that, since bursting neurons are more hyperpolarized than spiking neurons, the overexpression of Kir channels would shift spiking neurons to bursting mode, leading to the hyperactivity of the habenula in depression condition. Thus, these Kir channels could be the target for new drugs to treat major depressive disorder.

1.4 Synaptic plasticity

In this study, we collaborated again with (Laurent Venance's team from Collège de France) but also with computational scientists (Kim Blackwell team from George Mason University, Fairfax, VA, USA) to design a model accounting for synaptic plasticity at the molecular level. Synaptic plasticity is the capacity of synapses to adjust their efficiency depending on events. It is a phenomenon at the basis of memory and learning. However, the whole molecular machinery of synaptic plasticity is barely understood, in particular because of the many actors involved in it, but also because of the great diversity of plasticity rules. Indeed, these rules depend on the brain region, the neural types of the synapse and also the features of the stimuli. In order to restrain our study, we focused on spike-timing dependent plasticity (STDP) protocols with a model combining previous models of the literature to ours. These previous models presented either endocannabinoids or dopamine molecules shaping STDP, but not both. Our work was to unify them and their properties on STDP in one computational model.

Spike-timing dependent plasticity is highlighted with a specific experimental protocol, where pre- and post-synaptic neurons are firing at precise timing. The classical rule, called the Hebbian rule, specifies that neurons firing in the pre- then post-synaptic order increase the efficiency of the synapse whereas the reverse order decreases the efficiency of the synapse. Nevertheless, depending on the type of synapse (excitatory or inhibitory), the brain region or the neuromodulator molecules involved, this rule can be modified. In the first instance, the goal was to fit a model on experimental data of STDP with a clear calcium trace. We merged two computational models and preserved characteristics from both of them. A major issue was to find an equilibrium between each molecular pathway to preserve dynamics of interest while staying in a realistic range of parameter values. We successfully obtained a model reproducing some of the experimental results of plasticity, depending on the timing of stimulation and on the presence of dopamine. This model can now be specifically fitted on experiments recording realistic calcium's fluctuations, which has not been done yet and would be a huge breakthrough to understand synaptic plasticity.

1.5 Organisation of the manuscript

The rest of the thesis is organised as follows: in chapter 2 we describe the current state of our understanding of spike-timing dependent plasticity, depression and Parkinson. In chapter 3 we present a project at the brain region level, on the basal ganglia activity of Parkinsonian rats with a computational analysis of the experimental data, then in chapter 4 we describe the project on depression, at a cellular level, with two computational models; one involving a dopaminergic neuron and one involving a neuron of the habenula region, a surrounding astrocyte and the extracellular space between them. Finally, in Chapter 5 we show a computational model of a synapse, at the molecular scale, where synaptic plasticity is possible.

2. State of the art

2.1 Basal ganglia and Parkinson's disease

Basal ganglia constitute the main brain region involved in Parkinson's disease (PD). This section will present PD, starting with dopaminergic neurons, continuing with anatomical details and main functions of basal ganglia, and, finishing with the experiments and the computational models approaches used to better understand PD.

2.1.1 Dopamine and anatomy of the basal ganglia

Since the loss of dopaminergic neurons, in the basal ganglia, is the main consequence of Parkinson's disease, dopaminergic neurons and dopamine will be introduced, then, each nucleus that takes part into basal ganglia and how they are interconnected with each other.

Dopaminergic neurons and dopamine

In the brain, there are around ten areas producing dopamine (DA) (Kandel et al., 2013); however, the two main areas are the substantia nigra pars compacta, part of the basal ganglia, and the ventral tegmental area, part of the midbrain (Berger et al., 1991)(Schultz, 1998). One nomenclature of these cell groups respectively designated them as A9 and A10 (Dahlström and Fuxe, 1964). These two brain regions are related to executive functions such as motivation, reward learning and working memory, a cognitive capacity combining temporary storage and manipulation of information (Seamans, 2007).

The dopaminergic neurons present two major patterns of firing activity, tonic and phasic, which could encode different signals (Grace, 1991)(Grace, 2000). The tonic activity is a regular spike-firing pattern, between 1 Hz and 6 Hz, usually exhibited in the absence of salient stimuli (Grace and Bunney, 1984a)(Schultz et al., 1997). The tonic activity maintains a basal level of DA in afferent regions. However this level can be increased or decreased by stimuli and influence the number of DA receptors (Grace, 1991), between 0.3 and 15 nM in the striatum and the prefrontal cortex (Devoto et al., 2001)(Shoblock et al., 2003).

On the contrary, in phasic activation, DA neurons can reach 20 Hz of firing rate (Grace and Bunney, 1984b)(Kiyatkin and Stein, 1995), consequently, extracellular DA concentration increases significantly and transiently, evoking a wide range of changes on efferent neurons (Phillips et al., 2003)(Lavin et al., 2005) (Seamans and Durstewitz, 2008) (see also part 2.3.4 on modelling dopaminergic neurons).

Furthermore, dopamine is a neuromodulator. The action of a neuromodulator is larger than a neurotransmitter. A neurotransmitter is restricted to the synapse where it has been released. When it has been used, it is reuptaken and recycled. On the contrary a neuromodulator is not reabsorbed or broken down into a metabolite, instead, it is spread in different areas of the brain through the cerebrospinal fluid and regulate diverse populations of neurons (Burrows, 1996)(Schwartz and Javitch, 2013).

Finally, in the context of PD, the dopaminergic neurons loss of the substantia nigra pars compacta involves the basal ganglia.

Nuclei of basal ganglia

Basal ganglia form a brain region involved in diverse processes such as action selection (chose the next action among several possibilities, cf. part 2.1.2), reinforcement learning (learning from consequences of action in an environment cf. part 2.1.2) and procedural learning (involved in the acquisition of skills and habits cf. part 2.1.2). They receive inputs from the whole cortex and from the thalamus, and then, output back to the thalamus (forming a loop), to the brainstem and spinal centres, which then stimulate muscles. They are composed of six subnuclei, which have been grouped because of their close functionalities, not their proximity (Figure 2.1).

The basal ganglia contains two major input nuclei, the striatum and the subthalamic nucleus (STN), and two major output nuclei, the substantia nigra pars reticulata (SNr) and the internal globus pallidus (GPi) (Figure 2.2). The external globus pallidus (GPe) exchanges almost exclusively with the other structures of the basal ganglia. Finally, the substantia nigra pars compacta (SNc) is composed of dopaminergic neurons and project on other subnuclei, mainly on the striatum (Redgrave, 2007).

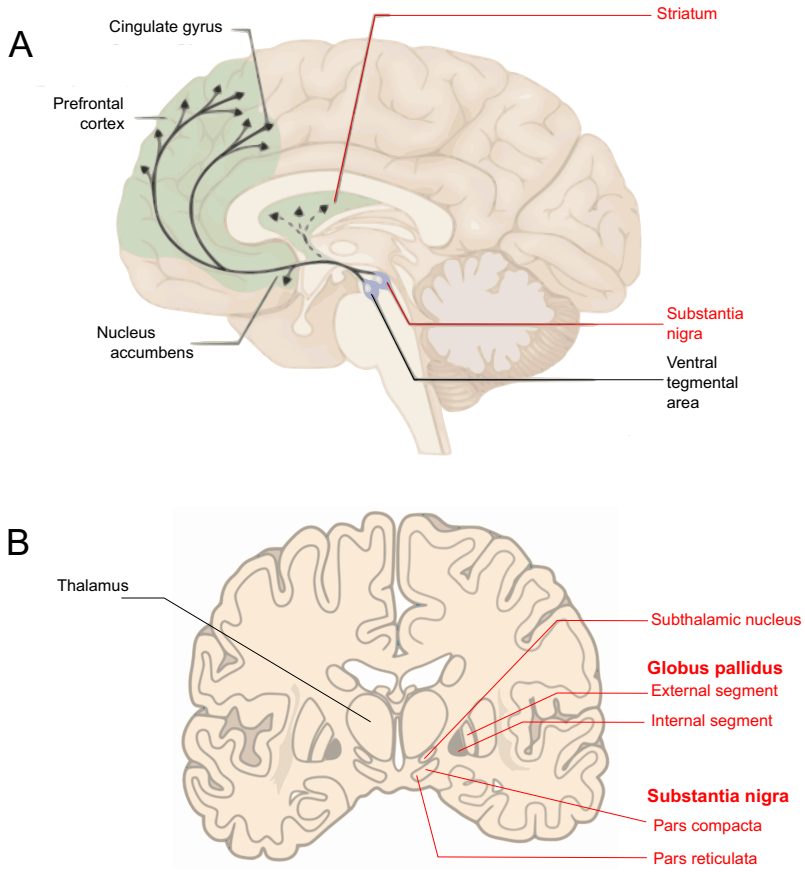

Figure 2.1: A) Sagittal view of the human brain. B) Coronal view of the human brain. In red are the nuclei of the basal ganglia. Modified from Kandel et al. (2013)

Striatum The striatum receives direct input from the cerebral cortex and thalamus (Figure 2.2). Indirect inputs come from the brainstem through the thalamus. Dopaminergic and serotoninergic inputs come from the midbrain, respectively from SNc and from the raphe nuclei. In the striatum, the dorsal part is usually distinguished from the ventral part. Besides, the dorsal striatum is composed by the putamen and the caudate nucleus

whereas the ventral striatumt is formed by the nucleus accumbens, the olfactory tubercle and the ventromedial caudate nucleus.

GABAergic medium spiny neurons (MSNs) are representing more than 90% of all neurons in the striatum. And spiny neurons have been divided into two populations depending on the dopamine receptor type D1 or D2 they express and according to the neuroactive peptide they hold, either substance P and dynorphin or Enkephalin (Surmeier et al., 2007).

Subthalamic nucleus The subthalamic nucleus is situated between the thalamus and the substantia nigra. It receives projections from the external segment of the globus pallidus, the cerebral cortex, the thalamus, and the brainstem, and sends output to both segments of the globus pallidus and to the substantia nigra pars reticulata (Figure 2.2) (Wichmann and DeLong, 2013). Moreover, the subthalamic nucleus is involved in hyperdirect and direct pathway. It receives afferents from the GPe but also directly from the cortex (Nambu et al., 2002).

External globus pallidus The external globus pallidus receives inhibitory input from the striatum, excitatory input from the subthalamic nucleus, and provides GABAergic inhibitory efferent connections to all the basal ganglia's input and output nuclei (Chan et al., 2005). It also provides inhibitory input to the SNc (Parent et al., 1999).

Internal globus pallidus / Substantia nigra pars reticulata Neurons of the internal globus pallidus are GABAergic and receives inhibitory GABAergic inputs from the striatum and the external globus pallidus, and excitatory glutamatergic input from the subthalamic nucleus (Parent et al., 1999). The substantia nigra pars reticulata also receives inhibitory (GABAergic) inputs from the striatum and the external globus pallidus and excitatory inputs from the subthalamus (Gerfen and Wilson, 1996). Neurons of the pars reticulata are GABAergic and inhibit strongly parts of the thalamus and brainstem (Chevalier and Deniau, 1990).

Substantia nigra pars compacta Substantia nigra pars compacta contains dopaminergic neurons; most of their dopaminergic terminals are in the striatum where they make synaptic and non-synaptic contact with both MSNs and interneurons (Sulzer, 2005).

Thus, this set of subnuclei forms the basal ganglia that are organised around three main pathways.

Three pathways between cortex and SNr

Two pathways were discovered from the cortex to the output nuclei of the basal ganglia (the SNr and the GPi); the direct pathway and the indirect pathway (Albin et al., 1989) (Figure 2.2). Inputs from the cortex reach the two populations of neurons of the striatum, neurons with D1-type dopamine receptors and neurons with D2-type dopamine receptors. Then, in rodents, D1 neurons of the striatum make exclusively direct contact to the GPi/SNr, forming the direct pathway. On the contrary, D2 neurons of the striatum connect exclusively to the globus pallidus and subthalamic nucleus, which then connect to the GPi/SNr, forming the indirect pathway. However, in primates, this segregation of dopamine receptors on MSNs between the direct and the indirect pathway is not so clear (Lévesque and Parent, 2005).

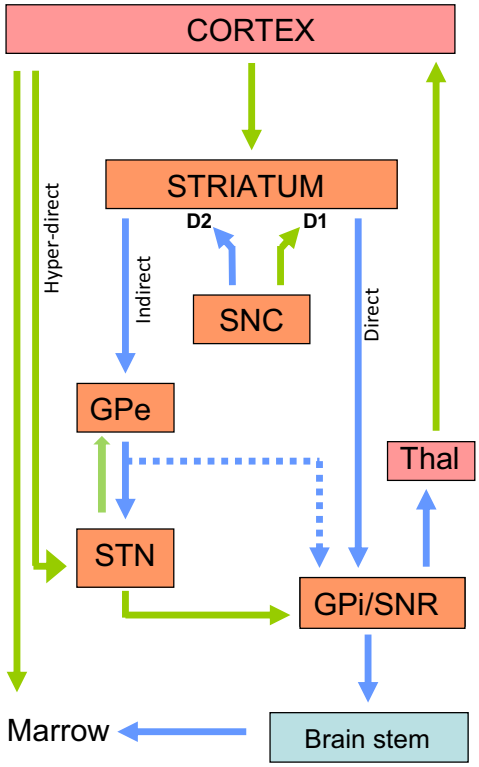

Figure 2.2: Scheme of the three pathways between the cortex and the SNr, in the basal ganglia circuit. Nuclei of the basal ganglia are orange. Green arrows are excitatory whereas blue arrows are inhibitory. D1 and D2 are two different types of dopaminergic receptors. Many other connections are not shown.

In addition, the STN also receives a direct input from the cortex called the hyperdirect pathway (Berendse and Groenewegen, 1991)(Mathai and Smith, 2011) or the additional indirect pathway (Smith et al., 1998). This hyperdirect pathway has been discovered more recently and is less known. Thus, a cortical stimulation implies a response in the SNr with three phases, one for each pathway; hyperdirect, direct and indirect (Figure 2.3). This triphasic response is obtained by alternating disinhibition and direct inhibition, indeed, the hyperdirect pathway activates directly the GPi/SNr via STN relay, the direct pathway inhibits the GPi/SNr via the striatum and the indirect pathway activates the SNr via the disinhibition of the GPe-STN inhibition (Maurice et al., 1999)(Degos et al., 2005) (Figure 2.2). Moreover, each pathway latency is correlated with the number of nuclei constituting it, since there are very few connections between neurons within each nucleus. Thus, the fastest pathway is the one involving fewer nuclei, the hyperdirect one.

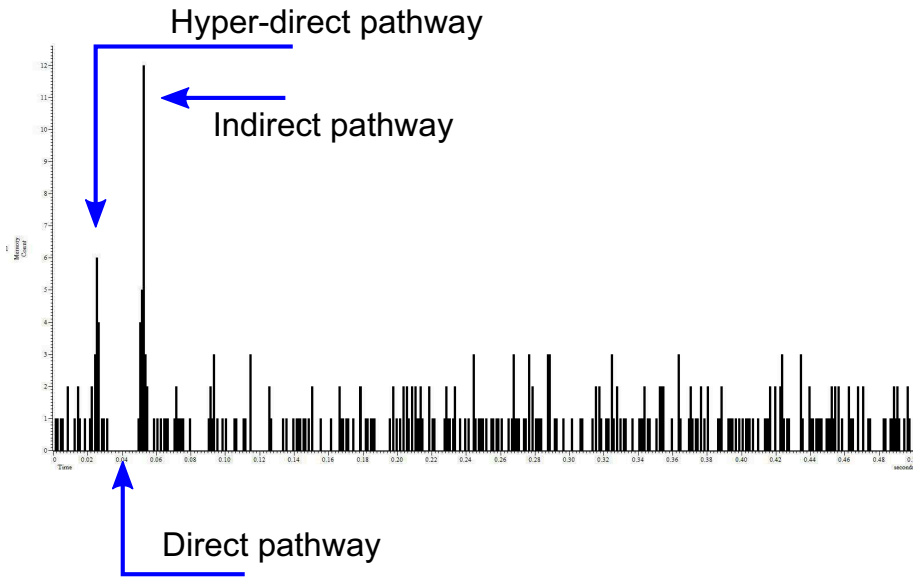

Figure 2.3: Aggregated spike series of the SNr after one stimulus in the cortex, over 50 repetitions.

Different approaches confirm this triphasic response associated with three pathways, for example, through technics to preserve the hyperdirect pathway in a rodent brain slice (Bosch et al., 2012). Or application of immunotoxin to eliminate a neuronal population of a particular pathway, leaving intact other pathways (Takada et al., 2013). Or else viral vectors which enable neuronal or glial subpopulations to be labelled and stimulated in a spatially restricted area with optogenetic and designer drugs and which could even lead to new treatments (Sizemore et al., 2016).

Since the SNr inhibits the brainstem, which then project on muscle fiber, the triphasic response can be interpreted as the selection of a motor action delimited in time by these three phases; first inhibition, then activation and inhibition again, where the inhibiting phases could act to prevent interferences with competing motor mechanisms generated by other parts of the brain (Mink, 1996), (Nambu et al., 2002).

In reality, there are more connections between nuclei of the basal ganglia that these three pathways. For example, both types of MSNs project to the GPe, directly for D2 neurons, whereas for D1 neurons it occurs via collateral from the fiber innervating the output nuclei (Parent et al., 2000). Also, neurons of the globus pallidus (GPe and GPi) directly connect to the subthalamus (Smith et al., 1998), moreover, they project back to the striatum (Bevan et al., 1998).

Nevertheless, there is a topographic order in these connections; some projections are more focused, and others are more diffused (Mink, 1996). Besides, some regions contain more neurons than other, suggesting a compression of information (Oorschot, 1996).

Thus basal ganglia are organised around six nuclei and three main pathways and the next part will expose how this organisation fulfill the main functions of the basal ganglia.

2.1.2 Main functions of the basal ganglia

In humans, many disabilities are associated with basal ganglia dysfunctions, including Parkinson's disease, Huntington's disease, Tourette's syndrome, schizophrenia, attention-deficit disorder, obsessive-compulsive disorder, and many of the addictions (Redgrave, 2007). It is essential to understand the normal behaviour of the basal ganglia to explain those pathologies. In the literature, there are three major functions with which basal ganglia are involved; action selection, reinforcement learning and procedural learning.

Action selection

Action selection is a task of decision-making in order for the agent to best achieve its goals. For example, a cyclist choose to turn left or right. The circuitry, implicated in voluntary movement initiation and execution, starts from the motor areas of the frontal cortex. These motor areas project to motor portions of the basal ganglia, in particular to the striatum and the subthalamic nucleus. These input structures of the basal ganglia connect to the external and internal globus pallidus external segments and the substantia nigra pars reticulata (Figure 2.2). The basal ganglia projects to the thalamus, which, in turn, projects back to the frontal motor areas of the cortex (Parent and Hazrati, 1993). These partially closed loops would modulate the neural activity issued from the frontal motor areas of the cortex to brainstem and spinal centres, which then stimulate muscles.

Although the basal ganglia are a highly conserved subcortical circuit in vertebrates (Medina and Reiner, 1995), the cortical motor and thalamic circuits have widely changed. Indeed, dorsal basal ganglia circuit receives around 20 million projection neurons in rats, from the neocortex (Zheng and Wilson, 2002) whereas the output by the SNr is around 25,000 projection neurons (Oorschot, 1996). This bottleneck functional organisation would be consistent with the idea that a motor movement is the combination of the output commands from the motor cortex with a motivation component from the basal ganglia (Dudman and Krakauer, 2016). This motivation component would act on the movement vigor, which corresponds to its speed, its amplitude or its frequency (Turner and Desmurget, 2010).

Thus, since vertebrates are noticeable for their capacity to select and execute goal-oriented actions, and since only the circuitry between the motor cortex and the basal ganglia has drastically changed, one can argue that, in early vertebrates, the basal ganglia played a direct role in the control of movement and has evolved to a more indirect and specific role in controlling movement vigor (Dudman and Krakauer, 2016). Besides, recent optogenetics experiments on rats, showed that the direct and the indirect basal ganglia pathways are necessary for both the initiation and the performance of an action sequence (Tecuapetla et al., 2016), suggesting that these pathways have a major role and a functional specificity in action selection.

Reward functions, reinforcement learning

Reinforcement learning (RL) is learning by interacting with an environment. RL is primarily a trial-and-error learning, where the RL agent learns from the consequences of its actions. It selects its actions on the basis of its experiences (exploitation) or it tests new choices (exploration) (Woergoetter and Porr, 2008).

The basal ganglia are largely involved in reinforcement learning through their properties of reward prediction errors. Indeed, dopaminergic neurons of the substantia nigra pars compacta, and also those of the ventral tegmental area, projecting to the striatum and frontal cortex, could signal expected reward value and motivational state in a context-dependent manner (Bayer and Glimcher, 2005). In effect, there is not a specific receptor to capture the motivational component of rewards, rewards affect our body through all sensory systems (Schultz, 2015).

Thus, dopaminergic neurons will fire more if the individual gets an unexpected reward after an action or a stimulus, on the contrary, the absence of a reward whereas it was expected, will inhibit dopaminergic neurons (Schultz et al., 1997). This comportment of dopaminergic neurons is known as a reward prediction error because dopaminergic neurons will change their firing frequency, in one way or the other, until the individual expects the exact reward it gets, after a stimulus or an action (Figure 2.4) (Schultz, 1998). A conditioned stimulus (CS) is a neutral stimulus, in this experiment it was a yellow light

turning on and reward (R) was a delivery of liquid, knowing that monkeys were deprived of fluids during weekdays. Hence, the dopaminergic discharge is shifted in time during the learning phase; before the learning phase is achieved, the dopaminergic neural discharge occurs just after the reward (Figure 2.4 Up panel) whereas after the learning phase, it occurs just after the conditioned stimulus (Figure 2.4 middle and down panels).

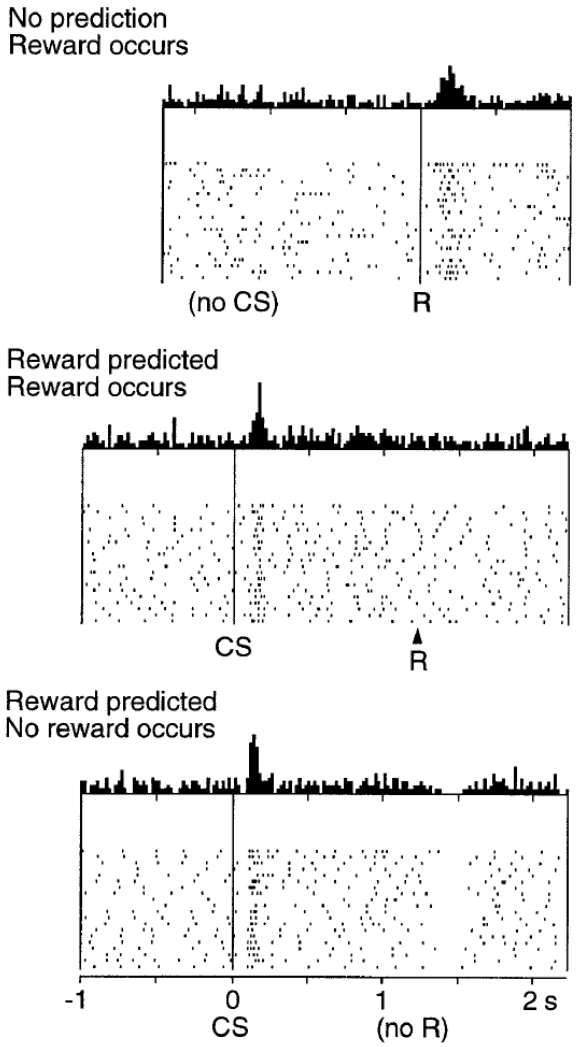

Figure 2.4: Each panel represents a specific combination of conditioned stimulus (CS) and reward (R) through recordings of twenty dopaminergic neurons. Each horizontal dot line represents the firing activity of one recorded dopaminergic neuron over time. Only one neuron at a time was recorded in each trial and the barplot at the top of each panel is the aggregation of firing rate activity of twenty trials over time. Conditioned stimulus (CS) is a yellow light turning on and reward (R) is a delivery of liquid directly in the mouth of monkeys. The upper panel shows a positive reward prediction error because the reward (R) was not expected, there is no conditioned stimulus (no CS). On the contrary, the intermediate panel presents zero error in prediction because the reward was expected and occurred. Finally, the lower panel shows a negative reward prediction error because the reward was expected and did not occur (Schultz et al., 1997)

This signal from dopaminergic neurons is proportional to reward probability, to reward magnitude and includes negative reward prediction errors (Tobler et al., 2005). Besides, dopaminergic neurons can also signal punishments, since the activity of dopaminergic neurons is inhibited by them. Thus, they can integrate both, reward and punishment to direct learning (Matsumoto et al., 2016). They may also code the uncertainty (Niv et al.,

2005) (Fiorillo et al., 2003) and the salience of a reward (Redgrave and Gurney, 2006). The saliency of a reward stands for the quality which contrasts with the environment or neighboring rewards. Moreover, as it has been shown in singing zebra finches, dopaminergic error signals can evaluate behaviours that are not learned for rewards and are instead learned by matching performance outcomes to internal goals (Gadagkar et al., 2016).

Furthermore, by locally inactivating associative part of the monkey striatum, the acquisition of novel motor sequences is impaired, however, the execution of learned sequences is not affected. On the contrary, inhibiting the sensorimotor part of the putamen (component of the dorsal striatum) prevents the execution of learned sequences, but animals could still acquire new ones (Miyachi et al., 1997). As a confirmation, neurons, in the sensorimotor part of the putamen, were mostly activated when monkeys performed learned sequences of moves whereas the neurons of the striatum associative part were mostly activated when monkeys were learning new motor sequences (Miyachi et al., 2002). Thus, exploration (acquisition of new motor sequences) and exploitation (activation of learned sequences), composing reinforcement learning, request two well distinct regions of the striatum in monkey.

Finally, the basal ganglia, through their involvement in reinforcement learning and in action selection, are directly linked to movement control, which is largely corroborated by diseases and lesions of this region. The following section is about procedural learning, a specific form of implicit learning. There are several implicit learning, like priming learning, procedural learning (skills and habits), associative learning (classical and operant conditioning) and non-associative learning (habituation and sensitization). They are grouped under the label "implicit" because they take place without recourse to conscious thought and subjects are unable to express what they have learned.

Procedural learning

Procedural learning is a type of implicit learning exclusively found in the basal ganglia, in particular in the striatum, that is involved in skills and habits acquisition. Procedural learning often takes place without consciously thinking about it and skills can be retained for long periods of time without practice (e.g. riding a bicycle) (Kandel et al., 2013).

In order to study procedural learning, one can use a "choice reaction time" experiment, where subjects, presented with four buttons that light up in sequence, have to press as fast as they can each button after it lights up. The subject does not know that the buttons light up in a particular sequence. Obviously, knowing the sequence enables the subject to predict which button will light up next and thus to press it more quickly. In fact, responses become faster once the sequence is predicted, even when the subject is totally unable to describe the sequence, showing the effect of procedural learning in an unconscious way (Kandel et al., 2013).

Moreover, executing habitual movements would involve different areas of the striatum. The ventral striatum and caudate nucleus (part of the dorsal striatum) activate first, during early stages of procedural learning, whereas during later stages of learning and the execution of learned movements, the dorso-lateral striatum is more active (Kandel et al., 2013). As an illustration in primates, the experimental inactivation of the caudate nucleus impairs the acquisition of movement sequences, whereas inactivation of the putamen interferes with the performance of previously learned sequences (Miyachi et al., 2002).

Habits are routines that are acquired progressively by repetition and are the result of an implicit learning specific form. A habit is an association between a stimulus and a response, a behaviour that is triggered simply by particular stimuli rather than by desire for (or fear of) some outcome.

The caudate nucleus is implicated in certain forms of procedural learning, such as

stimulus-response associations and some forms of skill learning. Together with the ventral striatum dysfunction in several diseases in which habit learning is impaired, including obsessive-compulsive disorder and addiction (Kandel et al., 2013).

Furthermore, implicit memory based on striatum differs from explicit memory based on hippocampus. Both have been distinguished by Packard et al. (1989) using an eight-arm maze for rats. First, explicit memory is highlighted with a "win shift" foraging tasks where the rat has to find food, the reward, from every arm of the maze. The rat's task is to optimize its path by remembering the arms already visited and to shift its focus to the unvisited one. In this task, the rat has to recall specific locations it has explored on a given day, since the experiment is repeated several consecutive days. To acquire and use information about single events is a type of learning requiring the hippocampus, indeed, this task is impaired by its lesion whereas damage to the caudate nucleus has no impact. On the other hand, the same maze can be used to test implicit learning by teaching a "win-stay" strategy to the rat. In this task, the rat has to learn to visit only four arms of the maze, where there is food, identified by a light at the arm entrance. After two weeks of practice, rats visit only arms that were lit. This win-stay task, in contrast to the win-shift task, is impaired by lesions to the caudate nucleus but not by damage to hippocampus. Thus the win-stay task requires the animal to learn about regularities (light always refers to food) whereas the win shift involves remembering events on a given day (which arms have been already visited) (Packard et al., 1989).

Thus, the basal ganglia are involved in several processes such as action selection, reward functions, reinforcement learning and procedural learning, therefore their malfunction causes a large variety of symptoms.

2.1.3 Basal ganglia diseases

Basal ganglia dysfunctions are involved in various diseases, for example, hemiballism, Tourette's syndrome, Huntington's disease or Parkinson's disease.

Hemiballism

Hemiballism is a movement disorder, presenting unilateral flinging movements of the limbs, seen with acute lesions of the subthalamic nucleus. Antidopaminergic drug is the most standard treatment used and it works in ninety percent of cases (Posturna and Lang, 2003).

Tourette's syndrome

Tourette syndrome patients show behavioural and motor tics, obsessive-compulsive disorder (OCD), and attention-deficit hyperactivity disorder (ADHD). Basal ganglia seem implicated since dopamine receptor-blocking drugs suppress tics (Kandel et al., 2013).

Huntington's disease

Huntington's disease (HD) is caused by a mutation in the gene encoding huntingtin. In early stages, patients with HD, have spiny striatal neurons proliferating, later, these neurons become degenerative (Ferrante et al., 1991). In later stages, neurodegeneration occurs in both striatum and cortex, reducing their volume in living patients (Rosas et al., 2001) and at autopsy (Halliday et al., 1998). This reduction of volume is present before symptoms occur (Aylward et al., 2004).

The cognitive deficits related to HD include distractibility, impaired processing speed or emotion recognition, which suggests a role for the basal ganglia in many cognitive

functions, habitually attributed to the frontal cortex (Paulsen, 2011). Thus, behavioural abnormalities, motor or cognitive, are present during the early stage of HD (Tabrizi et al., 2013) and HD cognitive onset may precede motor (Paulsen and Long, 2014), suggesting a major role for the basal ganglia in affective control.

At the circuitry level, HD causes progressive loss of striatal medium spiny neurons (MSNs) that form direct and indirect pathways. MSNs of the indirect pathway are more vulnerable than MSNs of the direct pathway (Albin et al., 1990) (Deng et al., 2004)(Tippett et al., 2007).

One hypothesis to explain chorea movements, a symptom of HD (Albin et al., 1989), is that the loss of striatal neurons, involving the indirect pathway, could result in increasing the inhibitory action of the GPe upon the STN. The STN then is less active and causes a reduction in the inhibitory action of the GPi upon the thalamus. This disinhibition of the thalamus is supposed to result in the appearance of uncontrolled chorea movement (Singh-Bains et al., 2016).

In advanced cases of HD, the loss of substance-P in MSNs of the direct pathway, projecting from striatum to the GPi, could contribute to dystonia and the complete loss of this projection system could be associated with the akinesia of terminal HD (Albin et al., 1989). It could be explained by an increase of the inhibition of the GPi upon the thalamus, diminishing thalamus input to the cortex, contributing to a shift from hyperkinesia to hypokinesia (Deng et al., 2004).

Thus, basal ganglia impairments cause diverse form of troubles and Parkinson's disease, which is one of them, will be now described through its symptoms, its therapies and the characteristic oscillatory neuronal activity it presents in basal ganglia.

Parkinson's disease symptoms

Parkinson's disease is a common neurodegenerative disorder characterized by a progressive cell loss in multiple brain regions, particularly brainstem nuclei and the SNc. During the initial stages of Parkinson's disease, post-mortem data show that the most important loss of dopaminergic innervation is from the putamen (Kish et al., 1988) and that there is a corresponding loss of dopaminergic cells in the SNc (Fearnley and Lees, 1991). This dopaminergic deficiency in the motor circuit implies motor symptoms like tremor, muscle rigidity and hypokinesia. Besides, in early PD, dopamine deficiency in the caudate nucleus and dysfunction of the associative circuits drive impairments in executive functions such as planning and problem solving. Finally, the major psychiatric manifestations in untreated PD are apathy, anxiety and depression (Rodriguez-Oroz et al., 2009).

Thus, the loss of striatal dopamine induces basal ganglia dysfunctions which contribute to both motor and non-motor symptoms (Cools, 2006). However, post-mortem studies comparing the brains of Parkinsonian and control patients, in addition of animal experiments, show that the first motor symptoms of the disease occur when more than 70% of striatal dopamine are lost. That is, the basal ganglia-thalamocortical network can strongly compensate for changes in dopamine levels (Wichmann and DeLong, 2013).

Post-mortem studies of animal models and PD patients have also revealed significant pathology of glutamatergic synapses, dendritic spines and microcircuits in the striatum of parkinsonians (Villalba et al., 2015). Moreover, recent findings have shown a significant defect of the glutamatergic corticosubthalamic system in Parkinsonian monkeys.

Furthermore, patients with PD have troubles expressing automatic components of behaviour (Hoshiyama et al., 1994) and are disturbed in their implicit learning of habits (Knowlton et al., 1996) (Wu et al., 2010). This disruption of automatic and well-learned movements seems to reflect a loss of the basal ganglia's role in procedural learning (Wichmann and DeLong, 2013). Indeed, in 6-hydroxydopamine lesioned rats (see section 2.1.3),

a selective loss of dopamine from the lateral SNc and the lateral striatum prevents them from developing habits, instead, their behaviour stayed goal-oriented, compared to control animals (Faure et al., 2005).

Because of this constant goal-directed processing in PD patients, their tasks are subject to interference (Benecke et al., 1986) (Nieuwboer et al., 2009). Indeed, since they require a conscious decision to start a task, a different external stimulus can then stop them abruptly (Hallett, 2008)(Okuma and Yanagisawa, 2008).

Impairments of the basal ganglia and its classical triphasic response (see section 2.1.1), caused by Parkinson's disease, can lead to a variety of symptoms, for example, abulia, bradykinesia, dystonia and changes in the basal ganglia output activity, which will be detailed in the next paragraphs.

Abulia The abulia refers to a lack of motivation, and can be produced by many diseases involving impairments into the basal ganglia like depression, Huntington's disease or PD. There would be a double dissociation between the neural substrates associated with goal-directed and stimulus-response habitual. Indeed, in animals, inactivating the rostromedial striatal loops disturbs goal-directed control, but not stimulus-response habitual (Yin et al., 2005a) (Yin et al., 2005b). On the contrary, inhibiting the caudolateral striatal loops impairs habitual responding, but not goal-directed control (Yin et al., 2004)(Yin et al., 2006). As a parallel, comparing PD patients and those having abulia shows a similar dissociation.

The abulia symptoms are apathy and poverty of thought, however, if they are instructed to do so, patients with abulia can perform a wide variety of task. The initiation of the behaviour must be maintained by external stimuli (Cutsuridis, 2013). Focal lesions to medial sectors of the basal ganglia, which could involve both associative and mesolimbic territories (Redgrave et al., 2010) would cause abulia. Thus, abulia would be characterized by a major loss of the internally motivated goal-directed behaviour with a relative preservation of the stimulus-response (Vijayaraghavan et al., 2002) (Habib, 2004).

Bradykinesia Bradykinesia corresponds to slowness of movement and is one of the PD major symptoms. To further extend, bradykinesia leads to akinesia, where, cognitively, the generated movements are not automatic anymore and require more attention and concentration. Besides, movements are interfered when novel movements are attempted (Connor and Abbs, 1991) or when there is a sequence of movements to execute (Benecke et al., 1986) (Lazarus and Stelmach, 1992).

The optogenetic activation of the indirect pathway (see section 2.1.1) would cause bradykinesia by increasing freezing of the mouse, on the contrary, the activation of the direct pathway increases the locomotion (Kravitz et al., 2010). In the same idea, repetitive optogenetic activation of the indirect pathway prevents animals from moving whereas the direct pathway reinforces the animal's movement (Kravitz et al., 2012). At the opposite, during normal movement, the direct and indirect pathways are concurrently activated (Cui et al., 2013).

More specifically in the striatum, the average firing rate of medium spiny neurons increased as axial dyskinesia developed, and both medium spiny neurons and fast spiking interneurons were modulated around axial dyskinesia (Alberico et al., 2017).

Dystonia Dystonia is defined clinically by slow twisting movements, which may resemble tremor, and often resulting in abnormal postures. Voluntary movements trigger dystonic movements and they result from the co-action of agonist and antagonist muscles. Besides patients are unable to restrict movements to a single body part.

Dystonia originates mostly from impairment in the basal ganglia-thalamocortical network, because of genetic defects, focal lesions or disorders of dopamine structures. In the case of dopamine-responsive dystonia, resulting of gene mutations, the symptoms can be treated with dopamine replacement.

Moreover, dopaminergic dysfunction can cause the development of dystonia. Indeed, dystonia can occur when alterations take place in striatal dopamine transmission, when PD is not treated and when some patients receive dopamine receptor-blocking drugs, such as neuroleptics treating schizophrenia (Wichmann and DeLong, 2013).

Basal ganglia output in PD In PD patients and animals, the pattern of activity at the output of basal ganglia is different from controls (DeLong and Wichmann, 2007) (Obeso et al., 2008). The STN and the GPi neurons, in Parkinsonian condition, show increased firing activity (Figure 2.5) (Filion and Tremblay, 1991)(Rodriguez-Oroz et al., 2001) and other patterns of synchronized oscillations that in control conditions (Wichmann and Soares, 2006) (López-Azcárate et al., 2010) (Galvan et al., 2014). Contributing to the definition of the rate-model (see section 2.1.4) these increased firing activities would result in increased activity in the indirect pathway and decreased activity in the direct pathway (Figure 2.5) (Galvan and Wichmann, 2008) (Rubin et al., 2012). Futhermore, the hyperdirect pathway would also decrease in the Parkinsonian condition (Degos et al., 2005). Moreover, this increase in basal ganglia output is thought to inhibit, even more, the thalamocortical and midbrain tegmental neurons, which would explain the hypokinetic features of the disease (Wichmann and DeLong, 2013).

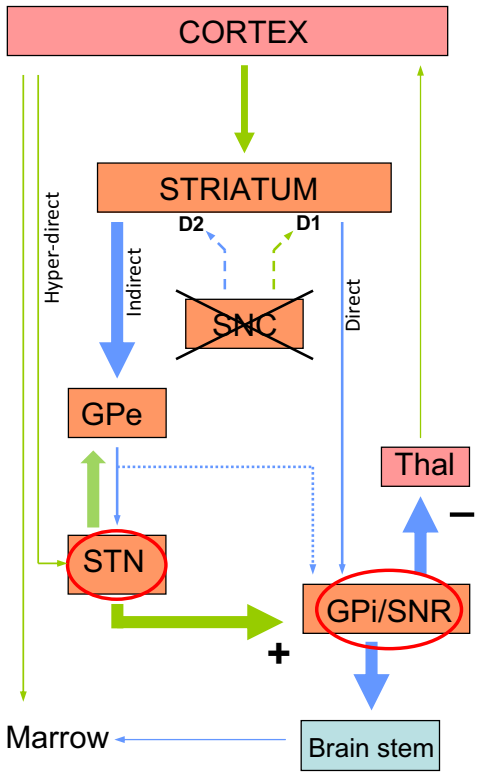

Figure 2.5: Scheme of the three pathways between the cortex and the SNr, in the basal ganglia circuit, in Parkinsonian condition. Nuclei of the basal ganglia are orange. Green arrows are excitatory whereas blue arrows are inhibitory. In Parkinsonian condition, dopaminergic neurons of the SNc are lost. The activity of the indirect pathway is increased, whereas the activity of the direct pathway is decreased. Besides, the output nuclei are hyperactivated (red circles) (Galvan and Wichmann, 2008).

As aforementioned, PD causes both motor and non-motor symptoms, however, several kinds of therapies have been explored, like injections, surgery or electromagnetic stimulation.

Parkinson's disease therapies

One way to treat PD is to use dopamine replacement therapies, such as the injection of L-3,4-dihydroxyphenylalanine (L-DOPA) (Melgari et al., 2014)(Lloyd et al., 1975). With these injections, movement abnormalities are reduced, however, non-motor symptoms such as depression, anxiety or sleep disturbances do not respond to the treatment (Wichmann and DeLong, 2013). The reason why L-DOPA is used instead of dopamine is that L-DOPA can cross the protective blood-brain barrier whereas DA cannot. Once L-DOPA has penetrated the central nervous system, the enzyme aromatic L-amino acid decarboxylase (DOPA decarboxylase) turns it in DA. Besides, pyridoxal phosphate (vitamin B6) is a cofactor in this reaction that is sometimes administered along with L-DOPA. Moreover, L-DOPA can also be turned in dopamine within the peripheral nervous system, and excessive level causes negative side effects. To bypass them, an inhibitor of DOPA decarboxylase is generally coadministered with L-DOPA.

Another way to treat movement disorders is by stereotaxic surgery. Indeed, the lesioning of the basal ganglia does not seem to aggravate motor problems and does not create new motor difficulties when lesions are unilateral (Marsden and Obeso, 1994). Besides, this treatment does not seem to induce huge effects on behaviour (Brown and Eusebio, 2008). This could lead to the conclusion that it would be better to have no output from stimulus-response habitual control circuits than a noisy one (Redgrave et al., 2010).

Furthermore, adding deep brain stimulation (DBS), after the ablation of the basal ganglia, would be an efficient way for many patients with advanced PD by targeting and compensating the basal ganglia more accurately than with drugs (DeLong and Wichmann, 2015). More precisely, subthalamic nucleus DBS decreases pathological signals to the thalamus (Anderson et al., 2015) (see also part 2.1.3).

Moreover, bee venom would have a beneficial action on motor symptoms of PD by acting on the cortico-basal ganglia circuits and could be relevant to the symptomatic treatment of this disease (Maurice et al., 2015) (Hartmann et al., 2016).

Finally, a promising path is the electromagnetic therapies such as transcranial magnetic stimulation (TMS) or pulsed electromagnetic fields (PEMF). Indeed, they are non-invasive and effective in treating both motor and non-motor symptoms PD patient (Vadalà et al., 2015).

In spite of the several kinds of therapies, most of them are only counterbalancing symptoms rather than treating the cause Besides, their functioning are not fully understood. To provide new insights on PD, another way is to explore the specific oscillations found in basal ganglia of PD patients.

Oscillations in basal ganglia

PD shows abnormal oscillations in the basal ganglia (pairs of STN neurons oscillate in phase at the beta frequency band, 15-30 Hz) and a computational approach supports that the inhibitory inputs from the striatum to the GPe form a major parameter driving oscillations. Indeed, an increase in striatal activity would unleash oscillations in the basal ganglia (Kumar et al., 2011). As PD severity increases, the information exchange between the GPe and the GPi would also increase, hence, with PD progression, the direct and indirect pathways are not working independently anymore and start to convey redundant information (Dorval et al., 2015). The loss of parallel processing would impair the ability of the network to select and implement motor commands, hence promoting the

hypokinetic symptoms of PD. However, these views of independent working pathways, in control condition, start to be controversial. Emerging evidence present the direct and indirect pathways in competition during action selection rather than as independent facilitation and suppression levers. Besides, this competition would be critical for integrating contextual uncertainty during decision-making (Dunovan and Verstynen, 2016).

The next sections will present respectively the last breakthrough with computational approaches and experimental stimulation to study these oscillations.

Computational approaches Below is a specific section dedicated to computational approaches of oscillations in PD, however, computational models of PD will be described further in section 2.1.4.

In their first model, Merrison-Hort and Borisyuk (2013) considered only the direct and indirect pathways, from the cortex to the globus pallidus (GP), one via the striatum and another one via the STN. To better understand how these pathways produce oscillations in the Parkinsonian GP, they used a neural network model. To model pallidal neurons they used Hodgkin-Huxley like models (see part 2.3.2) receiving oscillatory cortex inputs from integrate-and-fire STN neurons (see part 2.3.1)(Figure 2.6). By using a homogeneous population of GP neurons they observed a self-organised dynamic behaviour where two groups of neurons emerge: one population of GP neurons spike in-phase with the cortical rhythm (SWA) while another population spikes in anti-phase, in agreement with experiments (Merrison-Hort and Borisyuk, 2013).

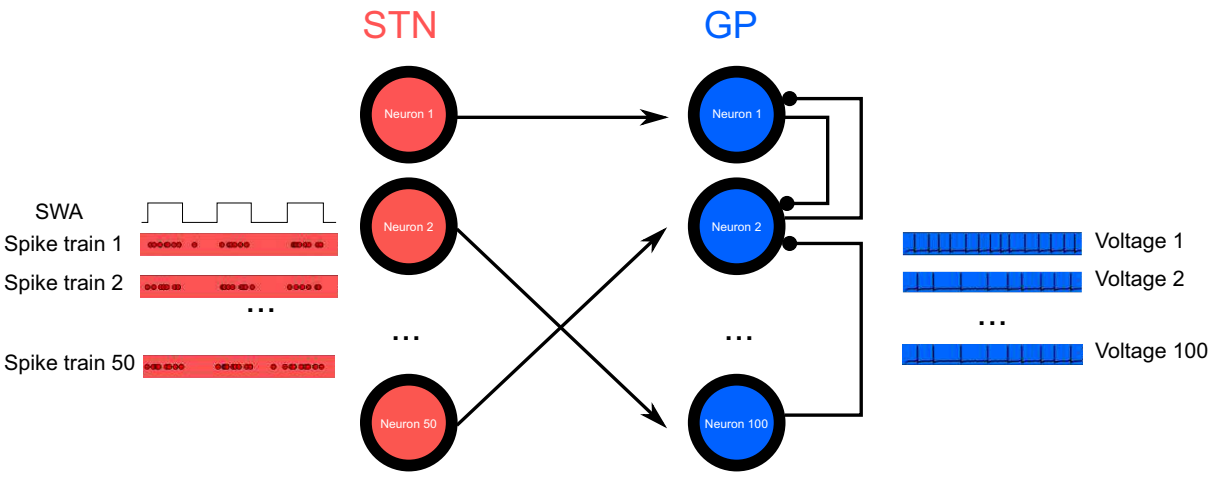

Figure 2.6: Integrate-and-fire STN neurons, modulated by an approximately 1 Hz rhythm, a slow-wave activity (SWA), provide excitatory synaptic input to a population of GP neurons. Local inhibitory synaptic connections between GP neurons have random connectivity (Merrison-Hort and Borisyuk, 2013).

Another biophysical network model, based on Hodgkin-Huxley equations, predicts that the pallidostriatal pathway (from globus pallidus to the striatum) influences striatal output preferentially during periods of synchronized activity within GPe (Corbit et al., 2016). Hence, GPe may play a central role in propagating abnormal circuit activity to the striatum, which in turn projects to downstream basal ganglia structures.

Wei et al. (2015) studied the role of the indirect basal ganglia pathway in decision-making with a neural network based on integrate-and-fire model (see part 2.3.1), and observed the emergence of oscillations. The indirect pathway would counterbalance the direct pathway in their projections to the output nucleus. Moreover, in the model, changing the connections of basal ganglia, in a similar way that in PD, give rise to beta oscillations. In particular, beta oscillations are produced by an abnormal increase of interactions

between the STN and the GPe in the indirect pathway. The oscillation frequency depends on the excitatory cortical input to the STN and the inhibitory input to the GPe from the striatum (Wei et al., 2015).

Consistent with experiments (Tachibana et al., 2011), Pavlides et al. (2015) used a firing-rate model (see part 2.3.5) and by assuming that Parkinsonian beta oscillations are generated in the cortex could explain the data when the STN-GPe circuit resonates at the same frequency. This model also reproduces the data by assuming that the feedback from the STN-GPe circuit to cortex is important for maintaining the oscillations in the network (Pavlides et al., 2015).

Thus, through different approaches, all these computational models are converging to support the hypothesis that the abnormal apparition and sustainability of beta oscillations in the basal ganglia depends on the interaction between the STN and the GPe nuclei.

High-frequency (HF) and deep brain (DB) stimulations The neuroleptics can be used to block dopaminergic receptors and hence can mimic some effects of PD due to the decrease of dopamine levels. Then, by using rats with neuroleptic-induced catalepsy, considered to be an animal model of the akinesia and the rigidity seen in Parkinson's disease, Degos et al. (2005) showed that high frequency stimulation of the STN (HFS) permits to reverse this catalepsy. Indeed, neuroleptic injection alters the tonic and regular mode of SNr neurons discharge, most of them becoming irregular with bursts of spikes and pauses. Besides, the direct pathway in the basal ganglia has a decreased activity whereas the indirect pathway has an increased activity. However, during STN HFS, the SNr firing pattern was regularized, and the bias between the direct and the indirect pathways was reversed (Degos et al., 2005).

To go further, the thalamo-cortical network of Parkinsonian rats, corresponding to the output of the basal ganglia, is also changed electrophysiologically. And STN HFS applied at parameters alleviating Parkinsonian signs regularized the firing pattern of pyramidal cells and restored their electrical membrane properties (Degos et al., 2013). Thus, converging with computational results in the previous section 2.1.3, direct HFS treatment on the STN seems to support the idea that the abnormal activity of this nucleus is a key factor in PD symptoms.

In order to study PD, neurobiologists use several models of rats. In one of them, they induce lesions in the substantia nigra pars compacta with surgery, where they specifically kill dopaminergic neurons by injecting 6-hydroxydopamine (6-OHDA) (Figure 2.7) (Simola et al., 2007) (Koob et al., 1978) (Blesa and Przedborski, 2014). The loss of dopamine includes electrophysiological changes in firing rates, bursting activity, neuronal oscillations, and synchrony. These symptoms are characteristic of PD (Ellens and Leventhal, 2013). A biophysical model, based on Izhikevitch equations, of the cortex-basal ganglia-thalamus network, in the Parkinson's disease 6-OHDA lesioned rats model, suggests that high frequency (HF) DBS in the STN suppresses pathological oscillations in GPe/GPi both by exciting and inhibiting the firing in GPe/GPi neurons. Besides, the number of GPe/GPi influenced neurons was greater with HF stimulation than with low-frequency stimulation (Kumaravelu et al., 2016). This paper suggests that the action of DBS in the STN diminishes the pathological oscillations in the globus pallidus (GPe/GPi).

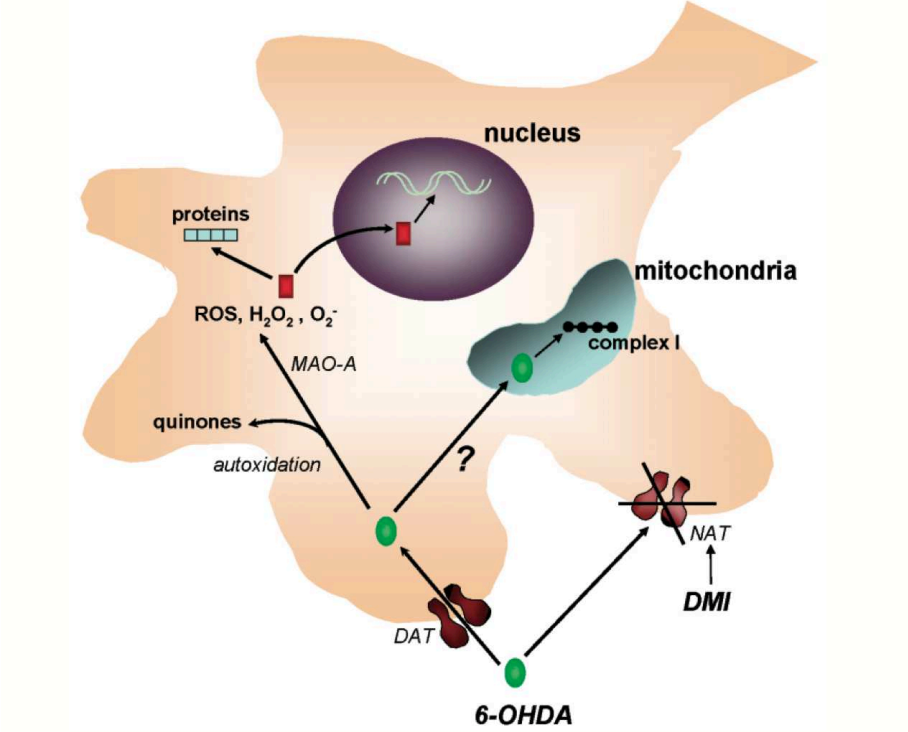

Figure 2.7: Mechanisms of 6-OHDA-induced neurotoxicity. After being taken up from the extracellular space by DAT or NAT, 6-OHDA is stored in catecholaminergic neurons. Inside these neurons, 6-OHDA undergoes both enzymatic degradation by MAO-A and autoxidation, generating several cytotoxic species that, by damaging endocellular proteins and nuclei, produce neuronal damage. Moreover, 6-OHDA might induce neurotoxicity by impairing the activity of mitochondrial complex I. In experimental animals, 6-OHDA is usually administered in association with NAT blockers, such as DMI, to prevent its uptake by noradrenergic terminals and to selectively target dopaminergic neurons (Simola et al., 2007).

DBS is known to be more efficient in the STN than in the striatum (Odekerken et al., 2016).

Furthermore, Hahn and McIntyre (2010) used a Hodgkin-Huxley like computational model of the subthalamopallidal network, trained to fit in vivo recordings from Parkinsonia monkeys, to evaluate its response to STN DBS. The model also provides predictions on GPi bursting activity. For example, the reduction of GPi bursting activity is proportionally reduced to the volume of STN activated by DBS. Another prediction is that the ablation of STN neurons, reported generating similar therapeutic outcomes as STN DBS, also reduced GPi bursting.

Using the previous model and a mean-field model (see part 2.3.6), Holt and Netoff (2014) determined that the oscillation could emerge from the coupling between the GPe and the STN. When coupled, the two resonate with each other in the PD state but not in the control state. By characterizing how subthreshold DBS pulses affect this oscillation, the model could predict stimulus frequencies capable of suppressing this oscillation (Holt and Netoff, 2014).

Thus, HFS and DBS, either in experiments or computational modelling, converge to suggest that the abnormal beta oscillation in PD would come from the STN and the GPe activities and that HFS and DBS are efficient to counterbalance these oscillations.

Beyond oscillations in the basal ganglia, the next section will introduce several computational models on PD.

2.1.4 Computational modelling approaches of Parkinson's disease

Computational modelling allows testing hypotheses and exploring ideas that are not always possible to realize experimentally. Thus, several computational models of PD have been published. The most representatives ones, will are introduced in the subsequent sections.

The Rate Model

One of the first modelling approaches to explain PD is the so-called Rate Model (Albin et al., 1989). It is not a computational model (there is no link with firing-rate models described in section 2.3.5) but a description of the basic anatomical and neurochemical connections between basal ganglia nuclei which generated testable hypotheses regarding physiology and connectivity, influencing the subsequent computational models on Parkinson's disease. The Rate Model also assumed that human movement disorders are caused by imbalanced activity in basal ganglia nuclei and sprang, in large part, from observations about deviations in basal ganglia structure and function in disease, particularly Huntington's disease, Parkinson's disease, and hemiballism. It postulated that the basal ganglia process cortical input through parallel pathways from the striatum to the basal ganglia output nuclei, and feed it back to the cortex via a thalamic relay.

The simplest formulation of the Rate Model treats the direct and indirect pathways as groups of neurons with uniform responses. However, given the functional and synaptic organisation of the basal ganglia, a diversity of responses is more likely (Nelson and Kreitzer, 2014). Indeed, physiological recordings from normal nonhuman primates during motor and cognitive tasks show a wide variety of responses during a single task, even within the same anatomic region. Besides, the Rate Model assumptions cannot account for the lack of akinesia following thalamic lesions and of involuntary movements following lesions of the internal pallidum, as demonstrated in both experimental animal models and surgically treated patients (Wichmann and DeLong, 2013).

Oscillatory models

Several other approaches to model PD have been proposed, for example, mean-field-based models (see section 2.3.6) of the basal ganglia and thalamocortical system (van Albada and Robinson, 2009) (van Albada et al., 2009) reproducing realistic firing rates of each neuronal population in both healthy and PD states. Also, a Hodgkin-Huxley like (see section 2.3.2) neural network model of the GPe and STN suggested that this circuit is capable both of correlated rhythmic activity and of irregular autonomous patterns of activity that block rhythmicity (Terman et al., 2002). This would explain the appearance of correlated oscillatory activity in the GPe-STN circuit after destruction of dopaminergic neurons in Parkinson's disease. Another set of Hodgkin-Huxley like neural network models were used to predict the impact of DBS (see section 2.1.3) and suggests that delayed feedback DBS in Parkinson's disease may boost rather than suppress excessively synchronous beta-band oscillatory activity, believed to enhance hypokinetic motor symptoms of Parkinson's disease (Goldberg et al., 2002)(Guo and Rubin, 2011)(Dovzhenok et al., 2013).

Furthermore, Leblois et al. (2006) explored the competition between the hyperdirect and the direct pathways with a firing-rate model (see part 2.3.5), suggesting that PD impairs this balance which results in the incapacity of the network to select motor programs. Besides, another firing-rate model studying motor selection presents the dopamine decrease as responsible for the impairment of the basal ganglia's ability to select actions (Humphries et al., 2006).

As a last example, in a composite firing-rate and mean-field neural network model, the basal ganglia are represented by a mean-field model interacting with a detailed firing-rate model of the thalamus and six-layered cortex (Figure 2.8). The firing-rate network model consisted of 4950 spiking neurons, divided into 15 excitatory and inhibitory cell populations in the thalamus and cortex whereas the field model consisted of the cortex, thalamus, striatum, subthalamic nucleus, and globus pallidus. Since the field model represents a brain region much larger than the firing-rate network model, the field causally influences the network, but not vice versa.

To obtain realistic firing rates in the firing-rate network model, the input spiking rate each neuron receives was bounded, by normalizing it. Then, the input was obtained by treating each of these normalized instantaneous firing rates as the rate of an ensemble of Poisson processes for generating spikes. These spikes were used to drive each population of spiking neurons, using the same connections as used in the field model itself. The key methodological novelty of this work is that the spiking network model is thus embedded in an environment with physiologically realistic dynamics (as provided by the field model), rather than a white noise environment (Oswald et al., 2009)(Muller and Destexhe, 2012). Hence, they could explore the effects of driving a spiking network model with several different types of input, including those corresponding to the healthy brain and to PD. For example, in accordance with experimental results, they found increased synchrony among basal ganglia neurons in their PD model.

Thus, several computational models suggest that studying oscillations in the cortex and the basal ganglia is a promising lead to explore PD, and all of them support the hypothesis of the involvement of the GPe and the STN activities.

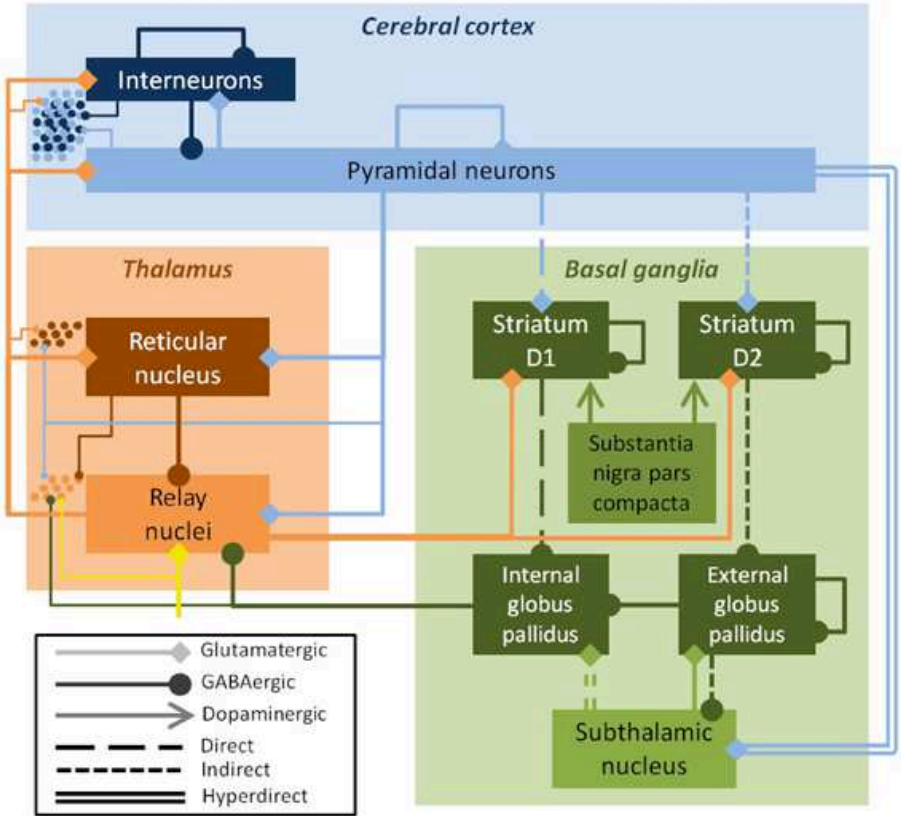

Figure 2.8: Mean-field model schematic of Kerr et al. (2013), showing excitatory populations and connections (light colors, diamond arrows) and inhibitory ones (dark colors, round arrows). The key efferent nucleus of the basal ganglia is the internal globus pallidus, which receives cortical input via direct, indirect, and hyperdirect pathways. The mean-field model drives an integrate-and-fire network model (shown here schematically with dots at left); the thin lines indicate the inputs from the mean-field model to the integrate-and-fire model. The substantia nigra pars compacta modulates parameters, but is not explicitly modelled. Inputs to the thalamus (yellow arrow) were modelled as white noise (Kerr et al., 2013).

Action selection and Go/No-Go models

The basal ganglia are involved in action selection (see part 2.1.2) and hence, in Go/No-Go behaviours. An example of Go/No-Go behaviours is the one of a cyclist stopped at a traffic light. The green light (stimulus) requires the biker to start cycling (Go) whereas red light (other stimulus) prevents the biker to start cycling (No-Go).

Lindahl and Hellgren Kotaleski (2016) included realistic details, such as the connectivity patterns and dopamine effects, in a basal ganglia spiking neural model containing the dynamic of synapses, based on Izhikevich equations (see section 2.3.3). The dopamine was regulated by a parameter representing the relative level of dopamine receptor occupancy. Depending on the region, if dopamine has, for example, a known depolarizing effect, then this parameter will directly multiply the voltage of this region in order to fit on experimental results.

These computational simulations predict that both local inhibitions in striatum and the presence of an indirect pathway are essential for the basal ganglia to properly select action over. Besides, by decreasing dopamine in the model, the efficiency of AMPA was increased in corticostriatal synapses to medium spiny neurons (MSNs) and to the MSN lateral connectivity, these changes enhance synchrony and oscillations observed in PD. On the contrary, increasing DA, could improve or restore basal ganglia action selection

ability and reduce oscillations (Lindahl and Hellgren Kotaleski, 2016).

Mandali et al. (2015) presented another model of basal ganglia, where each nucleus is reduced to 2500 Izhikevich spiking neurons and the dopamine signal represents reward prediction error, in a reinforcement learning framework (see part 2.1.2). The strength of STN lateral connections would control exploration levels and the synchrony levels in the STN-GPe circuit. An increase in STN's lateral strength led to a decrease in exploration, which could be related to the reduced exploratory levels in Parkinson's patients. Besides, a complete removal of the indirect pathway leads to a model exhibiting only Go and No-Go behaviours, without any exploration (Mandali et al., 2015). These results suggest that the indirect pathway and the STN have a crucial role in exploration.

At the scale of basal ganglia pathways Frank (2005) realized a computational model of the basal ganglia and the premotor cortex with the direct and indirect pathways, based on the Leabra algorithm. The Leabra algorithm is a firing-rate like model coupled with a learning algorithm, changing the weight of connection between basal ganglia nuclei, depending on their activation. The input activates both the premotor cortex and the striatum. In this model, the direct pathway selects the appropriate action (Go) whereas the indirect pathway inhibits inappropriate actions (No-Go). Both pathways converge in the GPi and compete to control its activation. Besides, this competition is modulated by dopamine. In particular, higher DA levels increase the activation of the direct pathway (e.g. through D1 receptors) and reduce the activation of the indirect pathway (e.g. through D2 receptors). Thus, simulation results suggest that the dynamic range of the DA signal is crucial in probabilistic learning and reversal learning (e.g. by changing the association between response and reward during learning). Moreover, by reducing DA level, to mimic PD, simulations reproduce Parkinsonian symptoms, for example, in the probabilistic reversal learning task (Frank, 2005).

Furthermore, the reduction of dopamine in the basal ganglia and also in cortical and spinal regions would activate inadequately motor cortical and spinal cord centres and cause the slowness of movement in PD bradykinesia. To explore this hypothesis, Cutsuridis (2013) used mean-field-based models of a cortical module and a spino-muscular module, both modulated by dopamine. Model simulations showed that reduction of DA in cortical and sub-cortical motor areas disrupts, via several pathways, the developmental rate and peak neuronal activity of primary motor cortical cells. These changes lead to delays in recruiting the appropriate level of muscle force sufficiently fast and cause a reduction of the peak muscle force required to complete the movement. Repetitive and sometimes co-contractive patterns of muscle activation are needed to complete the movement. These disruptions result in an abnormal slowness of movement (Cutsuridis, 2013).

To go further, Cutsuridis (2013) investigated the origins of the experimentally observed repetitive and co-contractive pattern of muscle activation in Parkinson's disease. Computer simulations showed that an oscillatory disrupted GPi segment response signal induces repetitive movements but not co-contractive agonist-antagonist pattern of muscle activation. However, when dopamine is also diminished in the cortex, a repetitive and co-contractive pattern of muscle activation occurs. Finally, additional dopamine depletion in the spinal cord sites results in a reduction of the size, duration and changing rate of the repetitive and co-contractive EMG bursts (Cutsuridis, 2013).

Thus, these models studying Go/No-Go behaviours suggest that PD motor symptoms are mainly caused by the interaction between the direct and the indirect pathways and the modulation of this interaction by dopamine.

SNr synaptic short-term plasticity model

The substantia nigra pars reticulata is the output of the basal ganglia and is subject to short-term plasticity. To quantitatively investigate how synaptic short-term plasticity affects the SNr, Lindahl et al. (2013) used a model of the basal ganglia network with Izhikevich like neurons. SNr becomes particularly responsive to the characteristic burst-like activity seen in both direct and indirect pathway striatal medium spiny neurons (MSN). As expected, direct pathway MSNs are responsible for decreasing the activity in SNr as illustrated in SNr response of figure 2.9. In particular, simulations indicate that bursting in only a few percentage of the direct pathway MSNs is sufficient for completely inhibiting SNr neuron activity. However, the model rather indicates that the direct GPe-SNr projections control the SNr activity. This can be explained by the strong inhibition of GPe on SNr but also the depressing STN-SNr synapses. Furthermore, depressing GPe-SNr synapses allows the system to become sensitive to irregularly firing GPe subpopulations, as seen in dopamine depleted conditions, even when the GPe mean firing rate does not change (Lindahl et al., 2013).

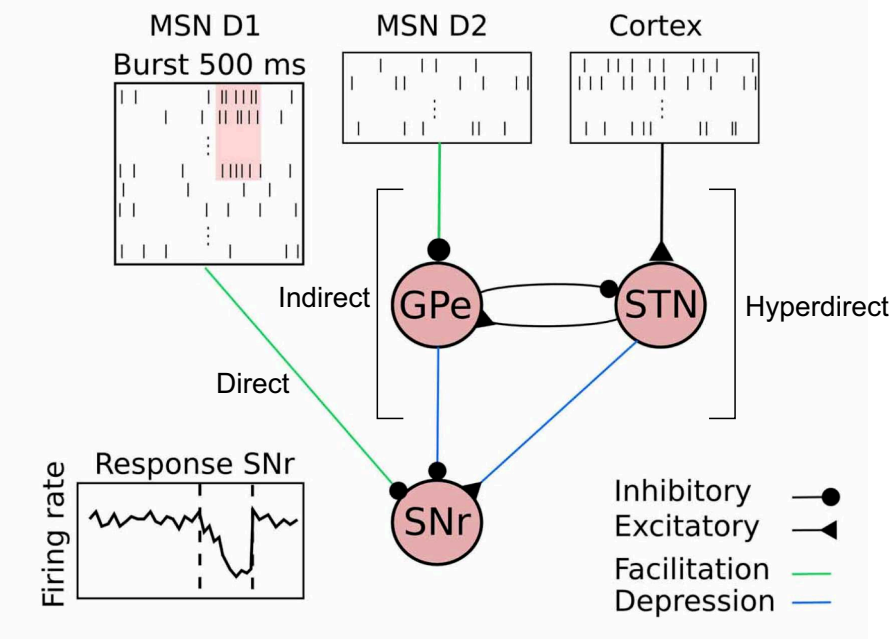

Figure 2.9: Illustration of the complete network model, with emulated input from 15,000 MSN D1 and 15,000 MSN D2 as well as a summed background input of 189 Hz from cortex to STN neurons. In the illustration, a subpopulation of MSN D1 bursts and this leads to a delayed decrease of activity in SNr (Lindahl et al., 2013).

2.2 Habenula and depression disease

The habenula is the main brain region known to be involved in depression disease. This section will present depression disease, starting with neurons and potassium dynamics in the habenula, and, continuing with anatomical details and main functions of this region. We will conclude on the few experiments and computational models approaches designed to better understand depression.

2.2.1 The anatomy of the habenula

Habenula The habenula is a brain region (Figure 2.10) composed of two main sub-nuclei; the medial and the lateral habenula (MHb, LHb) (Bianco and Wilson, 2009) (Hikosaka, 2010). The pineal gland, the habenula and the stria medullaris form together the epithalamus (Figure 2.11). The epithalamus lies on top of the thalamus.

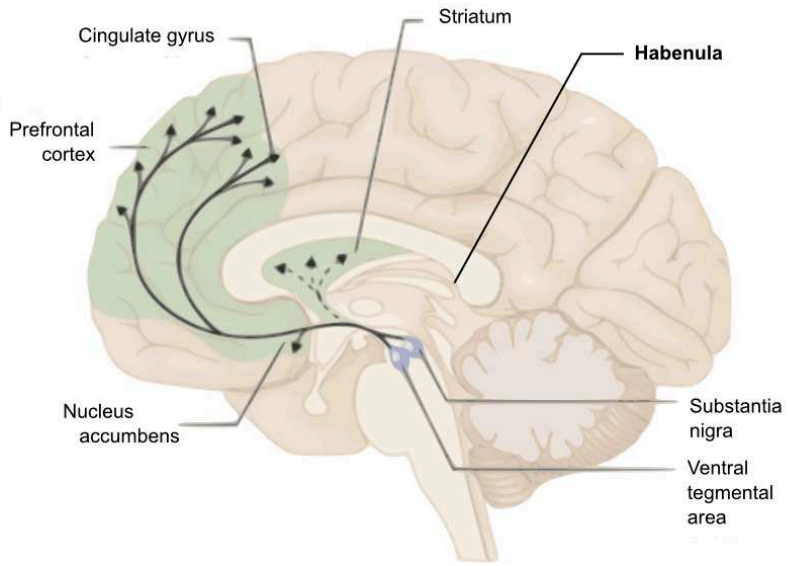

Figure 2.10: Sagittal view of the human brain.

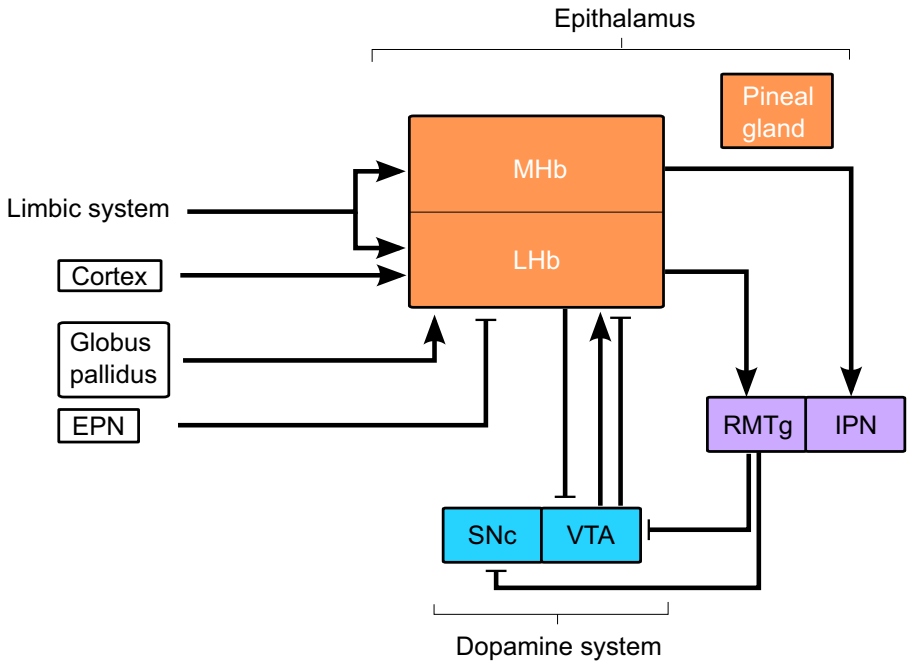

Figure 2.11: Afferent and efferent connections of the habenula. The MHb, LHb and pineal gland are collectively called the epithalamus. The MHb receives inputs mainly from the limbic system and sends outputs to the interpeduncular nucleus (IPN). The LHb receives inputs mainly from the globus pallidus (see section 2.1.1) and also from the cortex and the entopeduncular nucleus (EPN) and sends outputs to the brain structures that contain dopaminergic neurons, partly through the rostromedial tegmental nucleus (RMTg). Arrows indicate excitatory glutamatergic connections whereas bar-headed lines are inhibitory GABAergic connections. Many of the existing connections are not shown, including reverse connections.

Functional connectivity of the LHb The LHb receives a strong innervation from the globus pallidus (see section 2.1.1) and the limbic system, a set of structures including the olfactory bulbs, the hippocampus, the hypothalamus, the amygdala... (Hikosaka, 2010).

Moreover the LHb receives glutamatergic afferents from the lateral hypothalamus and from cortical inputs (Li et al., 2011) and GABAergic afferents from the entopeduncular nucleus (EPN) (Shabel et al., 2012). Besides, tetanic stimulation in the ventral tegmental area enhances LHb activity whereas, on the contrary, a single-pulse inhibits response by 90% of the LHb neurons (Shen et al., 2012). Moreover, optogenetic experiments show that a subpopulation of VTA dopaminergic-GABAergic neurons inhibits LHb neurons during rewards (Stamatakis et al., 2013). Therefore, the VTA projection to the LHb comprises both inhibitory and excitatory connections.

LHb efferents are predominantly mediated by the GABAergic rostromedial tegmental nucleus (RMTg) (Jhou et al., 2011) and reach the dopaminergic subnuclei (ventral tegmental area and substantia nigra pars compacta) (Hikosaka, 2010). Thus, LHb neuronal activity exerts principally an inhibition onto DA neurons of basal ganglia (substantia nigra) and in the VTA (Hikosaka, 2010), indeed a single stimulation of LHb inhibits by 90% the firing activity in both regions (Matsumoto and Hikosaka, 2007).

Therefore, the habenula is organised around two subnuclei which project to the basal ganglia through inhibitory brain regions. The next section will expose how this organisation fulfill the main functions of the habenula.

2.2.2 Neurons of the habenula

Neurons populations of the LHb The neurons of the LHb are heterogeneous in their morphology and particularly in their firing patterns. Indeed, there are three types of activity pattern in LHb; silent, tonic and phasic (Weiss and Veh, 2011). For both tonic and phasic activity, regular firing neurons and irregular firing neurons can be distinguished (Figure 2.12).

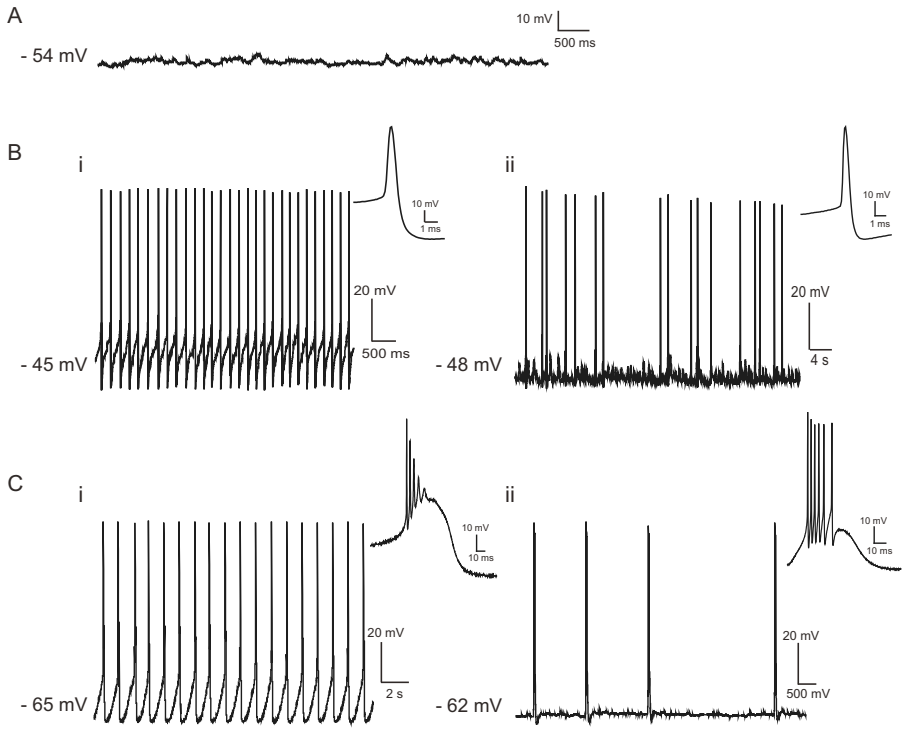

Figure 2.12: Five types of activity pattern in LHb neurons. (A) Silent (B) tonic regular(i)/irregular(ii) (C) burst regular(i)/irregular (ii) data obtained by Hu's lab.

But there is a lack of literature about modelling these neurons because they are difficult to describe properly. Indeed, habenular neurons are very sensitive. For example, their resting membrane potential is hard to define with certainty because it varies greatly during recordings, however, some of them tend to have a resting membrane potential at -70 mV. Furthermore, when neurons in the habenula are hyperpolarized, they present different kind of unclear responses such as continuous spiking, big sag or massy epileptic current (Neumann et al., 2015). Hence, because habenular neurons are not easy to record properly and because habenula became only recently a region of interest, there is a lack of literature concerning models to describe them. On the contrary, dopaminergic neurons and Kir channels, also involved in depression disease, are known for a longer time and their studies, in both experiments and computational models, is more advanced as it will be presented in sections 2.3.4 and 2.4.3.

2.2.3 Main functions and dysfunctions of habenula

The habenula is involved in reward and punishment processes, by projecting indirectly to the dopaminergic nuclei (VTA and SNc).

Reward and aversive functions

The behavioural functions of the LHb can be approached with experiments on rhesus monkeys, which perform on a visually guided saccade task with a biased reward outcome

(two fixation spots can appear on the screen as a target, only one is rewarding) while recording the activity of their LHb neurons and their substantia nigra dopaminergic neurons (Matsumoto and Hikosaka, 2007). As a result, the habenula neurons were excited by the no-reward-predicting target and inhibited by a reward-predicting target. At the opposite, dopaminergic neurons were excited and inhibited by reward-predicting and no-reward-predicting targets, respectively. In unrewarded trials, the excitation of habenula neurons started earlier than the inhibition of dopaminergic neurons. Besides, unexpected delivery of rewards inhibits LHb activity (Matsumoto and Hikosaka, 2007). This is coherent with the fact that LHb signal to midbrain dopaminergic neurons is mainly inhibitory since it is mediated by RMTg, composed by GABAergic inhibitory neurons (Jhou et al., 2009). This evokes a picture whereby negative reward prediction error (reward not supplied) activates the LHb, which inhibits DA firing (see figure 2.4) whereas positive reward prediction error (unpredicted reward supplied) inhibits LHb, thus activates DA neurons by disinhibition of SNc.

However, the situation is more complex since there are also direct LHb excitatory projections to the VTA that activate DA neurons (Lammel et al., 2012), but optogenetic activation shows that this LHb-VTA pathway is aversive. When blocking dopamine in the medial prefrontal cortex (mPFC), the aversion is stopped. Thus, LHb activity can reduce DA activity through the RMTg or directly increase it, but, in both cases, it results in aversion-like behaviour. For example, in rats, deep-brain stimulation (DBS) of the LHb provokes conditioned place avoidance (Friedman et al., 2011), it led to aversion to the context associated with stimulation of this brain region. Also, while rats explore an environment, optogenetic stimulation of EPN inputs onto the LHb triggers avoidance of specific areas in that environment (Shabel et al., 2012). Consequently, aversive stimuli activate the LHb, which in turn triggers circuits that lead to aversive behaviours (Proulx et al., 2014).

In fact, LHb seems to play a role in encoding “disappointment” since negative unexpected events activate LHb neurons. Indeed, either an aversive event, such as an air puff in the eye, or the simple omission of an expected reward, enhances LHb activity; as long as it is unpredicted (Figure 2.13) (Matsumoto and Hikosaka, 2009).

Hence, LHb would have the possibility to drive reward-seeking and punishment-avoidance behaviours.

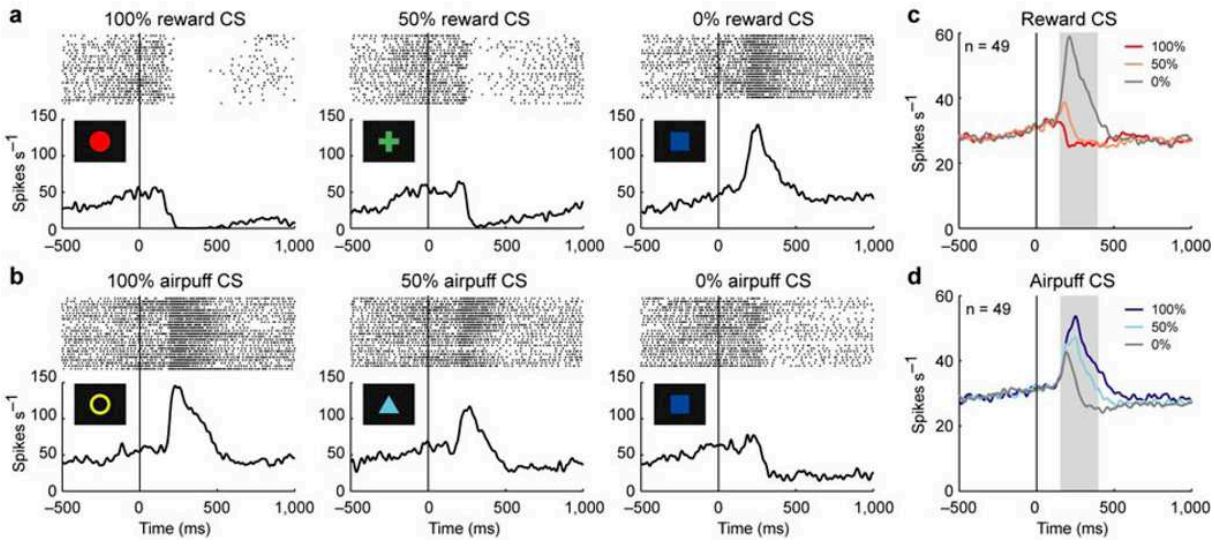

Figure 2.13: Responses of lateral habenula neurons to conditional stimuli (CS) and where the reward is an amount of liquid. (a) Activity of an example neuron during the reward block. Rasters and spike density functions (SDFs) are aligned by CS onset and shown for 100% reward with CS, 50% reward with CS (half of the initial liquid amount), and 0% reward with CS. (b) Activity of the same neuron as in (a) during the punishment block. Rasters and SDFs are shown for 100% airpuff with CS, 50% airpuff with CS, and 0% airpuff with CS. (c) Averaged activity of the 49 neurons during the reward block. SDFs are shown for 100% reward with CS (dark red), 50% reward with CS (light red), and 0% reward with CS (gray). Gray area indicates the period that was used to analyse CS response. (d) Averaged activity of the 49 neurons during the punishment block. SDFs are shown for 100% airpuff with CS (dark blue), 50% with airpuff CS (light blue), and 0% airpuff with CS (gray) (Matsumoto and Hikosaka, 2009).

Depression

Major depressive disorder (MDD) presents a large variety of symptoms such as low mood, loss of motivation, feelings of despair and inaptitude to feel pleasure (anhedonia) (Li et al., 2013).

Experiments on rodents, dogs or humans show that exposure to uncontrollability debilitates escape learning, this is called the "learn helplessness effect". Helpless animals show many depression-like symptoms such as loss of appetite, lowered activity and sleep disturbances (Henn et al., 1985). Besides, exposure to helplessness is strongly heritable, therefore, some rat strains have been selectionned on these criteria, such as the congenitally learned helplessness (cLH) rat strain (Henn and Edwards, 1994). cLH rats show a prompt helpless response to stress and are widely used as a rat model of depression (Shumake et al., 2003).

Hence, in rodents, aversive events such as the repetition of shocks, physical restraint, open field exposure and social defeat are capable of inducing depressive symptoms. Interestingly, these events also increase the metabolism in LHb neurons like mitochondrial enzyme (i.e. cytochrome oxidase) (Shumake et al., 2003) and transcription factors expression (i.e. cFos, involved in long-term adaptive changes in the brain) (Brown and Shepard, 2013).

On the contrary, acute learned helplessness (aLH) is induced by submitting wild-type rats to periods of inescapable and unpredictable aversive events (Maier, 1984). For example, in a first phase, rats receive unavoidable random foot shocks (Figure 2.14) and, in a second phase, they are placed in the same context, however, they can escape by

pressing a lever. If the first phase is too long, rats will not find the solution in the second phase. Thus, animals experiencing unavoidable stress may turn "helpless" and become unable to avoid controllable stress.

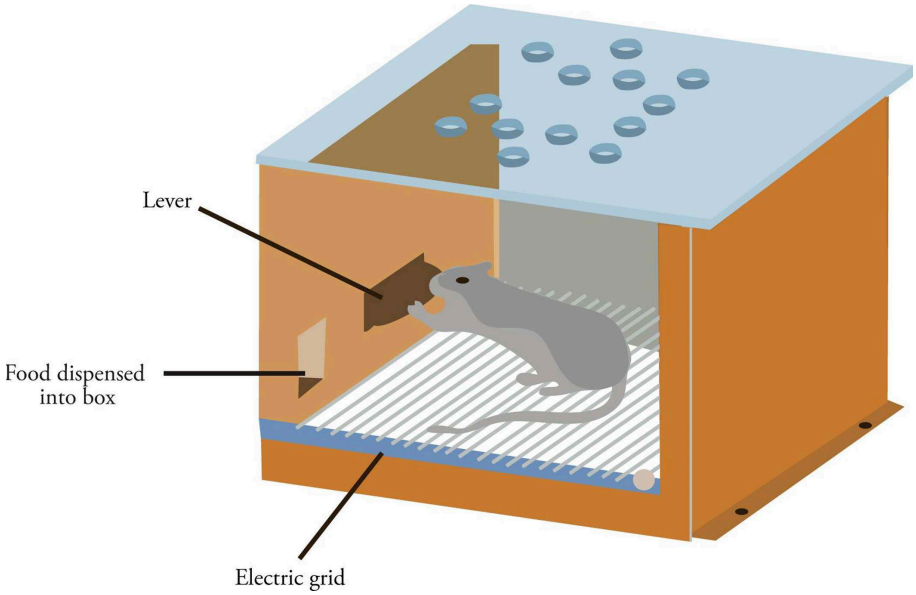

Figure 2.14: The learned helplessness test. The subject cannot escape the box and receives randomly electric shocks from the ground. The fact that it cannot escape shocks or even predict them is supposed to induce helplessness which would lead to depression.

In rodents and humans, LHb shows hyperactivity during depressive-like states (Li et al., 2011) (Li et al., 2013). Besides, in humans, positron emission tomography (PET) shows that the LHb activity is strongly correlated with depressive symptoms, which were induced by depleting serotonin levels (Morris et al., 1999).

Accordingly, lesions in the LHb of congenitally learned helplessness (cLH) rats reduces serotonin levels and depression-like behaviour, such as decreasing immobility time in the forced swim test (Yang et al., 2008). The forced swim test consists in placing the subject in a tube of water from which it cannot escape. Then, it can swim or stay immobile and floating, the assumption of this test is that the more the rodent is depressed, the more it will stay immobile, not trying to escape.

Concerning cLH rats, intra-cerebral administration of GABA agonist muscimol into the LHb decreases depressive-like behaviour, measured with the number of successful trials in an escape paradigm to avoid electric foot shocks (Winter et al., 2011).

In control rats, microinjections of substance P in LHb produce depressive-like behaviours in the forced swim test (FST); the immobility time increases and the climbing time decreases. On the contrary, when substance P receptor antagonist (SPA) was administered in the LHb of depression rats models the immobility time decreases and the climbing time increases in the FST, promoting antidepressive-like behaviours (Yang et al., 2014).

Hence, data converge to suggest that LHb hyperactivity is correlated to depression symptoms.

Another lead to cure depression is to directly stimulate the brain. Deep brain stimulation (DBS) is based on the empirical observation that high-frequency electrical stimulation of specific brain targets can mimic the effect of a lesion without the need for destroying brain tissue (Volkmann and Deuschl, 2007). Treating rats exposed to chronic mild stress (CMS) rats with DBS, performed by an implanted electrode into the LHb, seems to reduce depressive-like symptoms (Meng et al., 2011). In this study, as a measure of depression,

the authors employed open-field tests, which consists in counting the number of crossing and rearing and measure the concentration of monoamines such as norepinephrine (NE), dopamine and serotonin in blood serum and brain tissue. Both these measures were lower in CMS rats than in control rats. Four weeks of DBS alleviates depressive behaviour, indeed the number of crossing and rearing is increased as well as the monoamines levels.

Curiously, inhibiting the LHb did not show immediate antidepressant properties. Indeed muscimol treatment in cLH rats decreases the number of failed trials in the escape paradigm only one week after administration (Winter et al., 2011). Concerning the use of DBS with humans, a study with one patient presenting resilient depression shows that it required four months of stimulation for an almost total remission; depression was quantified with the Hamilton depression scale (Sartorius et al., 2010). Hence, even if this treatment seems promising its effects are not instantaneous suggesting that even if the LHb would induce changes there are other brain regions involved in their maintenance.

Remitted major depressive disease subjects in fMRI display a habenula blood flow increased right after they receive acute tryptophan depletion (ATD), which reduce the serotonin synthesis in the brain, suggesting increased habenula activation (Roiser et al., 2009).

Furthermore, LHb neurons projecting directly to VTA are glutamatergic and have an aversive effect when activated. The mean frequency of miniature excitatory post-synaptic currents (mEPSC) is larger in aLH and cLH rats than in wild-type rats (Li et al., 2011). By stimulating electrically the LHb with successive pulses, helpless animals show a higher decrease in the amplitude of EPSCs than control rats, reflecting higher presynaptic vesicle depletion. Since more depletion correlates with higher release probability (Zucker and Regehr, 2002), repeated stimulation in helpless animals depletes synaptic vesicles faster suggesting that the LHb of depressed animals inhibits more efficiently the VTA.

In the LHb of cLH rats, the beta form of the calcium/calmodulin-dependent protein kinase type II (β-CaMKII) is up-regulated compared to control rats (Li et al., 2013). Besides, antidepressant treatment reversing depressive symptoms of cLH rats down regulate βCaMKII in LHb. The overexpression of β-CaMKII in the LHb of wild-type rats increased the immobility time in the forced swim test and also provoked anhedonia with a reduction in preference for the sucrose solution. In addition, when using a kinase-dead version of β-CaMKII, wild-type rats did not present depressive-like behaviours. In the same idea, by using RNA interference to knock down β-CaMKII protein in LHb of cLH rats, the immobility time in the forced swim test was reduced and the escape behaviour in the learned helpless test was increased. In fact, up-regulation of β-CaMKII causes more GluR1 insertion into synapses which increases synaptic efficacy. Thus, increasing β-CaMKII in the LHb causes hyperactivity of neurons which leads to depression-like symptoms, on the contrary, blocking β-CaMKII, reverses the depressive symptoms (Li et al., 2013). These results show that β-CaMKII levels act directly on synaptic plasticity and appears as a post-synaptic molecular actor of major depressive disease.

2.3 Computational modelling overview

Integrate-and-fire models are the first models accounting for neural firing activity and used in networks in the late 1930s (Cowan, 1988). However, the field of computational neuroscience really started in 1952, with the paper of Hodgkin-Huxley and their model on action potential formation and propagation in giant squid axon. In parallel, neural networks models appeared such as firing-rate models (McCulloch and Pitts, 1943) and mean-field models. From there, a large family of neural model was developed, such as Izhikevich models or compartmental neural models.

2.3.1 Integrate-and-fire model

The integrate-and-fire model is a very simple model of the neuronal voltage, proposed by Louis Lapicque in 1907, it is still used in large neural network because of its low computational cost. The principle is that if the current I is constant, then $V(t) = \frac{I}{C_M}t$ until it reaches V_{peak}, where V is set back to V_{reset}. It can be described with the current voltage relation of a capacitor:

$$\begin{aligned} &C_M \tfrac{dV(t)}{dt} = I(t) \\ &\text{if } V \geq V_{peak}, \text{then } V \leftarrow V_{reset} \end{aligned} \tag{2.1}$$

Where V is the membrane potential over time, I is the current applied to the neuron over time, C_M is the membrane capacitance, V_{peak} is the maximum voltage set to the neuron and V_{reset} is the resting potential.

2.3.2 Hodgkin-Huxley model

The Hodgkin-Huxley model is a mathematical model describing how action potentials are initiated and propagated (Hodgkin and Huxley, 1952). It treats neural components as electrical elements through ordinary differential equations (ODE). It is the same equation as integrate-and-fire models except that I_{Na} and I_K have dynamics explicitely describing the action potential. In integrate-and-fire models the action potential is not described.

The expression of voltage depends on three currents, I_{Na}, I_K and I_{leak}.

$$C_M \frac{dV}{dt} = -I_{Na} - I_K - I_{leak} \tag{2.2a}$$

With $C_M = 1\mu F.cm^{-2}$, the membrane capacitance as in Hodgkin and Huxley (1952), and the following expression of currents:

$$I_{Na} = g_{Na} m^3 h \times (V - E_{Na}) \tag{2.3a}$$
$$I_K = g_K n^4 (V - E_K) \tag{2.3b}$$
$$I_{leak} = g_{leak}(V - E_{leak}) \tag{2.3c}$$

To match their experimental data, Hodgkin and Huxley fitted data from the giant axion of squids and got the following parameter values for conductances: $g_{Na} = 120$ mS.cm^{-3}, $g_K = 36$ mS.cm^{-3}, $g_L = 0.3$ mS.cm^{-3}, and for equilibrium potentials: $E_{Na} = 50$ mV, $E_K = -77$ mV, $E_{leak} = -54.4$ mV.

n, m and h are described with the following gating functions:

$$\frac{dn}{dt} = -\alpha_n(V) \times (1 - n) - \beta_n(V) \times n \tag{2.4a}$$
$$\frac{dm}{dt} = -\alpha_m(V) \times (1 - m) - \beta_m(V) \times m \tag{2.4b}$$
$$\frac{dh}{dt} = -\alpha_h(V) \times (1 - h) - \beta_h(V) \times h \tag{2.4c}$$

with the rate equations:

$$\alpha_n(V) = 0.01\frac{V+55}{1-\exp(-\frac{V+55}{10})} \tag{2.5a}$$

$$\beta_n(V) = 0.125\exp(-\frac{V+65}{80}) \tag{2.5b}$$

$$\alpha_m(V) = 0.1\frac{V+40}{1-\exp(-\frac{V+40}{10})} \tag{2.5c}$$

$$\beta_m(V) = 4\exp(-\frac{V+65}{18}) \tag{2.5d}$$

$$\alpha_h(V) = 0.07\exp(-\frac{V+65}{20}) \tag{2.5e}$$

$$\beta_h(V) = \frac{1}{1+\exp(-\frac{V+35}{10})} \tag{2.5f}$$

The gating function describes equilibrium between open and closed forms of the corresponding ionic channels, and their voltage induced transitions.

2.3.3 Izhikevich neuronal model

In order to develop large neural networks, the model for a single neuron needs to be both computationally simple and able to reproduce several realistic firing patterns. The Hodgkin-Huxley is computationally too heavy, therefore, Izhikevich came up with lighter spiking neuron models, it is an integrate-and-fire model, rendering neuronal properties such as firing rate and spike pattern (Izhikevich, 2003). This model follows the two following equations:

$$\frac{dV}{dt} = 0.04(V)^2 + 5V - u + 140 + I + I^{syn} \tag{2.6a}$$

$$\frac{du}{dt} = a(bV - u) \tag{2.6b}$$

$$\text{if } V \geq V_{peak} \left\{ \begin{array}{l} V \leftarrow c \\ u \leftarrow u + d \end{array} \right\} \tag{2.6c}$$

where, V is the membrane potential, u is the membrane recovery variable, I^{syn} is the total synaptic current received, I is the external current applied to the neuron, $V_{peak} = 30$ mV is the maximum voltage. Besides, a, b, c and d are parameters set depending on the brain region. For example, in the STN, a = 0.005, b = 0.265, c = -65mV, d = 1.5 (Mandali et al., 2015).

2.3.4 Compartmental neural model: the dopaminergic neuron

Dopaminergic neurons are spontaneously firing (Grace and Bunney, 1984b) (Grace and Bunney, 1984a) (Nedergaard and Greenfield, 1992). They deliver spikes either regularly, or irregularly, forming a background activity, on which bursting pattern may be superposed (Celada et al., 1999), (Hyland et al., 2002). Sodium and potassium concentration dynamics, modulated by channels, pumps or stimulation are the basis of the different firing pattern (Yu et al., 2012) (Owen et al., 2013). The bursting activity of dopaminergic neurons seems to be correlated to reward prediction error (Schultz, 2002) (see also part 2.1.1 on dopaminergic neurons and dopamine).

The pace-making activity is due to the interaction between ion channels. Regular firing and bursting seems to be linked to slow calcium dynamics and can be modelled as a

two components model with a Hodgkin-Huxley-type membrane model and a compartment model for the neuronal cytosol (Amini et al., 1999). Furthermore, the spontaneous bursts of midbrain dopaminergic neurons (VTA) depend on the activation of NMDA receptors (Overton and Clark, 1997). Therefore, in a multi-compartmental computational model, sodium dynamics would underlie slow oscillations which drives NMDA-bursting activity (Canavier, 1999).

To model dopaminergic neuron and their bursting activity, one can use a coupled oscillator model where the soma and the dendrites are different compartments, coupled electrically and with different natural firing frequencies (Wilson and Callaway, 2000) (Medvedev et al., 2003).

This compartmental model can be extended by adding dendritic AMPA or NMDA synaptic conductance where the effect on the soma of the high-frequency oscillation of the dendrites is amplified by NMDA receptor activation (Kuznetsov et al., 2006).

The dopaminergic neurons of the substantia nigra pars compacta receive inputs from GABAergic neurons of the substantia nigra pars reticulata, the globus pallidus and the RMTg, and from glutamatergic neurons of the subthalamic nucleus. A computational approach with the model of Kuznetsov et al. (2006) (detailed below) and an integrate-and-fire-based model of the basal ganglia (Humphries et al., 2006) shows that phasic bursts in dopaminergic neurons of the midbrain (acounting for both VTA and SNc) can be triggered by a phasic disinhibition (Figure 2.15) (Lobb et al., 2011).

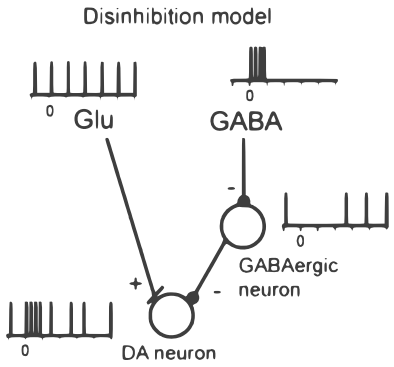

Figure 2.15: The disinhibition Bursting of Dopaminergic Neurons. In the disinhibition model, the activation of NMDA receptors is continually suppressed by tonic activation of GABAA receptors from a GABAergic neuron. Phasic inhibition of this GABAergic neuron by a secondary GABAergic source evokes phasic bursting in dopaminergic neurons. Reward is received at time 0 (Lobb et al., 2011).

The following equations detail the compartmental dopaminergic model defined by (Kuznetsov et al., 2006).

Initial conditions, parameter values, and descriptions are given in the table A.2 and the table A.3. The equation of the soma's voltage V_1 follows a Hodgkin-Huxley like model (see section 2.3.2) with additional currents (Ca, KCa, K current voltage-dependent):

$$\begin{aligned}\frac{dV_1}{dt} = {} & i_1 + g_{Ca_1}(V_1) \times (E_{Ca} - V_1) + g_{K_{Ca_{1_u}}}(u_1) \times (E_K - V_1) + g_{K_{1_V}}(V_1) \\ & \times (E_K - V_1) + g_{K_{2_n}}(n_1) \times (E_K - V_1) + g_{L_1} \times (E_{L_1} - V_1) \\ & + g_{Na_{1_{V_h}}}(V_1, h_1) \times (E_{Na} - V_1) + nd \times gc \times (V_2 - V_1) \times \frac{r_1 r_2^2}{r_1^2 + r_2^2}\end{aligned} \tag{2.7}$$

Then, the concentration of calcium:

$$\frac{du_1}{dt} = 2.0 \times \frac{\text{buf}_1}{r_1} \times \left(g_{Ca_1}(V_1) \frac{E_{Ca} - V_1}{H} - \frac{u_1}{t_{C_1}} \right) \tag{2.8}$$

The activation variable for the delayed rectifier:

$$\frac{dn_1}{dt} = \alpha_{n_V}(V_1) \times (1.0 - n_1) - \beta_{n_V}(V_1) \times n_1 \tag{2.9}$$

The sodium inactivation variable:

$$\frac{dh_1}{dt} = \alpha_{h_V}(V_1) \times (1.0 - h_1) - \beta_{h_V}(V_1) \times h_1 \tag{2.10}$$

As previously described for the soma, we have the equivalent set of equation for the dendrites.

$$\begin{aligned} \frac{dV_2}{dt} = {} & g_{Ca_1}(V_2) \times (E_{Ca} - V_2) + g_{K_{Ca_{1_u}}}(u_2) \times (E_K - V_2) + g_{K_{1_V}}(V_2) \\ & \times (E_K - V_2) + g_{K_{2_n}}(n_2) \times (E_K - V_2) + g_{L_1} \times (E_{L_1} - V_2) \\ & + g_{Na_{1_{V_h}}}(V_2, h_2) \times (E_{Na} - V_2) + gc \times (V_1 - V_2) \times \frac{r_1^2 r_2}{r_1^2 + r_2^2} + g_{NMDA_{V_2}} \\ & \times (E_{NMDA} - V_2) + g_{AMPA} \times t_{NMDA} \times (E_{AMPA} - V_2) + I_{GABA_{A_{V_2}}} \end{aligned} \tag{2.11}$$

$$\frac{du_2}{dt} = 2.0 \times \frac{\text{buf}_1}{r_2} \times \left(g_{Ca_1}(V_2) \times \frac{E_{Ca} - V_2}{H} - \frac{u_2}{t_{C_1}} \right) \tag{2.12}$$

$$\frac{dn_2}{dt} = \alpha_{n_V}(V_2) \times (1.0 - n_2) - \beta_{n_V}(V_2) \times n_2 \tag{2.13}$$

$$\frac{dh_2}{dt} = \alpha_{h_V}(V_2) \times (1.0 - h_2) - \beta_{h_V}(V_2) \times h_2 \tag{2.14}$$

The set of functions associated with concentration of calcium, the delayed rectifier and the sodium inactivation are of the Hodgkin-Huxley type:

$$\alpha_{n_V}(V) = -3.2 \times 10^{-3} \times \text{tk} \times \frac{V + 5.0}{\exp(-\frac{V+5.0}{10.0} - 1.0)} \tag{2.15a}$$

$$\beta_{n_V}(V) = 0.05 \times \text{tk} \times \exp(-\frac{V + 10.0}{16.0}) \tag{2.15b}$$

$$\alpha_{m_V}(V) = -0.32 \times \frac{V + 31.0}{\exp(-\frac{V+31.0}{4.0} - 1.0)} \tag{2.15c}$$

$$\beta_{m_V}(V) = 0.28 \times \frac{V + 4.0}{\exp(\frac{V+4.0}{5.0} - 1.0}) \tag{2.15d}$$

$$\text{minf}_V(V) = \frac{\alpha_{m_V}(V)}{\alpha_{m_V}(V) + \beta_{m_V}(V)} \tag{2.15e}$$

$$\alpha_{h_V}(V) = 0.2 \times \text{th} \times \exp(-\frac{V + 47.0}{18.0}) \tag{2.15f}$$

$$\beta_{h_V}(V) = 25.0 \times \frac{\text{th}}{1.0 + \exp(-\frac{V+24.0}{5.0})} \tag{2.15g}$$

The sodium and potassium conductances are given by:

$$g_{Na1_{V_h}}(V, h) = g_{bar_{Na1}} \times (\text{minf}_V(V))^3 \times h \tag{2.16a}$$

$$g_{K2_n}(n) = g_{bar_{K2}} \times n^4 \tag{2.16b}$$

$$g_{K1_V}(V) = \frac{g_{bar_{K1}}}{1.0 + \exp(-\frac{V - vHk}{vSk})} \tag{2.16c}$$

$g_{NMDA_V}(V)$ is the voltage-sensitive NMDA conductance density:

$$g_{NMDA_V}(V) = \frac{t_{NMDA} \times g_{bar_{NMDA}} + g_{bar_{NMDAc}}}{1.0 + 0.28 \times Mg \times \exp(-me \times V)} \tag{2.17}$$

$g_{Ca_1}(V)$ is the voltage-sensitive calcium conductance:

$$g_{Ca_1}(V) = g_{bar_{Ca1}} \times cs_{\inf_V}(V)^4 \tag{2.18}$$

with cs_{inf_V} defined as:

$$cs_{inf_V}(V) = \frac{\alpha_{c1_V}(V)}{\alpha_{c1_V}(V) + \beta_{c1_V}(V)} \tag{2.19}$$

Furthermore, $\alpha_{c1_V}(V)$ depends on a threshold; if $\text{abs}(V + 50) > 10^{-5}$

$$\alpha_{c1_V}(V) = -3.2 \times 10^{-3}\text{tsc}\frac{V + 50.0}{\exp(-\frac{V+50.0}{5.0} - 1.0)} \tag{2.20}$$

otherwise,

$$\alpha_{c1_V}(V) = 0.016 \times \text{tsc}$$

$$\beta_{c1_V}(V) = 0.05 \times \text{tsc} \times \exp(-\frac{V + 55.0}{40.0}) \tag{2.21}$$

$g_{K_{Ca_{1_u}}}(u)$ is the calcium-dependent potassium conductance:

$$g_{K_{Ca1_u}}(u) = g_{bar_{KCa1}} \times \frac{u^4}{u^4 + k_1^4} \tag{2.22}$$

Values were taken from (Kuznetsov et al., 2006) and (Lobb et al., 2011), see table A.3 for parameters values and table A.2 for intial conditions.

2.3.5 Firing-rate model

One way to model large networks of neurons is to use simplified neurons. Instead of modelling each neuron with their spiking, firing-rate models track the averaged behaviour of neurons groups spike rates (Ermentrout and Terman, 2010). These models are also called population models since they can represent whole populations of neurons rather than single cells. Firing-rate models are useful in terms of computational efficiency but also to account for experimental preparations measuring the probability of firing with extracellular electrodes. Also, field potential recordings, electroencephalograms and functional magnetic resonance imaging record large population of neurons, better represented with population equations (Gerstner and Kistler, 2002).

$$\tau\frac{dr_i(t)}{dt} = -r_i(t) + F(\sum_{j=1}^{n} r_j(t) \times w_{(i,j)}) \tag{2.23a}$$

$$F(x) = \frac{1}{1 + \exp(-c \times x)} \tag{2.23b}$$

Where F is a non-linear function, for example, one of the most commonly used F function is a sigmoidal function and where r_i and r_j are the firing activity of, respectively, neuron i and j, $w_{(i,j)}$ is the weight of each connection from other neurons j and c is a constant that sets the slope of the sinusoidal function.

2.3.6 Mean-field model

Mean-field models consider a large number of individuals in interaction. The effect of all the other individuals on any given individual is approximated by a single averaged effect, thus reducing a many-body problem to a one-body problem (Gerstner and Kistler, 2002). This simplification allows computational efficiency while being quite realistic by keeping statistical features of the population activity. As an example, in the previous equation of the firing-rate model, $r_j(t)$ can be replaced by its means over all neurons, $\bar{r}(t)$:

$$\tau \frac{dr_i(t)}{dt} = -r_i(t) + F(\sum_{j=1}^{n} r_j(t) \times w_{(i,j)}) \tag{2.24a}$$

the mean-field approximation supposes the following equivalence:

$$\begin{aligned} \sum_{j=1}^{n} r_j(t) \times w_{(i,j)} &\approx \sum_{j=1}^{n} r_j(t) \times \sum_{j=1}^{n} w_{(i,j)} \\ &= n\bar{r}(t) \times \sum_{j=1}^{n} w_{(i,j)} \end{aligned} \tag{2.25a}$$

because $\bar{r}(t) = \frac{1}{n} \sum_{j=1}^{n} r_j(t)$
and finally gives the following equation:

$$\tau \frac{dr_i(t)}{dt} = -r_i(t) + \bar{r}(t) F(\sum_{j=1}^{n} w_{(i,j)}) \tag{2.26a}$$

where n is integrated in the definition of F.

2.4 Astrocyte and potassium

The tripartite synapse is a system involving the neuron, the astrocyte and the extracellular space (Perea et al., 2009). Two neurons are connected through their synapse, the space between the pre-synaptic and the post-synaptic synapses is the extracellular space and this connection can be wrapped by the astrocyte (see Figure 2.17), thus forming a tripartite synapse. In the next sections, we will focus on the astrocyte role to modulate the extracellular potassium released by the neuron.

2.4.1 Astrocyte

The astrocytes belong to the family of glia cells, found in all areas of the brain and constituting around half of the brain cells (Kandel et al., 2013). The early discovered cells looked star-shaped to their observers, after which astrocytes have been named, however, the majority of them have more sponge like shape. The astrocytes enfold blood vessels and hence, play major roles in nurturing neurons. Besides they regulate ion and neurotransmitters concentrations in the extracellular space. Indeed, because of the high concentration of K+ channels in their membrane, they can buffer potassium spatially, released by firing neuron into the extracellular space, by moving it at distant contact. Moreover, contacts between astrocytes and neuron are more often observed on the neural synapse and little is known on contacts of the astrocyte with neural soma (Cui et al., 2018).

Furthermore, astrocytes also recycle the glutamate released by neurons. In the glial cell, glutamate is converted to glutamine and then transferred to neurons, where it serves as an immediate precursor of glutamate. Besides, glutamate binding to glial receptors increases the intracellular free calcium concentration and since astrocytes are connected to neighboring astrocytes through gap junctions, it creates a wave of calcium spreading in the astrocyte network and modulating neuronal activity. The astrocytes are also involved in the development of synapses, for example, they secrete thrombospondins that induce the formation of new synapses. Finally, they protect other cells from the effects of oxidative stress by detoxifying toxic oxygen-free radicals during neuronal inflammation and degeneration (Kandel et al., 2013).

In the next sections, I will focus on the potassium uptake function of the astrocyte.

2.4.2 Passive ion diffusion

Ions can diffuse through a membrane with channels, it is a passive ion diffusion since it does not require ATP, compared to pumps. This passive transport can be described by the Nernst equation that defines the expression of the electrochemical potential $\bar{\mu}_{K^+_{out\to in}}$:

$$\bar{\mu}_{K^+_{out\to in}} = V - \frac{RT}{F}\ln(\frac{K^+_{out}}{K^+_{in}}) \tag{2.27}$$

with $R = 8.314\ J.mol^{-1}.K^{-1}$, the gas constant, $T = 308$ K, the temperature, $F = 96.4\ kC.mol^{-1}$, the Faraday constant, K^+_{in} and K^+_{out}, the concentrations in mM of potassium, respectively in and out, of the cell in question, and V, the membrane voltage in mV.

The value of the electrochemical potential results from the balance between the action of the chemical gradient and the action of the electrical gradient on the ion considered. Besides, by convention, if the electrochemical potential, $\bar{\mu}_{K^+_{out\to in}}$, is positive, K^+ exits the cell and if it is negative, K^+ enters the cell.

Thus, if we consider E_K, the equilibrium potential associated with potassium, as:

$$E_K = \frac{RT}{F}\ln(\frac{K^+_{out}}{K^+_{in}}) \tag{2.28}$$

we get:

$$\bar{\mu}_{K^+_{out\to in}} = V - E_K \tag{2.29}$$

In normal resting condition, the concentration of potassium inside both the neuron and the astrocyte is $K^+_{in} \simeq 135.0$ mM and the concentration of the extracellular space is $K^+_{out} \simeq 3.5$ mM. According to this data, equation (2.28) gives $E_K \simeq -97$ mV.

Moreover, experimental measurements give respectively $V \simeq -70$ mV for the neuron, and $V \simeq -80$ mV for the astrocyte, thus, at rest, K^+ are exiting the cell for both the neuron and the astrocyte because $V > E_K$, so $\bar{\mu}_{K^+_{out\to in}} > 0$. Therefore at rest, K^+, is extruded from ion channels in neurons and astrocytes.

However, because of the neuron firing, each spike releases some potassium into the extracellular space and K^+_{out} increases, and hence, E_K also increases (it becomes less negative). In the case of the astrocyte, which is more hyperpolarised than the neuron, this increase of E_K coupled to a more negative resting V can yield $V < E_K$. At that point, K^+ ions are entering through ion channels the cell because $\bar{\mu}_{K^+_{out\to in}} < 0$ (Figure 2.16, between the extracellular 1 and the astrocyte).

This alternation of the direction of passive transport is involved in spatial buffering (Figure 2.16). Spatial buffering is a mechanism which removes K+ from regions with

high concentration to spread it to regions with low concentration. For example, Muller cells, the main glial cells in the retina, play this role (Karwoski et al., 1989) (Kofuji and Newman, 2004). Besides, this process appears to be less costly in ATP for glia cells than for neurons (Amédée et al., 1997).

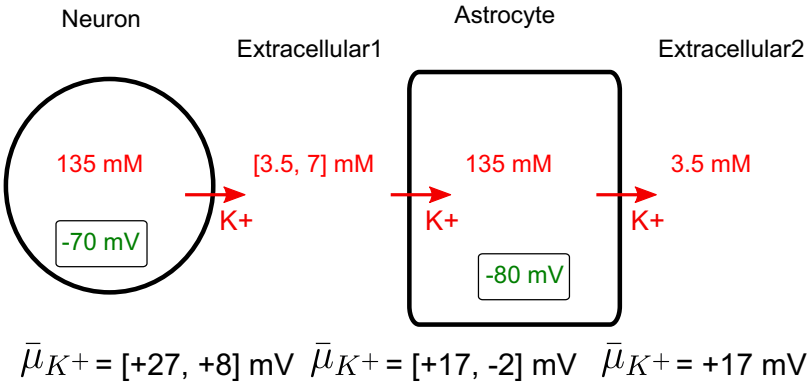

Figure 2.16: Scheme of potassium spatial buffering from the extracellular space 1 to the extracellular space 2 through the astrocyte. In red are the potassium concentrations and fluxes, in green are the voltage values. $\bar{\mu}_{K^+_{out \to in}}$ are calculated between two compartments.

2.4.3 Astroglial Kir4.1 channel

Inwardly rectifying K^+ (Kir) currents have been discovered in skeletal muscles (Katz, 1949). Their transport rate seems to depend more on the membrane voltage than predicted by the Nernst equation (Hibino et al., 2010). Therefore, at potentials more negative than E_K, Kir channels permit faster current flows than at potentials more positive than E_K (Hagiwara and Takahashi, 1974) (Sakmann and Trube, 1984).

In sheep cardiac cells, the inwardly rectifying K channels are controlled by a gating mechanism. During hyperpolarization, time- and voltage-dependent inactivation of the gating mechanism can be due to the binding of external Na, Ca or Mg to the channel (Carmeliet et al., 1987). The conductance of Kir current is proportional to the square root of K extracellular concentration in the membrane of starfish egg cell (Hagiwara and Takahashi, 1974) in ventricular cells from guinea-pig heart (Sakmann and Trube, 1984) or in embryonic chick ventricle cells (Mazzanti and DeFelice, 1988).

In addition, Kir channels have been found in different kinds of cells including glial cells (Hibino et al., 2010). The astrocyte seems to be a major actor in the modulation of the excitability and the transmission of the neuron (Fiacco and McCarthy, 2006). Due to its strong conductance to potassium, the astrocyte is very sensitive to changes in extracellular potassium levels (Dallérac et al., 2013) (Olsen et al., 2006). The balance between potassium influx and outflux determines the resting membrane potential in microglial and astrocyte cells in rat (Chung et al., 1999). Besides, when blocking Kir4.1 channels with barium, a selective blocker of Kir channels (Ransom and H, 1995) (D'Ambrosio et al., 2002), glia cells are highly depolarized (Djukic et al., 2007) (Figure 2.17).

Thus, the astrocyte uptakes the extracellular K^+ released by discharges of the neuron (Amzica et al., 2002). This K^+ spatial buffering is possible through Kir channels (Oakley II et al., 1992) (Olsen et al., 2006) and the first identified one is the Kir4.1 (Takumi et al., 1995).

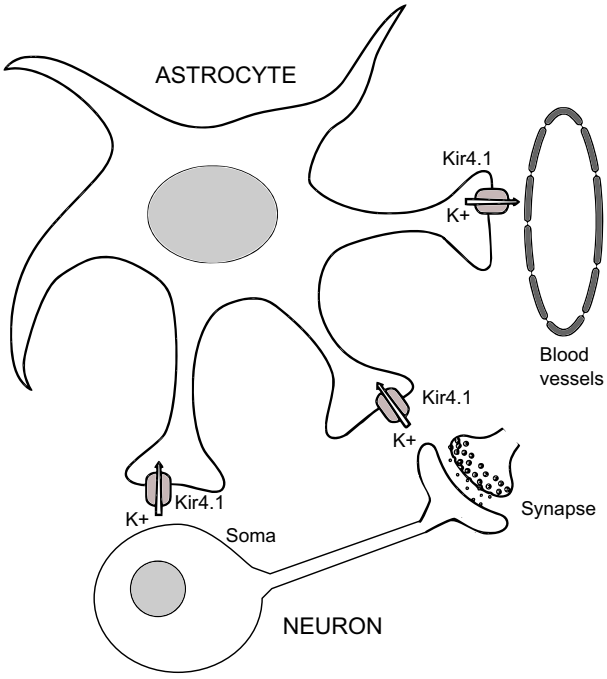

Figure 2.17: Localization of astroglial Kir channels and contact with neural soma, synapse and blood vessels.

Even if, in the rat hippocampus, Kir channels clearance seems to be minor compared to Na^+/K^+ ATPase (Xiong and Stringer, 2000), in ex vivo experiments of Kir4.1 knock-out mice, the regulation of extracellular K is less efficient than in wild type mice (Haj-Yasein et al., 2011) (Bay and Butt, 2012) suggesting that the Kir4.1 has a major role in clearance of extracellular potassium.

Moreover, in Huntington's disease, the expression of Kir4.1 channel functional is decreased and this decrease seems to elevate in vivo striatal extracellular K^+ and increase MSN excitability in vitro (Tong et al., 2014). When Kir4.1 function is restored with a viral delivery of Kir4.1 channels, this leads to a normalized extracellular K^+. However, the majority of published models make this hypothesis. In most cases, it has small consequences because K^+ presents small variations but to study Kir and the change of extracellular K^+, this hypothesis is not valid.

2.4.4 Computing dynamic potassium

The use of Hodgkin-Huxley model (see section 2.3.2) assumes that the intra- and extracellular ion concentrations of sodium and potassium are constant. The validity of this assumption in the mammalian brain is not that clear (Cressman et al., 2009) (Ullah et al., 2009). Thus, Cressman et al. (2009) computed the concentration of extracellular potassium, K_{out}, over time:

$$\frac{d[K_{out}]}{dt} = -0.33I_K - 2\beta I_{pump} - I_{glia} - I_{diff} \tag{2.30a}$$

$$I_K = -\left(g_K n^4 + \frac{g_{AHP}[Ca]_i}{1+[Ca]_i}\right)(V - V_K) - g_{KL}(V - V_K) \tag{2.30b}$$

$$V_K = 26.64\ln\left(\frac{[K_{out}]}{[K_i]}\right) \tag{2.30c}$$

$$\frac{d[Ca]_i}{dt} = -0.002g_{Ca}\frac{V - V_{Ca}}{1+\exp(-\frac{V+25}{2.5})} - \frac{[Ca]_i}{80} \tag{2.30d}$$

where the factor $0.33mM.cm^2.\mu coul^{-1}$ converts current density to rate-of-change of concentration I_K is the current associated to potassium, the factor β corrects for the volume fraction between the interior of the cell and the extracellular space when calculating the concentration change, I_{pump} is the current associated to Na/K pumps, I_{glia} is the current associated to the capacity of glial cells to remove excess potassium from the extracellular space, I_{diff} is the current associated to the diffusion of potassium away from the local extracellular space.

Then, in I_K equation, g_{AHP} is the conductance of afterhyperpolarization current, $[Ca]_i$ is the intracellular calcium concentration over time, V is the voltage, g_{KL} is the conductance of potassium leak current

Here, instead of using a constant E_K, as in the Hodgkin-Huxley model, the Nernst equation is updated dynamically with V_K over time, with $[K_i]$, the intracellular potassium concentration. g_{Ca} is the calcium conductance and V_{Ca} is the reversal potential of calcium. Similarly, Cressman et al. (2009) used equations to compute $[Na]_i$, the intracellular sodium concentration.

Therefore, the authors of this model could show that this model presents slow and large-amplitude oscillations in ion concentrations, similar to what is seen physiologically in seizures (Cressman et al., 2009) and periodic stimulation in the model could prevent them (Owen et al., 2013). Moreover, in the model, glia is involved in excitability of neurons (Ullah et al., 2009) and can exhibit periodic bursting (Barreto and Cressman, 2011). Hence, removing this assumption on potassium and sodium dynamics brought new insight on the role of astrocytes to shape neuronal activity.

With a similar Hodgkin-Huxley model with dynamic potassium and sodium concentrations Tagluk and Tekin (2014) created a neural network showing that potassium concentration significantly shape action potentials of the network, through their form, their regularity, and their synchrony. Another model developed by Hübel and Dahlem (2014) distinguished three distinct slow time scales, determined, respectively, by the cell volume-to-surface-area ratio and the membrane permeability (seconds), the buffer time constants (tens of seconds), and the slower backward buffering (minutes to hours).

However, in all these models, even if potassium and sodium are fluctuating, the effect of astrocytes, known to be involved in potassium dynamics, has not been tested.

2.4.5 Computational modelling approaches of tripartite synapse and astroglial Kir4.1 channel

Computational models involving Kir current confirm that Kir can act as a buffer for extracellular K^+ and influence the membrane potential at rest, like in mouse muscle fiber (Siegenbeek, 1994) or simulate seizure discharges and spreading depression in a Hodgkin-Huxley like hippocampal pyramidal cell model with an interstitial space and surrounding glia (tripartite model) (Kager et al., 2000) (Kager et al., 2007).

Inspired from the previous model, other tripartite models show that Kir currents are involved in neuron-glia interactions by influencing the firing pattern (Somjen et al., 2008) and the extracellular potassium homeostasis (Sibille et al., 2015).

Besides, its relevance during neuronal activity, a mathematical analysis shows that K^+ uptake by glial cells has an impact on the neural resting membrane potential, and the orientation of this impact depends strongly on the parameters values of their formula (Noori, 2011). Furthermore, at the scale of the network, sodium and potassium concentrations influence directly the shape, the regularity and the synchrony of the network-generated spikes as shown in a Hodgkin-Huxley model-based cortical network (Ullah et al., 2009) (Tagluk and Tekin, 2014).

Hence, these models support the idea that Kir channels expression influence the neural membrane potential through the regulation of extracellular potassium concentration.

2.5 Synaptic plasticity

In the following sections, we copied parts directly from a review on the modulation of the spike-timing dependent plasticity that we are currently submitting.

2.5.1 Spike-timing-dependent plasticity (STDP)

Spike-timing-dependent plasticity (STDP) is a Hebbian synaptic learning rule accounting for experience-dependent changes in neural networks. This synaptic rule has been explored in different cerebral structures, for different neuronal types and for different species, and displays numerous forms. These different forms rely on long-term plasticity expression (depression or potentiation), expression temporal windows of this plasticity and signaling pathways involved.

Canonical STDP is bidirectional and hebbian; i.e. post-pre pairings ($\Delta t_{STDP} < 0$) repetition drive timing-dependent long-term depression (tLTD) and pre-post pairings ($\Delta t_{STDP} > 0$) repetition drive timing-dependent long-term potentiation (tLTP). This plasticity is expressed in the narrow temporal window (10-100 ms); when pre- and post-synaptic activities are uncorrelated, no long-term synaptic change is observed (Bi and Poo, 1998; Markram et al., 1997). Hebbian STDPs have been observed in the neocortex (Feldman, 2000; Markram et al., 1997; Nevian and Sakmann, 2006; Sjöström et al., 2001), the hippocampus (Bi and Poo, 1998; Nishiyama et al., 2000; Wittenberg and Wang, 2006), and the striatum (Fino et al., 2008, 2009). In opposition to hebbian STDPs, bidirectional and anti-hebbian STDPs induced tLTP with post-pre pairings and tLTD with pre-post pairings repetition. A pioneer STDP study has described this synaptic plasticity in cerebellum-like structure of electrical fish (Bell et al., 1997). These STDP has been observed, more recently, in the striatum (Cui et al., 2015; Fino et al., 2010, 2005; Paille et al., 2013; Schulz et al., 2010) or in the somato-sensory cortex for instance (Letzkus et al., 2006).

Another kind of anti-hebbian STDP induced solely t-LTD and are named unidirectional and anti-hebbian (Han et al., 2000; Requarth and Sawtell, 2011; Zhao and Tzounopoulos, 2011). Overall, these STDP are asymmetric with a wider tLTD temporal window for pre-post pairings. These STDP have been observed in the neocortex (Lu et al., 2007), in the dorsal cochlear nucleus (Tzounopoulos et al., 2004) and in the somatosensory cortex (Egger et al., 1999).

2.5.2 The molecular pathways of STDP

Spike-timing dependence of plasticity can be categorized into two distinct molecular systems of coincidence detectors (Feldman, 2012). First system has been investigated in hippocampal CA1 neurons (Campanac and Debanne, 2008), neocortical L2/3 pyramidal cells (Nishiyama et al., 2000; Froemke et al., 2005), striatal spiny projection neurons (SPN) (Pawlak and Kerr, 2008), and gabaergic striatal interneurons (Fino et al., 2008). The first system comprises of just one coincidence detector, the NMDA receptor (NMDAR). Both spike-timing dependent potentiation (t-LTP) and spike-timing dependent depression (t-LTD) depend on NMDAR activation and calcium influx through the VGCCs. Second form of STDP, found in (Sjöström et al., 2003; Bender et al., 2006; Nevian and Sakmann, 2006; Corlew et al., 2007), cholinergic striatal interneurons (Fino et al., 2008), SPNs in the striatum (Fino et al., 2010), comprises of a NMDAR-dependent potentiation and

mGluR- and/or CB1R-dependent depression. The mGluR-CB1R-dependent form of LTD is independent of postsynaptic NMDARs, but often depends on activation of presynaptic NMDARs (preNMDARs) (Sjöström et al., 2003; Bender et al., 2006; Corlew et al., 2007). Recently a third, endocannabinoid-dependent form of bidirectional STDP was discovered in SPNs (Cui et al., 2015, 2016). Endocannabinoid-dependent t-LTP is induced by a low number of pairings (10, for more than 75 pairings t-LTP is NMDAR-dependent), requires TRPV1R activation (Cui et al., 2015) and presynaptic PKA and calcineurin recruitment (Cui et al., 2016).

One of the most popular parts of the brain for investigation of synaptic plasticity is the CA3 pyramidal neuron to CA1 pyramidal neuron synapse (Schaffer collateral synapse). Even though the largest bulk of studies have explored rate-dependent synaptic plasticity, there is a substantial number of studies investigating Hebbian, bidirectional STDP. For this type of plasticity the NMDA receptor serves as the coincidence detector for both potentiation and depression (Campanac and Debanne, 2008), therefore calcium amplitude determines plasticity direction (Lisman, 1989). For Pre-Post pairings, when the presynaptic activity precedes the back propagating action potential (bAP), the EPSP coincides with the bAP resulting in high, supralinear calcium influx through the NMDAR and voltage dependent calcium channels VDCCs (particularly L-type (Kim and Li, 2015; Pawlak and Kerr, 2008)) and t-LTP. For Post-Pre pairings, when the bAP precedes the presynaptic activity, calcium influx through the NMDARs and VDCCs is lower and sublinear (Magee and Johnston, 1997; Koester and Sakmann, 1998; Nevian and Sakmann, 2006) and as a result induces t-LTD.

Supralinear calcium elevation necessary for t-LTP can be caused by a number of molecular mechanisms. EPSP causes inactivation of the A-type K+ channels, possibly by a mitogen-activated protein kinase (MAPK) dependent mechanism (Watanabe et al., 2002) and, as a result, boosts calcium influx during the bAP. EPSPs activate sodium channels eliciting dendritic sodium spikes, which generate a brief temporal window for calcium influx (Hoffman et al., 1997; Stuart and Häusser, 2001; Kim and Li, 2015). A short positive interval between glutamatergic input and depolarization, which removes the Mg-block of the NMDARs, maximizes the NMDAR-current (Kampa et al., 2004). AMPAR-mediated EPSPs coinciding with bAPs provide a local depolarization, which results in supralinear calcium transient summation (Fuenzalida et al., 2009; Holbro et al., 2010).

EPSP following the bAP coincides with the more modest bAP-caused afterdepolarization. As a result calcium influx is only slightly higher than at rest (Karmarkar et al., 2002). At hippocampal Schaffer collateral synapses bAP triggers calcium influx that might cause calcium-dependent inactivation of the NMDARs (Rosenmund et al., 1995), lowering NMDA-dependent calcium transients following the bAP. This calcium-dependent NMDAR inactivation is mediated by phosphatase 2B (PP2B, calcineurin) (Tong et al., 1995). Another mechanism controlling calcium influx into the dendritic spines is provided by small conductance potassium channels (SK-channels). Calcium elevation activates SK-channels and causes hyperpolarization and consecutive inhibition of VDCCs and reduction of NMDAR-dependent calcium-transients (Ngo-Anh et al., 2005; Bloodgood and Sabatini, 2007). Even though calcium influx through NMDARs alone can activate SK-channels in CA1 pyramidal cells (Wang et al., 2015; Jones et al., 2017) due to NMDAR and SK-channel colocalization within the PSD (Lin et al., 2008), t-LTP induction inhibits SK-channels via a CaMKII-mediated mechanism and PKA-mediated endocythosis of SK-channels (Lin et al., 2008). In contrast to the hippocampal CA1 neurons, in the neocortex NMDAR-mediated calcium transients do not activate SK channels (cortical layer 2/3 and 5 pyramidal neurons (Jones et al., 2017). Only the higher amplitude calcium transients accompanying the bAPs activate SK channels and hence gate STDP in cortical

pyramidal neurons (Jones et al., 2017). Lin et al. (2008) showed that t-LTP at Schaffer collaterals is CaMKII-dependent, but not PKA-dependent. There is also experimental evidence of mGluR1-dependence of t-LTP (Tigaret et al., 2016). mGluR1 activation during t-LTP induction inhibits SK-channels possibly by a mechanism similar to M1-receptor mediated inhibition of SK-channels (Tigaret et al., 2016), as both M1R and mGluR1 are Gq-coupled. Carlisle et al. (2008) showed that two scaffolding proteins, PSD-93 and PSD-95, both play an important role in AMPA receptor trafficking and formation of NMDA receptor-associated signaling complexes involved in synaptic plasticity. As a result knocking-out PSD-93 disrupted t-LTP, whereas knocking-out PSD-95 disrupted LTD and AMPA receptor-mediated transmission.

Experimental findings concerning molecular pathways underlying spike-timing dependent-plasticity in spiny projection neurons, a major group of striatal output neurons, paint a very complicated picture. First of all, blocking gabaergic transmission transforms corticostriatal plasticity from Hebbian to anti-Hebbian (Paille et al., 2013). Secondly, experiments indicate a presence of 3 distinct systems of coincidence detectors. In addition to endocannabinoid-dependent bidirectional plasticity exhibited by SPNs (Cui et al., 2015, 2016), most studies indicate that corticostriatal hebbian t-LTP requires NMDA receptor activation (Pawlak and Kerr, 2008; Fino et al., 2010; Shen et al., 2008; Yagishita et al., 2014). Coincidence system of corticostriatal hebbian t-LTD depends on the induction protocol. Pawlak and Kerr (2008) reported dependence on NDMAR activation, whereas other studies (Fino et al., 2010; Shen et al., 2008; Cui et al., 2015) showed mGluR1 and eCB-dependence. For mGlur1-dependent LTD (Fino et al., 2010) PLCβ serves as a coincidence detector, which is activated by both glutamate and postsynaptic calcium and t-LTD is blocked by BAPTA when IP3R-gated calcium stores are depleted or unavailable. PLCβ and IP3 receptors activate retrograde endocannabinoid signaling, which is also required for t-LTD (Fino et al., 2010; Cui et al., 2015, 2016). Presynaptic eCB1R activation lowers the release probability depressing synaptic transmission (reference) . This form of plasticity is also D2R-dependent (Cui et al., 2015). Both NMDAR-dependent and eCB-dependent t-LTD (Pawlak and Kerr, 2008; Cui et al., 2015) require D1/D5R activation. Pawlak and Kerr (2008) and Yagishita et al. (2014) (t-LTP only) showed that time-course of bidirectional STDP is modulated by dopamine D2 receptors (D2R activation (t-LTD onset was more immediate, t-LTD onset was delayed)).

Spiny projection neurons can be divided into two groups: D1R expressing direct pathway SPNs (dSPNs) and D2R expressing indirect pathways SPNs (iSPN). The activation of D1 receptors coupled to Golf increases cAMP levels whereas the activation of D2Rs Gi/o-coupled decreases cAMP levels. It has also been shown that D1R activation attenuates both synaptic- and action potential-evoked calcium influx into dendritic spines via a PKA-dependent regulation of NMDARs. Activation of A2ARs counteracts this effect and enhances calcium influx into dendritic spines (Higley and Sabatini, 2010). Corticostriatal t-LTD of dSPNs, requiring blocking of D1/D5R, does not depend on the causality of the paradigm (Shen et al., 2008, 2015) and is inhibited by muscarinic M4 receptor antagonists. dSPN t-LTD also depends on mGlur5, RGS4 (Shen et al., 2015) and eCB1R activation (Wei et al., 2015). The iSPN t-LTD is blocked by D2R inhibitors and transformed to t-LTP by blocking of D2R and A2 adenosine receptors (A2aR) (Shen et al., 2008). Blocking A2aR and activating D2R transforms t-LTP to t-LTD (Shen et al., 2008). Downstream the NMDA receptor t-LTP of dSPNs depends on CaMKII, PKA, and DARP32 activation, protein synthesis (Yagishita et al., 2014) and MEK activation (Shen et al., 2015).

2.5.3 Neuromodulation of STDP

Neuromodulators such as dopamine, acetylcholine or noradrenaline and molecules such as GABA, brain-derived neurotrophic factor (BDNF), NO or endocannabinoids, plays an important role in synaptic plasticity regulation (Figure 2.18). However, the dynamic of this neuromodulation is about seconds or even minutes whereas STDP is taking place at the scale of milliseconds. This apparent discrepancy could be revised, for example, from the perspective of a learning system that would need to link recorded information (memory) with a value scale (a system of reward and punishment). Indeed, an individual acting on its environment needs to learn how to discriminate actions leading to reward from those leading to punishment, both possibly occurring seconds, minutes or even hours after the taken action. A system of memory and learning based only on the timescale of STDP would miss this essential information. Thus, one role of neuromodulation would be to link STDP and a system of reward and punishment, forming the basis of the learning system. In this context and depending on the brain regions, the next part will present how dopamine and endocannabinoids molecules modulate the induction, the orientation or the timing of the synaptic plasticity.

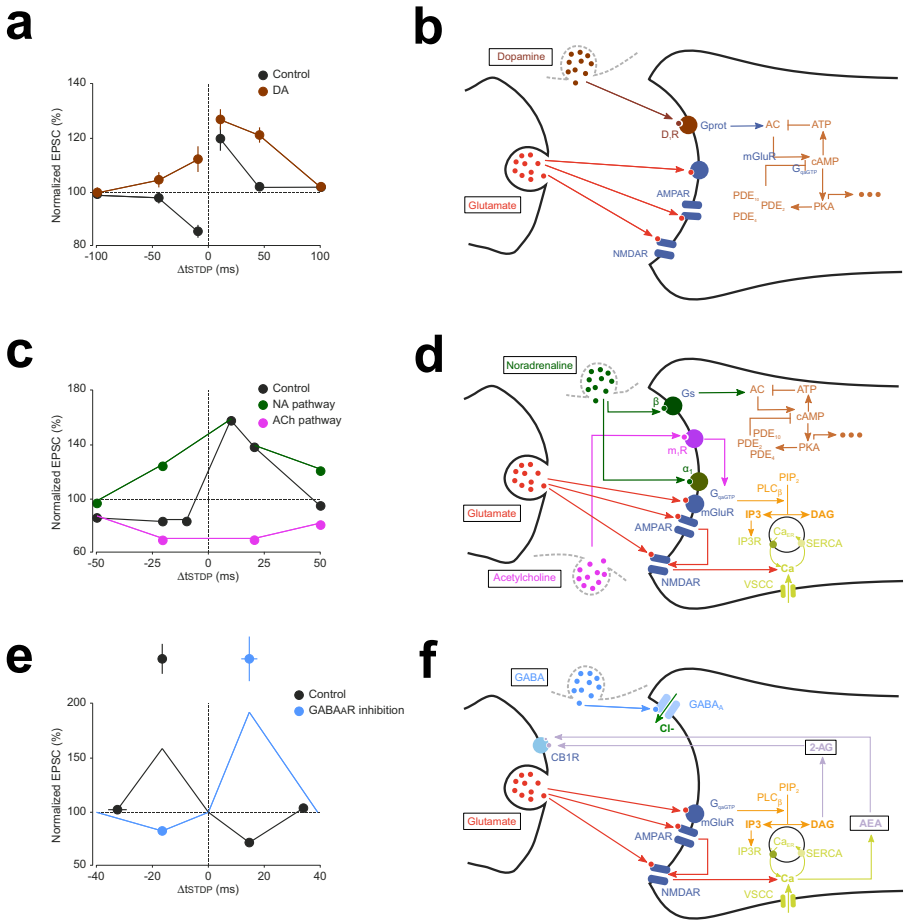

Figure 2.18: (a) Changes in the EPSPs elicited by pairing with different time delays after perfusion of dopamine (Zhanga et al., 2009) and (b) is the scheme of pre and post-synaptic components with the corresponding signaling pathways. (c) Changes in the EPSPs (30 min after conditioning) elicited by pairing with different time delays after 10 min perfusion of β-adrenergic and M1 muscarinic agonists (Seol et al., 2007) and (d) is the scheme of pre and post-synaptic components with the corresponding signaling pathways. (e) Changes in the EPSPs elicited by pairing with different time delays after a blockade of $GABA_A$ receptors (Paille et al., 2013) and (f) is the scheme of pre and post-synaptic components with the corresponding signaling pathways.

Dopamine

First, dopamine receptors are G-protein-coupled receptors (GPCRs) with seven transmembrane domains. GPCRs are mainly slow, metabotropic receptors that functionally modulate other receptor systems and/or ion channels (Lachowicz and Sibley, 1997; Missale et al., 1998) without inducing large postsynaptic current (Yang and Seamans, 1996). In the central nervous system (CNS), dopamine can interact with five receptors subtype: D1R, D2R, D3R, D4R and D5R. These dopaminergic receptors are classified into two families based on their G-protein coupling. Thus, the Gs-, Gq- or Golf-coupled D1 family includes D1R, D5R and the Gi/o D2 family includes D2R, D3R, D4R (Jackson and Westlind-Danielsson, 1994; Lachowicz and Sibley, 1997; Missale et al., 1998; Zhuang et al., 2000; Jin et al., 2001; Kimura et al., 1995; Sidhu and Kimura, 1997). D1/5 receptors activate cAMP and/or IP3 second messenger pathways, which lead to a cascade of intracellular signaling encoding membrane proteins and enzymes, to mediate long-term changes in intrinsic plasticity, and ionotropic and metabotropic glutamate receptors, to mediate changes in synaptic plasticity. D2 class receptors suppress cAMP synthesis and can also transactivate a platelet-derived growth factor to initiate intracellular Ca2+ release, stimulating calmodulin to inactivate NMDA receptors (Kotecha et al., 2002; Wang et al., 2003).

In culture, the STDP occurring at synapses of CA1 pyramidal neurons in the rat hippocampus is bidirectional and hebbian, meaning that repetition of pre-post sequences induces t-LTP whereas repetition of post-pre induces t-LTD (Zhanga et al., 2009). However, this STDP can be modulated by addition of exogenous dopamine in the bath, which enlarges the temporal window of t-LTP, transforming bidirectional STDP in unidirectional STDP, shifted toward t-LTP (pre-post sequences and post-pre sequences result both in t-LTP). Furthermore, addition of exogenous dopamine, in slices, causes also a reorientation of t-LTD into t-LTP (Brzosko et al., 2015).

This reorientation depends on the activation of D1-type dopaminergic receptors but it is independent of D2-type dopaminergic receptors (Zhanga et al., 2009). Indeed, addition of sucrose, in slices, diminishes the dopamine concentration and prevents induction of t-LTP, in response to STDP protocol (Edelmann and Lessmann, 2011). However, injecting dopamine, in addition of sucrose, activates D1 dopaminergic receptors, permitting to modulate back-propagation properties of action potentials and to restore t-LTP in response to STDP (Edelmann and Lessmann, 2011). Besides, subsequent DA application changes also acetylcholine-facilitated synaptic depression into potentiation and the effect of DA is irrespective of the precise spike order. It is mediated, at least in part, via the activation of the cyclic adenosine monophosphate (cAMP) signaling cascade (Brzosko et al., 2017).

Still in the hippocampus, the activation of D1 and D5 receptors (D1R and D5R) is also required for the induction of t-LTP at the synapses between the mossy fiber pathway and the dentate gyrus cells (Yang and Dani, 2014). Indeed, the inactivation of potassium currents IA by D1R and D5R makes these neurons more excitable, thus, in presence of dopamine, the amplitude of the back-propagating action potential rises and, consequently, the induction threshold of t-LTP is reduced (Yang and Dani, 2014).

Altogether, these results in hippocampus suggest a particular form of plasticity rule with, at least, 3 main components: the pre- and post-synaptic inputs and also, reward signals through dopamine release. With this system, DA signal, induced by unexpected and rewarding events, allows to extend LTP induction temporal window. And thus, any pre-synaptic activity occurring concomitantly with post-synaptic activity (regardless of temporal order) is more susceptible for potentiation.

The striatum is strongly modulated by dopaminergic inputs from the substantia nigra pars compacta (SNc). The striatal output neurons (the medium-sized spiny neurons, MSNs) belong either to the direct either indirect trans-striatal pathways (Gerfen and

Surmeier, 2011; Calabresi et al., 2014) regarding basal nuclei targeted. These two MSN subpopulations also show different neurochemical identity since direct MSNs (dMSNs) express the dopaminergic receptor D1R and indirect MSNs (iMSNs) express the dopaminergic receptor D2R in mice (Matamales et al., 2009). In anesthetized rats, the induction of cortico-striatal STDP, which is bidirectional and anti-hebbian, necessitates phasic dopaminergic release (Schulz et al., 2010). In vitro, two studies focusing on dopaminergic modulation have shown that cortico-striatal STDP is bidirectional and hebbian (Pawlak and Kerr, 2008; Shen et al., 2008) when GABAergic transmission is inhibited (cf GABAergic modulation). In GFP transgenic mice, Shen et al. (2008) observed that cortico-striatal t-LTD in iMSNs requires D2R activation whereas cortico-striatal t-LTP in dMSNs requires D1R activation. However, in rats, Pawlak and Kerr (2008) described that both t-LTD and t-LTP requires D1R, and no D2R, activation. In the basal ganglia and especially at striatum level, dopaminergic release is linked to associative learning and habit formation (Shen et al., 2008). However, all these publications show variation in results underlying the complex role of dopamine on the two trans-striatal pathway modulation and hence, on the basal ganglia output modulation. In the prefrontal cortex, dopamine permits the induction of t-LTP (for a repetition of pre-post sequences) at cortico-cortical synapses of pyramidal cells of layer 5 (Xu and Yao, 2010). This t-LTP is directly dependent upon activation of D1 dopaminergic receptors expressed by post-synaptic neuron and indirectly upon D2 dopaminergic receptors expressed by surrounding GABAergic interneurons. The activation of D2 receptors allows to block inhibition of GABAergic interneurons and lets emerge t-LTP with pre-post interval up to 10 ms. Besides, by combining activation of D2 receptors with the one of D1, this temporal window of t-LTP can extend to 30 ms (Xu and Yao, 2010). More recently, it has been observed that the addition of exogenous dopamine also permits the emergence of anti-hebbian t-LTP (for a repetition of post-pre sequences) via the activation of D1 dopaminergic receptors (Ruan et al., 2014).

This mechanism, in which DA acts as a signal that enables and/or facilitates synaptic modifications to reinforce post-trial memory traces in the PFC, could play a crucial role in PFC-mediated cognitive functions that depend on activity-dependent synaptic plasticity (Xu and Yao, 2010; Ruan et al., 2014). Finally, in the lateral nucleus of the amygdala, the t-LTP requires the activation of D2 dopaminergic receptors (Bissière et al., 2003). As for the prefrontal cortex, the D2 receptors are expressed on GABAergic interneurons and their activation allows inhibiting GABAergic transmission (Bissière et al., 2003). Interestingly, dopamine is released upon stress in amygdala (Inglis and Moghaddam, 1999). Hence, dopaminergic neuromodulation of inhibitory synaptic transmission seems to be a crucial mechanism underlying the acquisition of fear conditioning.

Thus, depending on the brain region, dopamine can simply modulate spike-timing plasticity or be used as a detector of coincidences and be necessary for its induction, making the link between neurons events at the time scale of milliseconds with stimuli at higher time scales. Dopamine plays a crucial role as neuromodulator of STDP for learning.

Endocannabinoids

The endocannabinoid (eCB) signaling system in mammals is comprised of the endogenous lipid messenger anandamide and 2-arachidonoylglycerol (2-AG) and CB1 GPCRs (CB1R) in the CNS (Mechoulam and Parker, 2013). CB1R regulates diverse brain functions and behaviours, modulating neurotransmitter release and neuronal excitation through presynaptic activation of Gi/o, GIRK channels, and arrestin/MAP kinase signaling (Howlett et al., 2004). Endocannabinoids are synthesized postsynaptically by lipases, travel across synapses in a retrograde manner (Wilson and Nicoll, 2002), and become embedded in the

presynaptic membrane where they can activate CB1R (Fowler, 2013). In the somatosensory cortex, at layer 4 to layer 2/3 synapses, the pyramidal cells STDP is bidirectional, hebbian, and relies on two different coincidence detectors (Bender et al., 2006). Indeed, t-LTP is NMDAR dependent whereas t-LTD expression involves signaling molecules including mGluRs, calcium from IP3R-gated internal stores and VSCCs and retrograde eCB signaling (Bender et al., 2006).

In the dorsolateral striatum, corticostriatal (projection from somatosensory cortex) STDP [100 pairings at 1 Hz] at MSN's level displays bidirectional and Hebbian properties (Fino et al., 2005, 2010; Paille et al., 2013; Cui et al., 2015, 2016; Valtcheva and Venance, 2016; Valtcheva et al., 2017). t-LTP is dependent on NMDAR activation, while t-LTD depends on retrograde eCB signaling. The action of eCB on CB1R constitutes the last step of a signaling cascade involving activation of mGluR5/M1Rs/VSCCs, and then PLCβ and IP3Rs (Fino et al., 2010). Interestingly, robust eCB-mediated t-LTP emerges for a low number of post-pre pairings (5-10) and depends on the activation of CB1R and transient receptor potential vanilloid type-1 (Cui et al., 2015, 2016). This eCB-LTP may represent a molecular substrate operating during rapid learning. Indeed, in the cortex or striatum, neurons with behaviour-related activities fire a few spikes upon behaviourally relevant events during each trial (Schultz et al., 2003; Pasupathy and Miller, 2005; Quilodran et al., 2008), suggesting that a few trials should be sufficient to induce synaptic plasticity.

In the ventral striatum, corticostriatal (projection from prefrontal cortex) STDP, with pre-post pairings [100 pairings at 1 Hz], induces eCB-mediated t-LTD (Bosch-Bouju et al., 2016). Besides, endocannabinoid modulations of cortico-striatal synaptic efficacy in the dorso-medial striatum are involved in behavioural adaptations to social stress (Bosch-Bouju et al., 2016). Thus, STDP mediated by endocannabinoids is critical in the striatum either for quick learning or in reaction to a stressful environment.

At hippocampal CA3-CA1 synapses, STDP is bidirectional and hebbian in pyramidal cells (Campanac and Debanne, 2008; Kwag and Paulsen, 2009; Andrade-Talavera et al., 2016). Both t-LTD and t-LTP require NMDA receptors for their induction, but with two different populations of NMDA receptors involved. Unlike t-LTP, t-LTD also requires postsynaptic Ca2+ for their induction, and t-LTD also requires activation of mGlu5 receptors, PLC and postsynaptic IP3 receptor-mediated Ca2+ release from internal stores, eCB synthesis and then, activation of CB1R (Andrade-Talavera et al., 2016). This t-LTD is observed in developing P12-P18 animals and doesn't exist after P21 suggesting that eCB-LTD during development is possibly linked to the refinement of synaptic connections and remodeling of neuronal circuits.

In the dorsal cochlear nucleus, STDP observed at parallel fiber-cartwheel cell synapses is characterized by an anti-hebbian timing rule, for which only t-LTD is induced using a pre-post pairing (Tzounopoulos et al., 2004, 2007). This anti-hebbian t-LTD required simultaneous activation of presynaptic NMDA and CB1 receptors (Tzounopoulos et al., 2007). Moreover anti-Hebbian STDP observed in cartwheel cells may underlie a filtering role in the DCN and help in responding to novel sounds by suppressing the response to self-generated or expected sounds.

Thus, these findings present endocannabinoids as necessary for synaptic plasticity in different brain regions, and may underlie a large variety of learning abilities, depending on activity patterns and on the behavioural context.

The difference of time scale between STDP and neuromodulators seems to allow selectivity and robustness for plasticity and which has a meaning in a learning system based on the reward.

2.5.4 Molecular pathway-based computational models of STDP

In an attempt to better understand mechanisms governing learning and memory and determine which mechanisms control input-dependent plasticity numerous models of STDP have been created. These models range in molecular complexity from single ions (i.e. calcium) to signaling pathways, and in spatial complexity from a single compartment to multi-compartmental. In the following, we subdivide the models into two types: those evaluating the control of plasticity from calcium alone, and those which add one or more downstream signaling pathway molecules. In addition, we try to distinguish single compartment models from those that add some degree of spatial structure to the post-synaptic neuron. We acknowledge that in both of these dimensions the classification is not binary and some models bridge the divide.

Models of calcium dynamics in response to STDP stimuli are the most common type of models, and are justified both by the critical role of calcium in plasticity and also by the stimulation protocol in which neuromodulator release does not change. The only difference between protocols that produce t-LTP and protocols that produce t-LTD is the timing between the pre-synaptic stimulation and the post-synaptic action potential; thus the number and frequency of pre-synaptic stimulation does not differ between t-LTP and t-LTD. This implies that pre-synaptic release of neuromodulators does not differ, and post-synaptic molecules activated by calcium dynamics determine the direction of plasticity.

Calcium predicting the direction of synaptic plasticity is one of the ideas that are popular among theoreticians. In the simplest form the peak calcium (or indeed the amplitude of the current through the calcium permeable, NMDA subtype of the glutamate receptor) controls the direction of plasticity (Evans and Blackwell, 2015; Graupner and Brunel, 2010). This is known as the "two-threshold" rule: if calcium (either peak or integrated calcium) is above the higher, potentiation threshold, t-LTP is induced, whereas if calcium is between the lower depression threshold and the potentiation threshold, t-LTD occurs. Pre-post pairings produce a large calcium influx through the NMDA receptor channel with calcium concentration above the high threshold; whereas post-pre pairings produce a moderate calcium influx with calcium concentration between the thresholds. One of the first models of NMDAR-dependent synaptic plasticity was proposed by Shouval et al. (2002). This model, using simplified calcium dynamics inside a dendritic spine, accounted for a diverse range of stimulation protocols such as STDP and classical rate-based plasticity; however it predicted depression for long positive ISIs, a model prediction which is not confirmed by experiments (but see REFS. In the striatum, a model of calcium dynamics (Evans et al., 2012) evaluated the role of NMDAR subunits in shaping the sensitivity to timing dependence, and correctly predicted that NR2A would require a small ISI, whereas NR2B can support t-LTP with a wide ISI. Several extensions or modifications to the basic model have been made both to account for results with spike triplets (i.e., when either two pre-synaptic stimuli or two post-synaptic APs are generated) and to minimize the t-LTD window for long positive ISIs. Adding an additional coincidence detection of pre-synaptic NMDA receptors and endocannbinoids is one mechanism utilized in a neuromorphic implemention of calcium based synaptic plasticity (Rachmuth et al., 2011). Alternatively, incorporating short term depression of transmitter release or AP back propagation (Shouval and Kalantzis, 2005; Bush and Jin, 2012) minimizes the t-LTD seen with long positive ISIs and can account for other experimental results; however, a more broadly applicable study (Rubin et al., 2005) showed that plasticity rules that use calcium amplitude alone cannot completely avoid predicting t-LTD for long positive timing intervals.

An extension of the two threshold rule states that duration of calcium elevation is

equally important in determining direction of plasticity. Several models of STDP explicitly take into account both the amplitude and the duration of calcium in predicting plasticity outcome (Kumar and Mehta, 2011; Graupner and Brunel, 2012). Including the duration threshold or integrating the total calcium response allows correctly predicting experimental outcomes for both traditional STDP curves and STDP curves produced by spike triplets. Another extension of Shouval et al. (2002) model (Standage et al., 2014) implements a calcium-dependent, sigmoid-shaped time constant of calcium decay, which represents saturation of Ca extrusion from the spines. This model shows that saturation of Ca extrusion might be responsible for dependence of t-LTP on the (theta-frequency like) inter-spike interval for triplet stimulation protocols. Including the duration of calcium does not exclude consideration of pre-synaptic release probability on STDP. Indeed, gliotransmission may change the shape of the STDP curve depending on whether gliotransmitters increase or decrease pre-synaptic release (De Pittà et al., 2016).

Most of the aforementioned models use simplified calcium dynamics instead of explicitly, implementing the mechanisms underlying control of calcium, which might improve predictions of synaptic plasticity. In other words, the next set of models used neither single time constant of decay nor summation of independent pre-synaptic and post-synaptic components for calcium dynamics. Though not explicitly implementing an STDP rule, Griffith et al. (2016) indirectly consider the effect of calcium duration by using calcium-bound calmodulin to assess how bAP timing influences calcium concentration. They use a 3-dimensional, deterministic reaction-diffusion model of calcium interactions with calmodulin and other calcium binding proteins within a dendritic spine to show that calcium-bound calmodulin is a more sensitive indicator of spike timing than free calcium. They further demonstrate the role of neuromodulators in regulating synaptic plasticity through their activation or inhibition of calcium dependent potassium (SK) channels during an STDP protocol, which greatly modulates calmodulin activation.

Several studies explicitly investigate how the dendritic location and inhibitory inputs shape the local calcium-based plasticity rules (Bar-Ilan et al., 2013; Jedrzejewski-Szmek and Blackwell, 2016). Bar-Ilan et al. (2013) showed that inhibition shapes the spatial profile of dendritic calcium concentration in neocortical pyramidal neurons. Depending on the location of the excitatory and inhibitory inputs on the dendritic tree, t-LTP may be blocked, transformed to t-LTD, or the synapse may undergo plasticity. Similarly, Jedrzejewski-Szmek and Blackwell (2016) developed a computational model of the major neuron type in the striatum, the spiny projection neuron, including both electrical activity and calcium dynamics. They demonstrated that calcium amplitude and duration together can predict a wide range of experimental plasticity outcomes, and further demonstrated a distance dependence of STDP caused by the back-propagating action potential. This demonstrates that by modelling mechanisms controlling calcium dynamics, including diffusion, buffers and pumps, and by considering calcium duration, the LTD window for long positive ISIs is avoided.

An aspect of calcium dynamics often ignored in modelling studies is calcium release from intracellular stores. This has been shown to contribute to t-LTP under some conditions (Plotkin and Surmeier, 2015). Thus, Nakano et al. (2013) included calcium release from stores in their multicompartmental model of a direct pathway spiny projection neuron. In addition, though not explicitly including other signaling pathways, they evaluated the effect of dopaminergic modulation of calcium, potassium and NMDAR channels. The main result of their simulations was showing that dopaminergic input preceding a bAP induced higher calcium responses than dopamine input following a bAP. This study also predicted that the timing dependence on calcium responses between the up- and down-states was similar.

Beyond calcium, several models add on simplified or abstract version of downstream

signaling molecules: Rubin et al. (2005) propose a three detector system, loosely based on pathways resembling the opposing CaMKII - protein phosphatase signaling pathways. In brief, three calcium-sensitive detectors are implemented: high, transient calcium levels activate the t-LTP detector; low and prolonged calcium elevations activate the t-LTD detector; and intermediate calcium levels activate a 'Veto' detector. The Veto detector suppresses the development of t-LTD, and is critical for avoiding t-LTP with long positive ISI. Cutsuridis (2011), using the three calcium detector system of Rubin et al. (2005), showed that single GABAergic inhibitory input can sharpen the shape of the STDP curve: narrowing the temporal window that supports t-LTD, whereas a train of GABAergic inputs both sharpens the t-LTD window and reduces the t-LTP amplitude. A follow-up study extended the model to burst stimulation, and predicted that GABAergic inputs would expose a t-LTD window for long positive ISIs. The timing of the GABA inputs determined whether the effect was predominantly depression or potentiation.

Several models have implemented more realistic representations of signaling pathway molecules, including the calcium activated phosphatase calcineurin, the calcium activated kinase, CaMKII, and the Gs-activated adenylyl cyclase, the latter of which produces cAMP to activate PKA. Additional pathways, such as protein kinase C (resulting from activation of Gq-coupled receptors such as m1 and mGluR) and ERK (downstream of PKA, PKC and TrkB receptors) are also involved. Several advantages accrue from these models, including the ability to make experimentally testable predictions regarding the role of specific molecules. Another key advantage of simulating signaling molecules is that the t-LTD window for long positive intervals is eliminated without arbitrarily assuming the existence of a calcium concentration range, between the t-LTD inducing calcium range and the t-LTD calcium range, that does not elicit synaptic plasticity. Again these models vary in complexity, such as the number of different signaling pathways included, and whether spatial aspects are included. Several models of these signaling molecules have been applied to STDP protocols in the cortex, hippocampus) and striatum.

Both Carlson and Giordano (2011) and Saudargiene et al. (2015) used a model of AMPAR insertion controled by the CaMKII/PP2A switch. Carlson and Giordano (2011) used a single compartment model of calcium dynamics (Shouval et al., 2002) to activate the biochemical network model of (Pi and Lisman, 2008). This one compartment model can explain spike-timing dependent plasticity and does not predict t-LTD for long positive inter-stimulus intervals. VDCC are critical for the latter effect, as blocking VDCCs allows t-LTD to emerge for long positive inter-stimulus intervals. Saudargiene et al. (2015) incorporated spatial aspects of calcium dynamics by using a detailed compartmental model of pyramidal CA1 neuron (Poirazi et al., 2003) to activate a biochemical network model derived from two earlier models (Pi and Lisman, 2008; Graupner and Brunel, 2007). Saudargiene et al. (2015) showed, by monitoring AMPAR phosphorylation by the CaMKII/PP2A switch, that t-LTD is indeed induced by lower calcium levels than t-LTP, and that t-LTD it also requires many more repetitions of this lower calcium (which is consistent with experimental results). Saudargiene et al. (2015) also looked at the influence of particular timings of inhibition associated with excitatory inputs, showing that inhibition affects t-LTD more than t-LTP, because t-LTD occurs for moderate calcium levels and is thus more vulnerable to any reduction in peak calcium.

Whereas spatial models of calcium dynamics typically include dendritic branching or explicit spines (microdomains), many signaling molecules are anchored via structural proteins into multi-protein complexes, effectively creating nanodomains of molecule interactions. One method for evaluating the effect of nanodomains (without explicitly creating a spatial model) is to couple different sources of calcium to different downstream signaling molecules. This approach was utilized by Mihalas (2011) who coupled three different calcium sources to three different signaling molecules: NMDAR to CaMKII, VDCC to

calcineurin, and PDE to calcium release. Adenylyl cyclase was coupled to both VDCC and NMDAR. The change in synaptic weight was calculated from kinase (t-LTP) and phosphatase (t-LTD) activity. This model investigated the role cAMP degradation in triplet-based STDP, and showed that, if cAMP activity is spatially enclosed to the plasmalemma, STDP profile is similar to that observed in cortical L2/3 slices. STDP profile for spread cAMP activity was consistent with that observed in hippocampal cell culture.

In the striatum, endocannabinoid production and activation of CB1 receptors are required for all forms of LTD, thus, Cui et al. (2016) adapted the signaling pathways from Graupner and Brunel (2007) by adding 2-AG production via mGluR- and M1R activation. They utilized a one compartment model of electrical activity of a spiny projection neuron for calcium dynamics, coupled with a model of signaling pathways underlying STDP in SPNs: this model using a combined 2-AG- and CaMKII-based plasticity rule, where resulting plasticity direction was determined by the product of the presynaptic weight (2-AG based,) and postsynaptic weight (CaMKII based,) A strength of this model is the ability to show the mechanism whereby decreasing the number of pairings converts NMDA dependent tLTD to an eCB dependent tLTD Prolonged and moderate activation of eCB caused eCB-mediated depression whereas large eCB transients resulted in eCB-mediated potentiation. The model predictions regarding the pairing frequency dependence of plasticity were confirmed experimentally. This study also showed the tLTP observed with 10 pairings is partly due to the insufficient CamKII activated by such a brief protocol, compared to the robust calcineurin activation .

3. Computational model of basal ganglia in the context of Parkinson's disease

Parkinson's disease (PD) relies on the dysfunction of the basal ganglia network, as described in chapter 2.1, section 2.1.3. In collaboration with the neurobiology team of Laurent Venance at College de France, in Paris, we explored how Parkinsonian rats differ from control ones at the scale of the basal ganglia network. Indeed, since first symptoms appear when already more than 70% of basal ganglia dopaminergic neurons are decimated (see section 2.1.3), it becomes a major issue to detect PD earlier, and basal ganglia seem to be an important target to investigate.

The way information navigates from the cortex to the basal ganglia has been mainly characterized by three independent pathways (see section 2.1.1). However, how these pathways are impacted by Parkinson's disease is still unclear and whether they are delayed, enhanced or diminished has not been characterized.

To answer these questions, Venance's team run experiments on anesthetized rats by stimulating their cortex and recording the resulting response in the SNR neurons with an extracellular glass electrode. As previously described in chapter 2.1, section 2.1.1, they obtained characteristic responses composed of different phases, triphasic, biphasic, monophasic or silent. The goal of the study was to investigate if there were any differences of response between control rats and Parkinsonian rats.

Venance's team uses rats in two conditions, SHAM and 6OHDA. SHAM condition is the control condition; surgery is done to inject only saline solution in the substantia nigra of the rat. On the contrary, 6OHDA condition is the Parkinsonian condition (see section 2.1.3); 6OHDA is injected, during the same surgery procedure, acting as a toxin to suppress dopaminergic neurons of the SNc.

After surgery, the protocol consists in stimulating the cortex of the rat, asleep, while recording one neural response of the substantia nigra pars reticulata (Figure 2.1). More precisely, cortical stimulation consisted of 600μs width pulses between 10-20V (corresponding to 200-400μA) delivered at a 1 Hz frequency. For each neuron of the SNR recorded, the entire experiment consists of around fifty cortical stimulation.

In order to compare between control and Parkinsonian conditions, the first step was to precisely characterize these voltage time series. By fitting a firing-rate neural network model (see section 2.3.5) on each cell, we could obtain a set of parameters for the weight and the delay of each connection. This set of parameters provides quantitative values that can be used as a comparison point of 6OHDA and SHAM conditions. In addition, the fitted response permits to analyse neural responses in a more automatized way.

Thus, from these voltage recordings of SNR's neurons, the idea is to extract all spikes of each repetition, sum them up by synchronizing each repetition with the stimulation time and finally obtain a time series representing the activity of the neural discharge after stimulation. Indeed, since spikes are summed up through many repetitions, one expects that a pattern would emerge from the noise (e.g. triphasic, biphasic, monophasic...). This time series representing the activity of discharge is then smoothed to a continuous curve,

so the model can easily be fitted on it. Once the model has been fitted on each neuron, in each condition, we compared parameters or the response pattern of each fit and explore differences between conditions. We are currently preparing a paper to publish the results.

3.1 Data pre-treatment

From the voltage recording, containing the fifty successive stimulation, we could extract spikes by setting a threshold value depending on the variation of the resting potential (Figure 3.1A). The time points of stimulation are already known because the timing of stimulation is precisely fixed. Thus, we could obtain the timing of stimulation and a regular and ordered spike timing series (Figure 3.1B), with 0.1 ms as timestep, which seems to be a good compromise between precision and storage. In addition, each subset of spikes recorded between two stimulation forms a cycle and each cycle is a repetition of the same experiment. From there, we synchronized and cumulated each cycle. Thus, from each cycle, spike series are interspersed and ordered, forming an aggregated spike series with a bin width of 0.1 ms (Figure 3.1C). In the rare cases where several spikes are at the exact same timing, they are summed up. This aggregated spike series of the experiment, over all repetitions, reveals the activity pattern of the neural discharge (e.g. triphasic, biphasic, monophasic...).

The series of spikes needed to be convolved in order to obtain a smoothed and continuous activity of discharge, so the model could be fitted on a regular and not too sharp time series. However, a classical Gaussian function did not work properly, instead we used a simple square function with a time window of 1 ms, it seemed to be a good compromise between precision and smoothness (see section 6.1 in discussion). The result is equivalent to extend the size of each spike to 1 ms and summed up the overlapping parts.

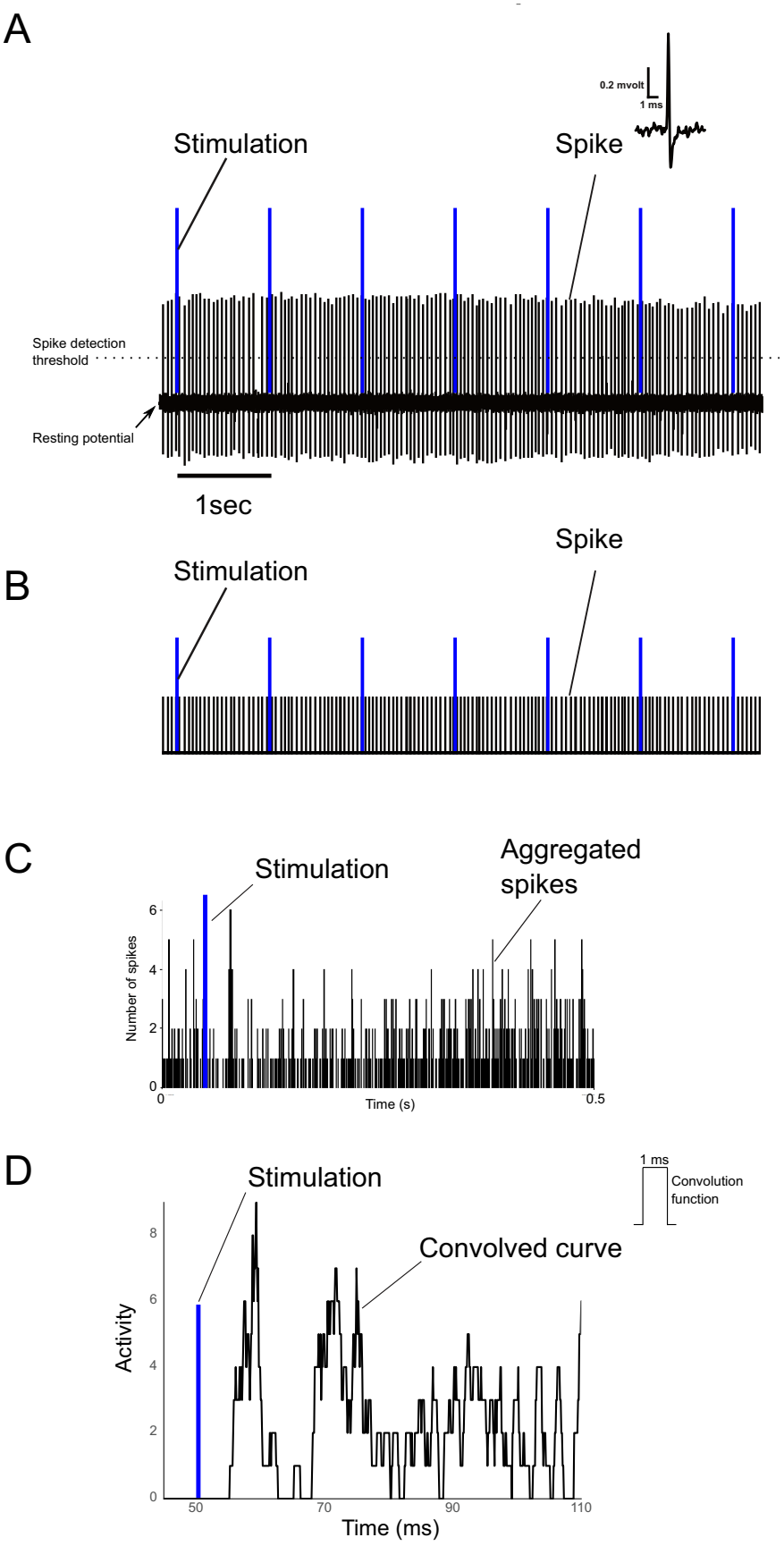

Figure 3.1: (A) Voltage of recorded neuron with several cycles. (B) Extracted series of spikes with several cycles. (C) Real example of aggregated spike series. (D) Smoothed curve obtained with squared convolution of 1 ms width.

3.2 Firing-rate neural network model

After pre-treating this data, our next step was to fit them. To this aim, we built a simple firing-rate neural network involving the three known pathways of the basal ganglia and their corresponding delays (Figure 3.2). This model is simple because it takes only into account the main pathways of the basal ganglia network to analyse experimental data and, in that way, it could be compared to a computational and recent version of the Rate Model (see section 2.1.4). Indeed, the network of the basal ganglia was simplified to explain the experiment with a minimal number of connections and parameters. For example, the feedback loop between the STN and the GPe has been removed as well as the one between the thalamus and the cortex. In both cases, this simplification has been made because the influence of these connections was expected to occur later than the dynamics of interest, indeed our recordings mostly focused on the first 40 ms after the stimulation.

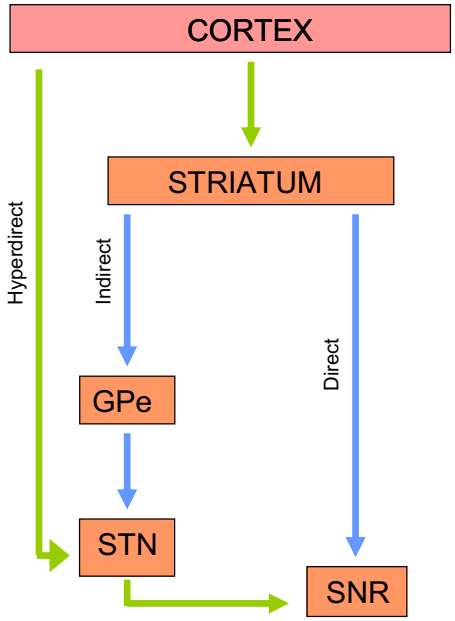

Figure 3.2: Simplified neural network model of the basal ganglia used to fit experimental recordings.

The corresponding set of ordinary differential equations (ODE) was solved with an Euler method.

We associated one firing rate activity, r_i for each nucleus of figure 3.2 (i.e. for the cortex i= 1, for the striatum i = 2, ...) and they are calculated with the following equation:

$$\tau \frac{dr_i(t)}{dt} = -r_i(t) + F(I_{basal_i} + S_{ext_i} + \sum_{j=1}^{5} r_j(t - t_{delay_{(i,j)}}) \times \frac{w_{(i,j)}}{\tau_{curr_i}}), \quad \forall \text{ i} = \{1, ..., 5\} \tag{3.1a}$$

$$F(x) = \begin{cases} x \text{ if } x >= 0 \\ 0 \text{ if } x < 0 \end{cases} \tag{3.1b}$$

where r_i is the firing activity of the nucleus i, I_{basal_i} is the basal activity received by the nucleus, S_{ext_i} is the external stimulus (non-zero value only for the cortex), $t_{delay_{(i,j)}}$ is the delay of each connection and according to literature (Lindahl et al., 2013), each delay is different. τ is the time constant, that was set to the same value for each nucleus in order to reduce the number of parameters, simplifying the convergence of the fitting

algorithm. τ_{curr_i} is another time constant acting on the sum of received currents, it has a different value for each nucleus i. $w_{(i,j)}$ is the weight of each connection and $F(x)$ is a rectifying function that sets negative values to zero, to avoid negative firing probabilities. This function was chosen because it is one of the simplest to capture the dynamics with weights and delays parameters.

3.3 Solving and fitting the model

To solve the system of ODE, the Euler method was coded in cython to improve performance. To take into account the dynamic of the network, the ODEs contain delays representing the time for the signal to propagate through the connection. Thus, considering these delays, the Euler method seemed to be the easiest and the most efficient way to solve the ODEs. Moreover a python script was used as a wrapper to handle repetitions, parameters values and plotting.

The time step of stimulation was set at 0.1 ms as a trade-off between precision and efficiency. Indeed, a time step of 0.01 ms has been tested over the same dataset and it provides similar results than the time step at 0.1 ms, whereas it takes ten times more time. The parameters of the model were fitted on each neuron's response aggregated spike series, such as the weight and delays of each connection and the basal input on each nucleus. We calculated the least squares between SNr data and SNr simulation and we used a particle swarm optimization (PSO) algorithm from PyGMO library to minimize this least squares. PyGMO also permitted to realize this PSO fit with a parallelized evolutionary algorithm. The covariance matrix adaptation evolution strategy (CMAES) and the differential evolution (DE) algorithms were also tested. The PSO converged more efficiently for this problem.

The PSO algorithm optimizes a problem by having a population of candidate solution, the swarm, distributed in the parameter space. Each particle of the swarm moves depending on two main variables, its own score and the best score of all particles (Figure 3.3). These rules are supposed to move the whole swarm to the best position in the space of solutions. However, if there are several local minima in a large space of parameters, the PSO algorithm can find different solutions depending on the initial conditions. This bias can be compensated by making repetitions but it can be costly in terms of machine-time. Using an evolutionary algorithm in parallel can deal with this bias. Indeed, if we consider one particle of the PSO algorithm as an individual, we can have a population of individuals exploring an "island" of solutions, this is the classical particle swarm optimization. Then, we can duplicate the "island" with a new population (meaning a swarm with a different initial condition) also exploring. In terms of computation, it can be done on a different core of the same machine, simultaneously with the exploration of the first island. Next, every fixed number of generations, the best individual of each island migrates to another island and the optimization continues, enriched with new individuals (Figure 3.4).

It seems important to note that to solve our system of delayed equations, we used the classical Euler method, however, these results could be compared with an adaptively stepping embedded Runge-Kutta 2, 3 scheme to evaluate how much they are dependent on the solving algorithm. In the same idea, we tested CMAES, DE and PSO algorithms, on a subset of pre-treated data, to fit our model. We kept PSO for its efficiency but it would be interesting to compare the results of this three optimization algorithms on the whole dataset, to test the robustness of our results.

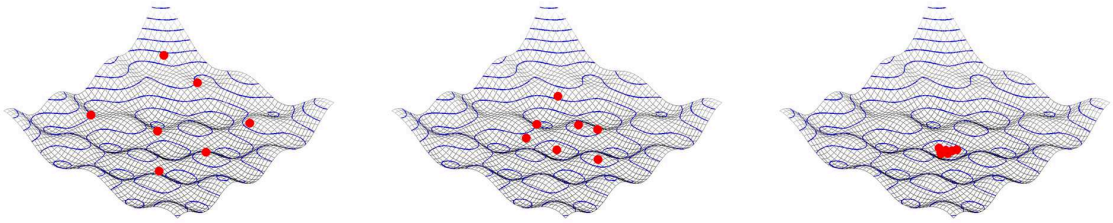

Figure 3.3: Illustration of Particle Swarm Optimization (PSO) algorithm convergence in two dimensions.

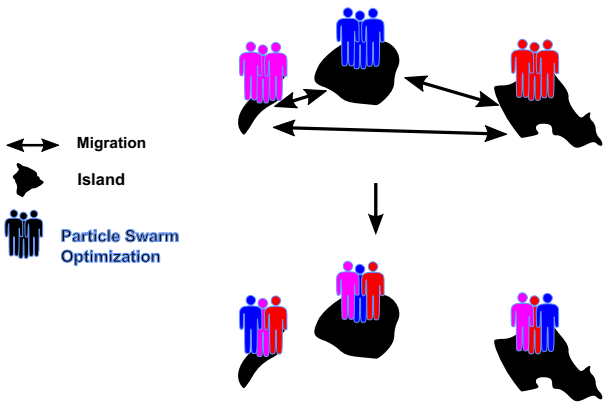

Figure 3.4: Particle Swarm Optimization (PSO) algorithm parallelized with an evolutionary algorithm with three islands.

To get enough precision and robustness, each fit was made on two islands, with one hundred and fifty individuals on each, and twenty migrations every twenty generations of the PSO algorithm. One fit lasted around twelve hours of machine-time using two core processors on a computer possessing twenty-four of them.

Furthermore, since we are mainly interested in the response right after the stimulation, we replaced the final part of the data (30 ms after the stimulation until the end) by its averaged value, constituting the baseline of the data (Figure 3.5).

Besides, depending on the timing from the stimulation, the fit is differentially weighted (Figure 3.6). Indeed, even if the fit differs a little from the average baseline, since the baseline part represents more than 80% of the simulation (cf. W_2 in Figure 3.6), the small error value accumulates and becomes large. Thus, in order to focus on the dynamic right after the stimulation, the 20 ms portion before the stimulation is weighted 100 times heavier than the rest of the simulation (cf. W_0 in Figure 3.6), whereas the 50 ms portion after the stimulation is weighted 100,000 times heavier than the rest of the simulation (cf. W_1 in Figure 3.6).

Moreover, in order for the system to start from a stable point, the simulation starts 300ms before any stimulation.

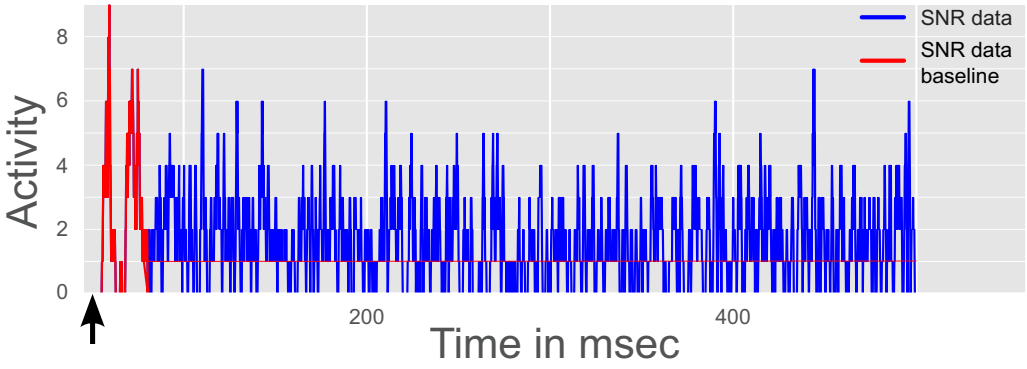

Figure 3.5: Convolution on a sham cell at 15V input - Blue : Convolved spike series (experimental data), Red : Convolved spike series with time window 80-500ms replaced by a baseline that is the average of the time series (experimental data). Cortical stimulation occurs at 20ms, symbolised by the vertical arrow.

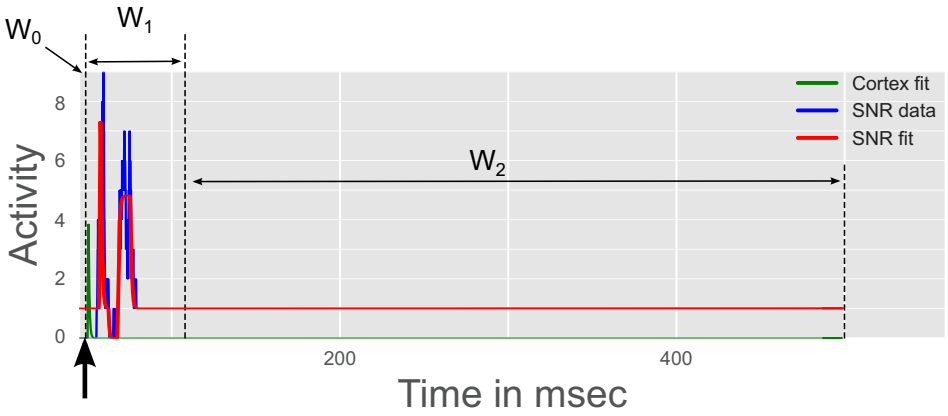

Figure 3.6: Convolution on a sham cell at 15V input - Green : cortex simulation (model), Blue : Convolved spike series with the baseline (experimental data), Red : SNr simulation (model). $W_0 = 100W_2$ and $W_1 = 100,000W_2$. Cortical stimulation occurs at 20ms, symbolised by the vertical arrow.

What is mostly difficult is that we are only fitting on the input and the output data of this network, the cortex and the SNr, respectively, and we have no information to constrain intermediary nuclei, the striatum, the GPe and the STN.

Finally, a way to optimize properly the fit is to diminish the number of free parameters. One way to know if a parameter needs to be fitted is to fix it and see if the algorithm can still fit correctly. Since the response of the SNR is the only one to be fitted, and that each pathway is composed of several connections between nuclei, some free parameters in each pathway could be fixed without preventing the convergence of the algorithm to a proper fit (Table 3.1). Moreover, the parametric space was bounded (table 3.1) to ensure, for example, that the weight of inhibitory connections stays negative or that delays of all connections stay in the same range as the literature (table A.4 (Lindahl et al., 2013)).

Name	Value	Name	Value
Basal activity		**Time constant on received currents**	
$I_{basal_{Cx}}$	0 pA	$\tau_{curr_{Cx}}$	[0.1, 15] ms^{-1}
$I_{basal_{Striatum}}$	0 pA	$\tau_{curr_{Striatum}}$	[0.1, 15] ms^{-1}
$I_{basal_{GPe}}$	0.15 pA	$\tau_{curr_{GPe}}$	[0.1, 15] ms^{-1}
$I_{basal_{STN}}$	3 pA	$\tau_{curr_{STN}}$	[0.1, 15] ms^{-1}
$I_{basal_{SNr}}$	1 pA	$\tau_{curr_{SNr}}$	[0.1, 15] ms^{-1}
Delay		**Weight**	
$t_{delay}^{Cx-Striatum}$	[0.5, 10] ms	$w^{Cx-Striatum}$	[0.1, 500] a.u.
t_{delay}^{Cx-STN}	[0.5, 10] ms	w^{Cx-STN}	[10., 1000] a.u.
$t_{delay}^{Striatum-GPe}$	5 ms	$w^{Striatum-GPe}$	[-1000, -0.1] a.u.
$t_{delay}^{Striatum-SNr}$	[0.5, 10] ms	$w^{Striatum-SNr}$	[-1000, -0.1] a.u.
$t_{delay}^{GPe-STN}$	[0.5, 10] ms	$w^{GPe-STN}$	[-1000, -0.1] a.u.
$t_{delay}^{STN-SNr}$	[0.5, 10] ms	$w^{STN-SNr}$	[0.1, 200] a.u.

Table 3.1: Free and fixed parameters table of the neural network. If there is one value, it means the parameter is fixed, otherwise it can vary in the provided range.

3.4 Results

First, in order to validate the model with a qualitative test, each of the three pathways were shut downed to see the impact on the SNr response. Indeed, experiments show that the first excitatory phase corresponds to the hyperdirect pathway (Takada et al., 2013), the middle inhibitory phase is due to the direct pathway and the last excitatory phase is caused by the indirect pathway (Figure 3.7). When each of the three pathways are extinguished in the model, the corresponding phase indeed disappears (Figure 3.8), confirming that the model is conformed to experimental results.

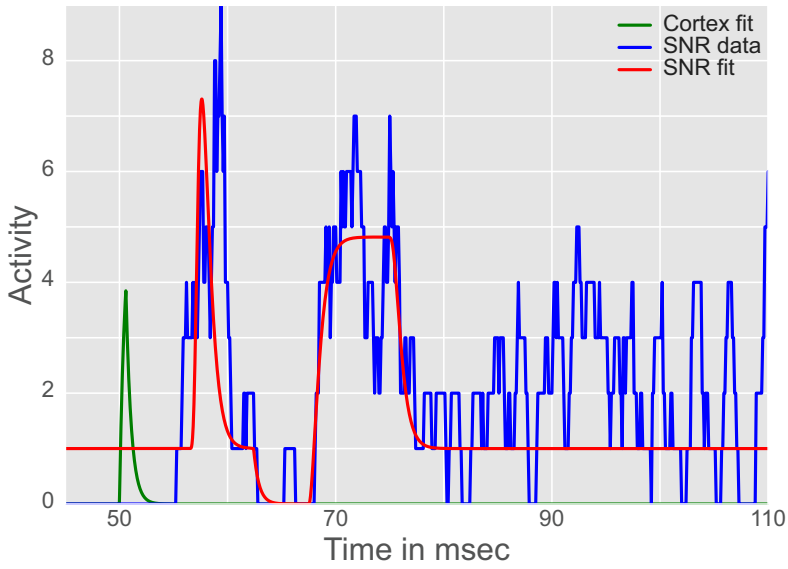

Figure 3.7: Convolution and fit of the model on a sham cell at 15V input - Green : cortex simulation (model), Blue : Convolved spike series (experimental data), Red : SNr simulation (model). Cortical stimulation occurs at 50ms.

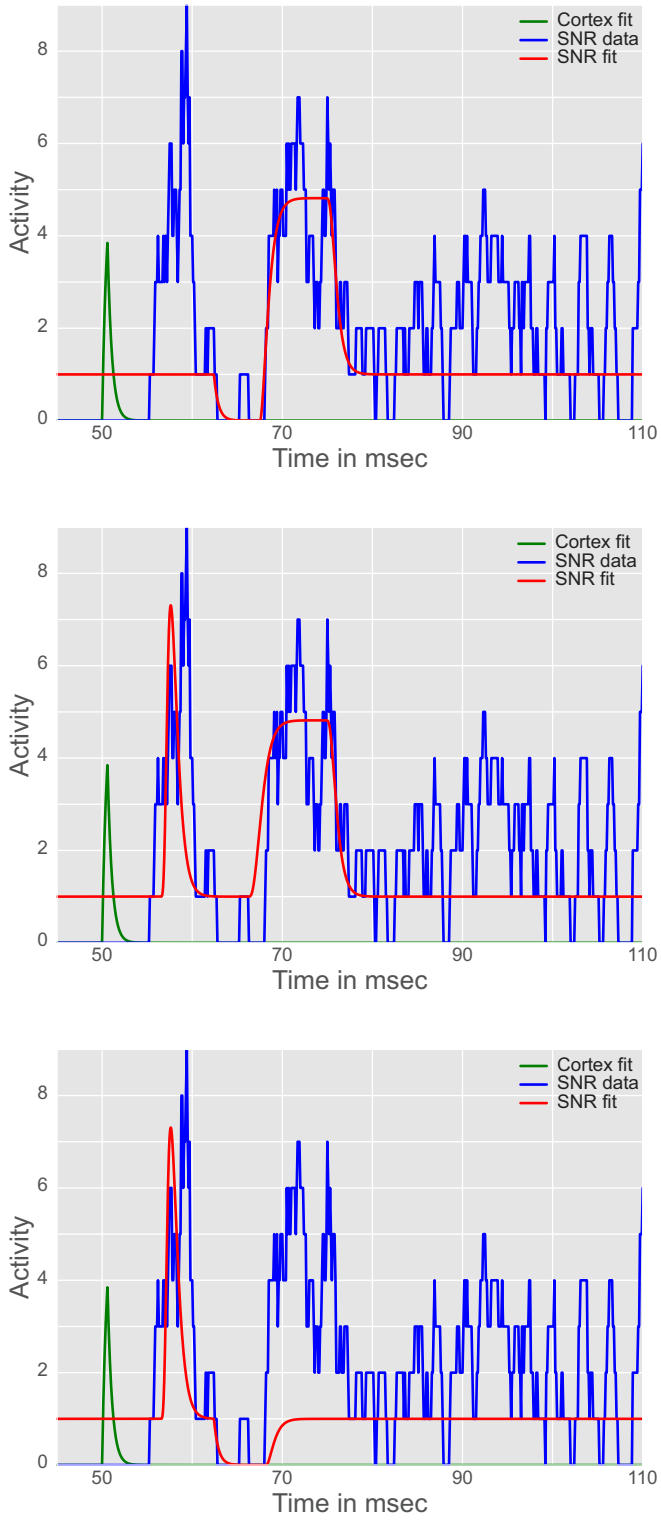

Figure 3.8: Simulations without some pathways. (Upper panel) Deleting the hyperdirect pathway causes extinction of the first excitatory phase. (Middle panel) Deleting the direct pathway causes extinction of the inhibitory phase. (Down panel) Deleting the indirect pathway causes extinction of the second excitatory phase. Cortical stimulation occurs at 50ms.

Furthermore, to check the robustness of the fitting algorithm, one set of 112 recordings (68 SHAM and 43 6OHDA recordings) were fitted ten times, with the least square and the PSO minimization, each time with different initial conditions (Figure 3.9). The firing rate standard deviation is calculated for each time point of the series, then averaged on all the

series. Firing rate standard deviation histograms in control and Parkinsonian condition (Figure 3.10), shows that the large majority of fits has a standard deviation, below 0.5 of firing rate. We visually inspected the convergence below this threshold and we considered that the algorithm was robust enough to be used as a categorization procedure.

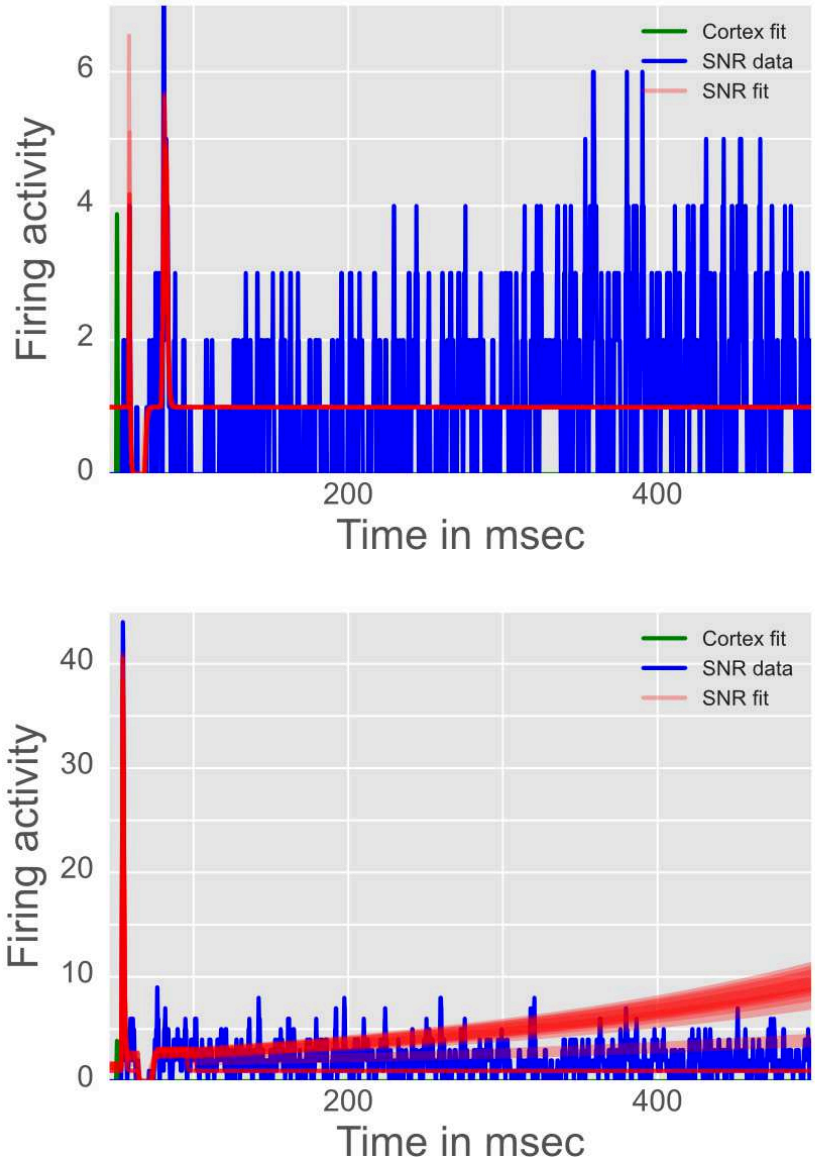

Figure 3.9: Robustness of fitting over 10 repetitions. The upper panel represents ten repetitions of fitting on one recording, with the least square and the PSO minimization, all superimposed, with a low firing rate standard deviation averaged on all time points of the series (0.007 firing rate). The bottom panel represents ten repetitions of fitting on one recording, with a high standard deviation (1.93 firing rate), averaged on all time points of the series. Cortical stimulation occurs at 20ms.

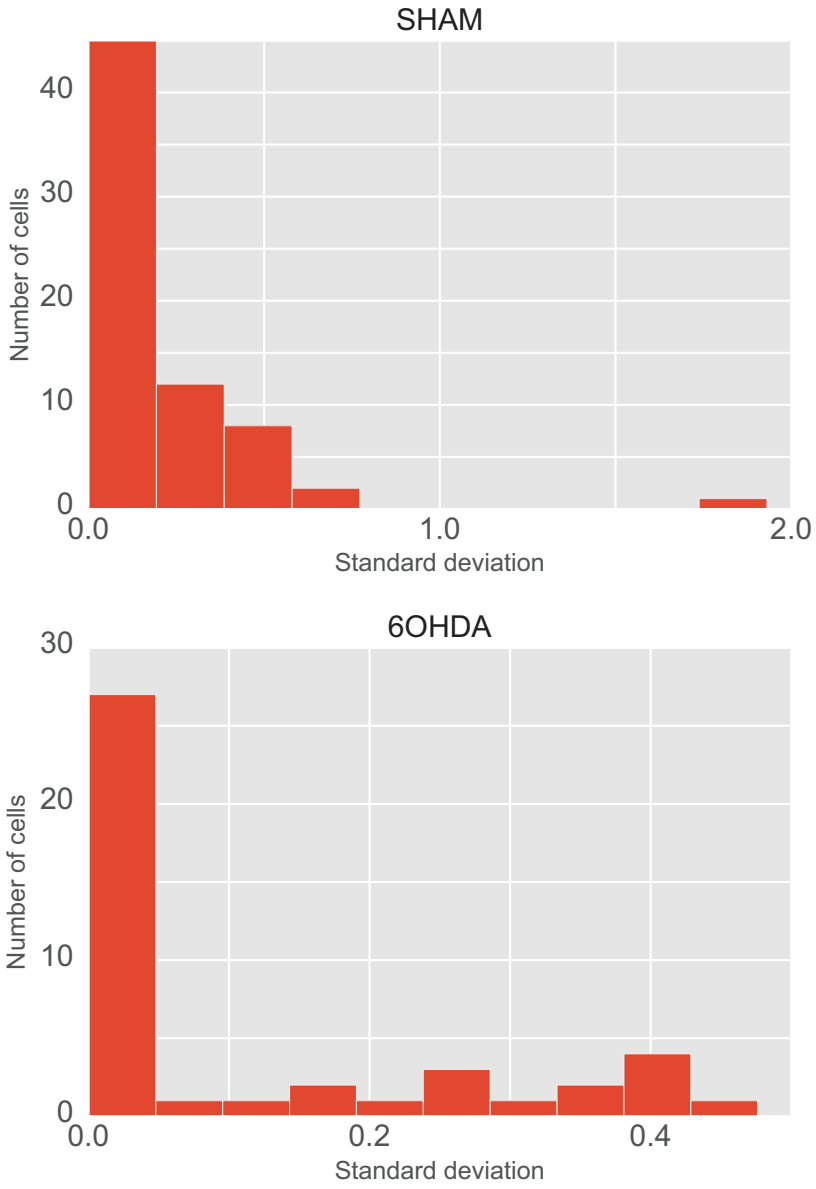

Figure 3.10: The histograms of firing rate standard deviation in both control (up panel) and Parkinsonian (down panel) conditions.

3.4.1 Model parameters comparison between SHAM and 6OHDA conditions

One way to discriminate each condition was to compare the parameters values of each connection of the neural network model. In total, 37 6OHDA cells and 41 SHAM cells were recorded at three different inputs (10V, 15V and 20V).

First, the neurons responses of each condition were averaged and fitted to constitute a representative response of each condition (control or Parkinsonian). However, this averaged response was not pertinent to distinguish between condition because it erases the variability of neuron's responses and the potential contrasts between each condition.

Then, instead, each individual neuron's response was fitted independently and each parameter of each connection was compared (e.g. weight, delay or basal activity). These comparisons were made with non-parametric statistical tests such as the Mann-Whitney-Wilcoxon test (MWW) or the Kolmogorov-Smirnov test (KS) implemented in the R software. Unfortunately, this test shown no significant difference between parameters values

of both conditions (SHAM or 6OHDA); either p-values of these tests were above 0.05 or parameters values were below 0.01% of difference, that was not considered to have a biological meaning.

In addition, we used a principal component analysis (PCA) permitting to maximize the variance of our dataset with an orthogonal linear transformation. The dataset is described in a new coordinate system built on a linear combination of our parameters. However, the resulting coordinate system describing our dataset does not correspond to the control versus Parkinsonian conditions or something biologically relevant.

In a generalized linear model (GLM), the explained variable is assumed to be generated from a particular distribution in the exponential family (i.e. normal, binomial, Poisson, or gamma), where the mean of the distribution depends on the explanatory variables. The standard GLM assumes that the observations are uncorrelated but generalized linear mixed-effect models (GLMMs) are a special case allowing to study correlations between observations. Since the same neuron was recorded at several inputs in our data, we counted the number of spikes and we used generalized linear mixed-effect models (GLMM) to compare statistically baseline values of the neural discharge rate depending on each condition (SHAM or 6OHDA), the input voltage and the recorded neuron, with the following GLMM formula in R:

$$\text{glmer}(\text{nb}_{\text{spike}} \sim \text{Cond} + \text{Input}_{\text{Voltage}} + (1|\text{ID}_{\text{Cell}}), \text{family} = \text{poisson})$$

where gmler() fits the generalized linear mixed-effects model, fixed effects and random effects are specified via the model formula where nb_{spike} is the explained variable, counting the number of spikes, Cond is an explanatory variable with either "SHAM" or "6OHDA" as qualitative value, $\text{Input}_{\text{Voltage}}$ is another explanatory variable, mentioning the input value of stimulation and $(1|\text{ID}_{\text{Cell}})$ provides the name of the neuron and accounts for the use of the same neuron at different cortical input value, it is called a random explanatory variable. Besides, family = poisson is the description of the error distribution and link function to be used in the model. Poisson type of model is used specifically for counting variable.

This analysis shows that switching from control to Parkinsonian condition multiplies the number of spikes by 1.03, with a 95% confidence interval [1.02, 1.05] and with a p-value = 0.0002, so it is statistically significative, but it is a poor effect; at the exact same intensity of stimulation in the cortex, if a control neuron fires, on average, 100 spikes for a limited period of time, a Parkinsonian neuron fires, on average, between 102 and 105 spikes, for the same period of time.

Thus, considering and comparing separately each parameter or baseline value does not show any significative difference between both conditions.

3.4.2 Response pattern categorization on a synthetic dataset

Furthermore, we noticed that there were two main patterns in the data: the triphasic response (first phase excitatory, second phase inhibitory and last one excitatory), and a biphasic response, where the first excitatory phase is absent.

In order to test the power of our modelling approach, we wanted to check that it could discriminate between these two patterns. Hence, we tested it on a small set of synthetic data.

These synthetic spike series were obtained with a Poisson process, a classical way to account for neural activity. In a Poisson process the size of the interval between consecutive events is exponential. Therefore, we obtained spike series with random numbers exponentially distributed. To represent the different phases, we applied different parameters values for λ, the Poisson process rate (Figure 3.11). This means we generated a

synthetic spike train using an heterogeneous Poisson process with the rate and duration of each phase set to emulate our experimental data.

Moreover, each synthetic train was the aggregation of 50 generated synthetic spike trains, as in experimental acquisition and these parameters were adjusted to get an amplitude of aggregated spikes comparable to real data. Finally, the only difference between triphasic and biphasic synthetic dataset is that in the biphasic series $\lambda_{hyperdirect} = \lambda_{baseline}$. We set up a small dataset, five triphasic and five biphasic cells, since the spikes series were very homogeneous.

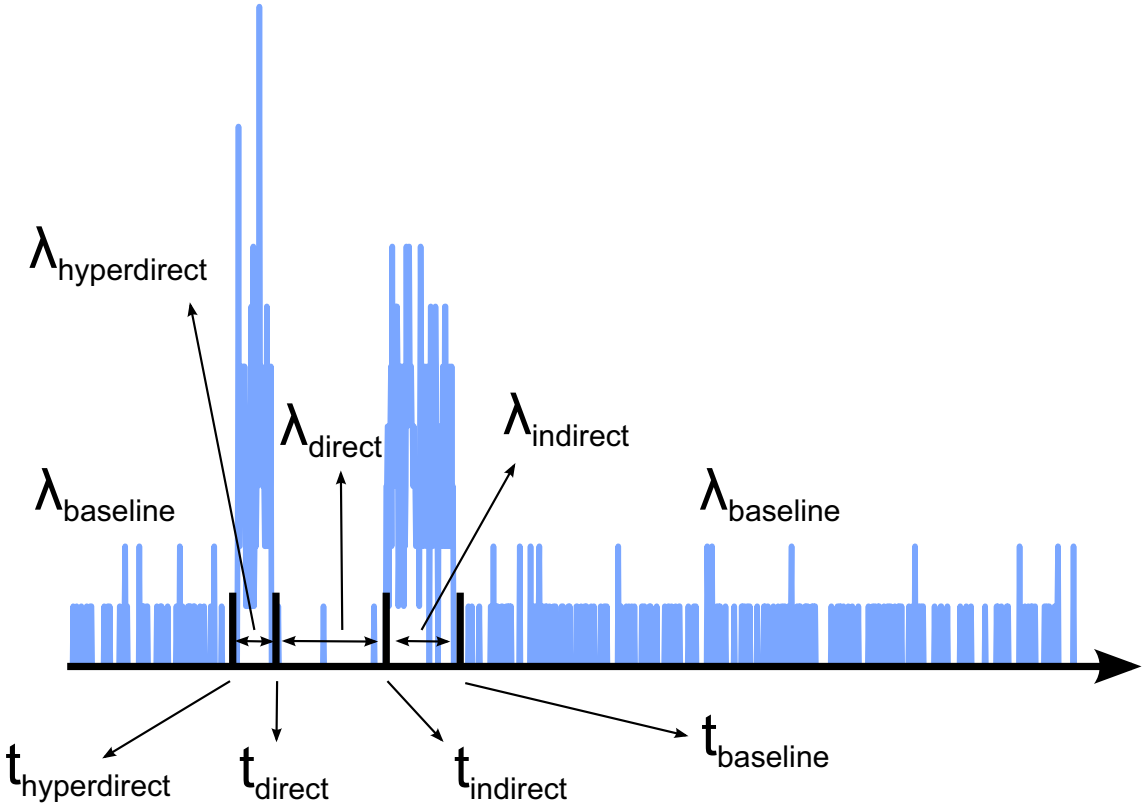

Figure 3.11: Synthetic triphasic spike series generated with Poisson process, with $t_{hyperdirect} = 25ms$, $t_{direct} = 30ms$, $t_{indirect} = 47ms$, $t_{baseline} = 57ms$, $\lambda_{baseline} = 0.04$, $\lambda_{hyperdirect} = 0.7$, $\lambda_{direct} = 0.001$, $\lambda_{indirect} = 0.7$.

We fitted our model on this synthetic dataset after convolutions (Figure 3.12). We found that some parameters of these fits were significantly different between biphasic and triphasic synthetic cells (p-value < 0.05 and effects $> 0.01\%$ of change), validating our fit to distinguish biphasic and triphasic. For example, the weights of the connection from cortex to striatum, striatum to SNr and GPe to STN are significantly different (not shown). Therefore, our model was able to distinguish biphasic from triphasic cells on synthetic data. The next step was to see if we could find the same differences on the real dataset.

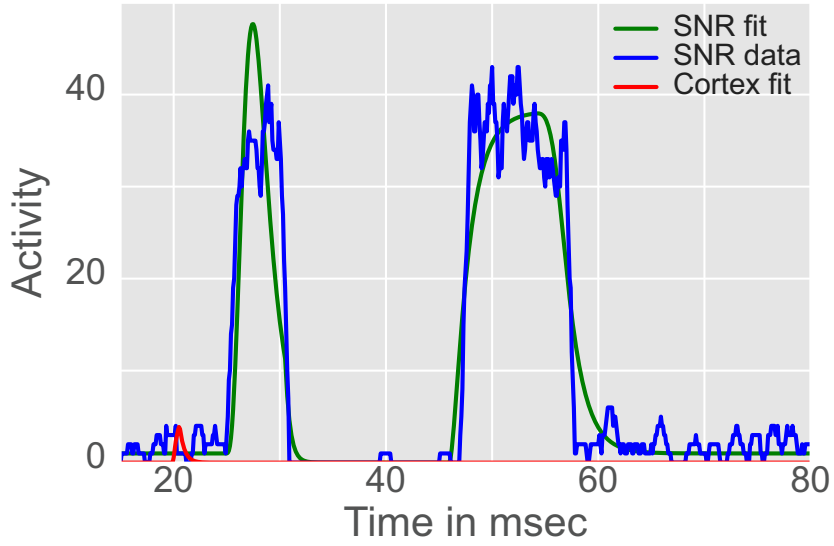

Figure 3.12: Fitting the model on the synthetic triphasic spike series generated with Poisson process. Cortical stimulation is at 20ms.

3.4.3 Response pattern categorization on the real dataset

In order to apply further our model fits on real dataset, we compared biphasic and triphasic on the real dataset. However, that meant that we needed first to label the type of response of each recording. We came up with a set of rules to apply on the fit of each recording and categorize them.

The first step was to identify if each phase of the triphasic response is present. Chronologically, the first is excitatory, the second is inhibitory and the third is excitatory. If all of them are present, the response of the SNR's neuron is classified as triphasic, if only two are present, the response is biphasic, with different sub-categories depending on which phases are present, and monophasic if there is only one phase. The category "other" stands for recordings which do not enter into the previous ones.

The following set of rules was used to classify the cells automatically:

- Initial baseline, (the 20 ms before cortical stimulation), is considered as the baseline for the whole recording.
- Everything above the baseline is excitatory, everything below is inhibitory.
- If there is a double peak (excitatory or inhibitory), it is considered as double only if it crosses the baseline between the two peaks.
- If there is a double peak, the simulation is categorized as "other".
- If there are more than three peaks, it is categorized in "other". For example, if there are more than two excitatory peaks or if there are more than one inhibitory peak, it is categorized in "other".
- If switching between phases is too fast or too slow the simulation is categorized as "other", the interval between the beginning of the first phase and the beginning of the third phase must be comprised in [10 ms - 40 ms].
- When there is more than 10 ms between the inhibition and the second excitation, it is categorized as "monophasic inhibition" rather than "other".

- If a phase is too small in amplitude (less than 80% of the baseline value), they are not considered as phases.

We applied this set of rules on the experimental dataset to classify the cells automatically. To this aim we pooled SHAM and 6OHDA data, representing a set of 231 recordings, where 77 were triphasic, 29 were biphasic (inhibitory phase followed by excitatory phase) and the rest classified as "other".

After fitting, we found that some weight are significantly different for connections GPe to STN and STN to SNr between triphasic and biphasic cells, by using the Mann-Whitney-Wilcoxon test (MWW) or the Kolmogorov-Smirnov test (KS) (Figure 3.13). The mean weight from GPe to STN and from STN to SNr connections are significatively lower in the triphasic condition than in the biphasic condition.

We could also significantly distinguish these two parameters in the synthetic dataset (as previously mentioned in the section 3.4.2), hence, these control tests suggest that our set of rules, to categorize the pattern response, and our fits are coherent and converging toward the same result.

Nevertheless, this result is difficult to interpret since we have differences between connections belonging to the indirect pathway whereas we rather expected differences in the connection of the hyperdirect pathway, namely the connection from the cortex to the STN. In fact, we noticed that variations of one parameter (e.g. the connection weight from GPe to STN) could be partially compensated by the variation of another (e.g. the connection weight from STN to SNr), diminishing differences between conditions. Even if we set constant values for some parameters to minimize the overlap of parameter action ranges, the heterogeneity of the dataset makes it difficult to fit over the majority of recordings while minimizing the overlap of parameter actions. Besides, interpreting the variation of one parameter between two conditions seems less accurate than the variation of whole pathways.

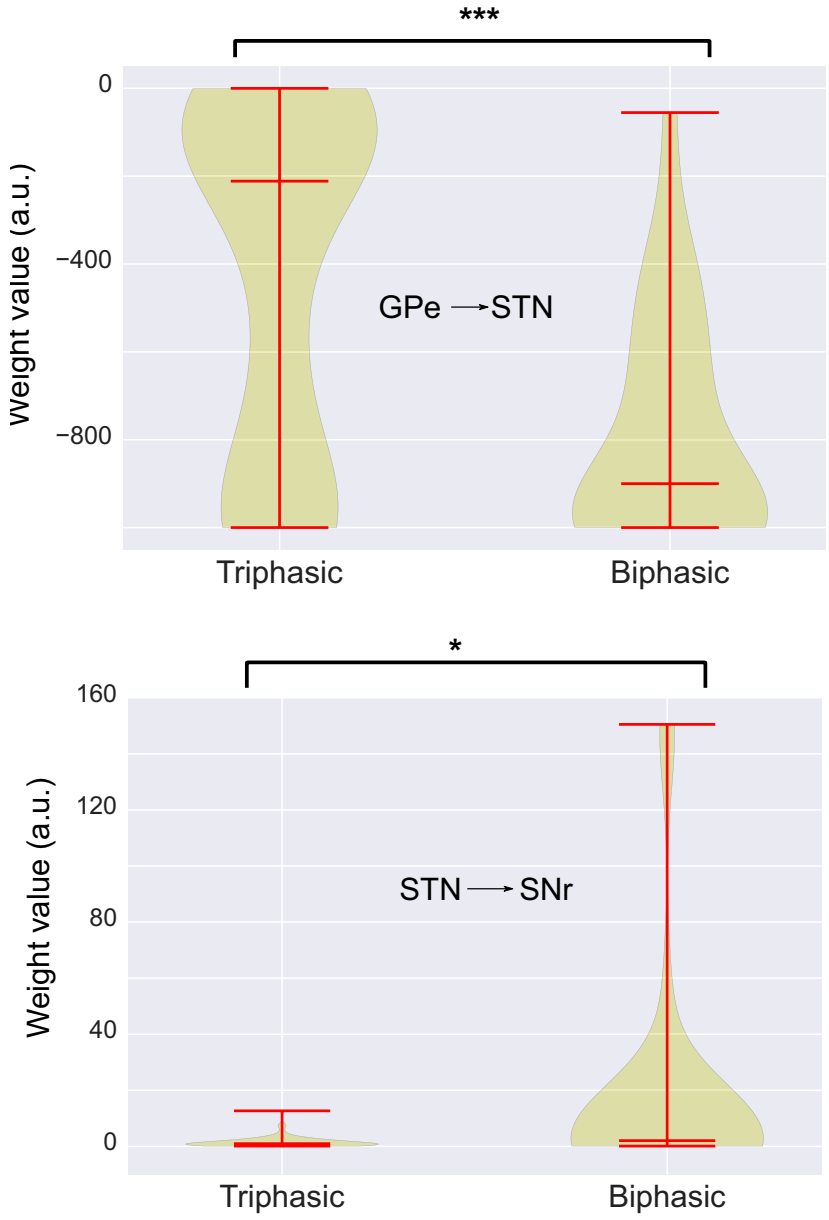

Figure 3.13: Distribution of weight of connection GPe-STN and STN-SNr respectively with triphasic and biphasic condition, represented with violin plots, medians and extrema. MWW: p-value = 0.0, KS: p-value = 0.0 and MWW: p-value = 0.003, KS: p-value = 0.045, respectively.

3.4.4 Scores associated with the three pathways of the neural network

Instead, associating a score to each pathway, hyperdirect, direct and indirect, permitted to compare each phase of the network dynamic. These scores were calculated using adjacency matrices from the graph theory. Indeed, our neural network is a simple directed graph where each nucleus is a node and each connection is a directed edge. Taking the power of adjacency matrices is equivalent to concatenate connections and forming a path. Hence, we can associate a score to the three pathways of our neural model by multiplying adjacency transition matrices, starting from the cortex to the SNr.

There is a distinction between the matrix of weight associated to the stimulation and the matrix of weight associated to basal activity. Indeed, because of delay, each pathway

is independently considered.

The vector of stimulation: $I_{stim} = \begin{matrix} Cx \\ Str \\ GPe \\ STN \\ SNR \end{matrix} \begin{pmatrix} 1 \\ 0 \\ 0 \\ 0 \\ 0 \end{pmatrix}$

The vector of basal activity: $I_0 = \begin{pmatrix} I_{0_{Cx}} \\ I_{0_{Str}} \\ I_{0_{GPe}} \\ I_{0_{STN}} \\ I_{0_{SNR}} \end{pmatrix}$

The matrix of weight associated to the hyperdirect pathway:

$$W_{Hyperdirect} = \begin{matrix} \\ Cx \\ Str \\ GPe \\ STN \\ SNR \end{matrix} \begin{matrix} \begin{matrix} Cx & Str & GPe & STN & SNR \end{matrix} \\ \begin{pmatrix} 0 & 0 & 0 & w_{Cx\rightarrow STN} & 0 \\ 0 & 0 & 0 & 0 & 0 \\ 0 & 0 & 0 & 0 & 0 \\ 0 & 0 & 0 & 0 & w_{STN\rightarrow SNR} \\ 0 & 0 & 0 & 0 & 0 \end{pmatrix} \end{matrix}$$

The matrix of weight associated to the direct pathway:

$$W_{Direct} = \begin{matrix} \\ Cx \\ Str \\ GPe \\ STN \\ SNR \end{matrix} \begin{matrix} \begin{matrix} Cx & Str & GPe & STN & SNR \end{matrix} \\ \begin{pmatrix} 0 & w_{Cx\rightarrow Str} & 0 & 0 & 0 \\ 0 & 0 & 0 & 0 & w_{Str\rightarrow SNR} \\ 0 & 0 & 0 & 0 & 0 \\ 0 & 0 & 0 & 0 & 0 \\ 0 & 0 & 0 & 0 & 0 \end{pmatrix} \end{matrix}$$

The matrix of weight associated to the indirect pathway:

$$W_{Indirect} = \begin{matrix} \\ Cx \\ Str \\ GPe \\ STN \\ SNR \end{matrix} \begin{matrix} \begin{matrix} Cx & Str & GPe & STN & SNR \end{matrix} \\ \begin{pmatrix} 0 & w_{Cx\rightarrow Str} & 0 & 0 & 0 \\ 0 & 0 & w_{Str\rightarrow GPe} & 0 & 0 \\ 0 & 0 & 0 & w_{GPe\rightarrow STN} & 0 \\ 0 & 0 & 0 & 0 & w_{STN\rightarrow SNR} \\ 0 & 0 & 0 & 0 & 0 \end{pmatrix} \end{matrix}$$

The matrix of weight associated to the whole network:

$$W = \begin{pmatrix} 0 & w_{Cx\rightarrow Str} & 0 & w_{Cx\rightarrow STN} & 0 \\ 0 & 0 & w_{Str\rightarrow GPe} & 0 & w_{Str\rightarrow SNR} \\ 0 & 0 & 0 & w_{GPe\rightarrow STN} & 0 \\ 0 & 0 & 0 & 0 & w_{STN\rightarrow SNR} \\ 0 & 0 & 0 & 0 & 0 \end{pmatrix}$$

The hyperdirect pathway is constituted as follows: Cx → STN → SNr. Since there are two connections, in order to get the score of its response, we needed to calculate adjacency matrix at the power of 2, by taking all inputs into account. Then, we kept only the response associated to the SNr.

Besides, we can decompose the adjacency matrix in two matrices, the matrix associated to the hyperdirect pathway, $W_{hyperdirect}$ and the matrix of the whole network, W. We linked the stimulation vector, I_{stim}, to $W_{hyperdirect}$ whereas the basal activity vector, I_0, is linked to W.

Hence, the hyperdirect score is calculated in two steps: Step 1 with basal activity input and stimulation activity: $\left(I_{stim}^T \times W_{hyperdirect}\right)^T + \left(I_0^T \times W\right)^T$

Step 2 with basal activity: $(\text{Step } 1 + I_0)^T \times W_{(*,SNR)}$

$$\text{Step 1: } \begin{pmatrix} 0 \\ 0 \\ 0 \\ w_{Cx\to STN} \\ 0 \end{pmatrix} + \begin{pmatrix} 0 \\ I_{0_{Cx}} \times w_{Cx\to Str} \\ I_{0_{Str}} \times w_{Str\to GPe} \\ I_{0_{Cx}} \times w_{Cx\to STN} + I_{0_{GPe}} \times w_{GPe\to STN} \\ I_{0_{Str}} \times w_{Str\to SNR} + I_{0_{STN}} \times w_{STN\to SNR} \end{pmatrix}$$

$$\text{Step 2: } \begin{pmatrix} I_{0_{Cx}} \\ I_{0_{Cx}} \times w_{Cx\to Str} + I_{0_{Str}} \\ I_{0_{Str}} \times w_{Str\to GPe} + I_{0_{GPe}} \\ w_{Cx\to STN} \times (I_{0_{Cx}} + 1) + I_{0_{GPe}} \times w_{GPe\to STN} + I_{0_{STN}} \\ I_{0_{Str}} \times w_{Str\to SNR} + I_{0_{STN}} \times w_{STN\to SNR} + I_{0_{Str}} \end{pmatrix}^T \times \begin{pmatrix} 0 \\ w_{Str\to SNR} \\ 0 \\ w_{STN\to SNR} \\ 0 \end{pmatrix}$$

Finally, all parameters were normalized, so we add a negative sign for negative parameters and we obtained the following hyperdirect score:

$$\begin{aligned} \text{Score}_{Hyperdirect} = &-\|w_{Str\to SNR}\| \times \Big(\|I_{0_{Cx}}\| \times \|w_{Cx\to Str}\| + \|I_{0_{Str}}\| \Big) \\ &+ \|w_{STN\to SNR}\| \times \Big(\|w_{Cx\to STN}\| \times (\|I_{0_{Cx}}\| + 1) - \|w_{GPe\to STN}\| \times \|I0_{GPe}\| + \|I0_{STN}\| \Big) \end{aligned}$$

We used the same procedure for the direct pathway constituted as follows: Cx → Str → SNr, except that we used the adjacency matrix, W_{direct}.

Hence, the direct score is calculated in two steps: Step 1 with basal activity input and stimulation activity: $\left(I_{stim}^T \times W_{direct}\right)^T + \left(I_0^T \times W\right)^T$
Step 2 with basal activity: $(\text{Step } 1 + I_0)^T \times W_{(*,SNR)}$

$$\begin{aligned} \text{Score}_{Direct} = &-\|w_{Str\to SNR}\| \times \Big((\|I_{0_{Cx}}\| + 1) \times \|w_{Cx\to Str}\| + \|I_{0_{Str}}\| \Big) \\ &+ \|w_{STN\to SNR}\| \times \Big(\|w_{Cx\to STN}\| - \|w_{GPe\to STN}\| \times \|I0_{GPe}\| + \|I0_{STN}\| \Big) \end{aligned}$$

We used the same procedure for the indirect pathway constituted as follows: Cx → Str → GPe → STN → SNr, except that we used the adjacency matrix, $W_{indirect}$.

Hence, the indirect score is calculated in four steps: Step 1 with basal activity input and stimulation activity: $\left(I_{stim}^T \times W_{indirect}\right)^T + \left(I_0^T \times W\right)^T$
Step 2 with basal activity: $(\text{Step } 1 + I_0)^T \times W$
Step 3 with basal activity: $(\text{Step } 2 + I_0)^T \times W$
Step 4 with basal activity: $(\text{Step } 3 + I_0)^T \times W_{(*,SNR)}$

$$\begin{aligned} \text{Score}_{Indirect} = \|w_{STN\to SNR}\| \times \Big(&\|I_{0_{STN}}\| + \|w_{Cx\to Str}\| \times \|w_{Str\to GPe}\| \\ &+ \|w_{Str\to GPe}\| \times \|I0_{GPe}\| \Big) \end{aligned}$$

3.4.5 Comparison of score pathway on triphasic and biphasic neural responses

To control the pertinence of theses scores we used again the synthetic dataset and compared both triphasic and biphasic groups. As expected, only the score associated to the hyperdirect pathway was significantly different between triphasic and biphasic cells (table 3.2).

	Hyperdirect	**Indirect**	**Direct**
MWW	0.009	0.117	0.754
KS	0.004	0.209	0.697

Table 3.2: Statistical p-values of the Mann-Whitney-Wilcoxon test (MWW) or the Kolmogorov-Smirnov test (KS) by comparing each score pathway calculated with adjacency matrix on the synthetic dataset.

Then, these scores were applied on the experimental dataset, where we already identified 77 triphasic neural responses and 29 biphasic neural responses with our model fits and our set of rules classification. First, there was no significative difference of scores pathways between SHAM and OHDA (not shown here). Hence, we could combine both conditions and observe that there was a significative difference for hyperdirect and indirect pathways between triphasic and biphasic conditions (Figure 3.14).

Thus, when pooling SHAM and 6OHDA conditions, the hyperdirect score is significantly higher in triphasic cells than in biphasic cells. However, these scores do not allow to differentiate SHAM and 6OHDA cells. However, the pathway scores support the idea that our model combined with our set of rules can discriminate between biphasic and triphasic.

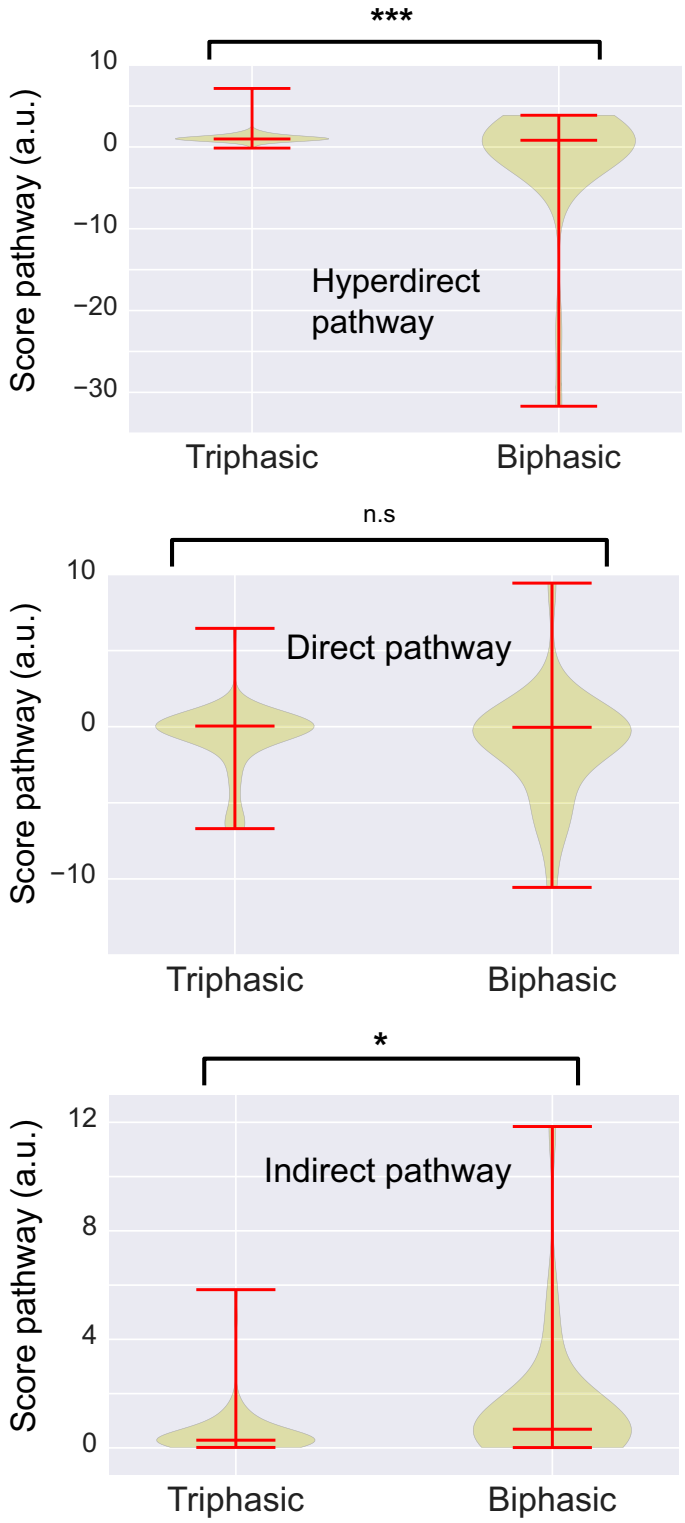

Figure 3.14: Comparison of each score pathway between triphasic and biphasic condition with violin plot and two statistical tests (MWW and KS), the hyperdirect pathway and the indirect pathway were significantly different between triphasic and biphasic: hyperdirect pathway, MWW: p-value = 0.0, KS: p-value = 0.0, direct pathway, MWW: p-value = 0.0759, KS: p-value = 0.0354, indirect pathway, MWW: p-value = 0.0041, KS: p-value = 0.0148

3.4.6 Comparing proportion of triphasic cell between SHAM and OHDA conditions

Since there was no significative difference between the response parameters or the score pathways of the two conditions SHAM and OHDA, and since we validated that we could discriminate between biphasic and triphasic cells. Our next question was to study if there was a significative proportion difference of triphasic cells between the control (SHAM) and Parkinsonian (6OHDA) condition, with the distribution following table 3.3.

	SHAM	**6OHDA**
Triphasic	51	26
Other	71	83

Table 3.3: Number of cells classified as triphasic or not in SHAM and 6OHDA conditions with our model fits and our set of rules classification.

To test for a difference in the proportion of triphasic cells, we used a binomial model with random effects:

$$\text{glmer}(\text{Triphasic} \sim \text{cond} + \text{Input}_{\text{Voltage}} + (1|\text{ID}_{\text{Cell}}), \text{family} = \text{binomial})$$

where gmler() fits the generalized linear mixed-effects model, Triphasic is the explained variable, marking if the neuron is classified as triphasic or not, cond is an explanatory variable characterizing the condition, SHAM or 6OHDA, $\text{Input}_{\text{Voltage}}$ is another explicatory variable, mentioning the input value of stimulation and $(1|\text{ID}_{\text{Cell}})$ is a random explanatory variable containing the name of the neuron. Besides, family = binomial is the type of model used specifically for counting variable.

It results that, with a 95% confidence interval, there is [1.14 - 7] times more triphasic cells in SHAM than in 6OHDA, p-value = 0.02 (Figure 3.15).

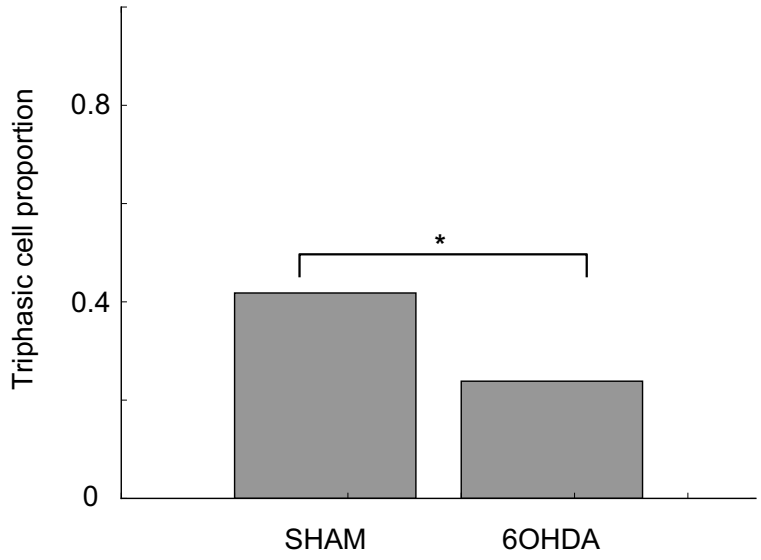

Figure 3.15: Barplot of the triphasic cell proportion in SHAM and 6OHDA conditions. There is [1.14 - 7] times more triphasic cells in SHAM than in 6OHDA with a p-value = 0.02

Thus there were no significant differences between the response of control and Parkinsonian neurons, nothing statistically or biologically significant came out, neither with non-parametric statistical test or with linear models. Besides, the baseline of firing rate

is significantly but not biologically different between both conditions; the difference of firing rate is too small to be meaningful ($< 0.001\%$). However, the proportion of triphasic neurons is significantly larger in SHAM than 6OHDA neurons.

Therefore, our conclusion is that triphasic SHAM cells do not differ from triphasic 6OHDA cells and biphasic SHAM cells do not significantly differ from biphasic 6OHDA cells. Nevertheless, the proportion of triphasic cells was found significantly smaller in 6OHDA cells. We conclude that the effect of 6OHDA lesions used in experiments is mostly to decrease the proportion of cells that exhibit a significant hyperdirect response. In other words, the parkinsonian condition seems correlated with a diminution of the proportion of cells with a hyperdirect response.

4. Computational model of Habenula in the context of major depressive disorder

We collaborated with the team of Hailan Hu (Univ. Zhejiang, Hangzhou, Chine) to better understand the role of the habenula in depression disease. All the experimental results presented below are their results, we only made the computational modelling part and our joint work resulted in a paper in Nature (Cui et al., 2018). In particular, we studied how the astrocyte regulation of potassium is linked to the activity of the lateral habenula (LHb).

Indeed, based on Hu's team previous observations (Li et al., 2013), they identified that the overexpression of β-CaMKII in depression animal models causes AMPA insertion onto the membrane, leading up to a hyperactive habenula in depressive status. β-CaMKII would have a key role in synaptic plasticity of LHb synapses by increasing their efficiency.

Furthermore, habenula neurons present three activity patterns (silent, spiking and bursting, see section 2.2.2), therefore, they postulated that the hyperactivity of habenula in depression animals could be due to the increase of burst weight. Indeed, they found that the number of bursting neurons is increased in the habenula of depressive rats (Figure 4.1A) and that the spontaneous burst firing frequency is significantly higher in depressive animals (Figure 4.1B).

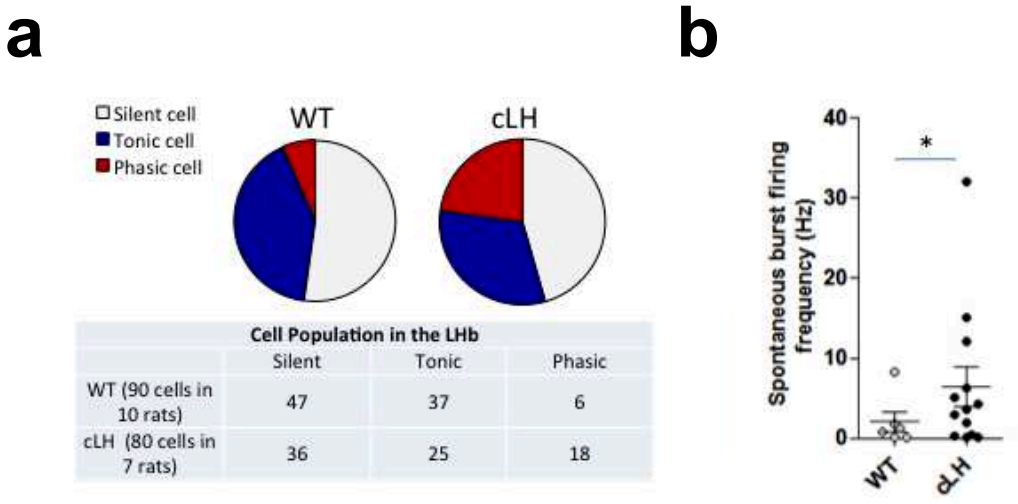

Figure 4.1: Experimental data. Proportion of silent, tonic (spiking) and phasic (bursting) cells in both control (WT) and depression (cLH) conditions (a). Comparison of spontaneous burst firing frequency between WT and cLH conditions (b).

Accordingly, using inter-spiking intervals (ISI) histograms to represent the distribution of the timing between each spike, they highlighted a higher proportion of small ISI (below 40 ms) in depressive rats compared to wild-type rats, corresponding to burst firing (Figure

4.2). In treatment with ketamine, an antidepressant, burst cell population was reduced and the total spontaneous frequency was reduced too.

Therefore, they have evidence that, in depression, the homeostasis of habenula is disturbed and the activity pattern of neurons is shifted toward bursting mode. The bursting weight would be the main cause of habenula's hyperactivity and to test this hypothesis, we built a computational model of a habenula's neural population projecting to a single VTA dopaminergic neuron. Thus, our model asks if LHb burst firing is more efficient to inhibit the VTA than spike firing.

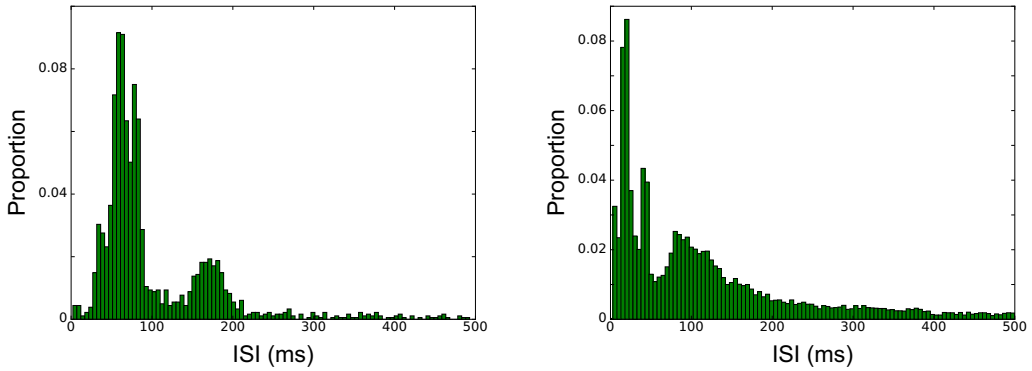

Figure 4.2: Experimental data. ISI histograms in habenula of WT rats (left panel) and cLH rats (right panel). Each histogram has been made from 10 neurons showing activity (not silent neurons) and recorded for 10 minutes.

4.1 Depression and bursting neurons

To better understand how an increased bursting activity of LHb neurons induces a decrease of VTA dopaminergic activity, we made a computational model and compared two conditions; the control condition, where the distribution of LHb neurons' population follows a specific proportion of silent, spiking and bursting cells and the depression condition, with a higher proportion of bursting cells. These proportions follow the ones obtained experimentally (Figure 4.3). If the model reproduces a stronger inhibition of the dopaminergic neuron when the proportion of bursting cells is increased, then we can study how it works.

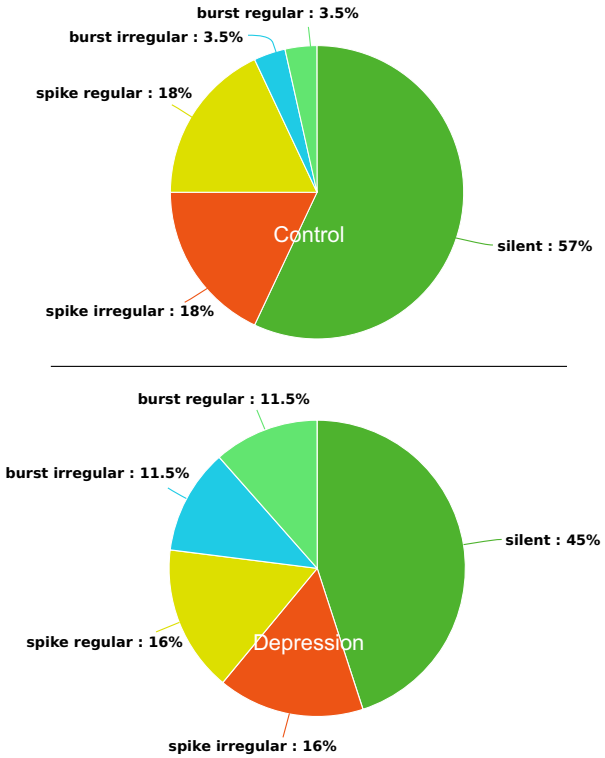

Figure 4.3: Experimental data. LHb neurons repartition in control condition (upper panel) LHb neurons repartition in depression condition (bottom panel).

Considering the neural network of interest, the connection of the habenula with the VTA is made through inhibitory neurons (Figure 4.4). The lateral habenula (LHb) sends glutamatergic efferents to GABAergic regions, either the rostromedial tegmental nucleus (RMTg) or GABAergic neurons in the VTA. Then, both GABAergic neurons project to dopaminergic neurons of the VTA. Finally, there is some feedback from the VTA to the habenula forming two loops, one inhibitory and the other excitatory (Figure 4.4).

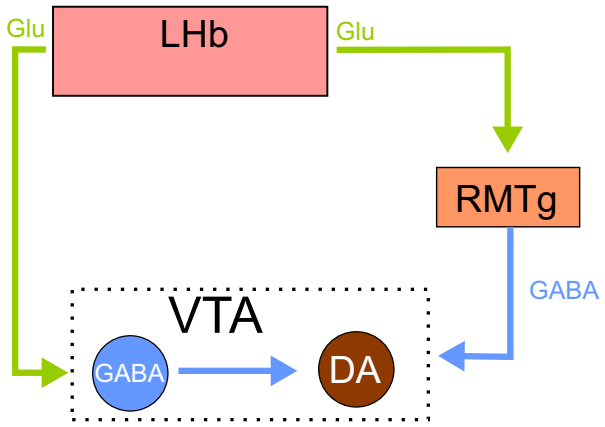

Figure 4.4: Circuitry between the habenula and the ventral tegmental area. The LHb projects to dopaminergic neurons of the VTA through inhibitory regions. DA neurons of the VTA project back to the LHb.

In order to investigate the activity pattern of the DA neuron depending on the habenula's neural population composition, we considered simply one DA neuron receiving inhibitory inputs from a population of habenula's neurons (Figure 4.5). Thus, our model

is in two parts, an effective inhibitory input, rendered by the population of the habenula and a DA neuron, the output of our model.

4.1.1 Modelling the habenula to VTA pathway

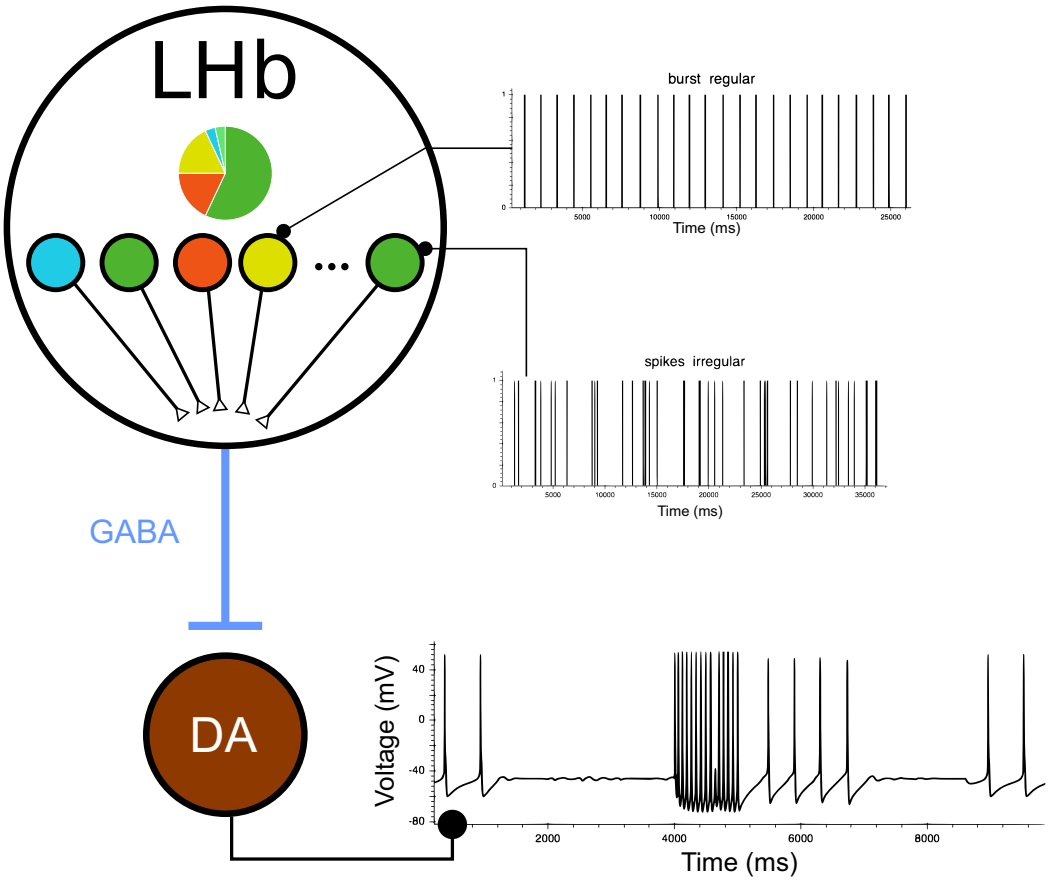

Figure 4.5: Model of the network LHb to VTA. (Up part) The LHb is modelled by a population of neurons, following the proportion of control or depressive condition. Each neuron is a spike train contributing to the whole inhibitory signal sent to the DA neuron. (Down part) Model of DA neuron (Kuznetsov et al., 2006)(Destexhe et al., 1998)(Lobb et al., 2011).

Habenula input

There are actually five different types of activity in habenula neurons: silent cells, regular or irregular spiking cells and regular or irregular bursting cells, according to the data of Hu's team (Figure 2.12). This lab recorded one voltage trace of each activity type and also derived ISI histograms over ten neurons with spontaneous activity (i.e. no silent neurons) in both control and learned helplessness conditions. These histograms contain few neurons, however, it was enough to qualitatively see that learned helplessness conditions showed more short spikes intervals than control condition, suggesting more bursting neurons (Figure 4.2).

To reproduce a realistic input from the habenula, we considered each type of neuron separately and from the samples of recorded voltage traces we extracted spikes and ISI series. Then, we generated synthetic ISI histograms from inter-spike time values with different laws of firing probability (uniform, Gaussian, poissonian, Rayleigh, gamma...). When the shape of ISI histograms generated by one probability law was qualitatively close

to the ISI histogram of experimental data, we kept this probability law. Each experimental firing pattern was thus associated to a given distribution and a set of parameters for this distribution. To generate the spike train for one LHb neuron, we used the distribution corresponding to its pattern, and the parameters corresponding to its pattern. The parameters for the neuron were chosen at random according to a gaussian distribution centered on the parameter value of the pattern. This last step was necessary to account for the heterogeneity of the experimental data.

Finally, to model the activity of the LHb, we summed up spikes series generated from one hundred neurons, following the firing pattern proportion of control or depressive conditions, taken from experimental data (Figure 4.3).

DA neuron and GABA current

Instead of modelling the RMTg, the GABAergic region between the habenula and the VTA (see section 2.11), we simplified the model by considering that the LHb neurons were directly GABAergic neurons contacting the DA cells (i.e. we fused the LHb $\xrightarrow{Glutamate}$ RMTg $\xrightarrow{GABA}$ VTA circuit into LHb $\xrightarrow{GABA}$ VTA).

To model the DA neuron, we used the two-compartment model described by (Kuznetsov et al., 2006) and (Lobb et al., 2011). There is a compartment for the soma (index 1) and another one for dendrites (index 2). Each compartment, depending on its diameter, has a specific natural oscillation frequency. If the coupling between the two compartments is strong, they show a slow periodic oscillation, however, if the coupling is too weak to synchronize both compartments, it generates an irregular oscillation (Kuznetsov et al., 2006). This coupled-oscillator model is described by the set of ordinary differential equations described in part 2.3.4 and with the parameters of simulation in section A.1.

The GABAergic current was made to reproduce the voltage clamp recordings in excised membrane patches showing that 1 msec pulses of 1 mM glutamate reproduced post-synaptic currents that were quite similar to those recorded in the synapse (Hestrin, 1992)(Colquhoun et al., 1992)(Standley et al., 1993). Then, Destexhe et al. (1998) assume that the transmitter, either glutamate or GABA, is released according to a pulse when an action potential invades the pre-synaptic terminal. In order to reproduce these results, each spike time in the spike train obtained as an output of the habenula region was associated to 1 msec and 1 mM amplitude GABA pulse. To calculate $\mathrm{GABA_A}$ current from these spikes GABA pulse train, we used the two states (open/close) kinetic model described by Destexhe et al. (1998).

In this model, r_{op} is defined as the fraction of the receptors in the open state, it is then described by the following first-order kinetic equation:

$$\frac{dr_{op}}{dt} = (\alpha_{GABA_A} \times [GABA] \times (1 - r_{op}) - \beta_{GABA_A} \times r_{op}) \tag{4.1}$$

with α_{GABA_A} and β_{GABA_A} the voltage-independent forward and backward rate constants, respectively. $I_{GABA_{A_{V_2}}}$ is the resulting GABA current through the dendrites (see table A.3):

$$\frac{dI_{GABA_{A_{V_2}}}}{dt} = g_{GABA_{A_{max}}} \times r_{op} \times (V_2 - E_{GABA_A}) \tag{4.2}$$

with $g_{GABA_{A_{max}}}$ the maximal conductance, V_2 the voltage associated to the dendrites compartment and E_{GABA_A}, the reversal potential for $\mathrm{GABA_A}$ current (see table A.3).

4.1.2 Results: the impact of increased bursting activity of habenula on DA neuron

Modelling LHb activity

We had one voltage trace of each cell type at our disposal. After extracting ISI histograms, we fitted them with distribution laws using scipy python library. For burst patterns, inter-spike-interval (ISI) train, $t_{intra-burst}$, are calculated with an exponential function, $t_{intra-burst}(i) = a \times e^{bi}$, $\forall i$ in $\{1, ..., \text{nb}_{\text{spikes}}\}$, where $\text{nb}_{\text{spikes}}$ is the number of spikes in burst. Parameters of the exponential function followed a distribution law, fitted on experimental data, to account for burst variability and described in the corresponding figure legends.

We compared ISI histograms of our fits with experimental data for regular spiking, irregular spiking, regular bursting and irregular bursting patterns, respectively, in figures 4.6, 4.7, 4.8 and 4.9. Besides, the parameter value results are given in the legend of the corresponding figures.

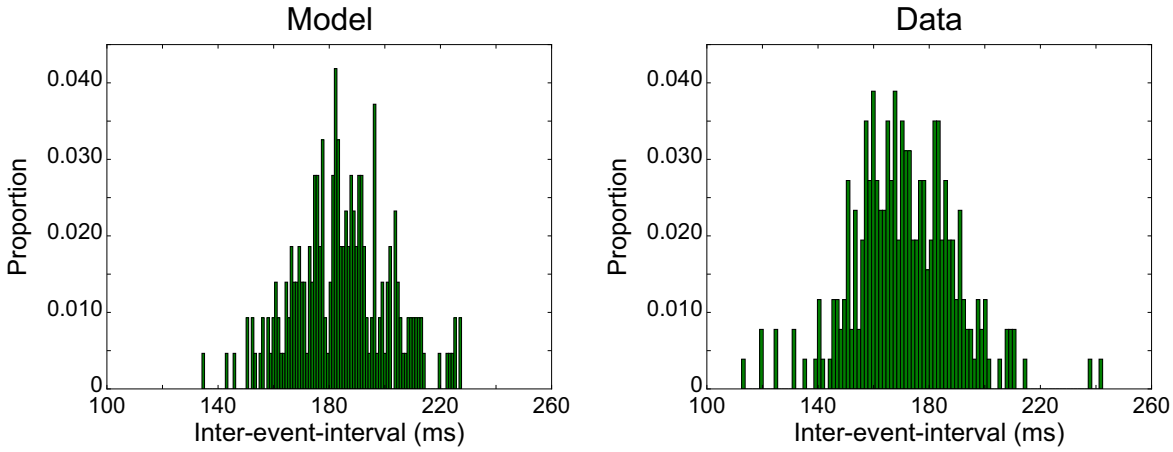

Figure 4.6: Regular spiking cells model (left) and data (right). The interspike interval timing, t_{ISI}, follows a normal distribution $t_{ISI} \sim \mathcal{N}(171, 18)$

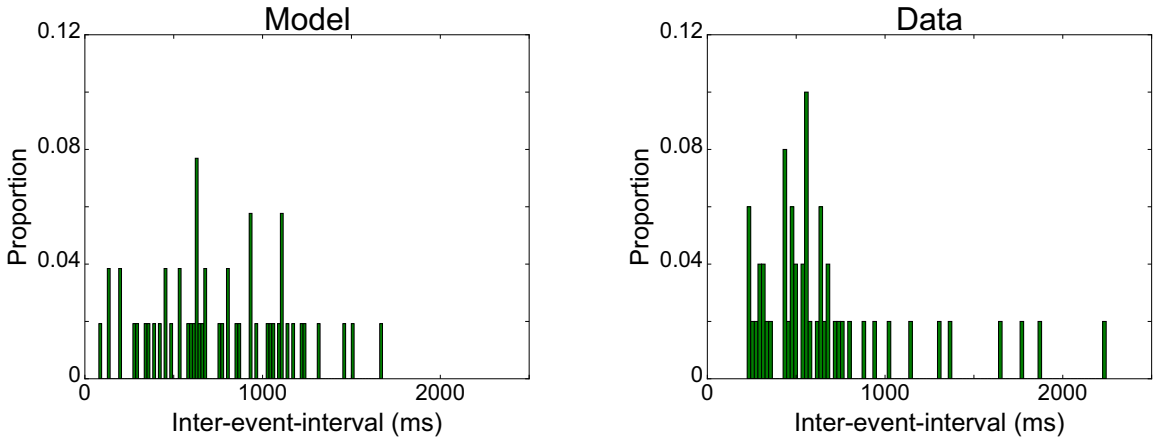

Figure 4.7: Irregular spiking cells model (left) and data (right). The interspike interval timing, t_{ISI}, follows a Rayleigh distribution, $t_{ISI} \sim \frac{x-\alpha}{\beta} \times \exp\left(\frac{-(\frac{x-\alpha}{\beta})^2}{2}\right)$ with the variable $x \geq 0$, and parameters $\alpha = 19$ and $\beta = 561$.

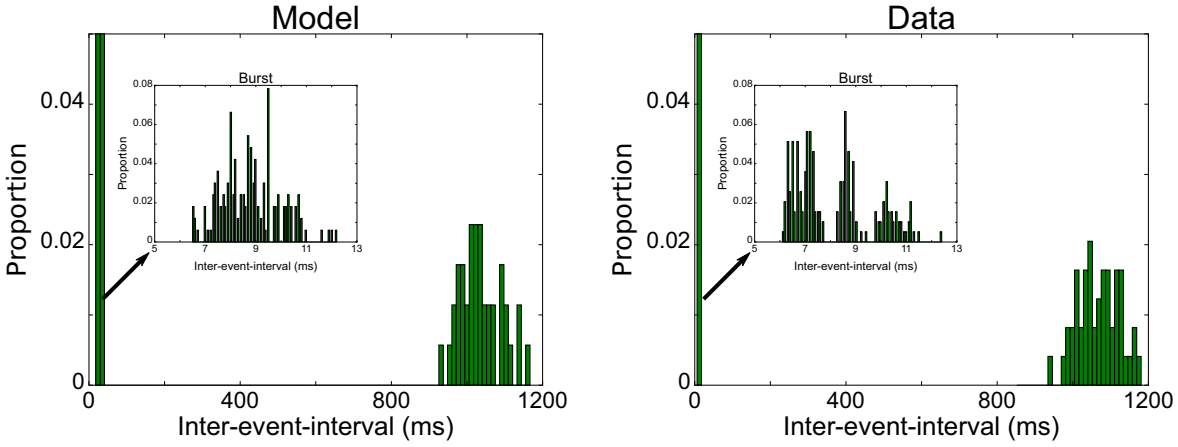

Figure 4.8: Regular bursting cells model (left) and data (right). The inter-burst interval timing, $t_{inter-burst}$, follows a normal distribution $t_{inter-burst} \sim \mathcal{N}(1068, 53)$. The intra-burst interval timing is calculated with an exponential function, where parameters a, b are normally distributed $a \sim \mathcal{N}(8, 0.8)$, $b \sim \mathcal{N}(0.16, 0.02)$ and where the number of spikes is an integer uniformly distributed in [2, 3].

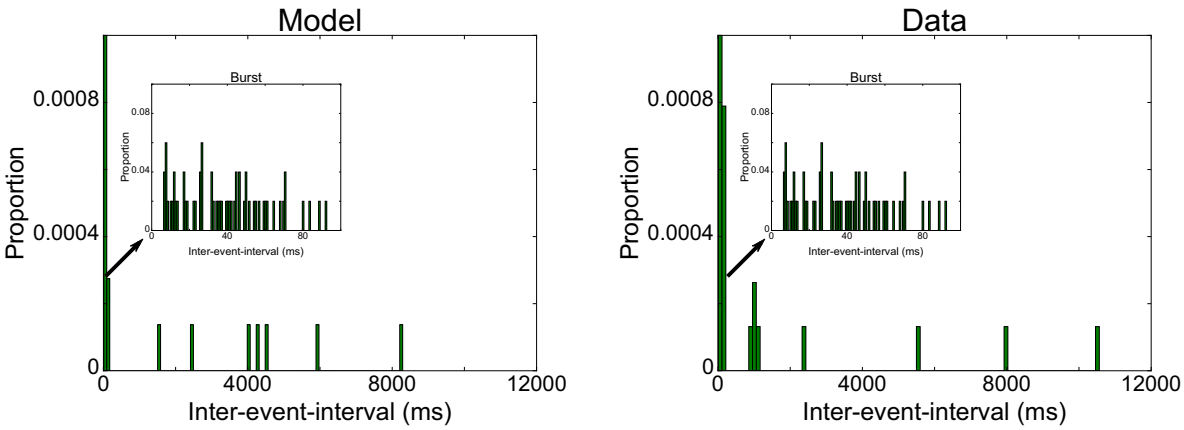

Figure 4.9: Irregular bursting cells model (left) and data (right). The inter-burst interval timing, $t_{inter-burst}$, follows a Rayleigh distribution, with parameters $\alpha = -1660$ and $\beta = 4598$, we discarded all negative output values. The intra-burst interval timing is calculated with an exponential function where parameter a is uniformly distributed $(a_{down}, a_{up}) = (7.5, 42.)$, and b is set at 0.15 and where the number of spikes is an integer uniformly distributed in [1, 13].

Then, we aggregated each firing pattern following the experimental proportion in control and cLH conditions (Figure 4.3)

In order to get the same experiment as Hu's team, we simulated 100 LHb neurons activity for ten minutes and extract ISI of each neuron, in both control (WT) and depressive (cLH) condition (Figure 4.11). As a result, in our simulations, we can observe that the main mode of short timing induced by bursting is shorter (below 10 ms in figure 4.10) than in experimental ISI histograms (around 70 ms in control condition and around 20 ms in cLH condition in figure 4.11). Alternatively, we could directly generate LHb activity from the experimental ISI histograms with a Monte Carlo sampling technics.

However, these histograms have been made from only 10 cells each, so these discrepancies might be a bias of sampling. Sticking closer to them would have implied changing the mean firing rate of spiking and bursting modes between control and cLH conditions. This

was not the question we built our model for, hence, in order to test only the difference of proportions, we kept the same distributions for each LHb neuron type and only changed the proportion between each condition.

Besides, to account for this heterogeneity, we kept the same probabilistic laws describing each pattern but we added randomness on their parameters.

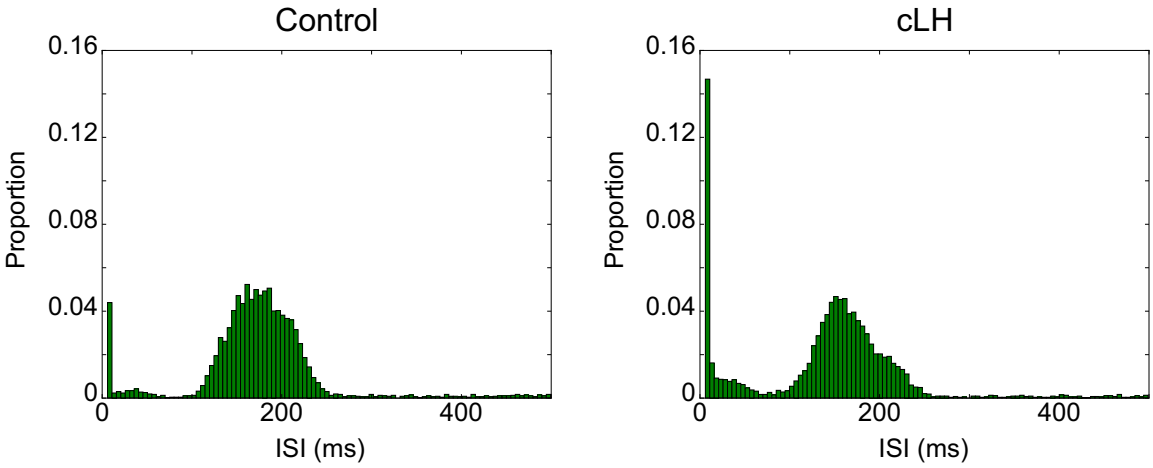

Figure 4.10: ISI histograms of simulated data following experimental proportion in figure 4.3. Control condition (left panel) and cLH condition (right panel).

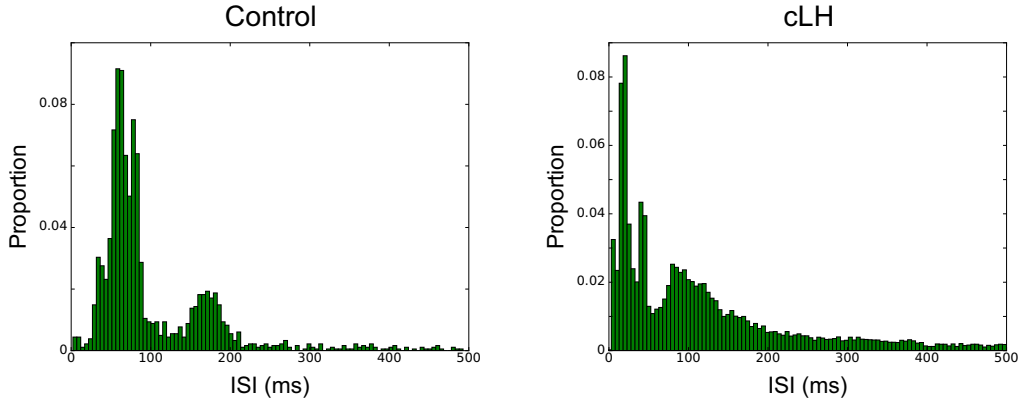

Figure 4.11: ISI histograms of experimental data. Control condition (left panel) and cLH condition (right panel).

Hence, we simply used a gaussian law over each parameters that we adjusted visually to obtain comparable results to experimental histograms in control and cLH conditions.

For regular spiking cells, the interspike interval timing, t_{ISI}, follows a normal distribution $t_{ISI} \sim \mathcal{N}(\mu, \sigma^2)$ (Figure 4.12), where the parameters μ and σ^2 are normally distributed, to account for the heterogeneity of recording cells, with $\mu \sim \mathcal{N}(120, 30)$ and $\sigma^2 \sim \mathcal{N}(10, 30)$).

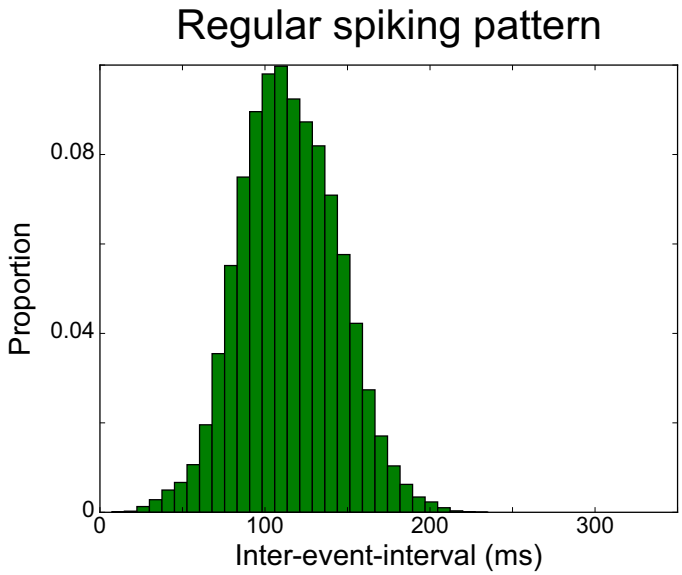

Figure 4.12: Model data of regular spiking LHb neuron.

For irregular spiking cells, the interspike interval timing, t_{ISI}, follows a Rayleigh distribution, $t_{ISI} \sim \frac{x-\alpha}{\beta} \times exp\left(\frac{-(\frac{x-\alpha}{\beta})^2}{2}\right)$ with the variable $x \geq 0$ (Figure 4.13) and where the parameters α and β are normally distributed with $\alpha \sim \mathcal{N}(60, 3)$ and $\beta \sim \mathcal{N}(60, 3)$.

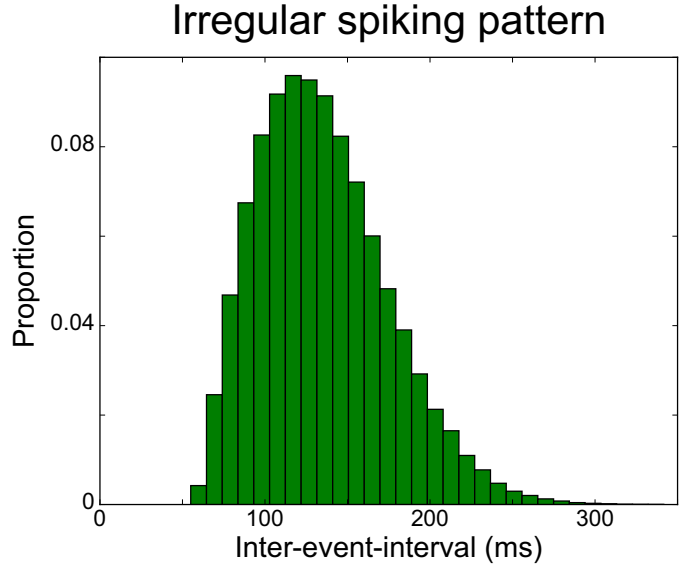

Figure 4.13: Model data of irregular spiking LHb neuron.

For regular bursting cells, the inter-burst interval timing, $t_{inter-burst}$, follows a normal distribution $t_{inter-burst} \sim \mathcal{N}(\mu, \sigma)$ (Figure 4.14) where the parameters μ and σ^2 are normally distributed, $\mu \sim \mathcal{N}(120, 30)$ and $\sigma^2 \sim \mathcal{N}(10, 30)$. The intra-burst interval timing, $t_{intra-burst}$, follows an exponential law, $t_{intra-burst} \sim a \times e^{bx}$ with the variable x and where the parameter a is normally distributed $a \sim \mathcal{N}(20, 1)$ and b is fixed at 0.15.

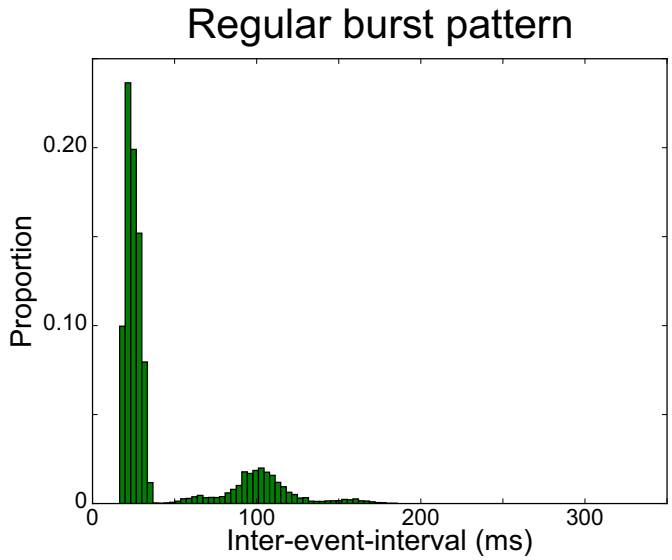

Figure 4.14: Model data of regular bursting LHb neuron.

For irregular bursting cells, the inter-burst interval timing, $t_{inter-burst}$, follows a Rayleigh distribution $t_{inter-burst} \sim \frac{x-\alpha}{\beta} \times exp\left(\frac{-(\frac{x-\alpha}{\beta})^2}{2}\right)$ with the variable $x \geq 0$ (Figure 4.15) and where the parameters α and β are normally distributed with $\alpha \sim \mathcal{N}(60, 3)$ and $\beta \sim \mathcal{N}(60, 3)$. The intra-burst interval timing, $t_{intra-burst}$, follows an exponential law, $t_{intra-burst} \sim a \times e^{bx}$ with the variable x and where the parameter a is uniformly distributed $(a_{down}, a_{up}) = (7.5, 42.)$ deduced from fitting experimental data, and b is fixed at 0.1.

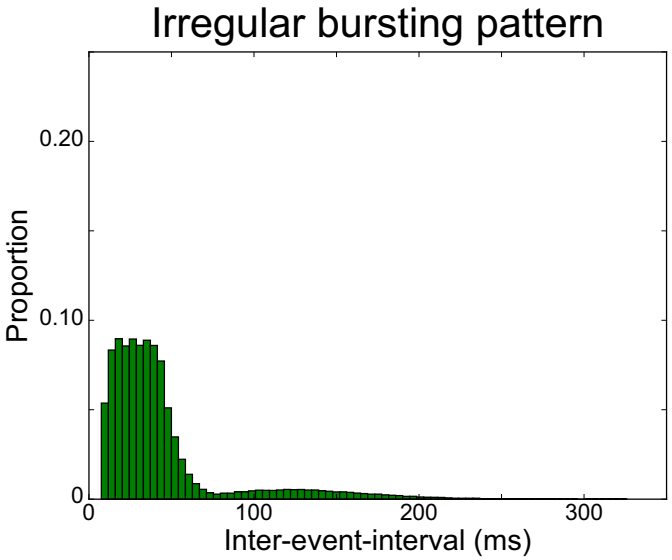

Figure 4.15: Model data of irregular bursting LHb neuron.

Then, again, we simulated 100 LHb neurons activity for ten minutes and extract ISI of each neuron, in both control (WT) and depressive (cLH) condition (Figure 4.16).

In both, experimental and computational histograms, when comparing depression condition to control condition one can see that there are more short intervals (Figures 4.16 and 4.17). Thus, these histograms validate qualitatively the model to reproduce both WT and cLH conditions when changing the proportion of bursting cells. Nevertheless, the model does not reproduce very accurately the WT condition, indeed, in experimental

data, the two modes of the distribution are around 70 ms and 180 ms whereas on the model data, the two modes are the same as in the depression condition and around 20 ms and 110 ms. Although the model reproduces almost the ISI histogram of the cLH condition, it is not good enough to reproduce the control condition. However, these histograms have been made from only 10 cells each, so these discrepancies might be a bias of sampling.

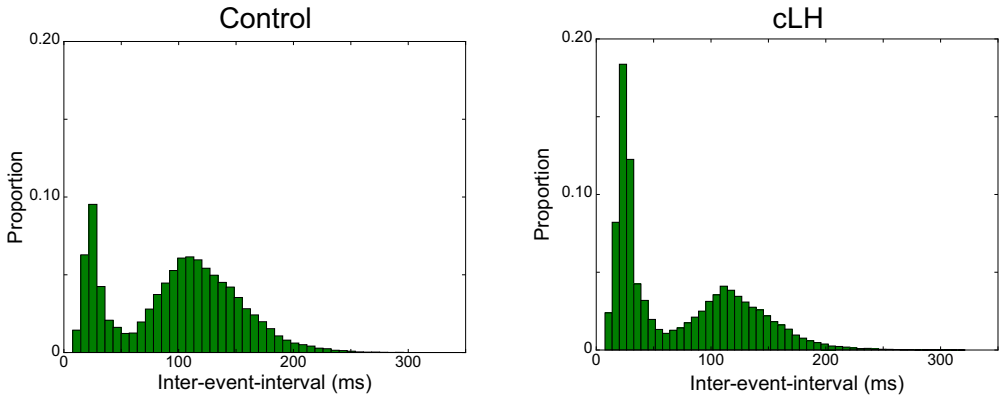

Figure 4.16: ISI histograms of simulated data following experimental proportion in figure 4.3 and accounting for heterogeneity of each firing pattern. Control condition (left panel) and cLH condition (right panel).

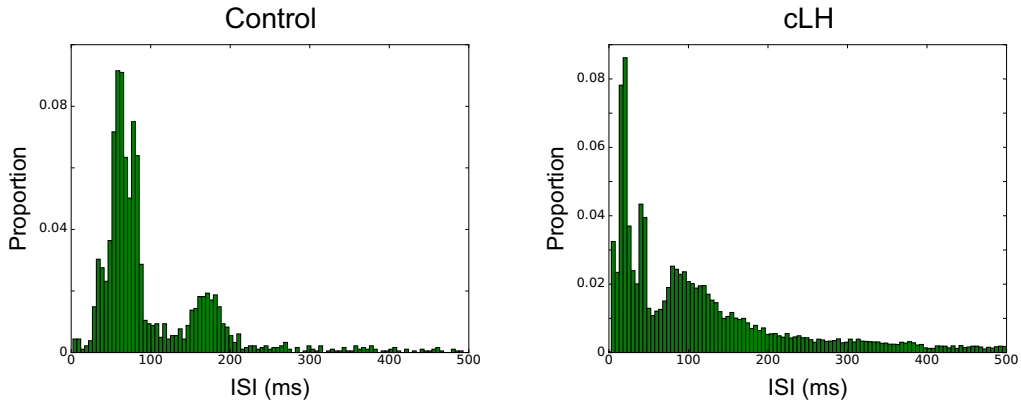

Figure 4.17: ISI histograms of experimental data. Control condition (left panel) and cLH condition (right panel).

Modelling DA activity

In vivo, in addition to the two major activity patterns, tonic and phasic, of the DA neuron, as previously mentioned in section 2.1.1, three distinct firing patterns of the DA neuron have been observed.

First, a regular spiking, i.e. a rhythmic single spiking pattern characterized by highly periodic low-frequency (< 10 Hz) firing. Then, an irregular single spiking pattern characterized by low frequency range (< 10 Hz). Finally, bursts of spikes, usually each burst is composed of less than 10 spikes, following a regular or an irregular firing.

To reproduce these features, we used the model of (Kuznetsov et al., 2006) with the parameters of (Lobb et al., 2011) described in section 2.3.4.

By applying constant NMDA and GABA currents, we get regular spiking at a frequency that matches the experimental data (< 10 Hz) (Figure 4.18) whereas if GABA current is irregular we get irregular spiking (Figure 4.19). Furthermore, if we set constant

$GABA_A$ and NMDA currents, but with a stronger NMDA current than in the regular spiking case, we get regular spiking at a larger frequency, considered by Kuznetsov et al. (2006) as regular bursting (Figure 4.20). Thus, the firing pattern of this DA neuron model depends on the balance between NMDA and GABA currents and their shape if they are constant or irregular. Since higher NMDA currents in this model only induced higher frequencies of discharge, to simplify, we removed NMDA currents and only study the impact of GABA current on the DA neuron activity.

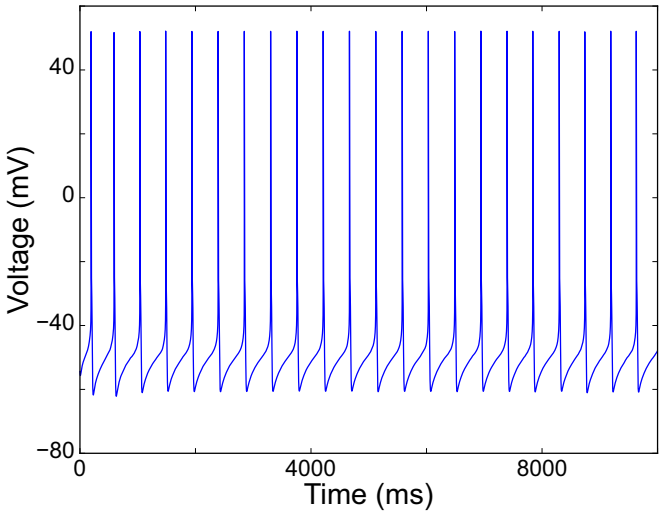

Figure 4.18: Regular spiking at around 2.2 Hz. NMDA and GABA conductances were respectively set at 28 and 4 $\mu S.cm^{-2}$

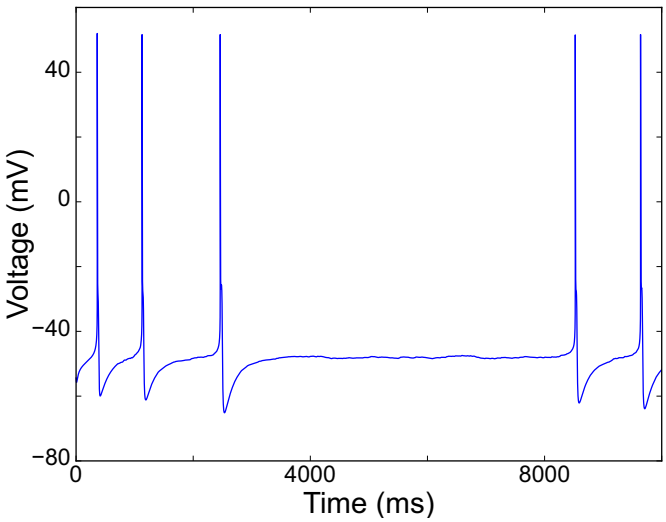

Figure 4.19: DA neuron in irregular spiking mode at around 0.5 Hz where there is no NMDA current and GABA current is irregular with conductance set at 4 $\mu S.cm^{-2}$.

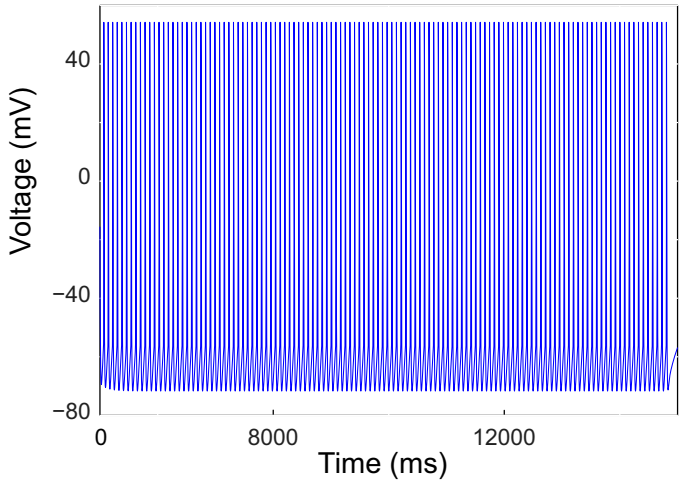

Figure 4.20: DA neuron in regular bursting mode at around 12.5 Hz where constant NMDA and GABA currents have their conductances respectively set at 400 $\mu S.cm^{-2}$ and 4 $\mu S.cm^{-2}$

Modelling WT and cLH conditions

In order to examine if the DA neuron response is different between control and cLH conditions, we first generated the activity of 100 LHb neurons. The neuron type among these two populations was distributed according to experimental data (Figure 4.3), and we can observe that the number of spikes is higher in cLH condition (Figure 4.21a, b).

Then, using this input in our model, we could see that the DA neuron activity is more inhibited in cLH condition than control condition, as illustrated with plots of the DA spiking activity, over 80 repetitions, on figure 4.22a, b.

Furthermore, we tested this result over several values of GABA conductance showing that cLH condition is always more inhibitory than control condition but this difference is at its maximum (0.4 Hz) for GABA conductance set at 6 $\mu S.cm^{-2}$ (Figure 4.23). For low and high conductances, inhibition is respectively so low or so high that it affects the DA neuron in the same way between each condition.

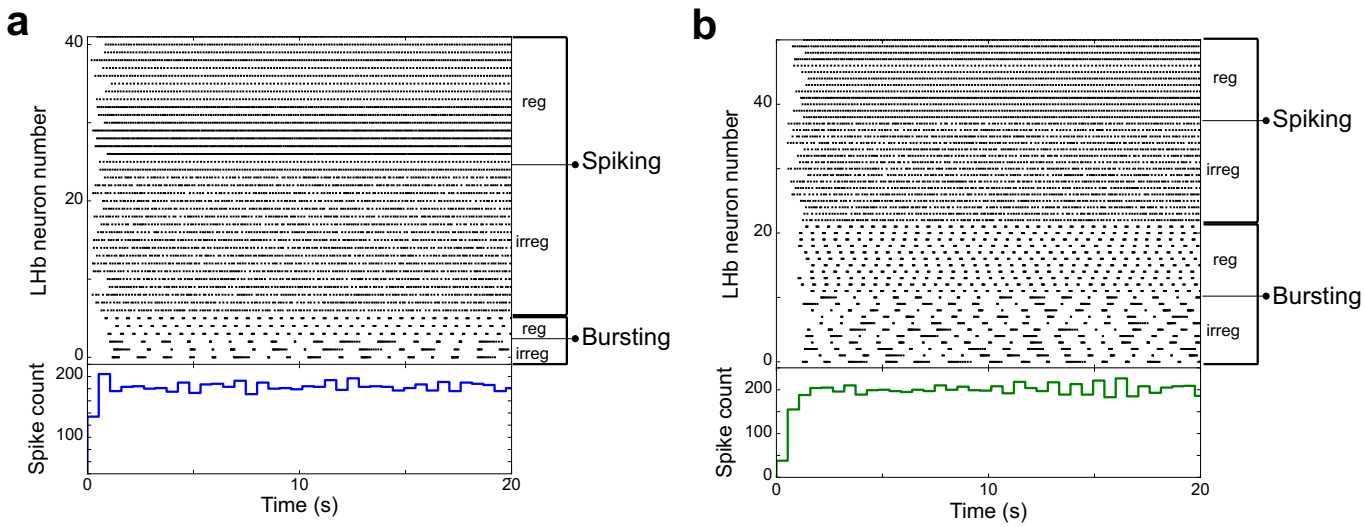

Figure 4.21: Spiking activity and spike count histograms from a population of 100 LHb neurons (however, silent neurons have been removed) in control condition (a) and in cLH condition (b).

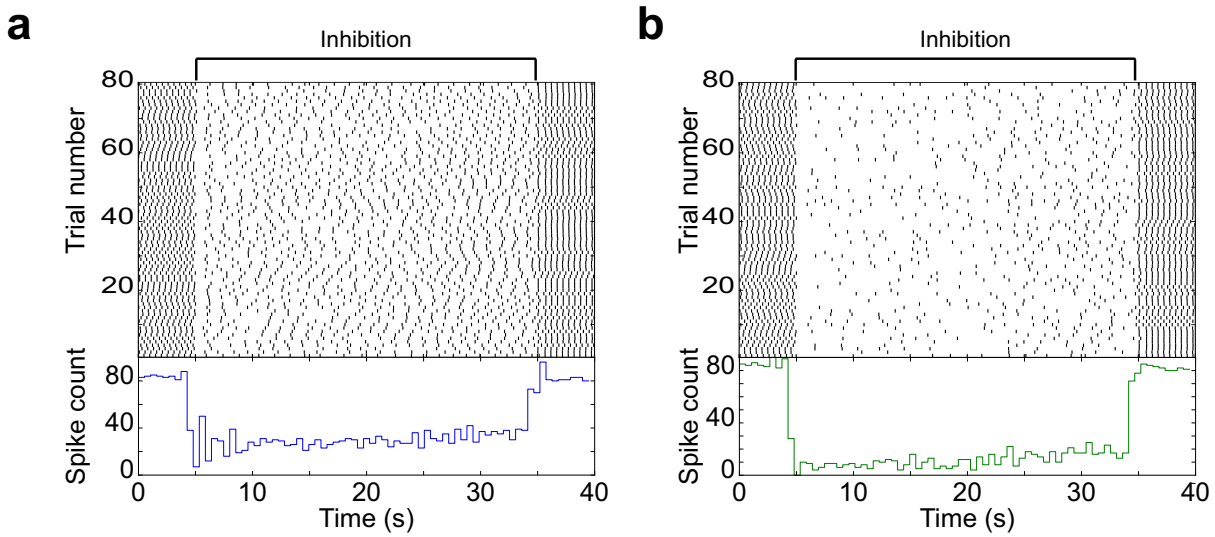

Figure 4.22: Spiking activity and spike count histograms of DA neuron in control condition (a), and of DA neuron in depression condition (b). Both plots are made over 80 repetitions, and the GABA conductance is set at 4 $\mu S.cm^{-2}$. Inhibition by LHb neurons is activated from 5 to 35 seconds.

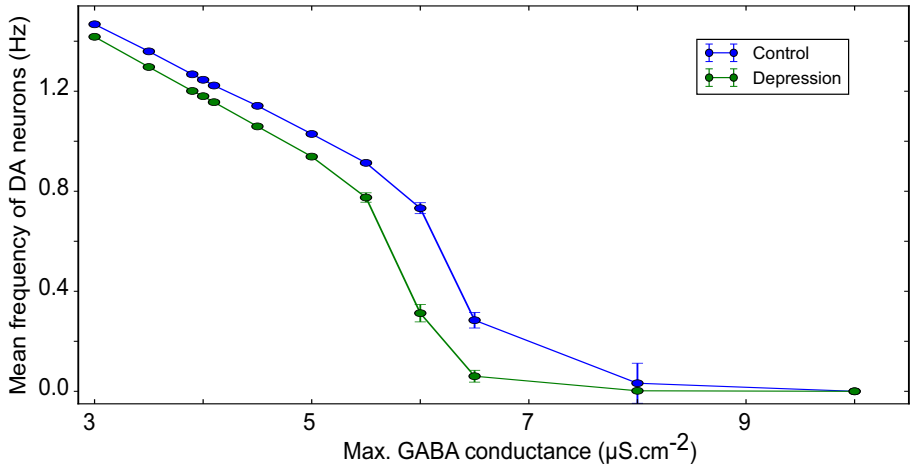

Figure 4.23: DA neuron frequency over GABA conductance, in both control and cLH conditions. Dots are made over 80 repetitions.

If we count all spikes, including the ones in burst, the firing frequency in cLH condition is larger than in WT condition. This observation raises the question of knowing if the increase of DA neuron inhibition is due to the cLH increased frequency or to the cLH increased proportion of the burst pattern.

To measure the effect of LHb neurons firing frequency on the DA neuron inhibition, we defined the frequency as the number of spikes, including the spikes inside bursts.

First, we distinguished each firing pattern of LHb neurons separately, regular spiking, irregular spiking, regular bursting and irregular bursting (Figures 4.24 and 4.26) and their effect on DA neuron (Figures 4.25 and 4.27). However, the LHb neurons firing frequencies are different, it is difficult to discriminate between the pattern and the frequency effect.

To compare them, we modulated the LHb frequency for each of the four LHb neuron activity patterns taken separately, and observed, as expected, that the DA response frequency decreased when LHb frequency increased (Figure 4.28). However, this figure also reveals that at a given frequency, the bursting pattern is less efficient to inhibit DA neuron than the spiking pattern.

The biological interpretation of this model thus suggests that the bursting pattern of cLH animals inhibits more DA response, not because of their firing pattern but rather because of the increased frequency, compared to the wild-type animals.

The model confirms that the firing pattern observed in cLH LHb should inhibit more VTA neurons, explaining a dopaminergic decrease leading to depression. But our model suggests that the key point is the global firing frequency increase of the cLH, not really the change of firing mode.

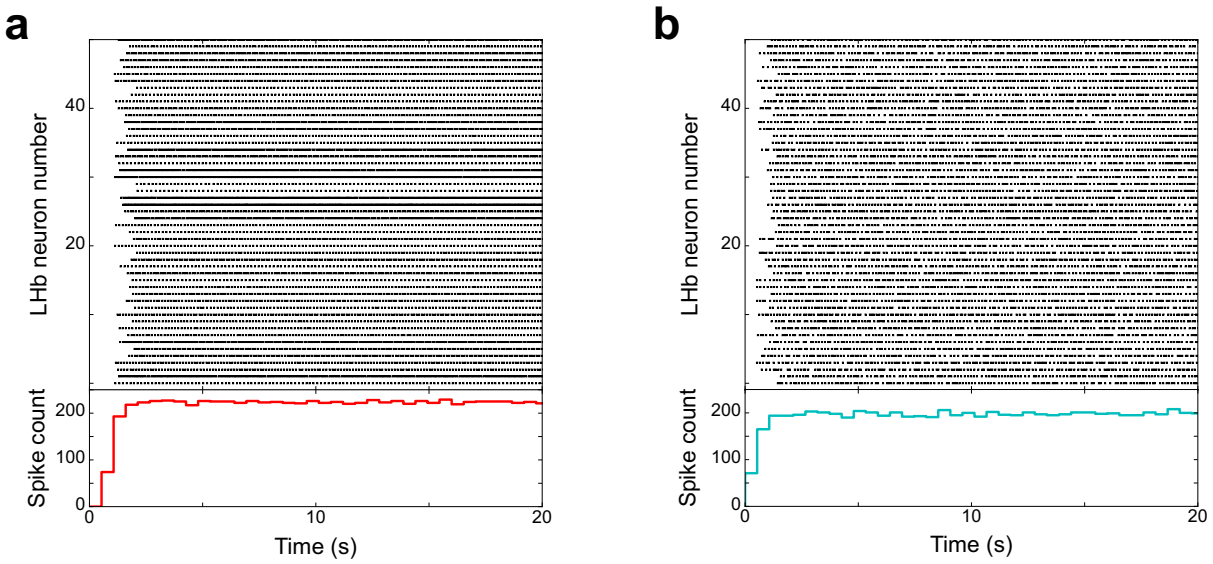

Figure 4.24: Spiking activity and spike count histograms from a population of 50 regular spiking LHb neurons, the mean firing frequency is 8.58 Hz (a) and from a population of 50 irregular spiking neurons, the mean firing frequency is 7.29 Hz (b).

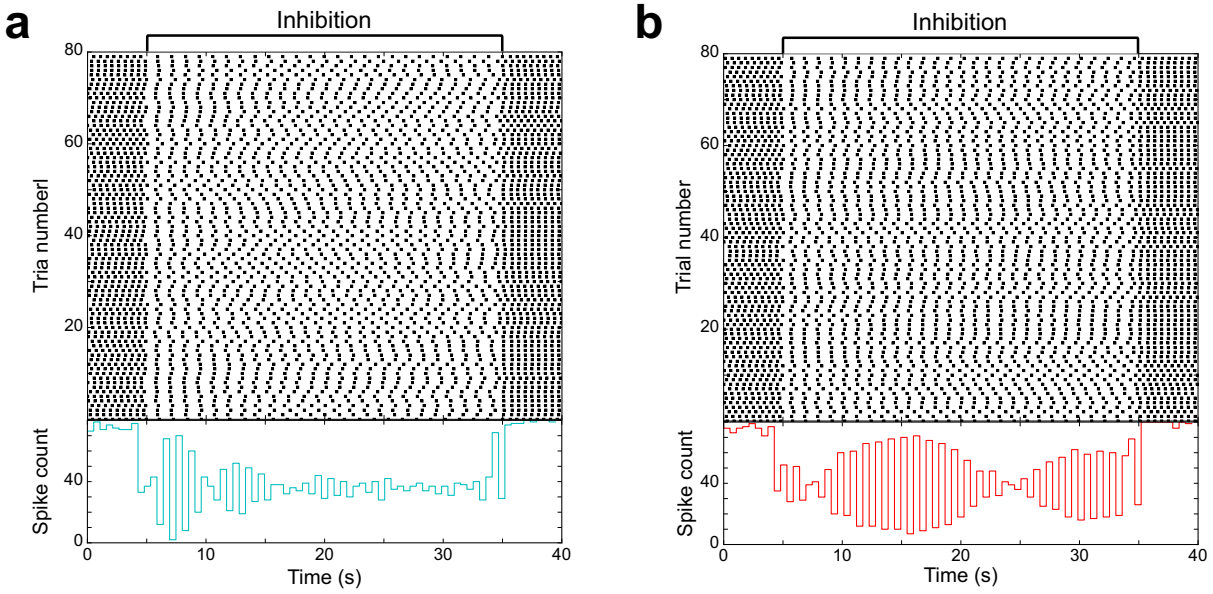

Figure 4.25: Spiking activity and spike count histograms of DA neuron receiving inhibition from 50 regular spiking LHb neurons, the mean firing frequency is 0.83 Hz (a) and of DA neuron receiving inhibition from 50 irregular spiking LHb neurons, the mean firing frequency is 0.9 Hz (b). Both plots are made over 80 repetitions, and GABA conductance is set at 4 $\mu S.cm^{-2}$. Inhibition by LHb neurons is activated from 5 to 35 seconds.

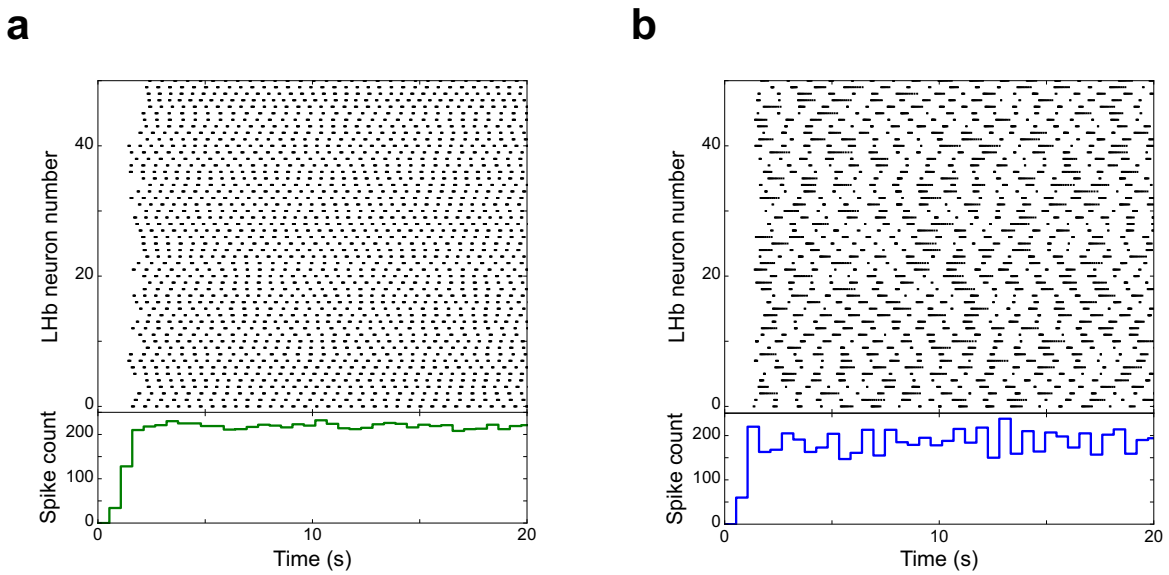

Figure 4.26: Spiking activity and spike count histograms from a population of 50 regular bursting LHb neurons, the mean firing frequency is 7.98 Hz (a) and from a population of 50 irregular bursting neurons, the mean firing frequency is 6.81 Hz (b).

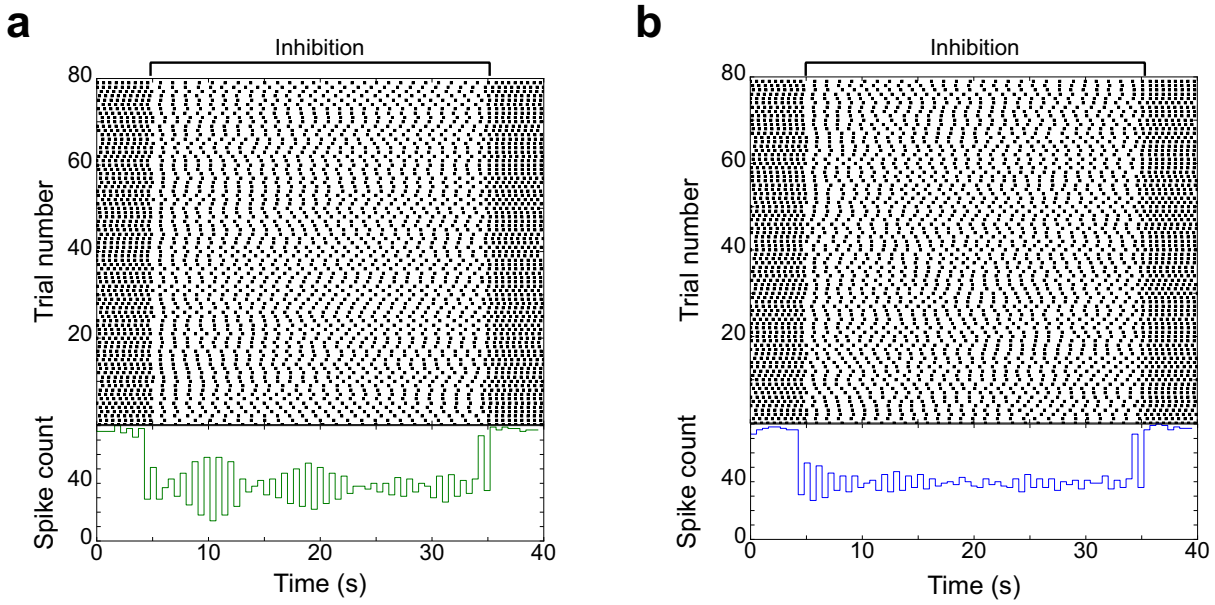

Figure 4.27: Spiking activity and spike count histograms of DA neuron receiving inhibition from 50 regular bursting LHb neurons, the mean firing frequency is 0.87 Hz (a) and of DA neuron receiving inhibition from 50 irregular bursting LHb neurons, the mean firing frequency is 0.91 Hz (b). Both plots are made over 80 repetitions, and GABA conductance is set at 4 $\mu S.cm^{-2}$. Inhibition by LHb neurons is activated from 5 to 35 seconds.

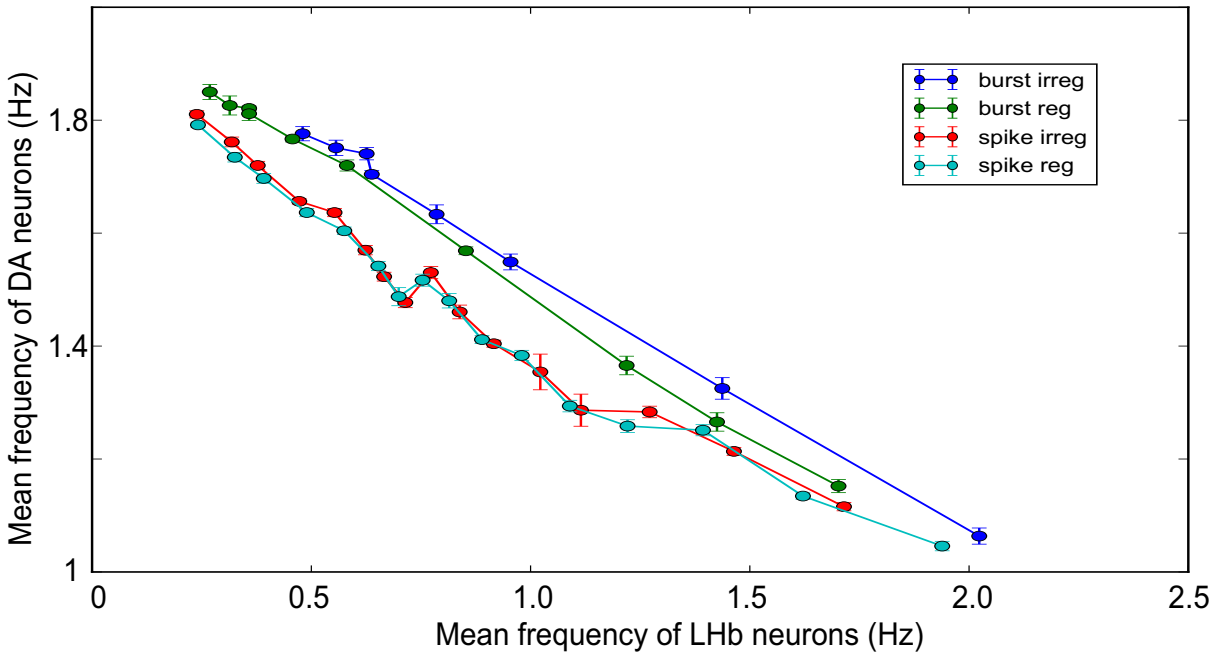

Figure 4.28: DA neuron frequency over LHb neurons frequency, with four firing modes. Dots are made over 80 repetitions, and GABA conductance is set at 4 $\mu S.cm^{-2}$.

4.2 Bursting neurons and overexpression of astrocytic Kir channel

We showed that the increase of bursting in the cLH increases the VTA inhibition and leads to depression. Our next question was to find which molecular or cellular mechanism causes this bursting increase.

To compare habenular protein expression of congenitally learned helpless (cLH) and wild-type (WT) rats, Hu's team screened quantitatively the proteins present in the habenula. They identified Kir4.1, an inward rectifying potassium channels, to be highly upregulated in the LHb of cLH rats. Western blot analysis confirmed that Kir4.1 had a significant increase (1.44-fold) in the membrane protein extraction of cLH habenula (Figure 4.29).

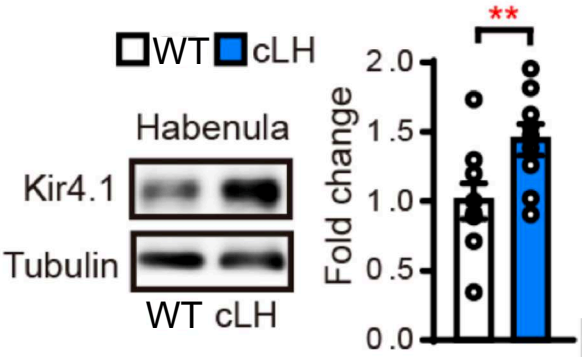

Figure 4.29: Western blot analysis (on the left) showing up regulation of Kir4.1 protein in the membrane fraction of cLH habenula compared to WT habenula (n = 9, from 9 rats). Tubulin is used as loading control. On the right is the fold change of Kir4.1 between WT and cLH.

These Kir4.1 channels are found on the membrane astrocyte, not on the neuron.

Besides, this lab discovered, by using viruses to manipulate the Kir4.1 levels in habenular astrocytes, that they were able to elicit depression symptoms in wild type mice.

Indeed, by increasing the level of Kir4.1 channels in the LHb astrocytes of WT rats, the resting membrane potentials (RMPs) of both astrocytes and neurons were more hyperpolarized (Figure 4.30a, b) and the percentage of bursting neurons were significantly higher (Figure 4.30c). Moreover, the mice with such overexpression of Kir4.1 in LHb astrocytes displayed severe depressive-like behaviours, including increased immobile duration and decreased latency to immobility in the forced swim test (FST in Figure 4.30d), and decreased sucrose preference in the sucrose preference test (SPT in Figure 4.30e). Furthermore, overexpression of Kir4.1 in astrocytes also increased neuronal bursts (not shown).

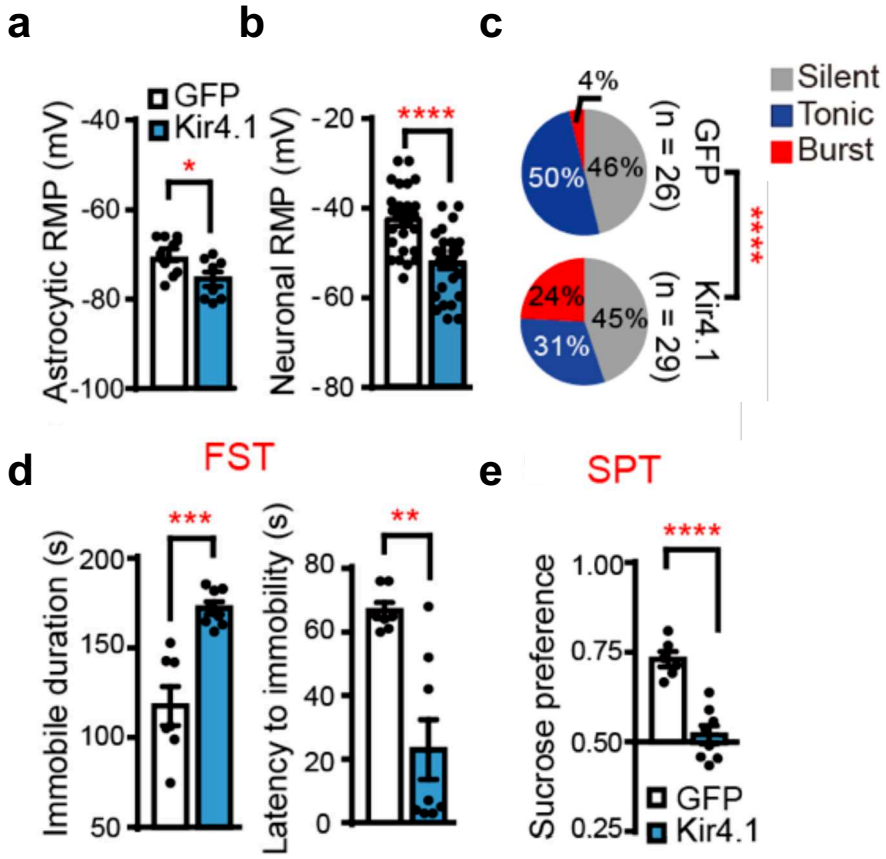

Figure 4.30: Astrocytic overexpression of Kir4.1 decreases RMPs of both astrocytes (a) and neurons (b) and increases the bursting population in neurons (c). Green Fluorescent Protein (GFP) overexpression is used as a control. Behavioural effects of expressing various viral constructs in LHb in FST (d) and SPT (e). Data are means ± s.e.m. *P < 0.05, **P < 0.01, ***P < 0.001, ****P< 0.0001. Two-tailed unpaired t-test (a, b, d, e) and Chi-square test (c).

On the contrary, by down regulating the Kir4.1 expression in the cLH habenula, with interferent RNA, they were able to reverse the depression symptoms. Indeed, knock-out of Kir4.1 in astrocytes had a global impact on RMPs of neighboring neurons by depolarizing them (Figure 4.31a, b). Besides, the bursting activity in the LHb of cLH rats was significantly eliminated by the knock out (Figure 4.31c).

Behaviourally, infection by modified viruses had a pronounced effect on rescuing the depressive-like phenotypes of cLH rats in three depression paradigms: reducing the immobility time and increasing latency to immobility in FST (Figure 4.31d), increasing the bar pressing number in the LHT (not shown), and increasing the sucrose preference score in SPT (Figure 4.31e).

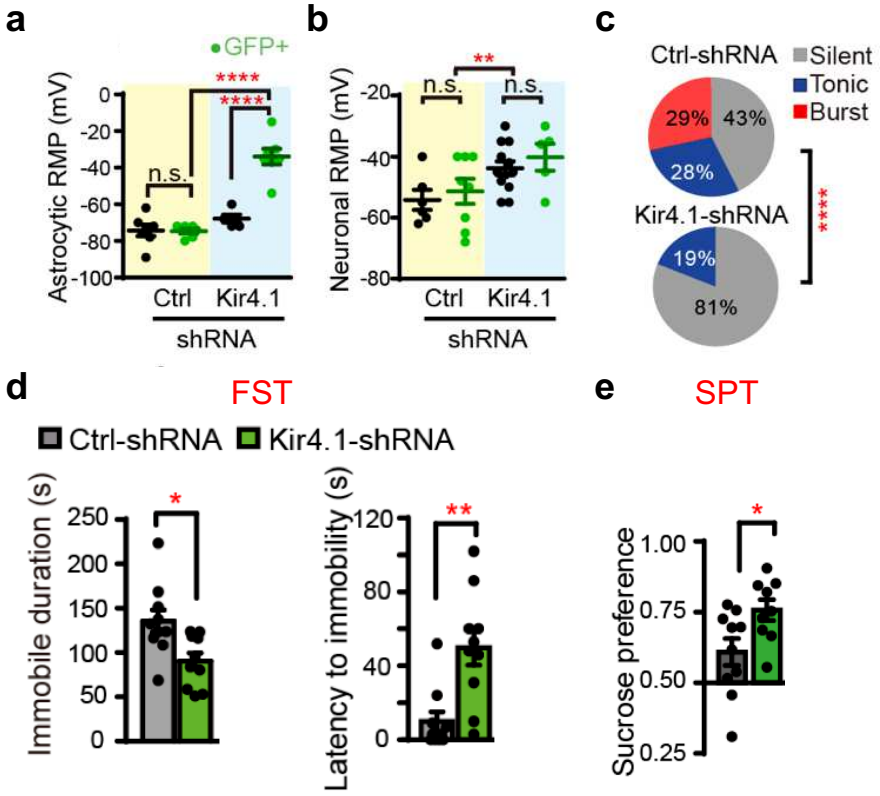

Figure 4.31: Short hairpin RNA (shRNA) is an artificial molecule used to silence target gene. Here, in cLH rats, Kir4.1-shRNA is used to block Kir4.1 channels whereas ctrl-shRNA is used as a control. Astrocytic subexpression of Kir4.1 depolarizes astrocytes (a) and neurons (b), and abolished neuronal bursting (c). Behavioural effects of expressing various viral constructs in the cLH LHb in FST (d) and SPT (e).

In agreement with these first results, Hu's team confirmed that the LHb neurons were hyperpolarized, by around 5 mV for bursting and spiking modes when receiving tetrodotoxin (TTX), which prevents neuronal action potentials by blocking sodium channels. (Figure 4.32b). On the contrary, when they bath applied barium chloride ($BaCl^2$), which selectively blocks Kir channels, the RMPs of LHb neurons were depolarized, by around 15 mV for bursting and spiking modes (Figure 4.32a). Moreover th perfusion of $BaCl^2$caused a dramatic increase of firing frequency until the neuron reached a sustained plateau of a tetanus response and stopped firing (not shown).

Thus, all these experimental results are converging to support the idea that the increase of Kir4.1 in LHb astrocytes depolarizes both the neuron and the astrocyte and increases the neuronal burst. The most probable hypothesis would be that the increase of Kir4.1 decreases the extracellular potassium concentration (K_{out}).

To test this idea, Hu's lab did a current-clamp recordings of LHb neurons in slices, while lowering K_{out} of the bath from 2.75 mM to 1.4 mM. This led to a decreased neuronal RMP by 13.7 ± 0.5 mV (Figure 4.33a) and to a direct shift of originally tonic-firing neurons (8 out of 15) into bursting mode (Figure 4.33a), suggesting a causal relationship between K_{out} and firing mode.

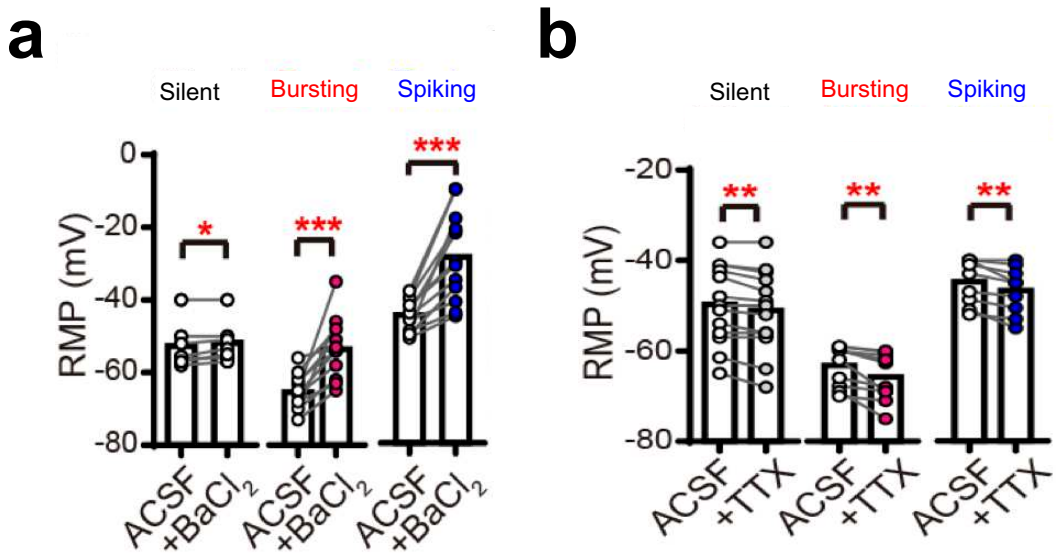

Figure 4.32: Changes of neuronal RMPs caused by (a) $BaCl^2$ ($100\mu M$) or (b) TTX ($1\mu M$) in different neuronal types. RMPs are measured at 15 min or 5 min after perfusion of $BaCl^2$ or TTX, respectively, when the RMPs stabilize. ACSF: Artificial cerebrospinal fluid.

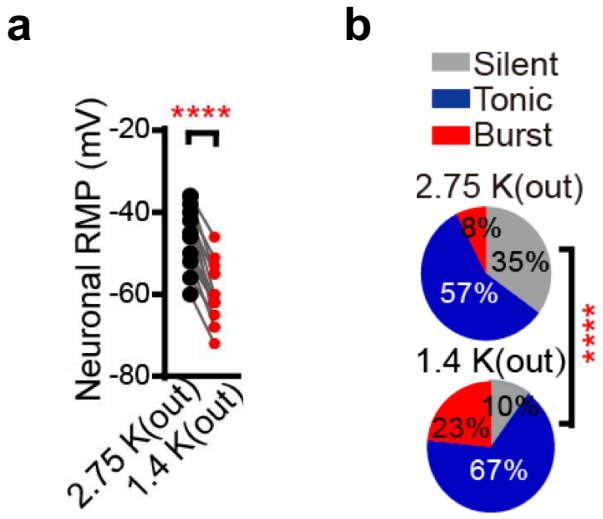

Figure 4.33: Lowering K_{out} in the bath by half hyperpolarizes neuronal RMPs (a) and increases bursting neural population (b).

The next step was to show how Kir4.1 overexpression in the astrocyte could lead to the decrease of K_{out} and the hyperpolarization of LHb neurons and astrocytes. To test plausible explanations, we built a mathematical model of ionic exchange between three compartments; a neuronal compartment, an astrocytic compartment and the extracellular space in between (Figure 4.34). This model allows to study theoretically the concentration variations of sodium and potassium ions in each of these compartments by explicitly describing their fluxes through Kir4.1 channels, Na/K-pump and voltage-gated sodium and potassium channels. In addition to those elements of interest, one expects the neuron or astrocyte plasma membrane to host many other transporters/channels for sodium or potassium, for example, gap junctions in astrocytes or diffusion between the artificial

cerebrospinal fluid (ACSF) and the extracellular space in the vicinity of the membranes. We lump all those fluxes in a single effective flux of the form $g_{eff_x}([X] - [X_0])$ where $[X]$ the ionic concentration of the ion being considered in the compartment being considered (e.g. K^+ in the extracellular medium of or Na^+ in the astrocyte cytoplasm) g_{eff_x} is the rate of this effective flux and $[X_0]$ is the concentration expected at equilibrium when all fluxes vanish. In the model, we considered only Kir4.1 channels wrapping the soma of the neuron and not the dendrites, this distinction is important since these channels can directly modulate the excitability of the neuron. Furthermore, Hu's team has observed with electro-microscopy that the majority of LHb Kir4.1 channels were around the neural soma.

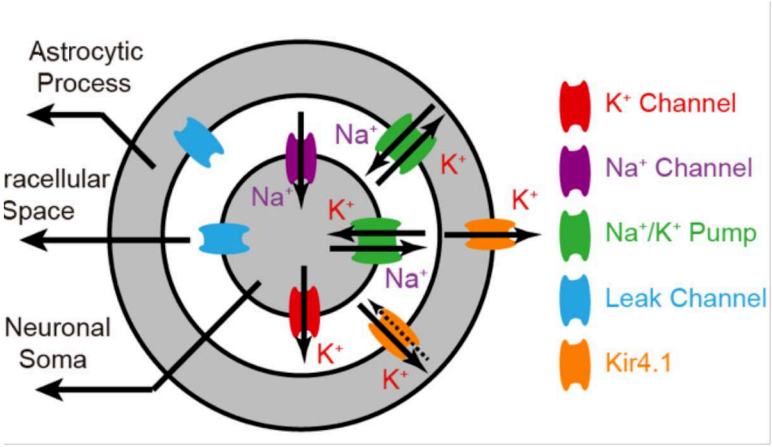

Figure 4.34: Scheme of the mathematical model used to study potassium (K^+) and sodium (Na^+) exchanges between an astrocyte and a neuron of the LHb. The model explicitly accounts for Kir4.1 currents in the astrocytes, around the neural soma and at the astrocyte end feet toward blood vessels, as well as Na/K pumps (neuron and astrocyte), and voltage-gated potassium and sodium channels (neuron).

4.2.1 Modelling the tripartite synapse with Kir channels

The evolution of potassium and sodium concentration in the extracellular medium ($[K]_O$ and $[Na]_O$, respectively), are modified from Sibille et al. (2015) and given by:

$$\frac{d[K]_O}{dt} = \frac{I_{Kir}}{F \times Vol_O} - 2i_{pump_A} + \frac{I_K}{F \times Vol_O} - 2i_{pump_N} - g_{eff\_K_{out}} \times ([K]_O - K_{out\_0}) \tag{4.3a}$$

$$\frac{d[Na]_O}{dt} = 3i_{pump_A} + \frac{I_{Na}}{F \times Vol_O} + 3i_{pump_N} - g_{eff\_Na_{out}} \times ([Na]_O - Na_{out\_0}) \tag{4.3b}$$

where I_{Kir} is the current from the Kir4.1 channels in the astrocyte membrane, i_{pump_A} and i_{pump_N} are the fluxes through the Na/K pump of the astrocyte and neuron membrane, respectively and I_K is the current from the neuronal voltage-gated potassium channels. The parameters Vol_O, Vol_A and Vol_N are the volumes of the extracellular, astrocytic and neuronal compartments respectively. We modelled all these currents using classical formulations available in the literature, as described in section 2.4.4. Parameter values and descriptions are given in table A.6.

The evolution of potassium and sodium concentration in the neuron ($[K]_N$ and $[Na]_N$, respectively), are given by:

$$\frac{d[K]_N}{dt} = \frac{I_K}{F \times Vol_N} - 2i_{pump_N} \times \frac{Vol_O}{Vol_N} - g_{eff\_K_N} \times ([K]_N - K_{N\_0}) \tag{4.4a}$$

$$\frac{d[Na]_N}{dt} = -\frac{I_{Na}}{F \times Vol_N} - 3i_{pump_N} \times \frac{Vol_O}{Vol_N} - g_{eff\_Na_N} \times ([Na]_N - Na_{N\_0}) \tag{4.4b}$$

and for the astrocyte ($[K]_A$ and $[Na]_A$, respectively), one gets:

$$\frac{d[K]_A}{dt} = -\frac{I_{Kir}}{F \times Vol_A} - \frac{I_{Kir_{vess}}}{F \times Vol_A} + 2i_{pump_A} \times \frac{Vol_O}{Vol_A} - g_{eff\_K_A} \times ([K]_A - K_{A\_0}) \tag{4.5a}$$

$$\frac{d[Na]_A}{dt} = -3i_{pump_A} \times \frac{Vol_O}{Vol_A} - g_{eff\_Na_A} \times ([Na]_A - Na_{A\_0}) \tag{4.5b}$$

Our model also accounts for the membrane voltage of the astrocyte and neuron compartment that we modelled using the classical Hodgkin-Huxley formalism, except that, to take into account the changes of potassium and sodium concentrations, we used Nernst potentials that vary according to the current concentrations of ions across the membrane (see section 2.4.4). For instance, the Nernst potential for potassium in the neuronal membrane was updated at each time step as $\frac{RT}{F} \times \ln(\frac{[K]_O(t)}{[K]_N(t)})$.

The membrane potential of the neuronal compartment was thus given by:

$$C_N \frac{dV_N}{dt} = -I_{Na} - I_K - I_{lN} + I_{app} \tag{4.6}$$

where I_{lN} is the leak current of the neuronal membrane and I_{app} is an injected current. Likewise, the membrane potential of the astrocyte compartment was modelled as

$$C_A \frac{dV_A}{dt} = -I_{Kir} - I_{Kir_{vess}} - I_{lA} \tag{4.7}$$

where we distinguished the Kir4.1 flux between the astrocyte and the extracellular compartment facing the neuronal soma, I_{Kir}, from that between the astrocyte endfeet and the blood vessel, $I_{Kirvessel}$.

We modelled all the currents in the above equations using classical formulations available in the literature. These formulations are described in detail in the following section. The model (eq 1-8) was solved numerically with an explicit Runge-Kutta Prince-Dormand 8th-9th order method with the GSL library in cython and python. Parameter values and descriptions are given in Table A.6. Initial conditions were set to the equilibrium value of each variable, as given in Table A.5.

Modelling neuronal activity

The dynamics of the neuronal membrane potential follow the classical Hodgkin Huxley (HH) equations (Abbott and Kepler, 1990) (Gerstner and Kistler, 2002):

$$I_{Na} = g_{Na} m^3 h \times (V_N - V_{Na_N}) \tag{4.8a}$$

$$I_K = g_K n^4 (V_N - V_{K_N}) \tag{4.8b}$$

$$\frac{dn}{dt} = -\alpha_n(V_N) \times (1 - n) - \beta_n(V_N) \times n \tag{4.8c}$$

$$\frac{dm}{dt} = -\alpha_m(V_N) \times (1 - m) - \beta_m(V_N) \times m \tag{4.8d}$$

$$\frac{dh}{dt} = -\alpha_h(V_N) \times (1 - h) - \beta_h(V_N) \times h \tag{4.8e}$$

with rate equations from the HH model (Abbott and Kepler, 1990)

$$\alpha_n(V) = 0.01\frac{V+55}{1-\exp(-\frac{V+55}{10})} \tag{4.9a}$$

$$\beta_n(V) = 0.125\exp(-\frac{V+65}{80}) \tag{4.9b}$$

$$\alpha_m(V) = 0.1\frac{V+40}{1-\exp(-\frac{V+40}{10})} \tag{4.9c}$$

$$\beta_m(V) = 4\exp(-\frac{V+65}{18}) \tag{4.9d}$$

$$\alpha_h(V) = 0.07\exp(-\frac{V+65}{20}) \tag{4.9e}$$

$$\beta_h(V) = \frac{1}{1+\exp(-\frac{V+35}{10})} \tag{4.9f}$$

V_{K_N} and V_{Na_N} are respectively the (time-dependent) K^+ and Na^+ Nernst potentials and are given by the Nernst equations:

$$V_{Na_N} = \frac{RT}{F}\ln\left(\frac{[Na]_O}{[Na]_N}\right) \tag{4.10a}$$

$$V_{K_N} = \frac{RT}{F}\ln\left(\frac{[K]_O}{[K]_N}\right) \tag{4.10b}$$

To complete the description of all the neuronal currents, we add a leak current:

$$I_{l_N} = g_{l_N}(V_N - V_{l_N}) \tag{4.11}$$

Modelling astrocytic activity

To take into account the K^+ dynamics in the astrocyte, we used the biophysical model of the Kir4.1 channel from (Sibille et al., 2015):

$$I_{Kir} = G_{Kir}\frac{\sqrt{[K]_O}}{1+\exp(\frac{V_A+V_{restA}-V_{K_A}+V_h}{V_s})}(V_A + V_{restA} - V_{K_A}) \tag{4.12}$$

I_{Kir} corresponds to the current through the astrocyte membrane facing the neural soma. We distinguish it from the Kir current between the astrocyte endfeet and the blood vessel:

$$I_{Kir_{vess}} = G_{Kir_{vess}}\frac{\sqrt{K_{vess}}}{1+\exp(\frac{V_A+V_{restA}-V_{K_{A\_vess}}+V_h}{V_s})} \times (V_A + V_{restA} - V_{K_{A\_vess}}) \tag{4.13}$$

where V_{K_A} and $V_{K_{A\_vess}}$ are respectively the K^+ and Na^+ equilibrium potentials and are given as above by:

$$V_{K_A} = \frac{RT}{F}ln\left(\frac{[K]_O}{[K]_A}\right) \tag{4.14a}$$

$$V_{K_{A\_vess}} = \frac{RT}{F}ln\left(\frac{[K]_{vess}}{[K]_A}\right) \tag{4.14b}$$

The astrocyte membrane potential equation also comprises a leak term:

$$I_{l_A} = g_{l_A}(V_A - V_{l_A}) \tag{4.15}$$

Na/K pump for the neuron and the astrocyte

The K^+ resting concentrations in neurons and astrocytes are maintained by Na/K pumps to counterbalance the outward K^+ and inward Na^+ fluxes (Sibille et al., 2015)

$$i_{pump_N} = i_{max_N} \times (1 + \frac{kmk}{[K]_O})^{-2} \times (1 + \frac{kna}{[Na]_N})^{-3} \tag{4.16a}$$

$$i_{pump_A} = i_{max_A} \times (1 + \frac{kmk}{[K]_O})^{-2} \times (1 + \frac{kna}{[Na]_A})^{-3} \tag{4.16b}$$

with the Na^+ equilibrium potentials given by the Nernst equation

$$V_{Na_A} = \frac{RT}{F} ln \left(\frac{[Na]_O}{[Na]_A} \right) \tag{4.17}$$

Parameter estimation of Kir current

Parameters values have been initially taken from Sibille et al. (2015), Abbott and Kepler (1990) and Gerstner and Kistler (2002). However they have all been adjusted manually to fit qualitative experimental results, see table A.5 and table A.6. Indeed, we did not have experimental data of all fluxes involved, such as the dynamics of potassium, sodium and calcium currents, neither in neuron nor astrocyte of the habenula. Hence, we keep values from previous models and modified them to reproduce experimental resting membrane potential in different conditions.

Nevertheless, Hu's team could record the Kir current while fixing the astrocytic voltage and the extracellular potassium concentration, so we could fit the equation 4.12 with the least square minimization algorithm, knowing V_A and I_{Kir}, at constant $[K]_O$ and fitting on the four parameters G_{Kir}, V_h, V_s and V_{rest_A} (Figure 4.35).

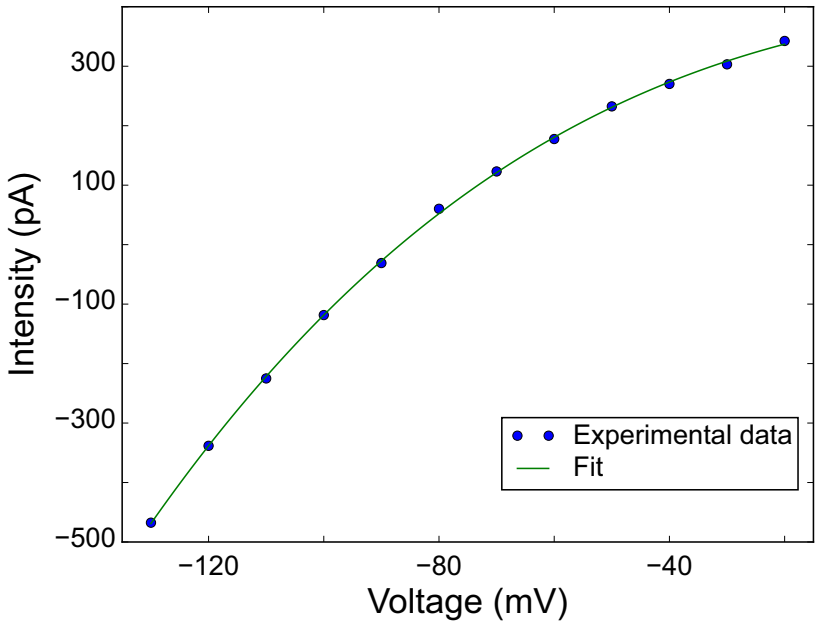

Figure 4.35: Experimental and fit data. Kir current measured in astrocytes by Hu's team and fitted with the equation of I_{Kir} with $G_{Kir} = 12nS$, $V_h = 178.46mV$, $V_s = 119.47mV$ and $V_{rest_A} = -10mV$.

4.2.2 Results: the impact of Kir channels on the neural resting membrane potential

The constantly released potassium from intrinsically active LHb neurons is quickly cleared by astrocytes through a Kir4.1-dependent mechanism, indeed, if we remove Kir4.1 currents, by setting its conductance to zero, we can see that when the neuron discharge, the extracellular potassium concentration increases twice higher (Figure 4.36). There is a clear action of the Kir4.1 to remove potassium from the extracellular compartment, because without it, the same neural activity releases much more K_{out}.

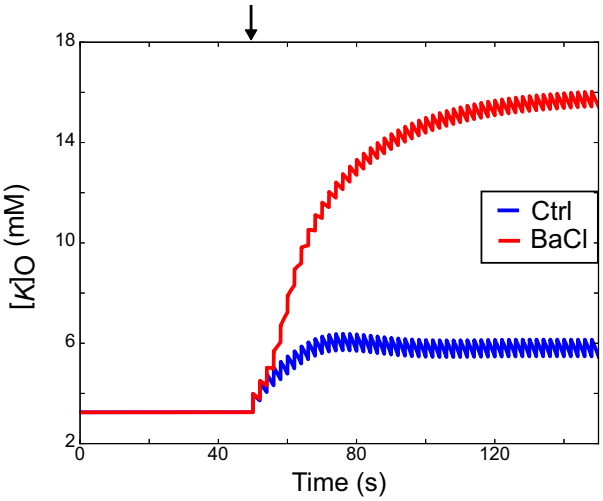

Figure 4.36: Comparison of two Kir4.1 conductances on extracellular potassium concentration when the neuron is firing. Ctrl: control condition with 1x G_{Kir} conductance; BaCl: G_{Kir} conductance set to zero. The vertical black arrow marks the beginning of neural stimulation at 0.5Hz.

In cLH condition, there are more Kir4.1 channels than in WT condition (Figure 4.29), hence we expect from our simulation a stronger clearance of extracellular potassium. Indeed, in our model, we could obtain this decrease of extracellular potassium concentration (K_{out}) when the neuron is firing, by multiplying the Kir current conductance by two (Figure 4.37a). When the neuron is not firing, the Kir current is positive, meaning that potassium ions leave the astrocyte, however, when the neuron fires and the extracellular potassium concentration increases, the Kir current is reversed, it becomes negative (Figure 4.37b) and potassium enters the astrocyte through Kir channels. Since the conductance is higher in depression condition, more potassium enters in cLH condition (Figure 4.37a).

Besides, during firing activity, both the neuron and the astrocyte are hyperpolarized when the model emulates depression condition (Figure 4.38) supporting the experimental results (Figure 4.30a, b). The neural RMP shifts from -47 mV to -53 mV in the model and from around -42 mV to -52 mV in the experimental data whereas the astrocytic RMP shifts from -69 mV to -74 mV in the model and from around -70 mV to -75 mV in the experimental data.

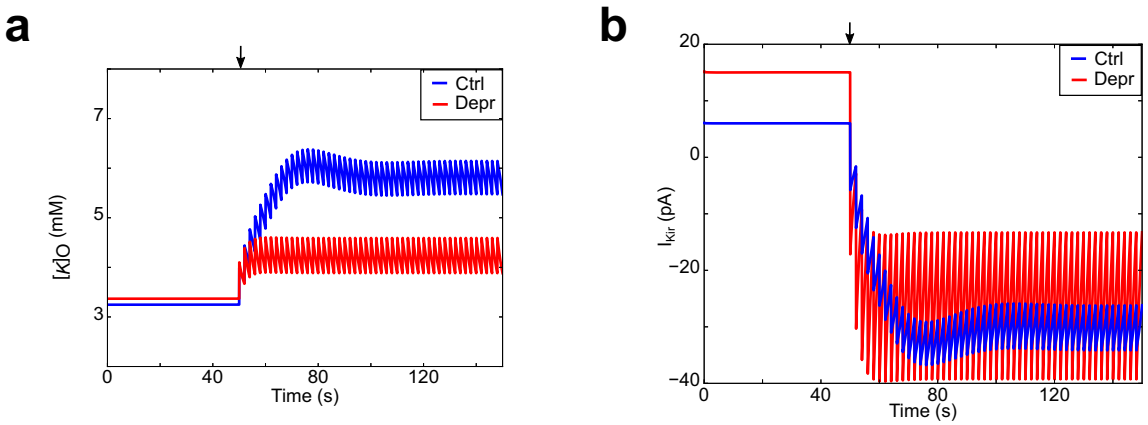

Figure 4.37: Comparison of two Kir4.1 conductances on extracellular potassium concentration (a) and Kir current (b) when the neuron is firing. Ctrl: control condition with 1x G_{Kir} conductance; Depr: depression condition with 2x G_{Kir} conductance. The vertical black arrow marks the beginning of neural stimulation at 0.5Hz.

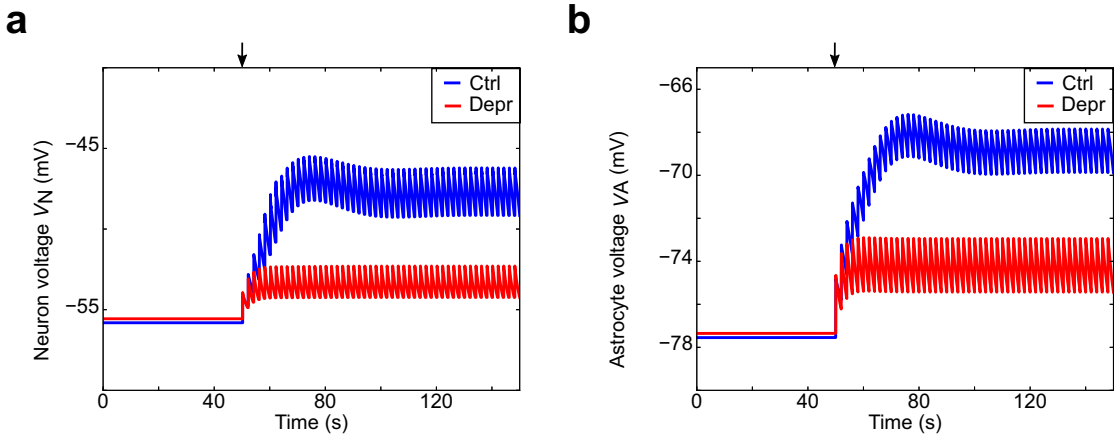

Figure 4.38: Comparison of two Kir4.1 conductances on neuronal membrane potential (a) and astrocytic membrane potential (b) when the neuron is firing. Ctrl: control condition with 1x G_{Kir} conductance; Depr: depression condition with 2x G_{Kir} conductance. The vertical black arrow marks the beginning of neural stimulation at 0.5Hz. Neuronal spikes are not shown for clarity of presentation.

In the experiments, the blockade of Kir4.1 channels by BaCl depolarizes neuronal RMPs (Figure 4.32a). Moreover, this blockage should compromise potassium spatial buffering, resulting in increased extracellular potassium (K_{out}), but this assumption is really difficult to test experimentally. However, we could test it in our model by reducing the conductance associated to Kir current to zero when the neuron was firing. As expected, blocking Kir4.1 channels (BaCl condition in figure 4.39b) increases K_{out} (from 6 mM to 16 mM, BaCl condition in figure 4.39a). Besides, it depolarizes both the neuron and the astrocyte (BaCl condition in figure 4.40a, b). The neural RMP depolarizes of around 20 mV in the model and it is around the same for both bursting and spiking neurons in experimental data.

On the contrary, blocking sodium channels with TTX in the neuron hyperpolarizes both the neuron and the astrocyte (Figure 4.32b) and should reduce extracellular potassium concentration.

In our model, TTX condition reduced by 4% the conductance of sodium channels and it is enough to decrease extracellular potassium concentration (from 6 mM to 5 mM, Figure 4.39a), correlated with a decrease of Kir current (from -30 pA to -20 pA, Figure 4.39b). Besides, as expected, it hyperpolarizes both the neuron and the astrocyte (TTX condition in figure 4.40a, b). The neural RMP hyperpolarizes of around 5 mV in the model and it is around the same for both bursting and spiking neurons in experimental data.

Thus, our study confirms that the increase of Kir4.1 diminishes K_{out} concentration and shows RMPs changes in the neuron and the astrocyte identical to experimental measures. However, it is still not clear how the decrease of K_{out} concentration hyperpolarizes the neuron and leads to switching from spiking neurons to bursting neurons. There is no explanation yet and it is difficult to tune a model since LHb neurons are not well electrophysiologicaly characterized.

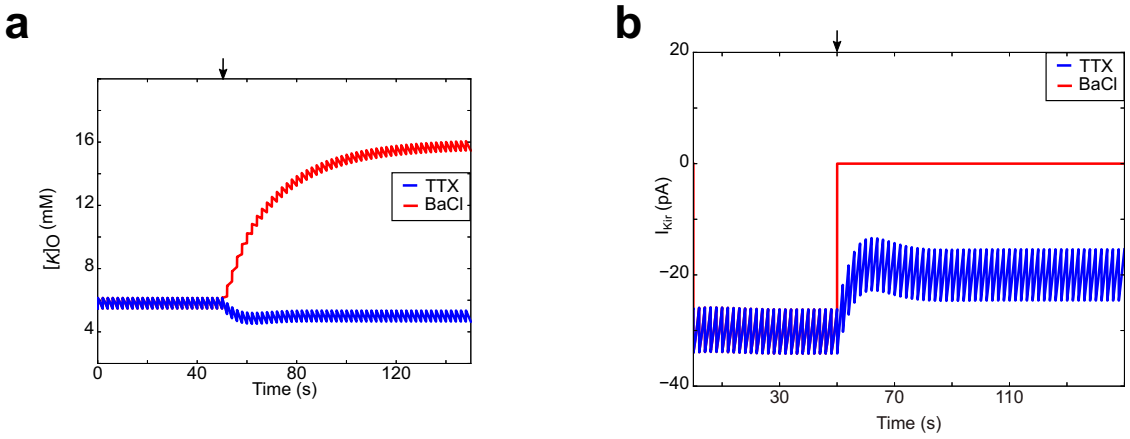

Figure 4.39: Comparison of TTX and $BaCl^2$applications in silico on extracellular potassium concentration (a) and Kir current (b) when the neuron is firing at 0.5 Hz. TTX application consists, here, in a reduction of 4% of neural sodium conductance whereas $BaCl^2$application sets Kir conductance to zero. The vertical black arrow marks the beginning of TTX or BaCl applications.

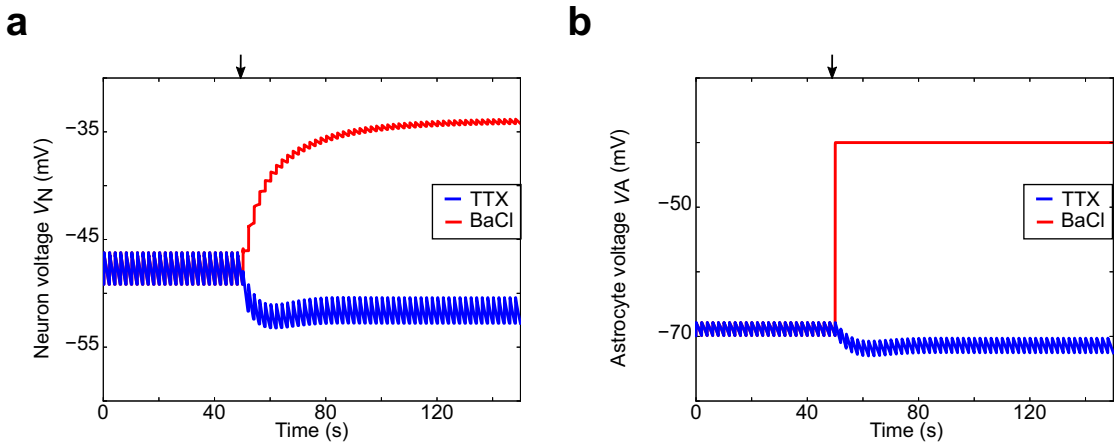

Figure 4.40: Comparison of TTX and $BaCl^2$applications in silico on neuronal membrane potential (a) and astrocytic membrane potential (b) when the neuron is firing at 0.5 Hz. TTX application consists, here, in a reduction of 4% of neural sodium conductance whereas $BaCl^2$application sets Kir conductance to zero. Neuronal spikes are not shown for clarity of presentation. The vertical black arrow marks the beginning of TTX or BaCl applications.

5. A computational model of STDP modulation by dopamine

Synaptic plasticity is the capacity of synapses to adjust their efficiency depending on synaptic events. It is a phenomenon at the basis of memory and learning (Martin et al., 2000), which relies on a complex molecular network. Spike-timing-dependent plasticity (STDP) is an experimental protocol way to explore it (see section 2.5.1). This project consisted in developing computational models to study the bidirectional interactions between dopamine and intracellular calcium dynamics in STDP. These models integrate several molecular signalisation pathways, such as endocannabinoids (eCB) and their interaction with dopamine. The goal is to predict, from STDP stimulation parameters, the orientation (LTP or LTD) and amplitude of the synaptic plasticity at the cortico-striatal synapse. Such a predictive function would let us study pathological conditions such as Parkinson's disease. Therefore, we were particularly interested in modelling striatal dopaminergic neurons.

Our approach was to combine two existing computational models, reproducing experimental known results on synaptic plasticity and its timing. One model was developed in our team and describes endocannabinoid-dependent and NMDAR-dependent STDP at the cortico-striatal synapse (Cui et al., 2016). The other one is developed by our colleagues in Blackwell's team, in George Mason University, Fairfax, VA, USA. It describes the effects of dopamine on the signaling pathways involved in synaptic plasticity.

The initial goal was to tune this model with new experimental results from Venance's team using a calcium analysing device. It is a microscope allowing to obtain calcium concentration imagery, in particular in the dendrites and the soma of MSN in slices. Unfortunately, it was a new device and its tuning needed more than two years, so we could not have access to these experimental results. However, we precalibrated the model to reproduce previous experimental results. The model is now ready for a proper calibration as soon as experiments of measures become available.

5.1 Computational models used in this project

5.1.1 A computational model of STDP at the corticostriatal synapse

The computational model of Cui et al. (2016) was developed to study the mechanisms of bidirectional eCB-dependent STDP at corticostriatal synapses. It allows to demonstrate that STDP outcome is controlled by eCB levels and dynamics. Prolonged and moderate levels of eCB lead to eCB-mediated long-term depression (eCB-tLTD) while short and large eCB transients produce eCB- mediated long-term potentiation (eCB-tLTP).

The calcium/calmodulin-dependent protein kinase II (CaMKII) plays a key role in the induction of tLTP modifications following calcium entry. It has been integrated in the Cui et al. (2016) model by using a detailed biochemical model of the CaMKII

autophosphorylation pathway and the protein signaling cascade governing the CaMKII dephosphorylation (Graupner and Brunel, 2007). This model presents two stable states of the CaMKII phosphorylation level at resting intracellular calcium concentration, and high calcium transients can switch the system from the weakly phosphorylated (down) state to the highly phosphorylated (up) state of the CaMKII (Figure 5.1). The change of post-synaptic weight is proportional to the phosphorylated CaMKII fraction. Transitions between those two states emulate transitions between no plasticity (down state) and tLTP (up state). The CaMKII phosphorylation is mainly due to calcium entrance by NMDAR and the activation of calmodulin, then CaMKII (Figure 5.1). Hence, it is a NMDAR-dependent tLTP occurring only for small post-pre pairings time intervals (around $\Delta t_{STDP} = -15$ ms) and for more than fifty pairings.

This model also features a pathway for the endocannabinoid signalisation, in which PLCβ gives DAG and then some 2AG which activates endocannabinoid receptor 1 (CB1R) (Figure 5.1).

On the one hand, the NMDAr to CaMKII pathway accounts for tLTP through calmodulin, PKA, CaN and PP1 (Figure 5.1). On the other hand, the eCB system accounts for tLTD and tLTP (eCB-STDP) through mGluR5, PLCβ, DAGL, MAGL, DAG-Kinase, calcium-induced calcium release (IP3R channels, SERCA pumps), IP3 dynamics (PLCd, PI3K), VSCC, TRPV1R and CB1R (Figure 5.1). Calcium-induced calcium release (CICR) takes into account the dynamics resulting from calcium exchange with internal calcium stores.

The mechanism proposed by this mathematical model to account for this eCB-STDP is the following: eCB-tLTD requires moderate levels of CB1R activation, which can be reached with pre-post pairings; eCB-tLTP demands higher levels of CB1R activation that are reached only with 5-30 post-pre pairings. Beyond 30 post-pre pairings, calcium efflux from the internal calcium stores decreases while in parallel CB1R desensitization increases. CB1R activation becomes insufficient to maintain the elevation of the synaptic weight, so that eCB-tLTP vanishes.

This model is non spatial, it contains around 30 ordinary differential equations (ODEs) and 185 parameters to express the cinetics of each signaling pathway actor with the law of mass action.

Hence, this mathematical model is able to predict the weight change when any of the STDP parameters is varied, that is, not only the spike timing, but also the number of pairings and the frequency. Nevertheless, this model does not involve the dopamine to explain these results and hence, does not make the link with the reward system of the basal ganglia.

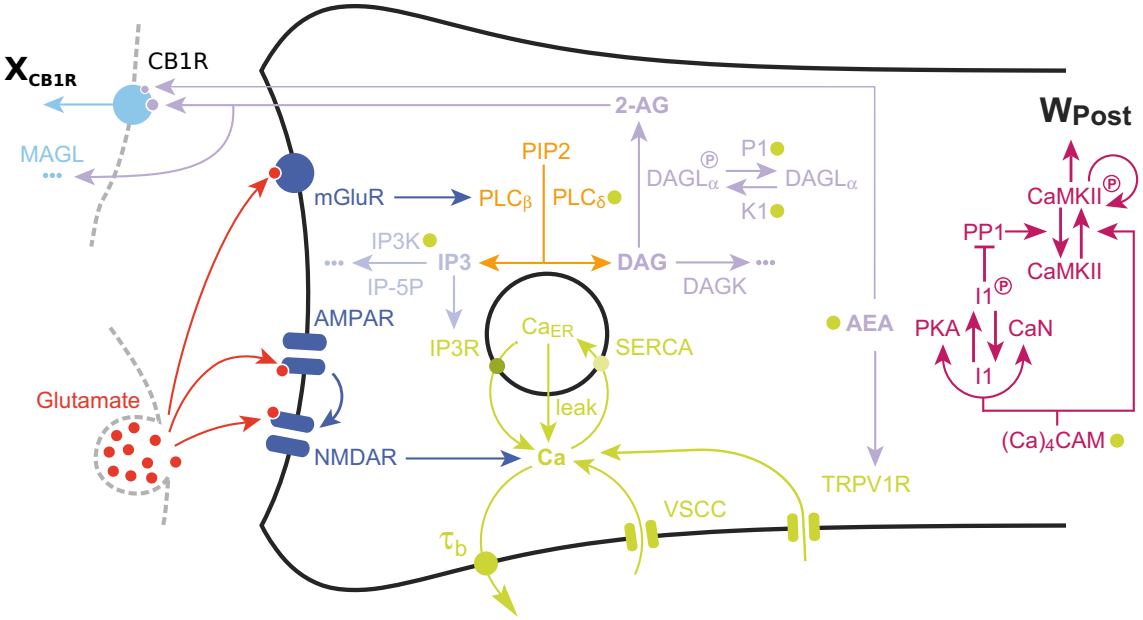

Figure 5.1: Scheme of the modelled signaling network of Cui et al. (2016). The NMDAR-based pathway sets Wpost as the phosphorylation state of postsynaptic CaMKII. In the second pathway, coincident activation of phospholipase Cβ by postsynaptic mGluR and calcium entry via VSCC and TRPV1 induces the production of 2-AG and AEA. 2-AG, and to a lower extent AEA, activates CB1R (xCB1R is the fraction of non-desensitized CB1R), which then modulates the presynaptic weight, Wpre. Color code: glutamate receptors: dark blue; PLC pathway: yellow; IP3 pathway: powderblue; calcium pathways: green (green disks indicate calcium-dependent steps); DAGLα pathway: lavender; AEA pathway: light blue; CB1R pathway: blue. Abbreviations: PIP2: phospatidylinositol 4,5-biphosphate; DAG: diacylglycerol; IP3: inositol-1,4,5-triphosphate; PLCβ/δ: phospholipase C β/δ; DAGK: diacylglycerol kinase; IP-5P: inositol polyphosphate 5-phosphatase; IP3K: IP3-kinase; DAGLa: diacylglycerol lipase α;B/BCa: free/bound endogenous calcium buffer; IP3R: IP3-receptor channel; SERCA: sarcoplasmic/endoplasmic reticulum calcium ATPase; CaER: calcium in the endoplasmic reticulum; (Ca)4CaM: fully bound calmodulin; CaN: calcineurin aka PP2B; PKA: protein kinase A; I1p/I1: phosphorylated/unphosphorylated protein phosphatase 1 inhibitor 1 (equivalent to dopamine- and cAMP-regulated neuronal phosphoprotein (DARPP-32) in striatal output neurons); PP1:protein phosphatase 1; pCaMKII/CaMKII: phosphorylated/unphosphorylated CaMKII; DAGK: diacylglycerol kinase; MAGL: monoacylglycerol lipase; the '...' sign indicates transformation into products that are considered not to interfere with the other interactions of the model.

5.1.2 Computational model on synpatic plasticity including dopaminergic pathway

The computational model of Blackwell's team represents a synthesis of the models presented by Oliveira et al. (2012) and the model presented by Kim et al. (2013) (Figure 5.2). It is a spatial approach using the neuroRD software available on github, hence, it is not constituted of ODEs but rather on the terms of the spatial Gillespie algorithm.

On neuroRD, Oliveira et al. (2012) set up a large scale stochastic reaction-diffusion model (spatial) of the signaling pathways in a medium spiny projection neuron dendrite with spines, based on published biochemical measurements. The model was stimulated with dopamine pulses mimicking those recorded in response to reward. In the model, dopamine leads to the production of cAMP and activation of protein kinase A (PKA),

which are involved in striatal synaptic plasticity and learning. Simulations show that PKA leads to phosphorylation of DARPP-32 on Thr34, a molecule mediating the interaction of several pathways.

Furthermore, in striatal medium spiny neurons (MSNs), both long term potentiation (LTP) and long term depression (LTD) require an elevation in intracellular calcium concentration. On neuroRD, Kim et al. (2013) implemented a spatial stochastic model of the post-synaptic signaling pathways in a dendrite with one or more diffusionally coupled spines and validated it by comparison to experiments. The model used Gq coupled pathways to investigate several calcium temporal pattern showing that patterns producing LTP activate more protein kinase C (PKC) than patterns producing LTD. Hence, all these signaling pathways complement the model of Oliveira et al. (2012).

Blackwell's model accounts for the fact that dopamine- and cAMP-regulated neuronal phosphoprotein (DARPP-32) sees its Thr34 phosphorylation increased in the presence of simultaneous dopamine and calcium transients (Lindskog et al., 2006). Hence, the model involves dopamine D1R coupled pathways, with the activation of Gs subtype of GTP binding protein, leading to cAMP, PKA and Epac (Figure 5.2). Also, it involves calcium activated pathways, leading to PP2B and metabotropic glutamate mGluR1/5 coupled pathways, with the activation of Gq subtype of GTP binding protein, leading to PLC and DAG (Figure 5.2). Besides, this model accounts for the effect of glutamate receptors (NMDAR and mGluR), muscarinic acetylcholine receptors (M1R, Gq coupled) and (M4R, Gi coupled) and dopamine receptors (D1R).

Thus, this spatial computational model simulates the signaling pathways underlying striatal LTP and LTD, in particular, the dopamine pathway, allowing to explore rewards processes. However, this model accounts for frequency-dependent plasticity, not STDP (t-LTP and t-LTD).

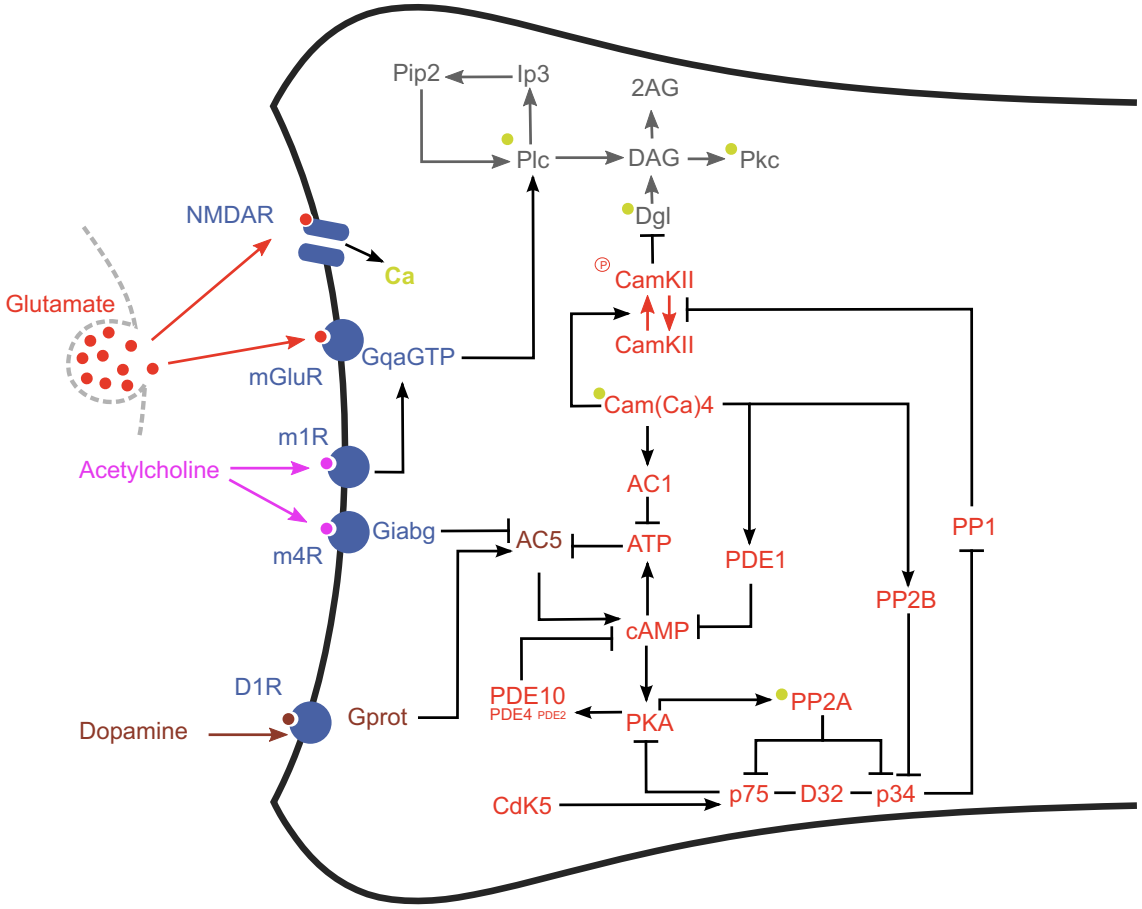

Figure 5.2: Scheme of the modelled signaling network of Blackwell's team. Color code: receptors: dark blue; PLC and IP3 pathways: gray; calcium pathways: green (green disks indicate calcium-dependent steps. Abbreviations: PKc: protein kinase C; PDE: phosphodiesterase; PP2A: protein phosphatase 2A; PP2B: protein phosphatase 2B or calcineurine; CdK5: Cyclin-dependent kinase 5; D32p34: DARPP32 phosphorylated at Thr34; D32p75: DARPP32 phosphorylated at Thr75; see figure 5.1 for other abbreviations.

5.1.3 Computational model of STDP synaptic plasticity including the NMDAR, the endocannabinoid system and the D1 dopaminergic pathway

In order to gather properties and results of these previous models, mainly the NMDAR and theendocannabinoid system of Cui et al. (2016) and the dopaminergic system of Blackwell's team, we set up a computational model of ordinary differential equations (Figure 5.3). We started from the Cui et al. (2016) model and we modified it with the one of Blackwell's team. Hence, we kept the eCB system, the calcium dynamic with CICR and equations accounting for CaMKII (Cui et al., 2016) then, we added dopamine and acetylcholine inputs and the signaling pathways associated to PKA, PKC, DARPP-32 and PP2B pathways from Blackwell's model. With the law of mass action, we translated the reaction of the Blackwell's model in ODEs.

Furthermore, we had to make some modelisation choices and adjust some parameter values to keep a global coherence in the model. For example, for the production of DAG and IP3 catalysed by PLCβ, we replaced the Blackwell's model by the equations of the model of Cui et al. (2016). Besides, to keep the Michaelis-Menten approximation used by Graupner and Brunel (2007) to describe dephosphorylation of CaMKII, the PP1 enzyme concentration must be present in small amounts compared to the substrate, the CaMKII

phosphorylated subunits. The whole model is described in appendix, all equations and reactions in table A.1, parameters description in table A.1.4 and initial conditions description in table A.1.5.

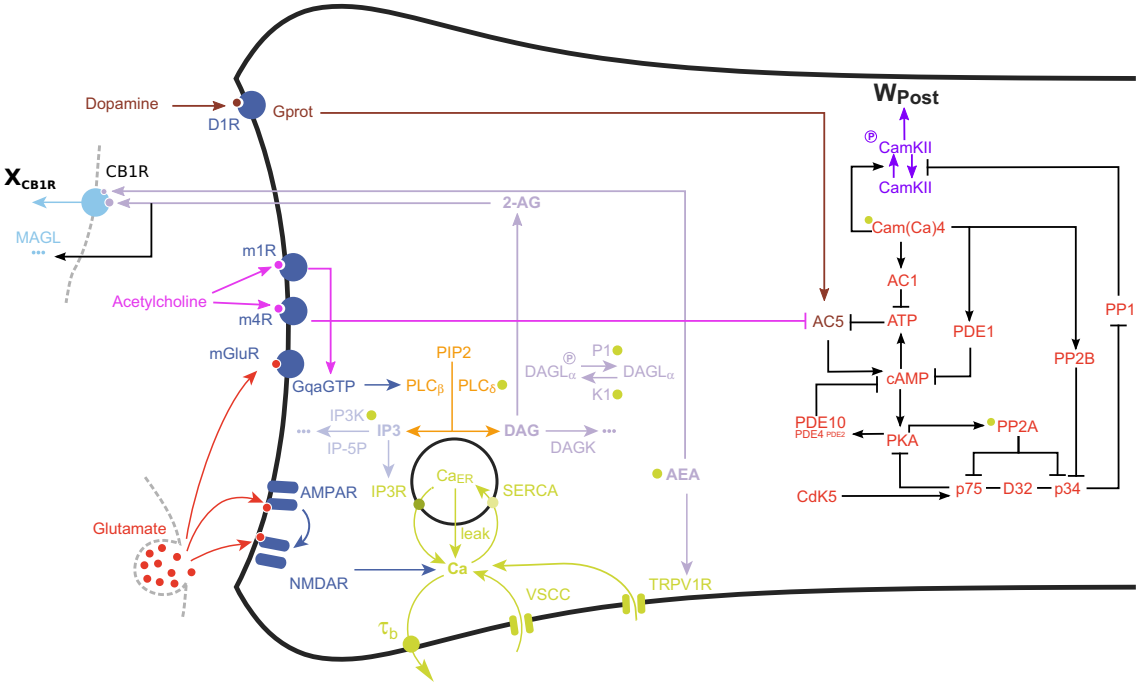

Figure 5.3: Scheme of our modelled signaling network. This scheme is equivalent to the scheme 5.1 except that we added dopaminergic and muscarinergic receptors and we replaced the pink network of CaMKII by the red one from scheme 5.2. Colors and abbreviations are the same as in figures 5.1 and 5.2.

Our system was quite large with around 170 ODEs and 550 parameters. Numerical resolution used an explicit embedded Runge-Kutta Prince-Dormand (8, 9) method, meaning that it uses a Taylor's development at the eighth and the ninth degrees and depending on the equation stiffness, the timestep size is adapted. By default, we used a timestep of 1 ms but its size depends on the relative and absolute error values acting as thresholds. Indeed, if between two points there is a high discontinuity, the absolute and error values are high and the algorithm has to reduce the timestep to pass the threshold condition.

We chose GSL libraries with cython, an interface between C and python, to have efficiency and access to several numerical algorithms. We also tested the explicit embedded Runge-Kutta-Fehlberg (4, 5) method and found similar results.

Several definition of plasticity in computational models

In all these computational models, one difficulty is to define when the system presents t-LTD, t-LTP or no plasticity. In their model, Cui et al. (2016) chose to use the bistable property of CaMKII, between a down state where CaMKII is inactive and an up state where CaMKII is highly activated. Indeed, a system of equation can present several equilibrium states, meaning that for the same set of parameters and variable values, one variable can reach different stable steady-states, for example, for the same calcium concentration the concentration of phosphorylated sub-units of CaMKII could either be high or low, both states being stable. Transitions between those two states therefore emulate transitions between no plasticity (down state) and NMDAR-tLTP (up state) (Cui et al., 2016).

In the same idea, we studied this kind of property in a simplified version of our system of equations, with around 20 ODEs. We used bifurcation diagram with XPPAUTO software or PyDSTool and PyCont, a version developed for python.

Although these analyses were very instructive to get a global picture of the dynamics of our system and to tune the model parameters in order to keep this bistable property in a realistic range for t-LTD and t-LTP, they were computationnally quite heavy.

Hence, we used another way to study our system bistability, over a variable of interest, is to find a cycle of hysteresis. First, the system has to present two stable states at different values of the variable of interest. Then, starting from one stable state, the variable of interest has to evolve slowly until it reaches the value of the second stable state. If the system stayed in the first stable state whereas the variable of interest has the same value as in the second stable state, then, the system is bistable. This method avoids a lot of calculation such as in the bifurcation process, because it needs only to let the system converge twice (one for each stable state) and simulate the transition from one to the other by changing slowly the value of the variable of interest.

For example, in the simplified version of our model, there were two stable states (Up and Down). Starting from the Down state, then increasing calcium concentration and slowly diminishing it until it reaches the one of the Down state again shows that the system stays in the Up state. Therefore, the system is bistable since for the same value of calcium there are two stable states Up and Down (Figure 5.4).

Nevertheless, although this method was quite efficient, when we complexified our model with 170 ODEs, we lost this bistability property of CaMKII. Hence, in order to characterize t-LTD and t-LTP, we used threshold values on the concentration of phosphorylated CaMKII sub-units, as in Blackwell's model.

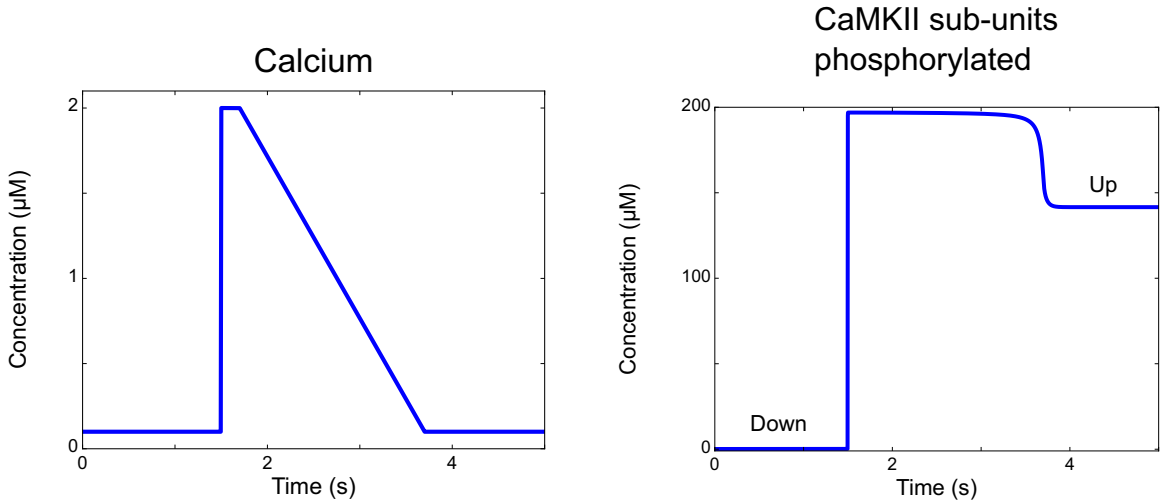

Figure 5.4: Calcium concentration pre-defined trace to navigate through the hysteresis cycle, with a slow descent from 1.75 to 3.75 seconds (Left panel) Corresponding evolution of the concentration of phosphorylated units of CaMKII in a simplified version of the model, alternating between Up and Down stable states (Right panel).

5.2 Results

First, with the eCB system in our model, we could reproduce eCB-tLTP and eCB-tLTD, for $\Delta t_{STDP} = -15$ ms and $\Delta t_{STDP} = 15$ ms, respectively, by adjusting thresholds of LTD and LTP areas.

Hence, we assume as in Cui et al. (2016), that eCB-tLTD requires moderate levels of CB1R activation, which can be reached with 40-50 pre-post pairings ($\Delta t_{STDP} = 15$ ms),

at 1 Hz, whereas eCB-tLTP demands higher levels of CB1R activation that are reached only with 5-30 post-pre pairings ($\Delta t_{STDP} = -15$ ms), at 1 Hz (Figure 5.5). Thus, we obtained a eCB-tLTP for 5-30 post-pre pairings and a eCB-tLTD for more than 50 pre-post pairings, as in experiments.

These results were independent of the presence or not of dopamine on the post-synaptic neuron. Dopamine has rather an effect on the concentration of phosphorylated CaMKII sub-units, and hence, on NMDA-LTP. Comparing post-pre spiking ($\Delta t_{STDP} = -15$ ms) with or without tonic dopamine, we can observe on figure 5.6 that in presence of dopamine we could obtain NMDA-tLTP (in blue) when the phosphorylated CaMKII sub-units concentration passes the threshold (95 μM), after around 50 stimulations. Besides, as expected experimentally (Pawlak and Kerr, 2008)(Shen et al., 2008), without DA, the NMDA-tLTP disappeared. This result is important because it shows the rewarding effect of DA on STDP, meaning that without DA, NMDA-LTP is not expressed. Hence, our model reproduces the emergence of NMDAr-LTP for more than 50 post-pre pairings.

However, with $\Delta t_{STDP} = 15$ ms and with dopamine, we can still observe some NMDA-LTP (not shown). This is not observed in experimental data and we still have to tune our model to prevent this behaviour.

In conclusion, we successfully merged the models of Cui et al. (2016) and Blackwell's team and we could reproduce one of the main results of plasticity with the eCB system and the addition of dopamine. However, we need to tune it more precisely with new experiments by continuing our collaboration with L. Venance's team. Thus, by experimentally validating our results we could have a predictive function of synaptic plasticity for MSN neurons and explore how its different actors are involved, for example, in the reward system or in Parkinson's disease.

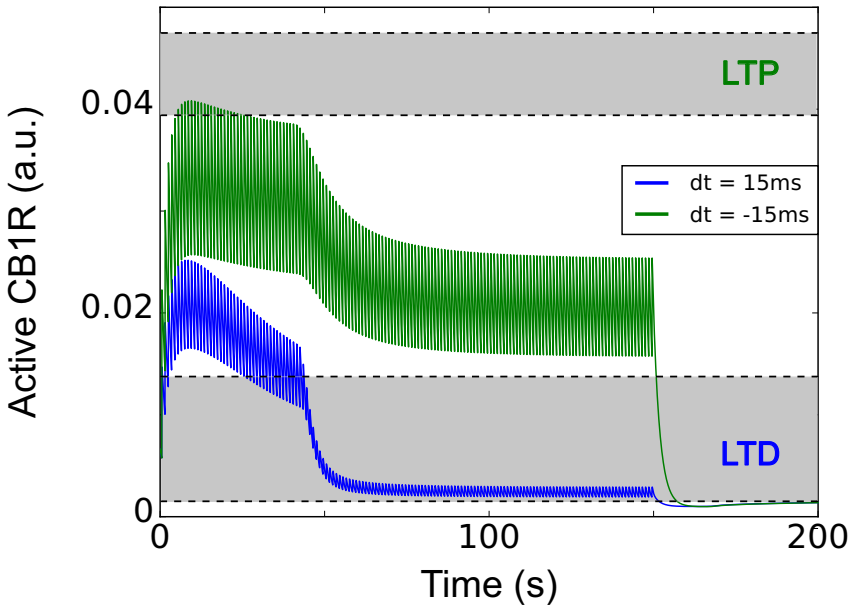

Figure 5.5: Simulation of active CB1R over time with 150 pairings at 1 Hz. The amplitude of active CB1R peaks first increases for the first 10-20 pairings, then decreases to converge to roughly constant amplitude. But active CB1R reaches large values (> 0.04, the LTP zone) only for short post-pre pairings (5-20 pairings with $\Delta t_{STDP} = -15$ ms), in green. On the contrary, with $\Delta t_{STDP} = 15$ ms, in blue, active CB1R does not reach the LTP area and stay in the LTD area from around 50 pairings. LTP and LTD areas were defined to obtain these results with LTD area in $[10^{-3}, 0.013]$ and LTP area in $[0.040, 0.048]$.

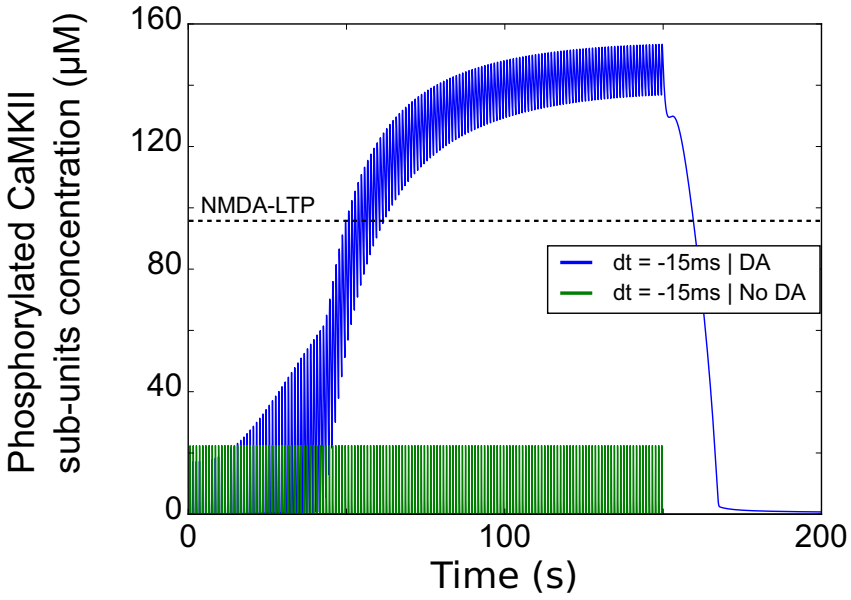

Figure 5.6: Simulation of the concentration of phosphorylated CaMKII sub-units over time with 150 pairings at 1 Hz ($\Delta t_{STDP} = -15$ ms) and injected tonic dopamine from 0 to 150 seconds. Dopamine allows this concentration to reach a threshold inducing NMDA-LTP from around 50 pairings.

6. Discussion & Perspectives

6.1 Parkinson's disease

The experimental voltage recordings of SNr neurons that we worked on were very noisy and heterogeneous. Our experimentalist collaborators had to check each series manually to remove stimulation artefacts and to set the proper spike detection threshold. After aggregating the spike series, we convolved them to get a smoother activity of discharge with a square function of 1 ms width. We dit not use Gaussian functions because they were either too strong or too weak to aggregate spikes, so we could not observe any pattern. We chose this width value because it is around the duration of a spike and it seemed to be a good compromise between precision and smoothness. However, it could be interesting to evaluate how much the categorization of our fits change depending on this value and of the choice of our function. We could add an interpolation step after our convolution step to better smooth the result, by making sure that we do not diminish the timestep of the resulting series to avoid efficiency and memory issues.

To fit these experimental recordings of the basal ganglia output nucleus (SNr) after cortical stimulation, we proposed a simple neural network model, with only the three main pathways between the cortex and the SNr (Figure 3.2). This firing-rate model follows the basic anatomical and neurochemical connections described by the so-called Rate Model (see section 2.1.4), although we added the hyperdirect pathway. In terms of structure, our model is close to the firing-rate model of Leblois et al. (2006), that studies oscillations in the basal ganglia but in terms of scientific questions, our model is rather aligned with the mean-field-based model of van Albada and Robinson (2009) that explores the impact of each pathway on basal ganglia output in several physiological and pathological conditions, including as PD (see section 2.1.4).

In our model, the network of the basal ganglia was simplified to explain the experiment with the least possible connections and parameters, such as in Leblois et al. (2006). For example, the feedback loop between the STN and the GPe has been removed as well as the one between the thalamus and the cortex. In both cases, this simplification has been made because the influence of these connections is hypothesized to occur later than the whole dynamics of interest following the stimulation. In a variant of the model, we added the GPe-STN loop to test whether our procedure was able to detect abnormal oscillations in the Parkinsonian condition (Degos et al., 2005). However, it resulted in poor fitting scores because the model generated regular oscillations whereas the data were too noisy to observe regular patterns. To study these oscillations, instead of recording only the SNr, it could be interesting to add simultaneous recordings of the GPe, the STN, or both, at the same time, and fit our model on all these recordings. Indeed, since we used all nuclei in our model, we already have access to their activity and we can easily extend our fitting procedure.

In addition, it could be interesting to model a spiking SNr neuron with a voltage membrane, instead of a firing rate model, to compare its activity directly to raw data and to study more biological relevant parameters (e.g. current conductances or equilibrium

potentials). Although we had no access to experimental parameters on each current involved in the SNr neuron, we could set a Hodgkin-Huxley like model (see part 2.3.2) for the SNr neuron. An Izhikevich model (see part 2.3.3) would have been easier to set up but its parameters are far from having a clear biological meaning. Considering our experimental data, our approach seemed simple and efficient enough but a deeper analysis of SNr neurons would provide the opportunity to fit them more realistically and maybe discriminate better each condition.

Furthermore, the rectifying transfer function (see equation 3.1b), that we used to transform the neural input into firing rate, only sets negative values to zero in order to avoid negative firing rates. We could use as alternative a sinusoidal (non-linear) transfer function, that is arguably closer to the function of a biological neuron (Kandel et al., 2013). However we expect that the parameters of each connection (e.g. weight) would be less constrained because the sinusoidal function has a closed output space, i.e. beyond a threshold, weight differences will yield the same result. Hence, the description of each experimental recording would be less specific and harder to categorize, even if it is more potentially realistic. Therefore, the choice of the transfer function can have a huge impact on our fitting procedure and it would be interesting to study how far it can influence our categorization results.

To categorize our cells, we did not consider clustering techniques directly on time series data because we wanted to compare control and Parkinsonian conditions based on parameters with a biological meaning (e.g. weight or delay of connections). However, we could have used an appropriate similarity metric between time series, and it would be interesting to compare the result of different clustering approaches, such as k-means or hierarchical clustering, with the results of our fits categorization (Liao, 2005).

Instead, we set up a set of rules. Although we already compared two slightly different set of rules and obtained similar categorization results (not shown), we could have done an analysis, for example, of the evolution of the results where threshold values change, such as the time window range or the minimal phase amplitude. Again, the aggregated spike series are very noisy and heterogeneous and the model was necessary to distinguish clear excitatory and inhibitory phases from smoothed data. A bigger set of rules alone would probably give the same result by taking each case into account, however, we needed a model to characterize each connection of the basal ganglia neural network. Without a model, we could only have characterized each phase by their duration and amplitude, and not take into account possible overlaps between phases (e.g. the hyperdirect excitatory phase can be interrupted by the direct inhibitory phase).

Furthermore, we noticed that, in the fits, variations of one parameter (e.g. the weight) could be partially compensated by the variation of another (e.g. the delay), thus diminishing differences between conditions. This means that all parameters are not all identifiable. We counterbalanced this effect by setting constant values for some parameters. However, the heterogeneity of the dataset makes it difficult to fit over the majority of recordings while minimizing this compensation between parameters. Besides, interpreting the variation of one parameter between two conditions seems less accurate than the variation of whole pathways. Hence, we used transition matrix to associate a score to each pathway. We tried less complex combinations of parameters, such as simply summing weights by pathways or multiplying them, but this was not statistically significative on our synthetic dataset and less pertinent.

As an alternative procedure, we also explored a Bayesian approach called Dynamic Causal Modelling (DCM) (Kiebel et al., 2008). The aim of DCM is to infer the causal architecture of dynamic systems. It is a Bayesian model comparison procedure that rests on comparing models of how data was generated. DCM has been applied to study Parkinson's disease (Moran et al., 2011)(Marreiros et al., 2013). Nevertheless, our experiment

records only one node in the whole network and, in this case, DCM is not directly applicable to our knowledge. Theoretically it seemed possible but these tools still need to be developed.

Finally, we used non-parametric statistical tests to compare parameters and pathway scores between control and Parkinsonian conditions or triphasic and biphasic conditions but we also tested several generalized linear models. However, the analysis of residual shows that the necessary conditions to use them were not fulfilled (e.g. residuals were not normally distributed). Besides, we tested principal component analysis (PCA) to find a linear combination of parameters to maximize the variance of the dataset but the best resulting factors of discrimination did not correspond to the control and Parkinsonian conditions or something biologically relevant.

According to figure 2.5, in Parkinsonian conditions, we expected a decrease of both the hyperdirect and the direct phases whereas the indirect pathway would increase, but we found no significative differences on these pathways. Our statistical power is reduced by the data noise, the low number of recordings and the diversity of responses (triphasic, biphasic and monophasic) giving even smaller populations to test. However, generalized linear mixed-effect models (GLMM) show that there was a signicatively smaller proportion of triphasic response in Parkinsonian condition than in control.

These results bring new ways to explore and understand this disease and suggests that in 6OHDA condition, the response of a lot of SNr cells is not affected (or not much affected). However, a portion of SNr cells seem to lose the hyperdirect pathway. Even if the biological interpretation is not clear yet, it suggests that the hyperdirect pathway has a major role in PD. Our next step is to test if treatments, such as L-DOPA (see section 2.1.3), can restore this proportion back to control proportion. For example, by treating 6OHDA rats with L-DOPA and compare the proportion of triphasic responses with SHAM and 6OHDA rats.

6.2 Major depressive disorder

To our knowledge, our model is the first time computational neural network model for the inhibitory effect of the LHb on the VTA dopaminergic neuron. However, our model was very simple and could be complexified to be more realistic. For example, we did not distinguish between GABAergic regions, RMTg and VTA GABAergic neurons, we only considered that the LHb directly inhibits the DA neuron with effective $GABA_A$ inputs. There is no available model of RMTg neuron nor of VTA GABAergic neuron. However neurons have been physiologically characterized by Matsui and Williams (2011) and Tan et al. (2012) respectively. It would be interesting to obtain the activity for these neurons and include them in our model. This would allow to study how spiking and bursting from the habenula can modulate the VTA output.

Moreover, the way we represented $GABA_A$ concentration is also quite simple, since we replaced each LHb spike by a square impulse of 1 mM $GABA_A$ with 1 ms duration. This simplicity is compensated by the expression of GABA current $I_{GABA_{A_{V_2}}}$ (see equation 4.1.1), which involves an exponential decrease after each spike given by the equation of r_{op}, the fraction of the receptors in the open state (see equation 4.1.1). Contrary to a square impulse, this decrease leaves a trace allowing overlapping spikes to build up. Hence, although we already studied the impact of the maximal GABA conductance on the DA neuron firing activity(Figure 4.23), it would be interesting to study, in addition, the change of α_{GABA_A} and β_{GABA_A} (see equation 4.1.1), the voltage-independent forward and backward rate constants, respectively to observe how the shape of inhibitory current impacts the DA neuron response.

Furthermore, to compare the effect of control and depressive conditions on our DA neuron model, we reproduced spike patterns of each LHb neuron type, following experimental proportions found by Hu's team. To choose the probability law describing each LHb firing mode, we had only one sample of each pattern type at disposal. After fitting them, when we followed experimental proportions in each condition, we were not able to reproduce the experimental ISI histograms (Figures 4.2). Hence, if these fits were enough to get the shape of firing, however, they were not representative of the heterogeneity of frequency we could observe with the histograms widths. Therefore, we add another Gaussian law on probability law parameters to introduce variability and obtain simulation histograms comparable to experimental ones. Nevertheless, it could be worth trying to reproduce our histograms with less variability or with other probability laws, to measure how robust they are and how the DA neuron activity depends on it.

In particular, an important limitation of our model is its "bursting mode". Indeed, Lobb et al. (2011) modified the model of Kuznetsov et al. (2006) to specifically tune it for VTA DA neuron, our region of interest. However, in their DA neuron model, the bursting mode is only a frequency elevation made by an increased NMDA current, i.e. it is rather a fast spiking mode and not really a bursting mode. To get a more realistic firing pattern dynamics, we could use an Izhikevich model, this is less specific to VTA DA neurons but could still be a way to test the robustness of our results.

Finally, as expected, the model supported experimental results, showing that more bursting pattern inhibits more the DA neuron. To distinguish if bursting pattern is more efficient because of higher frequency of spikes or if the bursting pattern is more efficient in itself we plotted the mean frequency of DA neuron over the one of each LHb neuron type, at equal frequency of LHb neurons types. This suggested that the spiking pattern is slightly more efficient than the bursting pattern at a given spike frequency, at most with 0.1 Hz difference, therefore, our model prediction is that it is the increase of spike firing in cLH that generates more inhibition on the VTA, rather than the emergence of the bursting pattern itself. However, to check experimentally this prediction, Hu's team carried out additional experiments that turned out to support the opposite idea, i.e. that the bursting pattern is far more efficient even at equal frequency. First they expressed eNpHR3.0 (a yellow light-gated chloride channel) to induce bursting mode or Ochief (a blue light-gate nonspecific cation channels) to induce regular spiking on the LHb cell (Figure 6.1a). They found that 1 Hz yellow light photostimulation caused depressive-like phenotypes in the FST (Figure 6.1b). To prove that it is the bursting firing mode but not the general increase in firing rate that is important for the induction of depressive-like behaviours, they applied 5 Hz blue light photostimulation that yields the same overall firing rate as that generated by the 1 Hz stimulation of eNpHR neurons (around 5 spikes per burst, Figure 6.1c) and this did not cause depressive-like phenotypes (Figure 6.1d).

Thus, our model permitted to point to this question on bursting pattern and to explore the limits of our assumptions with new experiments. The next step will be to understand how bursting patterns inhibits DA neuron better, starting to find how the GABA current acts on the DA neuron discharge and, then, to extend the model to a network of DA neurons to study how LHb could inhibit dopaminergic VTA activity.

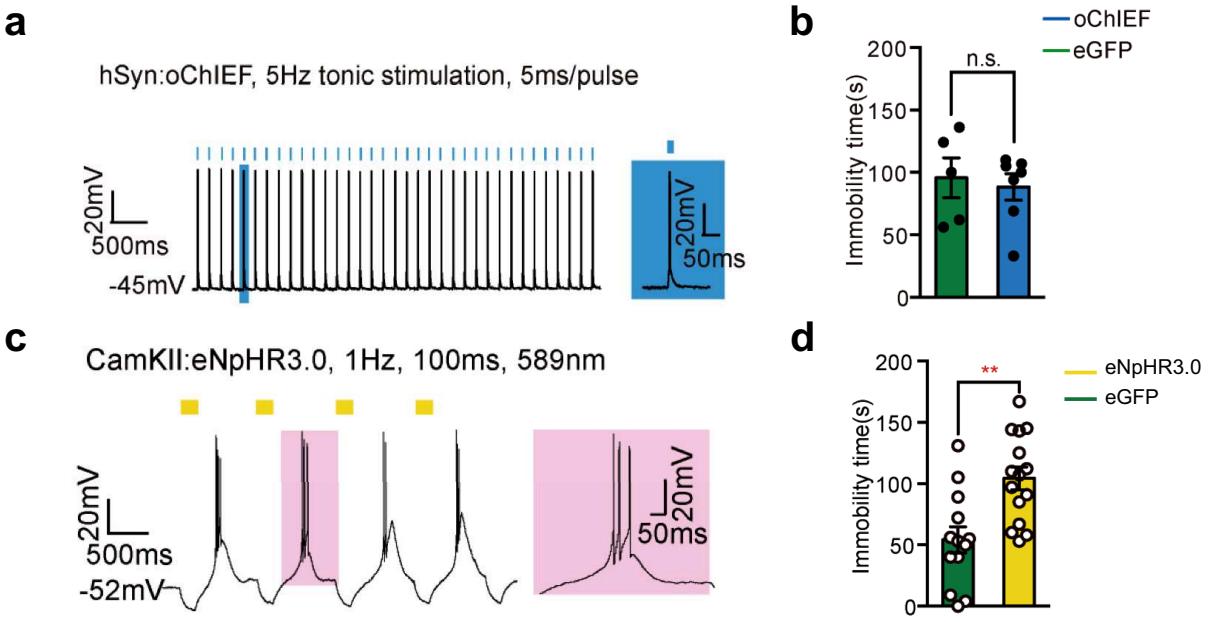

Figure 6.1: Representative traces showing rebound bursts reliably elicited by pulse photostimulation of eNpHR3.0 in slice recordings (c); eNpHR3.0-driven bursts induced depressive-like behaviours, including increased immobility in forced swim test (d); Representative trace of 5 Hz photostimulation of oChIEF evoked spikes in slice recordings (a); 5 Hz photostimulation of oChIEF failed to induce depressive phenotypes (b).

Our tripartite model, is to our knowledge, the first computational model of a habenula neuron. It links potassium dynamic with astrocytic Kir4.1 channels to explore major depressive disorder. We started with the computational model of Sibille et al. (2015), that explored the dynamics of potassium in a hippocampal tripartite synapse with Kir channels. However the parameters presented in the paper were not always coherent with associated figures. Therefore, we checked each current with the computational models of Somjen et al. (2008) also studying potassium dynamic with Kir channels and of Cressman et al. (2009) which explores potassium and sodium dynamic with a glial uptake. Moreover, we tuned our parameters directly from the experimental results of Hu's team.

We modelled a neuron with a RMP around -55 mV at rest and around -47 mV when firing while receiving an injected current. This RMP range is closer to the RMP of the tonic firing LHb neurons than the bursting ones. However, we can see on figure 4.34 that the variability range of the measured RMP can reach 20 mV, so that the RMP ranges of bursting and spiking neurons overlap. Thus, we tuned our model around these intermediate values of RMPs but it would be interesting to test its robustness by exploring the space of parameters allowing to obtain same qualitative results.

Furthermore, to account for the effect of $BaCl_2$ we set to zero the conductance associated to Kir current whereas the effect of TTX was modelized by reducing sodium conductance by 4%. Both these values were set with groping since no experiments have precisely characterized these effects in LHb neurons. Even if the high correlation between parameters would complicate it, it would be worth conducting a sensitivity analysis of our model to explore its robustness.

Hodgkin-Huxley like models have been designed for constant potassium and sodium equilibrium potentials and they are very sensitive to their variations. When the neuron fires, potassium exits the neuron whereas sodium enters. If these two fluxes are stronger than the Na/K-pump, the system will reach unrealistic values. To counterbalance these leaks we used simple buffering terms on potassium and sodium in neural and astrocytic compartments.

Nevertheless, the next step would be to develop a model with dynamic potassium and sodium and which can switch between LHb firing patterns. To do so, we would need to continue our work with Hu's team to acquire more experimental data on LHb neurons, such as the list of all fluxes involved, the dynamic of potassium, sodium and calcium currents. Indeed, up to now, only the Kir equation could be fitted from experimental data, the rest of the model has been adjusted manually to fit qualitatively experimental results, such as neural depolarization or hyperpolarization.

Finally, our model supported the hypothesis that an increase of astrocytic Kir channel decreases the extracellular potassium concentration in the synaptic cleft, hyperpolarising the RMPs of both the neuron and the astrocyte. This neural hyperpolarization would lead to a switch of firing pattern from spiking to bursting. Therefore, the global picture that emerges from these studies is that the overexpression of Kir4.1 in the astrocytes would be the main origin of the decrease of extracellular potassium, triggering hyperpolarization of the LHb neurons and a switch to their bursting mode. This bursting mode would then increase the inhibition of the LHb on the DA cells of the VTA, thus triggering a decrease of dopamine and the depression symptoms. The major remaining issue is how the hyperpolarization of the LHb neurons switches from spiking to bursting pattern. But this will again require a thorough investigation of the electrophysiological properties of these neurons.

6.3 Synaptic plasticity

In our project on synaptic plasticity, the initial goal was to create a computational model accounting for both dopamine and endocannabinoid signaling in corticostriatal STDP, based on the experimental results obtained by Venance's team with calcium imaging. We successfully mixed two previous models, in the same computational model, to gather their properties, reproducing experimental results such as NMDAR-LTP, eCB-LTP and eCB-LTD, including interactions with dopamine. However, the experimental part of the project has experienced technical issues and the calcium imaging set up was available in 2018, i.e. at the end of my thesis. Hence, we could not fit the model properly, but by pursuing our collaboration with Venance's team, we plan to study the phasic dopamine timing and reproduce experiments where DA is activated after STDP protocols (Brzosko et al., 2015) (Yagishita et al., 2014). This step would reconciliate spike-timing-dependent plasticity occurring at the scale of milliseconds and dopamine traces lasting several seconds, supporting the hypothesis that rewards and punishments act on memory through dopamine.

In the absence of bistability, thresholding some variables, such as yCB1R and the phosphorylated sub-units of CaMKII, seemed to be the easiest criteria to define if there was plasticity or not. One limit in our results is that the proportion of phosphorylated CaMKII units is as high for pre-post than post-pre pairing protocols whereas it should be low for pre-post pairing. Calibrating the model to these results should be possible with new experiments results from calcium imaging during STDP protocols where NMDAR-tLTP is not observed.

Finally, we obtained a model with more than 170 ODEs and more than 550 parameters, the last step would be to simplify it enough to have fewer than 10 equations and use them in a large neural network to observe what could emerge in a network embedded with such realistic learning rules.

6.4 Conclusion

In the field of neuroscience, as in many scientific fields, the amount and the complexity of data acquired increases. This makes computational power and models necessary to analyse them. Indeed, processing the information is now organised around automatic pre-treatment, computational modelling and statistics.

In this thesis, through three distinct projects, we showed how computational modelling could support neuroscientific experiments.

In our project on Parkinson's disease, modelling allowed us to classify semi-automatically and more objectively, the response of substantia nigra pars reticulata neurons, and hence, to compare several conditions with statistical tests. Thanks to this approach, we could detect that the SNr of Parkinsonian rats presented significatively less triphasic responses than in control condition, suggesting a new way to detect and to explore Parkinson's disease.

About our project on major depressive disorder, we developed two models. The first model was designed to question if neuron from the habenula of depressed animal models inhibits more the VTA dopaminergic neuron because of their bursting pattern or because of their higher firing frequency. Since experiments tend to show that the observed effect is attributable to the bursting pattern itself (even at constant firing rate), it opens new questions on how bursting patterns operate. Moreover, our second model supported the idea that the increase of astrocytic Kir4.1 channel is responsible for the neuronal hyperpolarization of these neurons linking Kir4.1 with the shift toward bursting pattern inducing habenula hyperactivity and depressive symptoms. These results may inspire the development of novel treatments of major depression targeting on maladaptive neuron-glia interactions in the LHb.

Our model on synaptic plasticity successfully unificated several experimental results of spike-timing-dependent plasticity. Although it still needs to be calibrated, it is ready to account for the future two-photons laser calcium imaging experiments of Venance's team to understand how dopamine signal can act on STDP.

A. Appendix

Variable	Value	Description
$idel_{GABA}$	2000.0	ms - Start of GABA current
$idur_{GABA}$	8000.0	ms - Duration of GABA current
g_{L1}	0.05 — 0.095	$mS.cm^{-2}$ - Leak conductance
E_{L1}	-50.0	mV - Reversal potential for leak current
buf_1	0.05	Cytosolic buffering constant - Kuz .ode
$g_{bar_{KCa_1}}$	0.3	potassium-calcium conductance - Kuz .ode
k_1	250.0 — 750.0	potassium-calcium constant
r_1	10.0	μmeter - Radius of somatic compartment
r_2	0.5	μmeter - Radius of dendritic compartment
t_{C1}	4.0	calcium pump constant - Kuz .ode
$g_{bar_{Ca_1}}$	0.15	calcium conductance - Kuz .ode
$g_{bar_{K2}}$	4.0 — 10.0	$mS.cm^{-2}$ - Delayed rectifier potassium conductance
$g_{bar_{K1}}$	0.4 — 0.0	$mS.cm^{-2}$ - Potassium channel conductance
vHk	-10.0	mV - Half activation voltage for potassium channel K1
vSk	7.0	No unit - Slope factor for potassium channel K1
i_1	0.0	$\mu A.cm^{-2}$ - applied current (as a current density)
gc	0.3 — 0.25	$mS.cm^{-2}$ - Intercompartment coupling conductance
E_{Na}	55.0	mV - Reversal potential for sodium
E_{Ca}	100.0	mV - Reversal potential for calcium
E_K	-90.0	mV - Reversal potential for potassium
H	0.019298	lumped terms involving valence of Ca and Faraday's number
tk	1.0	n-related factor - Kuz .ode
$g_{bar_{NMDA}}$	0.0	nS - Conductance of input of NMDA
$g_{bar_{NMDAc}}$	0.0 — 0.28	nS - Constant conductance of NMDA
Mg	0.5	mM - Extracellular magnesium concentration
me	0.08	NMDA conductance factor - Kuz .ode
E_{NMDA}	0.0	mV - Reversal potential for NMDA current
nd	10.0	Nb identic synchronous dendritic compartments attached to soma
$g_{bar_{Na_1}}$	150.0	$mS.cm^{-2}$ - sodium conductance
th	0.05	h-related factor - Kuz .ode

g_{AMPA}	0.0	$mS.cm^{-2}$ - AMPA conductance
E_{AMPA}	0.0	mV - Reversal potential for AMPA current
tsc	1.0	calcium-related constant - Kuz .ode
$g_{GABA_{A_{max}}}$	0.01 — 0.14	$mS.cm^{-2}$ - Max conductance GABA - (Lobb et al., 2011)
E_{GABA_A}	-80.0 — -60.0	mV - Reversal potential for GABA A current - (Destexhe et al., 1998)

Table A.3: Parameters of LHb to DA neuron model.

Parameter	Value	Description
Simulation		
t_{start}	0.0	ms - Time of starting simulation
t_{end}	5000.	ms - Time of ending simulation
timestep	0.1	ms - Time step of simulation
Constant		
Ftemp	9.64e1	kC.mol-1 - Faraday constant
R	8.314	J.mol-1.K-1 - Gaz constant
T	308.0	Kelvin - Temperature
Neuron		
g_{Na}	120.	nS - Neuronal sodium channel conductance
g_K	20.	nS - Neuronal potassium channel conductance
RTF	RT/Ftemp	mV - Approximation of the constants
g_{lN}	0.5	nS - Neuronal leak conductance
V_{lN}	-50.	mV - Neuronal leak potential
C_N	30.	pF - Neuronal membrane capacitance
Astrocyte		
G_{Kir}	12.	nS - Astrocytic single channel Kir conductance in extracellular side
g_{lA}	0.1	nS - Max conductance
V_{rest_A}	-10.	mV - Astrocytic resting membrane potential
V_h	178.46	mV - Half activation potential of Kir canals
V_s	119.47	mV - activation rate constant of Kir canals
C_A	1.	pF - Astrocytic capacitance
V_lA	-40.	mV - Astrocytic leaking potential
Pump		
kmk	3.0	mM - K activity (in pumps)
kna	10.	mM - Na activity (in pumps)
$imax_A$	0.12	mM.ms-1 - Astrocytic Na/K pump rate
$imax_N$	0.12	mM.ms-1 - Neuronal Na/K pump rate
F	96,500.0	C.mol-1 - Faraday constant
Volume		
Vol_O	0.01	pL - Extracellular volume
Vol_N	1.08	pL - Neuronal volume
Vol_A	1.08	pL - Astrocytic volume
ACSF		
K_{out_0}	3.5	mM - Extracellular potassium concentration of the effective flux

Na_{out_0}	144.	mM - Extracellular sodium concentration of the effective flux
$g_{eff_{K_{out_0}}}$	0.001	ms-1 - Rate of potassium effective flux in the extracellular space
$g_{eff_{Na_{out_0}}}$	0.01	ms-1 - Rate of sodium effective flux in the extracellular space
Effective fluxes		
$g_{eff_{K_N}}$	0.0001	ms-1 - Rate of potassium effective flux in the neuron
$g_{eff_{Na_N}}$	0.0001	ms-1 - Rate of sodium effective flux in the neuron
K_{N_0}	135.	mM - Neuronal potassium concentration of the effective flux
Na_{N_0}	12.0	mM - Neuronal sodium concentration of the effective flux
$g_{eff_{K_A}}$	0.1	ms-1 - Rate of potassium effective flux in the astrocyte
$g_{eff_{Na_A}}$	0.01	ms-1 - Rate of sodium effective flux in the astrocyte
K_{A_0}	135.	mM - Astrocytic potassium concentration of the effective flux
Na_{A_0}	7.0	mM - Astrocytic sodium concentration of the effective flux
Blood vessel		
$G_{\mathrm{Kir_{vess}}}$	12.5	nS - Astrocytic single channel Kir conductance in vessels side
K_{vess}	3.5	mM - Constant potassium concentration in the vessel
Input		
$\mathrm{freq_{stim}}$	10.	Hz - Frequency of stimulation
$I_{N_{\mathrm{inj_{spike}}}}$	5000.0	pA - Current applied to the neuron
$t_{\mathrm{stim_{start_{spike}}}}$	t_{start}	ms - Time starting stimulation
$t_{\mathrm{stim_{end_{spike}}}}$	t_{end}	ms - Time ending stimulation
$t_{\mathrm{stim\_on\_spike}}$	0	ms - Time starting spike
$t_{\mathrm{stim\_off\_spike}}$	0.1	ms - Time ending spike

Table A.6: Parameters of the tripartite synapse model with Kir channels.

A.1 Computational model of STDP

A.1.1 ODE

IP3, DAG, ECb

$$\frac{dIp3}{dt} = vip3prod - v3k - r5p_{IP3} \times Ip3$$

$$\frac{dDag}{dt} = vip3prod - rDGL \times DAGLP \times \frac{Dag}{Dag + KDGL} - kDAGK \times Dag - f66 \times PkcCa \times Dag + f\_66 \times PkcCaDag$$

Variable	Value	Description
t_{start}	0.0	ms - Start of the simulation
t_{end}	10,000.0	ms - End of the simulation
$t_{to\ steady\ state}$	50.0	msec - Time system to reach stability
$init_{step}$	0.01	ms - Initial step-size of the algorithm
max_{step}	10.0	ms - Maximal step-size
rtol	1e-13	Relative error tolerance
atol	1e-10	Absolute error tolerance
$P_{silent\ cell}$	0.57	Proportion of silent cell in control condition
$P_{burst\ regular\ cell}$	0.035	Proportion of burst regular cell in control condition
$P_{spike\ regular\ cell}$	0.18	Proportion of spike regular cell in control condition
$P_{burst\ irregular\ cell}$	0.035	Proportion of burst irregular cells in control condition
$P_{spike\ irregular\ cell}$	0.18	Proportion of spike irregular cells in control condition
tot neurons	50	Total number of neurons of LHb
up lim rand unif process	1000.0	ms - Upper time limit of first spike of a serie
durations spikes	1.0	ms
threshold spike	1.0	amplitude

Table A.1: Simulation parameters

Variable	Value	Description
$r_{op}(0)$	0.5	opened receptor fraction
Somatic		
$V_1(0)$	-54.4	mV - voltage
$u_1(0)$	91.6	calcium concentration
$n_1(0)$	0.17	activation variable for the delayed rectifier
$h_1(0)$	0.13	sodium inactivation variable
Dendritic		
$V_2(0)$	-60.0	mV - voltage
$u_2(0)$	149.0	μM - calcium concentration
$n_2(0)$	0.0025	activation variable for the delayed rectifier
$h_2(0)$	1.0	sodium inactivation variable

Table A.2: Initial conditions of LHb to DA neuron model.

Name	Value	Source
$t_{delay}^{MSN_{D1}-SNr}$	7ms	Connelly et al. (2010)
$t_{delay}^{GPe-SNr}$	3ms	Nakanishi et al. (1991)
$t_{delay}^{STN-SNr}$	4.5ms	Shen and Johnson (2006)Ammari et al. (2010)
$t_{delay}^{MSN_{D2}-GPe}$	7ms	Park et al. (1982)
$t_{delay}^{STN-GPe}$	5ms	Ammari et al. (2010)
$t_{delay}^{GPe-GPe}$	5ms	n.d.
$t_{delay}^{Ctx-STN}$	2.5ms	Fujimoto and Kita (1993)
$t_{delay}^{GPe-STN}$	5ms	Baufreton et al. (2005)

Table A.4: Connection delays values in the basal ganglia from Lindahl et al. (2013).

Variable	Value	Description
Neuron		
$n(0)$	0.34	[0, 1] - Quantity associated with potassium channel activation
$m(0)$	0.06	[0, 1] - Quantity associated with sodium channel activation
$h(0)$	0.55	[0, 1] - Quantity associated with sodium channel inactivation
$V_N(0)$	-63.76	mV - Neuronal membrane potential
$[K]_N(0)$	135.04	mM - Neuronal potassium concentration
$[Na]_N(0)$	11.16	mM - Neuronal sodium concentration
Astrocyte		
$V_A(0)$	-87.08	mV - Astrocyte membrane potential
$[K]_A(0)$	135.00	mM - Astrocytic potassium concentration
$[Na]_A(0)$	7.00	mM - Astrocytic sodium concentration
Extracellular		
$[K]_{out}(0)$	3.34	mM - Extracellular potassium concentration
$[Na]_{out}(0)$	145.95	mM - Extracellular sodium concentration

Table A.5: Initial conditions of the tripartite synapse model with Kir channels.

$$\frac{dtwo_{ag}}{dt} = rDGL \times DAGLP \times \frac{Dag}{Dag + KDGL} - kMAGL \times two_{ag}$$
$$\frac{do_{CB1R}}{dt} = Alpha_{CB1R} \times (two_{ag} + alphaAEACB1 \times AEA) \times c_{CB1R} - (Beta_{CB1R} + Gamma_{CB1R}) \times o_{CB1R}$$
$$\frac{dd_{CB1R}}{dt} = -Epsilon_{CB1R} \times d_{CB1R} + Gamma_{CB1R} \times o_{CB1R}$$

CaMKII sub-units

$$\frac{dB1}{dt} = 6 \times k6gamma2 \times B0 - 4 \times k6gamma2 \times B1 - k7gamma \times B1 - k10 \times B1 + 2 \times k10 \times (B2 + B3 + B4)$$
$$\frac{dB2}{dt} = k7gamma \times B1 + k6gamma2 \times B1 - 3 \times k6gamma2 \times B2 - k7gamma \times B2 - 2 \times k10 \times B2 + k10 \times (2 \times B5 + B6 + B7)$$
$$\frac{dB3}{dt} = 2 \times k6gamma2 \times B1 - 2 \times k7gamma \times B3 - 2 \times k6gamma2 \times B3 - 2 \times k10 \times B3 + k10 \times (B5 + B6 + B7 + 3 \times B8)$$
$$\frac{dB4}{dt} = k6gamma2 \times B1 - 2 \times k7gamma \times B4 - 2 \times k6gamma2 \times B4 - 2 \times k10 \times B4 + k10 \times (B6 + B7)$$
$$\frac{dB5}{dt} = k7gamma \times B2 + k7gamma \times B3 + k6gamma2 \times B2 - k7gamma \times B5 - 2 \times k6gamma2 \times B5 - 3 \times k10 \times B5 + k10 \times (2 \times B9 + B10)$$
$$\frac{dB6}{dt} = k6gamma2 \times B2 + k6gamma2 \times B3 + 2 \times k7gamma \times B4 - k6gamma2 \times B6 - 2 \times k7gamma \times B6 - 3 \times k10 \times B6 + k10 \times (B9 + B10 + 2 \times B11)$$
$$\frac{dB7}{dt} = k6gamma2 \times B2 + k7gamma \times B3 + 2 \times k6gamma2 \times B4 - k6gamma2 \times B7 - 2 \times k7gamma \times B7 - 3 \times k10 \times B7 + k10 \times (B9 + B10 + 2 \times B11)$$
$$\frac{dB8}{dt} = k6gamma2 \times B3 - 3 \times k7gamma \times B8 - 3 \times k10 \times B8 + k10 \times B10$$

$$\frac{dB9}{dt} = k7gamma \times B5 + k6gamma2 \times B5 + k7gamma \times B6 + k7gamma \times B7 - k6gamma2 \times B9 - k7gamma \times B9 - 4 \times k10 \times B9 + 2 \times k10 \times B12$$
$$\frac{dB10}{dt} = k6gamma2 \times B5 + k6gamma2 \times B6 + k7gamma \times B7 + 3 \times k7gamma \times B8 - 2 \times k7gamma \times B10 - 4 \times k10 \times B10 + 2 \times k10 \times B12$$
$$\frac{dB11}{dt} = k7gamma \times B6 + k6gamma2 \times B7 - 2 \times k7gamma \times B11 - 4 \times k10 \times B11 + k10 \times B12$$
$$\frac{dB12}{dt} = k7gamma \times B9 + k6gamma2 \times B9 + 2 \times k7gamma \times B10 + 2 \times k7gamma \times B11 - k7gamma \times B12 - 5 \times k10 \times B12 + 6 \times k10 \times B13$$
$$\frac{dB13}{dt} = k7gamma \times B12 - 6 \times k10 \times B13$$

Voltage-Dependent Calcium Channel L-type (1.3)

$$\frac{dh_{caL13}}{dt} = \frac{(Interpolation\_func[hinf_{caL13_{tab}}, n_{x_{caL13}}, \frac{V - xst_{caL13}}{xstep_{caL13}} - h_{caL13}]}{\frac{htau_{caL13}}{hqfact_{caL13}}}$$
$$\frac{dm_{caL13}}{dt} = \frac{Interpolation\_func[minf_{caL13_{tab}}, n_{x_{caL13}}, \frac{V - xst_{caL13}}{xstep_{caL13}} - m_{caL13}]}{\frac{Interpolation\_func[mtau_{caL13_{tab}}, n_{x_{caL13}}, \frac{V - xst_{caL13}}{xstep_{caL13}}]}{qfact_{caL13}}}$$

AMPA and NMDA

$$\frac{do_{AMPA}}{dt} = Alpha_{AMPA} \times Glu \times c_{AMPA} - (Beta_{AMPA} + Gamma_{AMPA}) \times o_{AMPA}$$
$$\frac{dd_{AMPA}}{dt} = -Epsilon_{AMPA} \times d_{AMPA} + Gamma_{AMPA} \times o_{AMPA}$$
$$\frac{do_{NMDA}}{dt} = Alpha_{NMDA} \times Glu \times (1 - o_{NMDA}) - Beta_{NMDA} \times o_{NMDA}$$

CICR

$$\frac{dh_{CICR}}{dt} = (a2_{CICR} \times d2_{CICR} \times \frac{Ip3 + d1_{CICR}}{Ip3 + d3_{CICR}}) \times (1 - h_{CICR}) - a2_{CICR} \times Ca_{cyt} \times h_{CICR}$$
$$\frac{dCa_{cyt}}{dt} = \frac{J_{tot} - (Ca_{cyt} - Cab)}{tauCab} - f152 \times Ca_{cyt} \times pmca + f\_152 \times pmcaCa - f79 \times Ca_{cyt} \times ncx + f\_79 \times ncxCa + f12 \times CaOutLeak - f99 \times Ca_{cyt} \times Calbin + f\_99 \times CalbinC - f69 \times Cam \times Ca_{cyt}^2 + f\_69 \times CamCa2C - f83 \times CamCa2C \times Ca_{cyt}^2 + f\_83 \times CamCa4 - f90 \times Cam \times Ca_{cyt}^2 + f\_90 \times CamCa2N - f82 \times CamCa2N \times Ca_{cyt}^2 + f\_82 \times CamCa4 - f77 \times Ca_{cyt} \times Pkc + f\_77 \times PkcCa - f129 \times PP2BCam \times Ca_{cyt}^2 + f\_129 \times PP2BCamCa2C - f94 \times PP2BCam \times Ca_{cyt}^2 + f\_94 \times PP2BCamCa2N - f65 \times PP2BCamCa2C \times Ca_{cyt}^2 + f\_65 \times PP2BCamCa4 - f146 \times PP2BCamCa2N \times Ca_{cyt}^2 + f\_146 \times PP2BCamCa4 - f111 \times PP2ABPR72 \times Ca_{cyt} + f\_111 \times PP2Acal)/tauCa(Ca_{cyt}, BT_{CaBuff}, KdB_{CaBuff})$$
$$\frac{dCa_{ER}}{dt} = -J_{CaER} \times rhoER_{CICR}/tauCa(Ca_{ER}, BT_{CaBuff}, KdB_{CaBuff})$$

DAG, ECb

$$\begin{aligned}\frac{dDAGLP}{dt} &= rK_{DAGLP} \times (alpha_{DAGLP_{Ca_{cyt}}} \times Ca_{cyt})^n K_{DAGLP} \\ &\quad \times (1 - DAGLP) - rP_{DAGLP} \times DAGLP \\ \frac{dAEA}{dt} &= vATAEA \times Ca_{cyt} - \frac{vFAAH \times AEA}{KFAAH + AEA} \\ \frac{dfpre}{dt} &= \frac{omega - fpre}{taufpre}\end{aligned}$$

PP1

$$\begin{aligned}\frac{dPP1}{dt} = &-f139 \times D32p34 \times PP1 + f\_139 \times D32p34PP1 + f18 \\ &\times D32p34PP1PP2BCamCa4 + f7 \times D32p34PP1PP2ABPR72 \\ &+ f34 \times D32p34PP1PP2AB56d - f58 \times pAKAR3 \times PP1 + f\_58 \\ &\times PP1pAKAR3 + f11 \times PP1pAKAR3 - f137 \times OA \times PP1 + f\_137 \times OA_{PP1}\end{aligned}$$

Voltage

$$\frac{dV}{dt} = \frac{Itotal}{Cm}$$

A.1.2 Auxiliary equations

CaMKII

$$\begin{aligned}occ_{r_{CaMKII}} &= B1 + B2 + B3 + B4 + B5 + B6 + B7 + B8 + B9 + B10 + B11 + B12 + B13 \\ B0 &= 2 \times CaMKT - occ_{r_{CaMKII}} \\ phos_{sum} &= B1 + 2 \times (B2 + B3 + B4) + 3 \times (B5 + B6 + B7 + B8) \\ &\quad + 4 \times (B9 + B10 + B11) + 5 \times B12 + 6 \times B13 \\ k10 &= k12 \times \frac{PP1}{KM + phos_{sum}} \\ gamma &= \frac{CamCa4}{K5 + CamCa4} \\ gamma2 &= gamma \times gamma \\ k6gamma2 &= k6 \times gamma2 \\ k7gamma &= k7 \times gamma\end{aligned}$$

AMPA and NMDA

$$\begin{aligned}c_{AMPA} &= 1 - o_{AMPA} - d_{AMPA} \\ G_{NMDA} &= o_{NMDA} \times Interpolation\_func[B_{NMDA_{tab}}, int(n_{x_{NMDA}}), \frac{V - xst_{NMDA}}{xstep_{NMDA}}] \\ I_{NMDA} &= gNMDA \times V \times G_{NMDA}\end{aligned}$$

Endocannabinoids

$$
\begin{aligned}
ctrl1 &= kCB1R \times o_{CB1R} + gamma1DA \times Da \\
ctrl2 &= kCB1R \times o_{CB1R} + gamma2DA \times Da \\
taufpre &= \frac{P1_{ECb}}{P2_{ECb}^{P3_{ECb}} + ctrl2^{P3_{ECb}}} + P4_{ECb} \\
c_{CB1R} &= 1 - o_{CB1R} - d_{CB1R}
\end{aligned}
$$

IP3, DAG, ECb

$$
\begin{aligned}
minf &= \frac{Ip3}{Ip3 + d1_{CICR}} \\
ninf &= \frac{Ca_{cyt}}{Ca_{cyt} + d5_{CICR}} \\
J_{IP3R} &= rc_{CICR} \times (minf \times ninf \times h_{CICR})^3 \times (Ca_{ER} - Ca_{cyt}) \\
J_{serca} &= ver_{CICR} \times hill_{func}(Ca_{cyt}, ker_{CICR}, 2) \\
J_{leak} &= rl_{CICR} \times (Ca_{ER} - Ca_{cyt}) \\
J_{CaER} &= J_{IP3R} - J_{serca} + J_{leak} \\
J_{Ca_{ch}} &= -VDCC \times I_{caL13} - NMDA \times I_{NMDA} - TRPV1 \times I_{TRPV1} \\
J_{tot} &= J_{CaER} + J_{Ca_{ch}} \\
Hill1 &= \frac{Ca_{cyt}}{Ca_{cyt} + kpi_{IP3}} \\
vglu &= vbeta_{IP3} \times \frac{Glu}{Glu + (kr_{IP3} \times (1 + \frac{kp_{IP3}}{kr_{IP3}} \times Hill1))} \\
vplcg &= \frac{vdelta_{IP3}}{1 + \frac{Ip3}{kappad_{IP3}}} \times hill_{func}(Ca_{cyt}, kdelta_{IP3}, 2) \\
vip3prod &= vglu + vplcg \\
v3k &= v3k_{IP3} \times phos_{sum} \times hill_{func}(Ip3, k3_{IP3}, n3_{IP3}) \\
Ileak &= gL \times (V - EL) \\
Itotal &= -Ileak - I_{caL13} - I_{TRPV1} - I_{AMPA} - I_{NMDA} - I_{action}
\end{aligned}
$$

A.1.3 Reactions

DARPP32

Reactions	forward rate	reverse rate
D32p75PP2Acal → PP2Acal+D32	f23 : 0.042	
D32p75pPP2A → pPP2A+D32	f53 : 0.042	
D32p75+pPP2A ↔ D32p75pPP2A	f59 : 1.5e-05	f_59 : 0.168
D32p75+PKAc ↔ D32p75PKAc	f73 : 3.7e-07	f_73 : 0.001
D32p75+PP2AB56d ↔ D32p75PP2AB56d	f96 : 2.3e-06	f_96 : 0.084
D32p75+PP2Acal ↔ D32p75PP2Acal	f101 : 1.5e-05	f_101 : 0.168
D32p75+PP2ABPR72 ↔ D32p75PP2ABPR72	f144 : 2.3e-06	f_144 : 0.084
D32p75PP2ABPR72 → D32+PP2ABPR72	f0 : 0.021	
D32p75PP2AB56d → D32+PP2AB56d	f6 : 0.021	
D32p34+PP1 ↔ D32p34PP1	f139 : 0.0004	f_139 : 0.00058
D32p34PP1+PP2BCamCa2C ↔ D32p34PP1PP2BCamCa2C	f132 : 1e-07	f_132 : 0.0004
D32p34PP1PP2BCamCa4 → D32+PP2BCamCa4	f18 : 0.0	
D32p34PP1+PP2BCamCa4 ↔ D32p34PP1PP2BCamCa4	f92 : 4e-06	f_92 : 0.004
D32p34PP2BCamCa4 → D32+PP2BCamCa4	f41 : 0.0	
D32p34+PP2BCamCa4 ↔ D32p34PP2BCamCa4	f124 : 4e-06	f_124 : 0.004
D32p34PP2AB56d → D32+PP2AB56d	f26 : 0.014	
D32p34PP1PP2AB56d → D32+PP2AB56d	f34 : 0.00336	
D32p34+PP2AB56d ↔ D32p34PP2AB56d	f151 : 1.52e-06	f_151 : 0.056
D32p34PP1+PP2AB56d ↔ D32p34PP1PP2AB56d	f141 : 3.6e-07	f_141 : 0.0146
D32p34PP2ABPR72 → D32+PP2ABPR72	f38 : 0.014	
D32p34PP1+PP2ABPR72 ↔ D32p34PP1PP2ABPR72	f75 : 3.6e-07	f_75 : 0.0146
D32p34PP1PP2ABPR72 → D32+PP2ABPR72	f7 : 0.00336	
D32p34+PP2ABPR72 ↔ D32p34PP2ABPR72	f97 : 1.52e-06	f_97 : 0.056
Cdk5D32 → D32p75+Cdk5	f28 : 0.01	
Cdk5+D32 ↔ Cdk5D32	f61 : 4.5e-06	f_61 : 0.04
D32+PKAc ↔ D32PKAc	f91 : 2.7e-06	f_91 : 0.008

Phosphodiesterase

PDE1CamCa4cAMP → PDE1CamCa4+AMP	f43 : 0.011	
PDE1CamCa4+cAMP ↔ PDE1CamCa4cAMP	f107 : 4.6e-06	f_107 : 0.044
PDE1+CamCa4 ↔ PDE1CamCa4	f143 : 1e-05	f_143 : 0.0001
PDE2cAMP2 → PDE2cAMP+AMP	f1 : 0.0054	
PDE2+cAMP ↔ PDE2cAMP	f131 : 2e-08	f_131 : 0.0005
PDE2cAMP+cAMP ↔ PDE2cAMP2	f109 : 5.9e-06	f_109 : 0.0005
PDE4+cAMP ↔ PDE4cAMP	f110 : 2.16e-05	f_110 : 0.06895
PDE4cAMP → PDE4+AMP	f42 : 0.017233	
Roli+PDE4 ↔ RoliPDE4	f133 : 1e-06	f_133 : 0.002
pPDE4+cAMP ↔ pPDE4cAMP	f136 : 8.64e-05	f_136 : 0.2758
pPDE4PP2A → PDE4+PP2ABPR72	f31 : 2.4e-06	
pPDE4PP2Ac → PDE4+PP2Acal	f24 : 4.8e-06	
pPDE4cAMP → AMP+pPDE4	f39 : 0.068932	
pPDE4+PP2ABPR72 ↔ pPDE4PP2A	f117 : 2.4e-08	f_117 : 9.6e-06
pPDE4+PP2Acal ↔ pPDE4PP2Ac	f114 : 4.8e-08	f_114 : 1.92e-05
PDE10+cAMP ↔ PDE10cAMP	f127 : 8.4e-05	f_127 : 0.0168
PDE10cAMP → AMP+PDE10	f25 : 0.0042	
pPDE10PP2A → PDE10+PP2ABPR72	f8 : 2.4e-06	
pPDE10+PP2Acal ↔ pPDE10PP2Ac	f130 : 4.8e-08	f_130 : 1.92e-05
pPDE10PP2Ac → PP2Acal+PDE10	f51 : 4.8e-06	
pPDE10cAMP → pPDE10+AMP	f37 : 0.0168	
pPDE10+cAMP ↔ pPDE10cAMP	f88 : 0.000336	f_88 : 0.0672
pPDE10+PP2ABPR72 ↔ pPDE10PP2A	f76 : 2.4e-08	f_76 : 9.6e-06
Pap+PDE10 ↔ PapPDE10	f108 : 1e-06	f_108 : 1.7e-05
Epac1+Epac1cAMP ↔ Epac1cAMP+PKAcAMP2	f62 : 3.3e-08	f_62 : 8e-05

Adenylate cyclase

AC1+CamCa4 ↔ AC1CamCa4	f55 : 6e-06	f_55 : 0.0009
AC1CamCa4 ↔ AC1CamCa4ATP	f60 : 1e-05	f_60 : 2.273
AC1Gsa+CamCa4 ↔ AC1GsaCamCa4	f56 : 6e-06	f_56 : 0.0009
AC1GsaCamCa4 ↔ AC1GsaCamCa4ATP	f72 : 1e-05	f_72 : 2.273
GsaGTP+AC1 ↔ AC1Gsa	f86 : 3.85e-05	f_86 : 0.01
AC1CamCa4ATP → AC1CamCa4+cAMP	f2 : 0.005684	
AC1GsaCamCa4ATP → cAMP+AC1GsaCamCa4	f50 : 0.05684	
GiaGTP+AC5 ↔ AC5Gia	f105 : 1.25e-05	f_105 : 0.002
GsaGTP+AC5 ↔ AC5Gsa	f102 : 1.48e-05	f_102 : 0.003996
GiaGTP+AC5Gsa ↔ AC5GsaGia	f121 : 1.25e-05	f_121 : 0.002
GsaGTP+AC5Gia ↔ AC5GsaGia	f138 : 3.7e-06	f_138 : 0.002997
AC5Gsa ↔ AC5GsaATP	f100 : 0.2552	f_100 : 0.0002612
AC5GsaGia ↔ AC5GsaGiaATP	f106 : 0.02552	f_106 : 2.612e-05
AC5GsaATP → GsaGDP+AC5	f16 : 3e-05	
AC5GsaATP ↔ cAMP+cAMP+AC5Gsa	f54 : 0.02846	f_54 : 2.592e-07
AC5GsaGiaATP ↔ cAMP+AC5GsaGia	f89 : 0.0002746	f_89 : 2.592e-07
AC5GsaGiaATP → cAMP+GiaGDP+AC5Gsa	f9 : 0.0004	

G-proteins

GqaGTP → GqaGDP	f3 : 0.0001	
GiaGTP → GiaGDP	f27 : 0.004	
GsaGTP → GsaGDP	f29 : 1e-05	
GiaGDP+Gbg → Giabg	f10 : 0.002	
GsaGDP+Gbg → Gsabg	f36 : 0.002	
GqaGDP+Gbg → Gqabg	f47 : 0.002	
Glu → GluOut	f46 : 0.0012	
GluGbuf → Gbuf	f48 : 0.02	
GluMgluRGq → GluMgluR+GqaGTP+Gbg	f40 : 0.0015	
GluMgluR ↔ GluMgluRdesens	f123 : 6.25e-05	f_123 : 1e-06
Glu+MgluRGq ↔ GluMgluRGq	f126 : 4e-06	f_126 : 0.001
Gqabg+GluMgluR ↔ GluMgluRGq	f140 : 9e-07	f_140 : 0.00136
Gqabg+MgluR ↔ MgluRGq	f145 : 2.25e-09	f_145 : 0.00068
Glu+MgluR ↔ GluMgluR	f63 : 1e-06	f_63 : 0.0005
Gqabg+m1R ↔ m1RGq	f80 : 5.76e-07	f_80 : 0.00042
telenz+m1R ↔ telenzm1R	f116 : 0.00095	f_116 : 0.0025
telenz+m1RGq ↔ telenzm1RGq	f85 : 0.0396	f_85 : 0.0025
Giabg+m4R ↔ Gim4R	f122 : 1.78e-06	f_122 : 0.00042
Gim4R+PD1028 ↔ PD1028m4RGi	f81 : 0.003024	f_81 : 0.02
PD1028+m4R ↔ PD1028m4R	f142 : 2.8e-05	f_142 : 0.0025

Acetycholine

ACh+m1R ↔ AChm1R	f64 : 9.5e-08	f_64 : 0.0025
ACh+m1RGq ↔ AChm1RGq	f118 : 3.96e-06	f_118 : 0.0025
AChm1RGq → AChm1R+GqaGTP+Gbg	f30 : 0.0005	
Gqabg+AChm1R ↔ AChm1RGq	f104 : 2.4e-05	f_104 : 0.00042
AChm4RGi → GiaGTP+Gbg+AChm4R	f35 : 0.008	
AChm4R+Giabg ↔ AChm4RGi	f112 : 0.000192	f_112 : 0.00336
Gim4R+ACh ↔ AChm4RGi	f120 : 3.65e-05	f_120 : 0.02
ACh+m4R ↔ AChm4R	f150 : 3.38e-07	f_150 : 0.0025

Protein Kinase A

PP1pAKAR3 → AKAR3	f11 : 0.000312	
pAKAR3+PP1 ↔ PP1pAKAR3	f58 : 2.5e-07	f_58 : 0.0012
AKAR3+PKAc ↔ PKAcAKAR3	f70 : 6.25e-06	f_70 : 0.00075
D32PKAc → PKAc+D32p34	f44 : 0.002	
PKAc+PDE4 ↔ PKAcPDE4	f103 : 2.5e-07	f_103 : 8e-05
PKAcPDE4 → PKAc+pPDE4	f13 : 2e-05	
PKAcAMP2+2cAMP ↔ PKAcAMP4	f78 : 3.5e-07	f_78 : 0.0006
PKAcAMP4 ↔ PKAr+PKAc	f149 : 0.00024	f_149 : 2.55e-05
PKAc+PDE4cAMP ↔ PKAcPDE4cAMP	f134 : 2.5e-07	f_134 : 8e-05
PKAcPDE4cAMP → pPDE4cAMP+PKAc	f17 : 2e-05	
PKAc+PDE10 ↔ PKAcPDE10	f147 : 2.5e-07	f_147 : 2.4e-05
PKAcPDE10 → pPDE10+PKAc	f14 : 6e-06	
PKAcPDE10cAMP → PKAc+pPDE10cAMP	f4 : 6e-06	
PKAc+PDE10cAMP ↔ PKAcPDE10cAMP	f57 : 2.5e-07	f_57 : 2.4e-05
PKAcAKAR3 → PKAc+pAKAR3	f21 : 0.0001875	
PKAcPP2AB56d → PKAc+pPP2A	f22 : 3e-05	
PKAc+DaD1RGs ↔ PKAcDaD1RGs	f87 : 6e-06	f_87 : 0.0006
PKAcDaD1RGs → PKAc	f33 : 0.00015	

Dopamine

Da ↔ DaOut	f135 : 0.001	f_135 : 5.5e-08
Da+D1R ↔ DaD1R	f113 : 1.66667e-06	f_113 : 0.005
DaD1RGs → DaD1R+GsaGTP+Gbg	f19 : 0.00015	
pDaD1RGs → D1R+Gsabg+Da	f5 : 2e-07	
pDaD1RGs → GsD1R	f49 : 2e-05	
pDaD1RGs ↔ Da+pGsD1R	f125 : 0.1	f_125 : 0.0001
DaDbuf → Dbuf+Da	f45 : 0.02	
GsD1R+Da ↔ DaD1RGs	f93 : 5e-06	f_93 : 0.005
DaD1R+Gsabg ↔ DaD1RGs	f95 : 3e-05	f_95 : 0.0004
Gsabg+D1R ↔ GsD1R	f148 : 1e-05	f_148 : 0.0004

Calcium and Calmoduline

CaOut+Leak ↔ CaOutLeak	f119 : 1e-08	f_119 : 0.0011
CaOutLeak → Leak	f12 : 0.0011	
ncxCa → CaOut+ncx	f15 : 0.0056	
pmcaCa → pmca+CaOut	f52 : 0.003	
Cam+2Ca˙cyt ↔ CamCa2N	f90 : 0.0001	f_90 : 50.0
Cam+2Ca˙cyt ↔ CamCa2C	f69 : 6e-06	f_69 : 0.91
CamCa2N+2Ca˙cyt ↔ CamCa4	f82 : 6e-06	f_82 : 0.91
CamCa2C+2Ca˙cyt ↔ CamCa4	f83 : 0.0001	f_83 : 50.0
CamCa2C+PP2B ↔ PP2BCamCa2C	f74 : 4.6e-05	f_74 : 1.2e-06
CamCa4+PP2B ↔ PP2BCamCa4	f67 : 4.6e-05	f_67 : 1.2e-06
CamCa2N+PP2B ↔ PP2BCamCa2N	f128 : 4.6e-05	f_128 : 1.2e-06
Cam+PP2B ↔ PP2BCam	f84 : 4.6e-06	f_84 : 1.2e-06
PP2BCam+2Ca˙cyt ↔ PP2BCamCa2N	f94 : 0.0001	f_94 : 0.1
PP2BCam+2Ca˙cyt ↔ PP2BCamCa2C	f129 : 6e-06	f_129 : 0.00091
PP2BCamCa2C+2Ca˙cyt ↔ PP2BCamCa4	f65 : 0.0001	f_65 : 1.0
PP2BCamCa2N+2Ca˙cyt ↔ PP2BCamCa4	f146 : 6e-06	f_146 : 0.0091
Ca˙cyt+Pkc ↔ PkcCa	f77 : 2e-05	f_77 : 0.05
Ca˙cyt+ncx ↔ ncxCa	f79 : 1.1e-05	f_79 : 0.0112
Ca˙cyt+Calbin ↔ CalbinC	f99 : 2.8e-05	f_99 : 19.6
Ca˙cyt+pmca ↔ pmcaCa	f152 : 5e-05	f_152 : 0.009
PkcCa+Dag ↔ PkcCaDag	f66 : 1.5e-08	f_66 : 0.00015
PP2ABPR72+Ca˙cyt ↔ PP2Acal	f111 : 2e-08	f_111 : 0.0001
PP2AB56d+PKAc ↔ PKAcPP2AB56d	f98 : 1.25e-06	f_98 : 0.000185
pPP2A → PP2AB56d	f20 : 2e-05	
OA˙PP2AB56d → OA+OA˙PP2AB56d+PP2AB56d	f32 : 5e-06	
OA+pPP2A ↔ OA˙pPP2A	f68 : 5e-06	f_68 : 1.5e-07
OA+PP2ABPR72 ↔ OA˙PP2ABPR72	f71 : 5e-06	f_71 : 1.5e-07
OA+PP2Acal ↔ OA˙PP2Acal	f115 : 5e-06	f_115 : 1.5e-07
OA+PP1 ↔ OA˙PP1	f137 : 1e-06	f_137 : 0.00015

A.1.4 Parameters

Parameter	value	unit
on_caL13	1.	No unit
pcaLbar	1.02e-09	microL.ms-1
mslope_caL13	-6.7	mV
hshift_caL13	0.0	not used
vm_caL13	-8.124	mV
mshift_caL13	0.0	not used
hslope_caL13	11.9	mV
kpr_caL13	31.4	mV
c_caL13	0.0398	mV-1.ms-1
k_caL13	9.005	mV
hvhalf_caL13	-13.4	mV
mvhalf_caL13	-33	mV
cpr_caL13	0.9900	ms-1
htau_caL13	44.3	ms
hqfact_caL13	3.0	No unit
qfact_caL13	3.0	No unit

I_to_Ca_flux

NMDA	70.0	nM.pA-1.ms-1
VDCC	84.0	nM.pA-1.ms-1
TRPV1	310.	nM.pA-1.ms-1

CaBuff

BT_CaBuff	4500.	nM
Cab	100.	nM
tauCab	7.	ms
KdB_CaBuff	500.	nM

CICR

a2_CICR	0.5e-6	nM-1.ms-1
ver_CICR	8.0	nM.ms-1
d3_CICR	943.4	nM
rc_CICR	4.0e-3	ms-1
rl_CICR	1.0e-4	ms-1
rhoER_CICR	0.3	No unit
d5_CICR	120.	nM
d2_CICR	3049.	nM
ker_CICR	50.	nM
d1_CICR	130.	nM

IP3

kappad_IP3	1500.	nM
kdelta_IP3	100.	nM
r5p_IP3	2.0e-4	ms-1
v3k_IP3	0.001e-3	ms-1
kd_IP3	1500.	nM
vdelta_IP3	0.02	nM.ms-1
k3_IP3	1000.	nM
kr_IP3	1300.	nM
kp_IP3	10000.	nM
vbeta_IP3	0.8	nM.ms-1
kpi_IP3	600.	nM
n3_IP3	1.0	No unit

DGLandDAG

KDGL	30000.	nM
kMAGL	0.5e-3	ms-1
rDGL	20000.0	nM.ms-1
kDAGK	2.0e-3	ms-1

KandP_on_DAGLP

nK_DAGLP	6.	No unit
rP_DAGLP	0.380	ms-1
rK_DAGLP	50.0e-3	ms-1

ECb

on_ECb	1.	No unit
ECb_CB1R_on	1.	No unit
kCB1R	3000.0	No unit
alphaAEACB1	0.1	No unit
P1_ECb	1e-06	ms
P2_ECb	1e-05	No unit
P3_ECb	7.	No unit
P4_ECb	2.0e3	ms
vATAEA	2.0e-4	ms-1
LTDstart	0.008	No unit
LTDstop	0.00823	No unit
LTDMax	0.65	No unit
LTPstart	0.01	No unit
LTPMax	13.5425	No unit
KFAAH	1000.	nM
vFAAH	4.0	nM.ms-1

post_CaMKII_plast

kpkaI1	4.67e-3	ms-1
PP10	200.	nM
KM	400.	nM
K5	700.	nM
k12	6.0	ms-1
k11	500.0e-6	nM-1.ms-1
kcan0I1	0.05e-3	ms-1
km11	1.0e-4	ms-1
CaMKT	16600.	nM
k7	6.0e-3	ms-1
k6	6.0e-3	ms-1
ncanI1	3.0	No unit
I10	1000.	nM
CaMT	70.52	nM
KdpkaI1	159.	nM
kcanI1	20.5e-3	ms-1
KdcanI1	53.	nM
kpka0I1	0.0025e-3	ms-1
Ka3	320.	nM
Ka2	25.	nM
Ka1	100.	nM
Ka4	400.	nM
npkaI1	3.0	No unit

post_CaMKII_bis

conc_max_sub_unit	200000.	nM
K9	1e-1	nM

DA

gamma1DA	0.7e-3	nM-1
gamma2DA	0.07e-3	nM-1
DA	10.	nM

AMPA

on_AMPA	1.	No unit
gAMPA	5.1	nS
Epsilon_AMPA	0.0	ms-1
Beta_AMPA	190.0e-3	ms-1
Alpha_AMPA	1.02e-6	nM-1.ms-1
Gamma_AMPA	0.0	ms-1

NMDA

on_NMDA	1.	No unit
gNMDA	1.53	nS
p_ca_NMDA	2.08324254657e-49	microL.ms-1
Mg_NMDA	1.0	mM
Alpha_NMDA	0.072e-6	nM-1.ms-1
Beta_NMDA	0.1	ms-1

membrane

EL	-70.0	mV
gL	10.0	nS
Cm	0.1e3	nF

CB1R

on_CB1R	1.	No unit
Alpha_CB1R	0.240194904182e-6	nM-1.ms-1
Beta_CB1R	11.0718971839e-3	ms-1
Gamma_CB1R	416.378884767e-3	ms-1
Epsilon_CB1R	0.0477956844649e-3	ms-1

common

R	8.3144621	J.mol-1.K-1
RT	2553.78703401	J.mol-1
T	307.15	K
F	96.5	kCoulomb.mol-1
zS	2.0	No unit
Ca_out	5000.0e3	nM

integration

t_step	time_step	ms
t_start	t_start	ms
t_end	t_end	ms
ATOL	1e-07	No unit
RTOL	1e-07	No unit
MXSTEP	1000.	No unit
HMAX	50.0e3	ms

action

APdur	30.	ms
action_as_VDCC	False	No unit
DPmax	495.0	pA
APmax	7020.0	pA
tausbAP	1.	ms

Glu_release

steadyrise_on	0.	No unit
Glumax	2000.0e3	nM
BaseLevel	0.0	nM
tauGlu	5.	ms

stimulation

regular_on	0.	No unit
tsdt	15.	ms
tpost	500.	ms
post_on	1.	No unit
Delta_t_STDP	20.	ms
num_stim	20	No unit — Integer
pre_on	1.	No unit
Freq	10.0	Hz
tables_step	5e-02	ms

trad_unit

betaAEACB1	1e3	ms
alphatwoAGCB1	1e-3	nM-1
alpha_DAGLP_Ca_cyt	1e-3	nM-1

A.1.5 Initial values of ODE variables

CaMKII

Variable	value
h˙caL13	0.991821379067138
m˙caL13	0.0036977671871038817
o˙AMPA	0.0
d˙AMPA	0.0
o˙NMDA	0.0
h˙CICR	0.8246676668946951
Ca˙cyt	121.32718966407073
Ca˙ER	63348.08768685364
DAGLP	4e-07
AEA	6.103384809978344
fpre	1.0
PP1	100.0
V	-69.99901620452822
o˙CB1R	3.4373437854140236e-07
d˙CB1R	0.002994487796947427
B1	233.16029213700182
B2	3.4298074889746086
B3	0.28889779878196253
B4	0.1375613348305254
B5	0.03636597678802968
B6	0.004127401745167649
B7	0.0042498580055485265
B8	0.00012513942987290664
B9	0.000326960829605911
B10	4.5484170099234245e-05
B11	3.078127923587743e-05
B12	2.797021154343162e-06
B13	1.3221817318283754e-08

Cam, DA, Glu, acetylcholine adn adenylate cyclase 5

pmca	473.33333333333337
pmcaCa	193.33333333333334
CaOut	1996038
ncx	18933.333333333336
ncxCa	1066.6666666666667
Leak	666.6666666666667
CaOutLeak	5333.333333333334
Calbin	159982
CalbinC	18
CamCa4	4.0
CamCa2N	15
DaDbuf	0
Dbuf	0
DaOut	200000
Da	10
DaD1R	0.0
Gsabg	11200.0
DaD1RGs	0.0
D1R	0.0
GsD1R	1333.3333333333335
pGsD1R	0
GsaGTP	0.0
Gbg	2400.0
PKAc	0.0
PKAcDaD1RGs	0.0

pDaD1RGs	0.0
GluGbuf	0
Gbuf	0
GluOut	200000
GluMgluR	0
GluMgluRdesens	0
MgluR	700.0
Gqabg	13000.0
MgluRGq	100.0
GluMgluRGq	0
GqaGTP	0
ACh	105
m1R	1000.0
AChm1R	0
AChm1RGq	0
m1RGq	333.33333333333337
m4R	33.333333333333336
AChm4R	0.0
Giabg	9853.333333333334
AChm4RGi	220.0
Gim4R	1080.0
GsaGDP	0.0
GqaGDP	0
GiaGTP	146.66666666666669
GiaGDP	0.0
AC5	1066.6666666666667
AC5Gsa	0.0
AC5GsaATP	100.0
cAMP	50
AC5Gia	2100.0
AC5GsaGia	0.0
AC5GsaGiaATP	133.33333333333334

Phosphodiesterase

PDE1	1700
PDE1CamCa4	300
PDE1CamCa4cAMP	0
AMP	0
PDE10	7833.333333333334
PDE10cAMP	1840.0
pPDE10	0.0
pPDE10cAMP	0.0
PKAcPDE10	0.0
PKAcPDE10cAMP	0.0
pPDE10PP2A	200.0
pPDE10PP2Ac	0.0
PDE2	1350
PDE2cAMP	0
PDE2cAMP2	0
PDE4	286
PDE4cAMP	0
pPDE4	10
pPDE4cAMP	0
PKAcPDE4	0
PKAcPDE4cAMP	0
pPDE4PP2A	40
pPDE4PP2Ac	0

Plc, PKA, PP2B and PP2A

Plc	7733.333333333334
PlcCa	0.5333333333333333
PlcCaGqa	0
PlcGqa	0
Pip2	127266.66666666667
PlcCaPip2	133.33333333333334
Ip3	600.0
Dag	2.666666666666667
PlcCaGqaPip2	0
Dgl	20.533333333333335
CaDgl	4.8
DagCaDgl	50.0
two˙ag	0
PIkinase	1.6
Ip3degPIk	266.6666666666667
two˙agDegrad	0
Ip3degrad	0.0
DagK	9.333333333333334
DagKdag	0
PA	0
Pkc	9750
PkcCa	250
PkcCaDag	0.0
PKA	5413.333333333334
PKAcAMP2	1120.0
PKAcAMP4	133.33333333333334
PKAr	0.0
Epac1	6500.0
Epac1cAMP	166.66666666666669
Cam	13900.0
PP2B	1.5
PP2BCam	300.0
CamCa2C	145
PP2BCamCa2C	171.0
PP2BCamCa2N	26.0
PP2BCamCa4	1.5
PKAcPP2AB56d	0
pPP2A	40
PP2ABPR72	1100
PP2Acal	20

DARPP32

D32	37560
D32PKAc	0
D32p34	0
D32p34PP1	20.0
D32p34PP2BCamCa4	0
D32p34PP1PP2BCamCa4	0
D32p34PP1PP2BCamCa2C	0
D32p34PP2ABPR72	0
D32p34PP2AB56d	0
D32p34PP1PP2ABPR72	1.0
D32p34PP1PP2AB56d	1.0
PP2AB56d	1080
Cdk5	370
Cdk5D32	1215
D32p75	10085
D32p75PKAc	0
D32p75pPP2A	40
D32p75PP2ABPR72	260
D32p75PP2AB56d	230
D32p75PP2Acal	10

AKAr and Adenylate Cyclase

pDgl	0.0
CapDgl	0.0
DagCapDgl	0.0
AKAR3	0
PKAcAKAR3	0.0
pAKAR3	0
PP1pAKAR3	0.0
AC1	333.33333333333337
AC1Gsa	0.0
AC1GsaCamCa4	0.0
AC1GsaCamCa4ATP	0.0
AC1CamCa4	0.0
AC1CamCa4ATP	0.0

Bibliography

Abbott, L. and Kepler, T. (1990). Model neurons: from hodgkin-huxley to hopfield. *Statistical mechanics of neural networks*, pages 5–18.

Aberkane, I. (2016). *Libérez votre cerveau! Traité de neurosagesse pour changer l'école et la société*. Robert Laffont.

Alberico, S. L., Kim, Y.-C., Lence, T., and Narayanan, N. S. (2017). Axial levodopa-induced dyskinesias and neuronal activity in the dorsal striatum. *Neuroscience*, 343:240–249.

Albin, R. L., Young, A. B., and Penney, J. B. (1989). The functional anatomy of basal ganglia disorders. *Trends in Neurosciences*, 12(10):366–375.

Albin, R. L., Young, A. B., Penney, J. B., Handelin, B., Balfour, R., Anderson, K. D., Markel, D. S., Tourtellotte, W. W., and Reiner, A. (1990). Abnormalities of striatal projection neurons and n-methyl-d-aspartate receptors in presymptomatic huntington's disease. *New England Journal of Medicine*, 322(18):1293–1298.

Amédée, T., Robert, A., and Coles, J. (1997). Potassium homeostasis and glial energy metabolism. *Glia*.

Amini, B., Clark, J. W., and Canavier, C. C. (1999). Calcium dynamics underlying pacemaker-like and burst firing oscillations in midbrain dopaminergic neurons: A computational study. *Journal of Neurophysiology*, 82(5):2249–2261.

Ammari, R., Lopez, C., Bioulac, B., Garcia, L., and Hammond, C. (2010). Subthalamic nucleus evokes similar long lasting glutamatergic excitations in pallidal, entopeduncular and nigral neurons in the basal ganglia slice. *Neuroscience*, 166(3):808–818.

Amzica, F., Massimini, M., and Manfridi, A. (2002). Spatial buffering during slow and paroxysmal sleep oscillations in cortical networks of glial cells in vivo. *The Journal of Neuroscience*.

Anderson, C. J., Sheppard, D. T., Huynh, R., Anderson, D. N., Polar, C. A., and Dorval, A. D. (2015). Subthalamic deep brain stimulation reduces pathological information transmission to the thalamus in a rat model of parkinsonism. *Frontiers in Neural Circuits*, 9:31.

Andrade-Talavera, Y., Duque-Feria, P., Paulsen, O., and Rodríguez-Moreno, A. (2016). Presynaptic spike timing-dependent long-term depression in the mouse hippocampus. *Cereb Cortex*, 26(8):3637–3654.

Aylward, E., Sparks, B., Field, K., Yallapragada, V., Shpritz, B., Rosenblatt, A., Brandt, J., Gourley, L., Liang, K., Zhou, H., Margolis, R., and Ross, C. (2004). Onset and rate of striatal atrophy in preclinical huntington disease. *Neurology*.

Bar-Ilan, L., Gidon, A., and Segev, I. (2013). The role of dendritic inhibition in shaping the plasticity of excitatory synapses. *Frontiers in neural circuits*, 6:118.

Barreto, E. and Cressman, J. R. (2011). Ion concentration dynamics as a mechanism for neuronal bursting. *Journal of Biological Physics*, 37(3):361–373.

Baufreton, J., Atherton, J. F., Surmeier, D. J., and Bevan, M. D. (2005). Enhancement of excitatory synaptic integration by gabaergic inhibition in the subthalamic nucleus. *Journal of Neuroscience*, 25(37):8505–8517.

Bay, V. and Butt, A. M. (2012). Relationship between glial potassium regulation and axon excitability: A role for glial kir4.1 channels. *Glia*, 60(4):651–660.

Bayer, H. M. and Glimcher, P. W. (2005). Midbrain dopamine neurons encode a quantitative reward prediction error signal. *Neuron*, 47(1):129–141.

Bell, C. C., Han, V. Z., Sugawara, Y., and Grant, K. (1997). Synaptic plasticity in a cerebellum-like structure depends on temporal order. *Nature*, 387(6630):278–281.

Bender, V. A., Bender, K. J., Brasier, D. J., and Feldman, D. E. (2006). Two coincidence detectors for spike timing-dependent plasticity in somatosensory cortex. *J Neurosci*, 26(16):4166–77.

Benecke, R., Rothwell, J. C., Dick, J. P. R., Day, B. L., and Marsden, C. D. (1986). Performance of simultaneous movements in patients with parkinson's disease. *Brain*, 109(4):739–757.

Berendse, H. W. and Groenewegen, H. J. (1991). *The Connections of the Medial Part of the Subthalamic Nucleus in the Rat: Evidence for a Parallel Organization*, pages 89–98. Springer New York, Boston, MA.

Berger, B., Gaspar, P., and Verney, C. (1991). Dopaminergic innervation of the cerebral cortex: unexpected differences between rodents and primates. *Trends in neurosciences*, 14(1):21–27.

Bevan, M. D., Booth, P. A. C., Eaton, S. A., and Bolam, J. P. (1998). Selective innervation of neostriatal interneurons by a subclass of neuron in the globus pallidus of the rat. *The Journal of Neuroscience*, pages 9438–9452.

Bi, G. and Poo, M. (1998). Synaptic modifications in cultured hippocampal neurons: Dependence on spike timing, synaptic strength, and postsynaptic cell type. *The Journal of Neuroscience*, pages 10464–10472.

Bianco, I. H. and Wilson, S. W. (2009). The habenular nuclei: a conserved asymmetric relay station in the vertebrate brain. *Philosophical Transactions of the Royal Society B: Biological Sciences*, 364(1519):1005–1020.

Bissière, S., Humeau, Y., and Lüthi, A. (2003). Dopamine gates ltp induction in lateral amygdala by suppressing feedforward inhibition. *Nature neuroscience*, 6(6):587.

Blesa, J. and Przedborski, S. (2014). Parkinson's disease: Animal models and dopaminergic cell vulnerability. *Frontiers in Neuroanatomy*, 8(155).

Bloodgood, B. L. and Sabatini, B. L. (2007). Nonlinear regulation of unitary synaptic signals by cav2. 3 voltage-sensitive calcium channels located in dendritic spines. *Neuron*, 53(2):249–260.

Bosch, C., Mailly, P., Degos, B., Deniau, J. M., and Venance, L. (2012). Preservation of the hyperdirect pathway of basal ganglia in a rodent brain slice. *Neuroscience*, 215:31–41.

Bosch-Bouju, C., Larrieu, T., Linders, L., Manzoni, O. J., and Laye, S. (2016). Endocannabinoid-mediated plasticity in nucleus accumbens controls vulnerability to anxiety after social defeat stress. *Cell Reports*.

Brown, P. and Eusebio, A. (2008). Paradoxes of functional neurosurgery: Clues from basal ganglia recordings. *Movement Disorders*, 23(1):12–20.

Brown, P. L. and Shepard, P. D. (2013). Lesions of the fasciculus retroflexus alter footshock-induced cfos expression in the mesopontine rostromedial tegmental area of rats. *PLoS ONE*, 8(4):e60678.

Brzosko, Z., Schultz, W., and Paulsen, O. (2015). Retroactive modulation of spike timing-dependent plasticity by dopamine. *Elife*, 4.

Brzosko, Z., Zannone, S., Schultz, W., Clopath, C., and Paulsen, O. (2017). Sequential neuromodulation of hebbian plasticity offers mechanism for effective reward-based navigation. *Elife*, 6.

Burrows, M. (1996). *Neurotransmitters, neuromodulators and neurohormones*. Oxford University Press.

Bush, D. and Jin, Y. (2012). Calcium control of triphasic hippocampal stdp. *Journal of computational neuroscience*, 33(3):495–514.

Calabresi, P., Picconi, B., Tozzi, A., Ghiglieri, V., and Di Filippo, M. (2014). Direct and indirect pathways of basal ganglia: a critical reappraisal. *Nature neuroscience*, 17(8):1022.

Campanac, E. and Debanne, D. (2008). Spike timing-dependent plasticity: a learning rule for dendritic integration in rat ca1 pyramidal neurons. *The Journal of physiology*, 586(3):779–793.

Canavier, C. C. (1999). Sodium dynamics underlying burst firing and putative mechanisms for the regulation of the firing pattern in midbrain dopamine neurons: a computational approach. *J Comput Neurosci.*, pages 46–69.

Carlisle, H. J., Fink, A. E., Grant, S. G., and O'Dell, T. J. (2008). Opposing effects of psd-93 and psd-95 on long-term potentiation and spike timing-dependent plasticity. *The Journal of physiology*, 586(24):5885–5900.

Carlson, K. D. and Giordano, N. (2011). Interplay of the magnitude and time-course of postsynaptic ca 2+ concentration in producing spike timing-dependent plasticity. *Journal of computational neuroscience*, 30(3):747–758.

Carmeliet, E., Biermans, G., Callewaert, G., and Vereecke, J. (1987). Potassium currents in cardiac cells. *Experientia*, 43(11).

Celada, P., Paladini, C. A., and Tepper, J. M. (1999). Gabaergic control of rat substantia nigra dopaminergic neurons: role of globus pallidus and substantia nigra pars reticulata. *Neuroscience*, 89(3):813–825.

Chan, C. S., Surmeier, D. J., and Yung, W. H. (2005). Striatal information signaling and integration in globus pallidus: Timing matters. *Neurosignals*, 14(6):281–289.

Chevalier, G. and Deniau, J. M. (1990). Disinhibition as a basic process in the expression of striatal functions. *Trends in Neurosciences*, 13(7):277–280.

Chung, S., Jung, W., and Lee, M.-Y. (1999). Inward and outward rectifying potassium currents set membrane potentials in activated rat microglia. *Neuroscience Letters*.

Clopath, C., Büsing, L., Vasilaki, E., and Gerstner, W. (2010). Connectivity reflects coding: a model of voltage-based stdp with homeostasis. *Nature neuroscience*, 13(3):344.

Colquhoun, D., Jonas, P., and Sakmann, B. (1992). Action of brief pulses of glutamate on ampa/kainate receptors in patches from different neurones of rat hippocampal slices. *The Journal of Physiology*, 458(1):261–287.

Connelly, W. M., Schulz, J. M., Lees, G., and Reynolds, J. N. J. (2010). Differential short-term plasticity at convergent inhibitory synapses to the substantia nigra pars reticulata. *Journal of neuroscience*.

Connor, N. P. and Abbs, J. H. (1991). Task-dependent variations in parkinsonian motor impairments. *Brain*, 114A(1):321–332.

Cools, R. (2006). Dopaminergic modulation of cognitive function-implications for l-dopa treatment in parkinson's disease. *Neuroscience & Biobehavioral Reviews*, 30(1):1–23.

Corbit, V. L., Whalen, T. C., Zitelli, K. T., Crilly, S. Y., Rubin, J. E., and Gittis, A. H. (2016). Pallidostriatal projections promote *beta* oscillations in a dopamine-depleted biophysical network model. *The Journal of Neuroscience*, 36(20):5556–5571.

Corlew, R., Wang, Y., Ghermazien, H., Erisir, A., and Philpot, B. D. (2007). Developmental switch in the contribution of presynaptic and postsynaptic nmda receptors to long-term depression. *Journal of Neuroscience*, 27(37):9835–9845.

Cowan, N. (1988). Evolving conceptions of memory storage, selective attention, and their mutual constraints within the human information-processing system. *Psychological bulletin*, 104(2):163.

Cressman, J. R., Ullah, G., Ziburkus, J., Schiff, S. J., and Barreto, E. (2009). The influence of sodium and potassium dynamics on excitability, seizures, and the stability of persistent states: I. single neuron dynamics. *Journal of computational neuroscience*, 26(2):159–170.

Cui, G., Jun, S. B., Jin, X., Pham, M. D., Vogel, S. S., Lovinger, D. M., and Costa, R. M. (2013). Concurrent activation of striatal direct and indirect pathways during action initiation. *Nature*, 494(7436):238–242.

Cui, Y., Paille, V., Xu, H., Genet, S., Delord, B., Fino, E., Berry, H., and Venance, L. (2015). Endocannabinoids mediate bidirectional striatal spike-timing-dependent plasticity. *The Journal of Physiology*.

Cui, Y., Prokin, I., Xu, H., Delord, B., Genet, S., Venance, L., and Berry, H. (2016). Endocannabinoid dynamics gate spike-timing dependent depression and potentiation. *Elife*, 5.

Cui, Y., Yang, Y., Ni, Z., Dong, Y., Cai, G., Foncelle, A., Ma, S., Sang, K., Tang, S., Li, Y., Shen, Y., Berry, H., Wu, S., and Hu, H. (2018). Astroglial-kir4.1 in lateral habenula drives neuronal bursts in depression. *Nature*.

Cutsuridis, V. (2011). Gaba inhibition modulates nmda-r mediated spike timing dependent plasticity (stdp) in a biophysical model. *Neural Netw*, 24(1):29–42.

Cutsuridis, V. (2013). Bradykinesia models of parkinson's disease. *Scholarpedia*, 8(9):30937.

Dahlström, A. and Fuxe, K. (1964). Localization of monoamines in the lower brain stem. *Cellular and Molecular Life Sciences*, 20(7):398–399.

Dallérac, G., Chever, O., and Rouach, N. (2013). How do astrocytes shape synaptic transmission? insights from electrophysiology. *Frontiers in Cellular Neuroscience*, 7(159).

D'Ambrosio, R., Gordon, D., and Winn, H. (2002). Differential role of kir channel and na+ /k+ -pump in the regulation of extracellular k+ in rat hippocampus. *J Neurophysiol*.

De Pittà, M., Brunel, N., and Volterra, A. (2016). Astrocytes: orchestrating synaptic plasticity? *Neuroscience*, 323:43–61.

Degos, B., Deniau, J.-M., Chavez, M., and Maurice, N. (2013). Subthalamic nucleus high-frequency stimulation restores altered electrophysiological properties of cortical neurons in parkinsonian rat. *PLoS ONE*, 8(12):e83608.

Degos, B., Deniau, J.-M., Thierry, A.-M., Glowinski, J., Pezard, L., and Maurice, N. (2005). Neuroleptic-induced catalepsy: Electrophysiological mechanisms of functional recovery induced by high- frequency stimulation of the subthalamic nucleus. *The Journal of Neuroscience*, 25(33):7687–7696.

DeLong, M. and Wichmann, T. (2007). Circuits and circuit disorders of the basal ganglia. *Archives of Neurology*, 64(1):20–24.

DeLong, M. and Wichmann, T. (2015). Basal ganglia circuits as targets for neuromodulation in parkinson disease. *JAMA Neurology*, 72(11):1354–1360.

Deng, Y. P., Albin, R. L., Penney, J. B., Young, A. B., Anderson, K. D., and Reiner, A. (2004). Differential loss of striatal projection systems in huntington's disease: a quantitative immunohistochemical study. *Journal of Chemical Neuroanatomy*, 27(3):143–164.

Destexhe, A., Mainen, F., and Sejnowski, J. (1998). Kinetic models of synaptic transmission. *Methods in Neuronal Modeling*, pages 1–25.

Devoto, P., Flore, G., Ibba, A., Fratta, W., and Pani, L. (2001). Lead intoxication during intrauterine life and lactation but not during adulthood reduces nucleus accumbens dopamine release as studied by brain microdialysis. *Toxicology letters*, 121(3):199–206.

Djukic, B., Casper, K. B., Philpot, B. D., Chin, L.-S., and McCarthy, K. D. (2007). Conditional knock-out of kir4.1 leads to glial membrane depolarization, inhibition of potassium and glutamate uptake, and enhanced short-term synaptic potentiation. *The Journal of Neuroscience*, 27(42):11354–11365.

Dorval, A. D., Muralidharan, A., Jensen, A. L., Baker, K. B., and Vitek, J. L. (2015). Information in pallidal neurons increases with parkinsonian severity. *Parkinsonism & related disorders*, 21(11):1355–1361.

Dovzhenok, A., Park, C., Worth, R. M., and Rubchinsky, L. L. (2013). Failure of delayed feedback deep brain stimulation for intermittent pathological synchronization in parkinson's disease. *PLoS ONE*, 8(3):e58264.

Dudman, J. T. and Krakauer, J. W. (2016). The basal ganglia: from motor commands to the control of vigor. *Current Opinion in Neurobiology*, 37:158–166.

Dunovan, K. and Verstynen, T. (2016). Believer-skeptic meets actor-critic: Rethinking the role of basal ganglia pathways during decision-making and reinforcement learning. *Frontiers in Neuroscience*, 10:106.

Edelmann, E. and Lessmann, V. (2011). Dopamine modulates spike timing-dependent plasticity and action potential properties in ca1 pyramidal neurons of acute rat hippocampal slices. *Frontiers in synaptic neuroscience*, 3:6.

Egger, V., Feldmeyer, D., and Sakmann, B. (1999). Coincidence detection and changes of synaptic efficacy in spiny stellate neurons in rat barrel cortex. *Nature neuroscience*, 2(12).

Ellens, D. J. and Leventhal, D. K. (2013). Electrophysiology of basal ganglia and cortex in models of parkinson disease. *Journal of Parkinson's disease*, 3(3):241–254.

Ermentrout, G. B. and Terman, D. H. (2010). Firing rate models. In *Mathematical foundations of neuroscience*, pages 331–367. Springer.

Evans, R. and Blackwell, K. (2015). Calcium: amplitude, duration, or location? *The Biological Bulletin*, 228(1):75–83.

Evans, R. C., Morera-Herreras, T., Cui, Y., Du, K., Sheehan, T., Kotaleski, J. H., Venance, L., and Blackwell, K. T. (2012). The effects of nmda subunit composition on calcium influx and spike timing-dependent plasticity in striatal medium spiny neurons. *PLoS computational biology*, 8(4):e1002493.

Faure, A., Haberland, U., Condé, F., and Massioui, N. E. (2005). Lesion to the nigrostriatal dopamine system disrupts stimulus-response habit formation. *The Journal of Neuroscience*, 25(11):2771.

Fearnley, J. M. and Lees, A. J. (1991). Ageing and parkinson's disease: substantia nigra regional selectivity. *Brain*, 114(5):2283–2301.

Feldman, D. E. (2000). Timing-based ltp and ltd at vertical inputs to layer ii/iii pyramidal cells in rat barrel cortex. *Neuron*, 27(1):45–56.

Feldman, D. E. (2012). The spike-timing dependence of plasticity. *Neuron*, 75(4):556–571.

Ferrante, R., Kowall, N., and Richardson, E. (1991). Proliferative and degenerative changes in striatal spiny neurons in huntington's disease: a combined study using the section-golgi method and calbindin d28k immunocytochemistry. *The Journal of Neuroscience*, 11(12):3877.

Fiacco, T. A. and McCarthy, K. D. (2006). Astrocyte calcium elevations: Properties, propagation, and effects on brain signaling. *Glia*, 54(7):676–690.

Filion, M. and Tremblay, L. (1991). Abnormal spontaneous activity of globus pallidus neurons in monkeys with mptp-induced parkinsonism. *Brain Research*, 547(1):140–144.

Fino, E., Deniau, J.-M., and Venance, L. (2008). Cell-specific spike-timing-dependent plasticity in gabaergic and cholinergic interneurons in corticostriatal rat brain slices. *J. Physiol.*

Fino, E., Glowinski, J., and Venance, L. (2005). Bidirectional activity-dependent plasticity at corticostriatal synapses. *Journal of Neuroscience*, 25(49):11279–11287.

Fino, E., Paille, V., Cui, Y., Morera-Herreras, T., Deniau, J.-M., and Venance, L. (2010). Distinct coincidence detectors govern the corticostriatal spike timing-dependent plasticity. *J Physiol*, 588(Pt 16):3045–62.

Fino, E., Paille, V., Deniau, J.-M., and Venance, L. (2009). Asymmetric spike-timing dependent plasticity of striatal nitric oxide-synthase interneurons. *Neuroscience*.

Fiorillo, C. D., Tobler, P. N., and Schultz, W. (2003). Discrete coding of reward probability and uncertainty by dopamine neurons. *Science*, 299(5614):1898–1902.

Forest, D. (2014). *Neuroscepticism: les sciences du cerveau sous le scalpel de l'épistémologue*. Editions d'Ithaque.

Fowler, C. J. (2013). Transport of endocannabinoids across the plasma membrane and within the cell. *The FEBS journal*, 280(9):1895–1904.

Frank, M. J. (2005). Dynamic dopamine modulation in the basal ganglia: A neurocomputational account of cognitive deficits in medicated and nonmedicated parkinsonism. *Journal of Cognitive Neuroscience*, 17(1):51–72.

Friedman, A., Lax, E., Dikshtein, Y., Abraham, L., Flaumenhaft, Y., Sudai, E., Ben-Tzion, M., and Yadid, G. (2011). Electrical stimulation of the lateral habenula produces an inhibitory effect on sucrose self-administration. *Neuropharmacology*, 60(2-3):381–387.

Froemke, R. C., Poo, M.-m., and Dan, Y. (2005). Spike-timing-dependent synaptic plasticity depends on dendritic location. *Nature*, 434(7030):221.

Fuenzalida, M., Fernández de Sevilla, D., Couve, A., and Buno, W. (2009). Role of ampa and nmda receptors and back-propagating action potentials in spike timing–dependent plasticity. *Journal of neurophysiology*, 103(1):47–54.

Fujimoto, K. and Kita, H. (1993). Response characteristics of subthalamic neurons to the stimulation of the sensorimotor cortex in the rat. *Brain research*, 609(1):185–192.

Gadagkar, V., Puzerey, P. A., Chen, R., Baird-Daniel, E., Farhang, A. R., and Goldberg, J. H. (2016). Dopamine neurons encode performance error in singing birds. *Science*, 354(6317):1278–1282.

Galvan, A., Hu, X., Rommelfanger, K. S., Pare, J.-F., Khan, Z. U., Smith, Y., and Wichmann, T. (2014). Localization and function of dopamine receptors in the subthalamic nucleus of normal and parkinsonian monkeys. *Journal of Neurophysiology*, 112(2):467–479.

Galvan, A. and Wichmann, T. (2008). Pathophysiology of parkinsonism. *Clinical neurophysiology : official journal of the International Federation of Clinical Neurophysiology*, 119(7):1459–1474.

Gerfen, C. R. and Surmeier, D. J. (2011). Modulation of striatal projection systems by dopamine. *Annual review of neuroscience*, 34:441–466.

Gerfen, C. R. and Wilson, C. J. (1996). *Handbook of chemical neuroanatomy, Vol 12: Integrated systems of the CNS, Part III*. Elsevier.

Gerstner, W. and Kistler, W. M. (2002). *Spiking neuron models: Single neurons, populations, plasticity*. Cambridge university press.

Gjorgjieva, J., Clopath, C., Audet, J., and Pfister, J.-P. (2011). A triplet spike-timing–dependent plasticity model generalizes the bienenstock–cooper–munro rule to higher-order spatiotemporal correlations. *Proceedings of the National Academy of Sciences*, 108(48):19383–19388.

Goldberg, J. A., Boraud, T., Maraton, S., Haber, S. N., Vaadia, E., and Bergman, H. (2002). Enhanced synchrony among primary motor cortex neurons in the 1-methyl-4-phenyl-1,2,3,6-tetrahydropyridine primate model of parkinson's disease. *The Journal of Neuroscience*, 22(11):4639.

Grace, A. (1991). Phasic versus tonic dopamine release and the modulation of dopamine system responsivity: a hypothesis for the etiology of schizophrenia. *Neuroscience*, 41(1):1–24.

Grace, A. A. (2000). The tonic/phasic model of dopamine system regulation and its implications for understanding alcohol and psychostimulant craving. *Addiction*, 95(8s2):119–128.

Grace, A. A. and Bunney, B. S. (1984a). The control of firing pattern in nigral dopamine neurons: burst firing. *The Journal of Neuroscience*.

Grace, A. A. and Bunney, B. S. (1984b). The control of firing pattern in nigral dopamine neurons: single spike firing. *The Journal of Neuroscience.*, 4(11):2866–2876.

Graupner, M. and Brunel, N. (2007). Stdp in a bistable synapse model based on camkii and associated signaling pathways. *PLoS Comput Biol*, 3(11):e221.

Graupner, M. and Brunel, N. (2010). Mechanisms of induction and maintenance of spike-timing dependent plasticity in biophysical synapse models. *Frontiers in Computational Neuroscience*, 4(136).

Graupner, M. and Brunel, N. (2012). Calcium-based plasticity model explains sensitivity of synaptic changes to spike pattern, rate, and dendritic location. *Proceedings of the National Academy of Sciences*, 109(10):3991–3996.

Graupner, M., Wallisch, P., and Ostojic, S. (2016). Natural firing patterns imply low sensitivity of synaptic plasticity to spike timing compared with firing rate. *Journal of Neuroscience*, 36(44):11238–11258.

Griffith, T., Tsaneva-Atanasova, K., and Mellor, J. R. (2016). Control of ca2+ influx and calmodulin activation by sk-channels in dendritic spines. *PLoS computational biology*, 12(5):e1004949.

Guo, Y. and Rubin, J. E. (2011). Multi-site stimulation of subthalamic nucleus diminishes thalamocortical relay errors in a biophysical network model. *Neural Networks*, 24(6):602–616.

Habib, M. (2004). Athymhormia and disorders of motivation in basal ganglia disease. *The Journal of Neuropsychiatry and Clinical Neurosciences*, 16(4):509–524.

Hagiwara, S. and Takahashi, K. (1974). The anomalous rectification and cation selectivity of the membrane of a starfish egg cell. *J. Membrane Biol.*

Hahn, P. J. and McIntyre, C. C. (2010). Modeling shifts in the rate and pattern of subthalamopallidal network activity during deep brain stimulation. *Journal of computational neuroscience*, 28(3):425–441.

Haj-Yasein, N. N., Jensen, V., Vindedal, G. F., Gundersen, G. A., Klungland, A., and Ottersen, O. P. (2011). Evidence that compromised k+ spatial buffering contributes to the epileptogenic effect of mutations in the human kir4.1 gene (kcnj10). *Glia*.

Hallett, M. (2008). The intrinsic and extrinsic aspects of freezing of gait. *Movement disorders : official journal of the Movement Disorder Society*, 23(0 2):S439–S443.

Halliday, G. M., McRitchie, D. A., Macdonald, V., Double, K. L., Trent, R. J., and McCusker, E. (1998). Regional specificity of brain atrophy in huntington's disease. *Experimental Neurology*, 154(2):663–672.

Han, V. Z., Grant, K., and Bell, C. C. (2000). Reversible associative depression and nonassociative potentiation at a parallel fiber synapse. *Neuron*, 27(3):611–622.

Hartmann, A., Müllner, J., Meier, N., Hesekamp, H., van Meerbeeck, P., Habert, M.-O., Kas, A., Tanguy, M.-L., Mazmanian, M., Oya, H., Abuaf, N., Gaouar, H., Salhi, S., Charbonnier-Beaupel, F., Fievet, M.-H., Galanaud, D., Arguillere, S., Roze, E., Degos, B., Grabli, D., Lacomblez, L., Hubsch, C., Vidailhet, M., Bonnet, A.-M., Corvol, J.-C., and Schüpbach, M. (2016). Bee venom for the treatment of parkinson disease –a randomized controlled clinical trial. *PLoS ONE*, 11(7):e0158235.

Henn, F. and Edwards, E. (1994). Animal models in the study of genetic factors in human psychopathology. *Genetic studies in affective disorders: overview of basic methods, current directions, and critical research issues. New York: John Wiley and Sons*, pages 177–192.

Henn, F., Johnson, J., Edwards, E., and Anderson, D. (1985). Melancholia in rodents: neurobiology and pharmacology. *Psychopharmacology bulletin*, 21(3):443.

Hestrin, S. (1992). Activation and desensitization of glutamate-activated channels mediating fast excitatory synaptic currents in the visual cortex. *Neuron*, 9(5):991–999.

Hibino, H., Inanobe, A., Furutani, K., Murakami, S., Findlay, I., and Kurachi, Y. (2010). Inwardly rectifying potassium channels: Their structure, function, and physiological roles. *Physiological Reviews*, 90(1):291–366.

Higley, M. J. and Sabatini, B. L. (2010). Competitive regulation of synaptic ca 2+ influx by d2 dopamine and a2a adenosine receptors. *Nature neuroscience*, 13(8):958.

Hikosaka, O. (2010). The habenula: from stress evasion to value-based decision-making. *Nat Rev Neurosci*, 11(7):503–513.

Hodgkin, A. L. and Huxley, A. F. (1952). A quantitative description of membrane current and its application to conduction and excitation in nerve. *The Journal of physiology*, 117(4):500–544.

Hoffman, D. A., Magee, J. C., Colbert, C. M., and Johnston, D. (1997). K+ channel regulation of signal propagation in dendrites of hippocampal pyramidal neurons. *Nature*, 387(6636):869.

Holbro, N., Grunditz, Å., Wiegert, J. S., and Oertner, T. G. (2010). Ampa receptors gate spine ca2+ transients and spike-timing-dependent potentiation. *Proceedings of the National Academy of Sciences*, 107(36):15975–15980.

Holt, A. B. and Netoff, T. I. (2014). Origins and suppression of oscillations in a computational model of parkinson's disease. *Journal of computational neuroscience*, 37(3):505–521.

Hoshiyama, M., Kaneoke, Y., Koike, Y., Takahashi, A., and Watanabe, S. (1994). Hypokinesia of associated movement in parkinson's disease: A symptom in early stages of the disease. *Journal of Neurology*, 241(9):517–521.

Howlett, A. C., Breivogel, C. S., Childers, S. R., Deadwyler, S. A., Hampson, R. E., and Porrino, L. J. (2004). Cannabinoid physiology and pharmacology: 30 years of progress. *Neuropharmacology*, 47:345–358.

Hübel, N. and Dahlem, M. A. (2014). Dynamics from seconds to hours in hodgkin-huxley model with time-dependent ion concentrations and buffer reservoirs. *PLoS Comput Biol*, 10(12):e1003941.

Humphries, M., Stewart, R., and Gurney, K. (2006). A physiologically plausible model of action selection and oscillatory activity in the basal ganglia. *J. Neurosci.*, 26(50):12921–12942.

Hyland, B. I., Reynolds, J. N. J., Hay, J., Perk, C. G., and Miller, R. (2002). Firing modes of midbrain dopamine cells in the freely moving rat. *Neuroscience*, 114(2):475–492.

Inglis, F. M. and Moghaddam, B. (1999). Dopaminergic innervation of the amygdala is highly responsive to stress. *Journal of neurochemistry*, 72(3):1088–1094.

Izhikevich, E. M. (2003). Simple model of spiking neurons. *IEEE Transactions on neural networks*, 14(6):1569–1572.

Jackson, D. M. and Westlind-Danielsson, A. (1994). Dopamine receptors: molecular biology, biochemistry and behavioural aspects. *Pharmacology & therapeutics*, 64(2):291–370.

Jedrzejewski-Szmek, Z. and Blackwell, K. T. (2016). Asynchronous τ-leaping. *The Journal of chemical physics*, 144(12):125104.

Jhou, T. C., Fields, H. L., Baxter, M. G., Saper, C. B., and Holland, P. C. (2009). The rostromedial tegmental nucleus (rmtg), a major gabaergic afferent to midbrain dopamine neurons, selectively encodes aversive stimuli and promotes behavioral inhibition. *Neuron*, 61(5):786–800.

Jhou, T. C., Geisler, S., Marinelli, M., DeGarmo, B. A., and Zahm, D. S. (2011). The mesopontine rostromedial tegmental nucleus: a structure targeted by the lateral habenula that projects to the ventral tegmental area of tsai and substantia nigra compacta. *J Comp Neurol*, pages 566–596.

Jin, L.-Q., Wang, H.-Y., and Friedman, E. (2001). Stimulated d1 dopamine receptors couple to multiple gα proteins in different brain regions. *Journal of neurochemistry*, 78(5):981–990.

Jones, S. L., To, M.-S., and Stuart, G. J. (2017). Dendritic small conductance calcium-activated potassium channels activated by action potentials suppress epsps and gate spike-timing dependent synaptic plasticity. *eLife*, 6.

Kager, H., Wadman, W. J., and Somjen, G. G. (2000). Simulated seizures and spreading depression in a neuron model incorporating interstitial space and ion concentrations. *Journal of Neurophysiology*, 84(1):495–512.

Kager, H., Wadman, W. J., and Somjen, G. G. (2007). Seizure-like afterdischarges simulated in a model neuron. *J Comput Neurosci*, 22(2):105–28.

Kampa, B. M., Clements, J., Jonas, P., and Stuart, G. J. (2004). Kinetics of mg2+ unblock of nmda receptors: implications for spike-timing dependent synaptic plasticity. *The Journal of physiology*, 556(2):337–345.

Kandel, E. R., Schwartz, J. H., Jessell, T. M., Siegelbaum, S. A., and Hudspeth, A. J. (2013). *Principles of neural science*, volume 4. McGraw-hill New York.

Karmarkar, U. R., Najarian, M. T., and Buonomano, D. V. (2002). Mechanisms and significance of spike-timing dependent plasticity. *Biological cybernetics*, 87(5-6):373–382.

Karwoski, C. J., Coles, J. A., Lu, H. K., and Huang, B. (1989). Current-evoked transcellular k+ flux in frog retina. *J. Neurophysiol.*

Katz, B. (1949). Les constantes electriques de la membrane du muscle. *Arch Sci Physiol*, 3.

Kempter, R., Gerstner, W., and Hemmen, J. L. v. (2001). Intrinsic stabilization of output rates by spike-based hebbian learning. *Neural computation*, 13(12):2709–2741.

Kerr, C. C., Van Albada, S. J., Neymotin, S. A., Chadderdon, G. L., Robinson, P. A., and Lytton, W. W. (2013). Cortical information flow in parkinson's disease: a composite network/field model. *Frontiers in Computational Neuroscience*, 7:39.

Kiebel, S., Garrido, M., Moran, R., and Friston, K. (2008). Dynamic causal modelling for eeg and meg. *Cognitive Neurodynamics*, 2(2):121–136.

Kim, B., Hawes, S. L., Gillani, F., Wallace, L. J., and Blackwell, K. T. (2013). Signaling pathways involved in striatal synaptic plasticity are sensitive to temporal pattern and exhibit spatial specificity. *PLoS computational biology*, 9(3):e1002953.

Kim, J. and Li, Y. (2015). Chronic activation of cb2 cannabinoid receptors in the hippocampus increases excitatory synaptic transmission. *The Journal of Physiology*, 593(4):871–886.

Kimura, K., White, B. H., and Sidhu, A. (1995). Coupling of human d-1 dopamine receptors to different guanine nucleotide binding proteins. evidence that d-1 dopamine receptors can couple to both gs and go. *Journal of Biological Chemistry*, 270(24):14672–14678.

Kish, S. J., Shannak, K., and Hornykiewicz, O. (1988). Uneven pattern of dopamine loss in the striatum of patients with idiopathic parkinson's disease. *New England Journal of Medicine*, 318(14):876–880.

Kiyatkin, E. and Stein, E. (1995). Fluctuations in nucleus accumbens dopamine during cocaine self-administration behavior: an in vivo electrochemical study. *Neuroscience*, 64(3):599–617.

Knowlton, B. J., Mangels, J. A., and Squire, L. R. (1996). A neostriatal habit learning system in humans. *Science*, 273(5280):1399.

Koester, H. J. and Sakmann, B. (1998). Calcium dynamics in single spines during coincident pre-and postsynaptic activity depend on relative timing of back-propagating action potentials and subthreshold excitatory postsynaptic potentials. *Proceedings of the National Academy of Sciences*, 95(16):9596–9601.

Kofuji, P. and Newman, E. A. (2004). Potassium buffering in the central nervous system. *Neuroscience*, 129(4):1045–56.

Koob, G. F., Riley, S. J., Smith, S. C., and Robbins, T. W. (1978). Effects of 6-hydroxydopamine lesions of the nucleus accumbens septi and olfactory tubercle on feeding, locomotor activity, and amphetamine anorexia in the rat. *Journal of comparative and physiological psychology*, 92(5):917.

Kotecha, S. A., Oak, J. N., Jackson, M. F., Perez, Y., Orser, B. A., Van Tol, H. H., and MacDonald, J. F. (2002). A d2 class dopamine receptor transactivates a receptor tyrosine kinase to inhibit nmda receptor transmission. *Neuron*, 35(6):1111–1122.

Kravitz, A. V., Freeze, B. S., Parker, P. R., Kay, K., Thwin, M. T., Deisseroth, K., and Kreitzer, A. C. (2010). Regulation of parkinsonian motor behaviors by optogenetic control of basal ganglia circuitry. *Nature*, 466(7306):622–626.

Kravitz, A. V., Tye, L. D., and Kreitzer, A. C. (2012). Distinct roles for direct and indirect pathway striatal neurons in reinforcement. *Nature neuroscience*, 15(6):816–818.

Kumar, A., Cardanobile, S., Rotter, S., and Aertsen, A. (2011). The role of inhibition in generating and controlling parkinson's disease oscillations in the basal ganglia. *Frontiers in Systems Neuroscience*, 5:86.

Kumar, A. and Mehta, M. (2011). Frequency-dependent changes in nmdar-dependent synaptic plasticity. *Frontiers in Computational Neuroscience*, 5:38.

Kumaravelu, K., Brocker, D. T., and Grill, W. M. (2016). A biophysical model of the cortex-basal ganglia-thalamus network in the 6-ohda lesioned rat model of parkinson's disease. *Journal of Computational Neuroscience*, 40(2):207–229.

Kuznetsov, A. S., Kopell, N. J., and Wilson, C. J. (2006). Transient high-frequency firing in a coupled-oscillator model of the mesencephalic dopaminergic neuron. *Journal of Neurophysiology*, 95(2):932–947.

Kwag, J. and Paulsen, O. (2009). The timing of external input controls the sign of plasticity at local synapses. *Nature neuroscience*, 12(10):1219.

Lachowicz, J. E. and Sibley, D. R. (1997). Molecular characteristics of mammalian dopamine receptors. *Basic & Clinical Pharmacology & Toxicology*, 81(3):105–113.

Lammel, S., Lim, B. K., Ran, C., Huang, K. W., Betley, M. J., Tye, K., Deisseroth, K., and Malenka, R. C. (2012). Input-specific control of reward and aversion in the ventral tegmental area. *Nature*, 491(7423):212–217.

Lavin, A., Nogueira, L., Lapish, C. C., Wightman, R. M., Phillips, P. E., and Seamans, J. K. (2005). Mesocortical dopamine neurons operate in distinct temporal domains using multimodal signaling. *Journal of Neuroscience*, 25(20):5013–5023.

Lazarus, J.-A. C. and Stelmach, G. E. (1992). Interlimb coordination in parkinson's disease. *Movement Disorders*, 7(2):159–170.

Leblois, A., Boraud, T., Meissner, W., Bergman, H., and Hansel, D. (2006). Competition between feedback loops underlies normal and pathological dynamics in the basal ganglia. *The Journal of Neuroscience*, 26(13):3567.

Legrenzi, P. and Umiltà, C. (2011). *Neuromania: On the limits of brain science*. Oxford University Press.

Letzkus, J. J., Kampa, B. M., and Stuart, G. J. (2006). Learning rules for spike timing-dependent plasticity depend on dendritic synapse location. *The Journal of Neuroscience*.

Lévesque, M. and Parent, A. (2005). The striatofugal fiber system in primates: A reevaluation of its organization based on single-axon tracing studies. *Proceedings of the National Academy of Sciences of the United States of America*, 102(33):11888–11893.

Li, B., Piriz, J., Mirrione, M., Chung, C., Proulx, C. D., Schulz, D., Henn, F., and Malinow, R. (2011). Synaptic potentiation onto habenula neurons in the learned helplessness model of depression. *Nature*, 470(7335):535–539.

Li, K., Zhou, T., Liao, L., Yang, Z., Wong, C., Henn, F., Malinow, R., Yates, J. R., and Hu, H. (2013). βcamkii in lateral habenula mediates core symptoms of depression. *Science (New York, N.Y.)*, 341(6149):1016–1020.

Liao, T. W. (2005). Clustering of time series data—a survey. *Pattern recognition*, 38(11):1857–1874.

Lin, M. T., Luján, R., Watanabe, M., Adelman, J. P., and Maylie, J. (2008). Sk2 channel plasticity contributes to ltp at schaffer collateral–ca1 synapses. *Nature neuroscience*, 11(2):170.

Lindahl, M. and Hellgren Kotaleski, J. (2016). Untangling basal ganglia network dynamics and function: Role of dopamine depletion and inhibition investigated in a spiking network model. *eNeuro*, 3(6):ENEURO.0156–16.2016.

Lindahl, M., Sarvestani, I. K., Ekeberg, Ö., and Kotaleski, J. H. (2013). Signal enhancement in the output stage of the basal ganglia by synaptic short-term plasticity in the direct, indirect, and hyperdirect pathways. *frontiers in computational neuroscience*.

Lindskog, M., Kim, M., Wikstram, M. A., Blackwell, K. T., and Kotaleski, J. H. (2006). Transient calcium and dopamine increase pka activity and darpp-32 phosphorylation. *PLoS Comput Biol*, 2(9):e119.

Lisman, J. (1989). A mechanism for the hebb and the anti-hebb processes underlying learning and memory. *Proceedings of the National Academy of Sciences*, 86(23):9574–9578.

Lloyd, K. G., Davidson, L., and Hornykiewicz, O. (1975). The neurochemistry of parkinson's disease: effect of l-dopa therapy. *Journal of Pharmacology and Experimental Therapeutics*, 195(3):453.

Lobb, C. J., Troyer, T. W., Wilson, C. J., and Paladini, C. A. (2011). Disinhibition bursting of dopaminergic neurons. *Frontiers in Systems Neuroscience*, 5(25).

López-Azcárate, J., Tainta, M., Rodríguez-Oroz, M. C., Valencia, M., González, R., Guridi, J., Iriarte, J., Obeso, J., Artieda, J., and Alegre, M. (2010). Coupling between beta and high-frequency activity in the human subthalamic nucleus may be a

pathophysiological mechanism in parkinson's disease. *The Journal of Neuroscience*, 30(19):6667.

Lu, J.-t., Li, C.-y., Zhao, J.-P., Poo, M.-m., and Zhang, X.-h. (2007). Spike-timing-dependent plasticity of neocortical excitatory synapses on inhibitory interneurons depends on target cell type. *Journal of Neuroscience*, 27(36):9711–9720.

Magee, D. and Johnston, D. (1997). A synaptically controlled, associative signal for hebbian plasticity in hippocampal neurons. *Science*, pages 209–2012.

Maier, S. F. (1984). Learned helplessness and animal models of depression. *Prog. Neuro-Psychopharmacol & Biol. Psychiat.*

Mandali, A., Rengaswamy, M., Chakravarthy, V. S., and Moustafa, A. A. (2015). A spiking basal ganglia model of synchrony, exploration and decision making. *Frontiers in Neuroscience*, 9:191.

Markram, H., Lübke, J., Frotscher, M., and Sakmann, B. (1997). Regulation of synaptic efficacy by coincidence of postsynaptic aps and epsps. *Science*, pages 213–214.

Marreiros, A., Cagnan, H., Moran, R. J., Friston, K. J., and Brown, P. (2013). Basal ganglia–cortical interactions in parkinsonian patients. *Neuroimage*, 66(C):301–310.

Marsden, C. D. and Obeso, J. A. (1994). The functions of the basal ganglia and the paradox of stereotaxic surgery in parkinson's disease. *Brain*, 117(4):877–897.

Martin, S. J., Grimwood, P. D., and Morris, R. G. M. (2000). Synaptic plasticity and memory: An evaluation of the hypothesis. *Annual Review of Neuroscience*, 23(1):649–711.

Matamales, M., Bertran-Gonzalez, J., Salomon, L., Degos, B., Deniau, J.-M., Valjent, E., Hervé, D., and Girault, J.-A. (2009). Striatal medium-sized spiny neurons: identification by nuclear staining and study of neuronal subpopulations in bac transgenic mice. *PloS one*, 4(3):e4770.

Mathai, A. and Smith, Y. (2011). The corticostriatal and corticosubthalamic pathways: Two entries, one target. so what? *Frontiers in Systems Neuroscience*, 5:64.

Matsui, A. and Williams, J. T. (2011). Opioid-sensitive gaba inputs from rostromedial tegmental nucleus synapse onto midbrain dopamine neurons. *Journal of Neuroscience*, 31(48):17729–17735.

Matsumoto, H., Tian, J., Uchida, N., and Watabe-Uchida, M. (2016). Midbrain dopamine neurons signal aversion in a reward-context-dependent manner. *eLife*, 5(OCTOBER2016).

Matsumoto, M. and Hikosaka, O. (2007). Lateral habenula as a source of negative reward signals in dopamine neurons. *Nature*, 447(7148):1111–1115.

Matsumoto, M. and Hikosaka, O. (2009). Representation of negative motivational value in the primate lateral habenula. *Nat Neurosci*, 12(1):77–84.

Maurice, N., Deltheil, T., Melon, C., Degos, B., Mourre, C., Amalric, M., and Kerkerian-Le Goff, L. (2015). Bee venom alleviates motor deficits and modulates the transfer of cortical information through the basal ganglia in rat models of parkinson's disease. *PLoS ONE*, 10(11):e0142838.

Maurice, N., Deniau, J.-M., Glowinski, J., and Thierry, A.-M. (1999). Relationships between the prefrontal cortex and the basal ganglia in the rat: Physiology of the cortico-nigral circuits. *The Journal of Neuroscience*, 19(11)59:4674–4681.

Mazzanti, M. and DeFelice, L. J. (1988). K channel kinetics during the spontaneous heart beat in embryonic chick ventricle cells. *Biophysical Journal*, 54(6):1139–1148.

McCulloch, W. S. and Pitts, W. (1943). A logical calculus of the ideas immanent in nervous activity. *The bulletin of mathematical biophysics*, 5(4):115–133.

Mechoulam, R. and Parker, L. A. (2013). The endocannabinoid system and the brain. *Annual review of psychology*, 64:21–47.

Medina, L. and Reiner, A. (1995). Neurotransmitter organization and connectivity of the basal ganglia in vertebrates: Implications for the evolution of basal ganglia (part 1 of 2). *Brain, Behavior and Evolution*, 46(4-5):235–246.

Medvedev, G., Wilson, C., Callaway, J., and Kopell, N. (2003). Dendritic synchrony and transient dynamics in a coupled oscillator model of the dopaminergic neuron. *J Comput Neurosci.*, 48:53–69.

Mein, M.-T. (1988). Les représentations du cerveau: modèles historiques. *Aster*.

Melgari, J.-M., Curcio, G., Mastrolilli, F., Salomone, G., Trotta, L., Tombini, M., di Biase, L., Scrascia, F., Fini, R., Fabrizio, E., Rossini, P. M., and Vernieri, F. (2014). Alpha and beta eeg power reflects l-dopa acute administration in parkinsonian patients. *Frontiers in Aging Neuroscience*, 6(302).

Meng, H., Wang, Y., Huang, M., Lin, W., Wang, S., and Zhang, B. (2011). Chronic deep brain stimulation of the lateral habenula nucleus in a rat model of depression. *Brain Research*, 1422:32–38.

Merrison-Hort, R. and Borisyuk, R. (2013). The emergence of two anti-phase oscillatory neural populations in a computational model of the parkinsonian globus pallidus. *Frontiers in Computational Neuroscience*, 7:173.

Mihalas, S. (2011). Calcium messenger heterogeneity: a possible signal for spike timing-dependent plasticity. *Frontiers in computational neuroscience*, 4:158.

Mink, J. W. (1996). The basal ganglia: focused selection and inhibition of competing motor programs. *Progress in Neurobiology*, 50(4):381–425.

Missale, C., Nash, S. R., Robinson, S. W., Jaber, M., and Caron, M. G. (1998). Dopamine receptors: from structure to function. *Physiological reviews*, 78(1):189–225.

Miyachi, S., Hikosaka, O., and Lu, X. (2002). Differential activation of monkey striatal neurons in the early and late stages of procedural learning. *Experimental Brain Research*, 146(1):122–126.

Miyachi, S., Hikosaka, O., Miyashita, K., Kárádi, Z., and Rand, M. K. (1997). Differential roles of monkey striatum in learning of sequential hand movement. *Experimental Brain Research*, 115(1):1–5.

Moran, R. J., Mallet, N., Litvak, V., Dolan, R. J., Magill, P. J., Friston, K. J., and Brown, P. (2011). Alterations in brain connectivity underlying beta oscillations in parkinsonism. *PLoS Comput Biol*, 7(8):e1002124.

Morris, J. S., Smith, K. A., Cowen, P. J., Friston, K. J., and Dolan, R. J. (1999). Covariation of activity in habenula and dorsal raphénuclei following tryptophan depletion. *NeuroImage*, 10(2):163–172.

Muller, L. and Destexhe, A. (2012). Propagating waves in thalamus, cortex and the thalamocortical system: Experiments and models. *Journal of Physiology-Paris*, 106(5):222–238.

Nakanishi, H., Kita, H., and Kitai, S. (1991). Intracellular study of rat entopeduncular nucleus neurons in an in vitro slice preparation: response to subthalamic stimulation. *Brain research*, 549(2):285–291.

Nakano, T., Yoshimoto, J., and Doya, K. (2013). A model-based prediction of the calcium responses in the striatal synaptic spines depending on the timing of cortical and dopaminergic inputs and post-synaptic spikes. *Frontiers in computational neuroscience*, 7:119.

Nambu, A., Tokuno, H., and Takada, M. (2002). Functional significance of the cortico–subthalamo–pallidal 'hyperdirect'pathway. *Neuroscience Research*, 43(2):111–117.

Nedergaard, S. and Greenfield, S. A. (1992). Sub-populations of pars compacta neurons in the substantia nigra: The significance of qualitatively and quantitatively distinct conductances. *Neuroscience*, 48(2):423–437.

Nelson, A. B. and Kreitzer, A. C. (2014). Reassessing models of basal ganglia function and dysfunction. *Annual review of neuroscience*, 37:117–135.

Neumann, P. A., Ishikawa, M., Otaka, M., Huang, Y. H., Schlüter, O. M., and Dong, Y. (2015). Increased excitability of lateral habenula neurons in adolescent rats following cocaine self-administration. *International Journal of Neuropsychopharmacology*, 18(6).

Nevian, T. and Sakmann, B. (2006). Spine ca2+ signaling in spike-timing-dependent plasticity. *Journal of Neuroscience*, 26(43):11001–11013.

Ngo-Anh, T. J., Bloodgood, B. L., Lin, M., Sabatini, B. L., Maylie, J., and Adelman, J. P. (2005). Sk channels and nmda receptors form a ca 2+-mediated feedback loop in dendritic spines. *Nature neuroscience*, 8(5):642.

Nieuwboer, A., Rochester, L., Müncks, L., and Swinnen, S. P. (2009). Motor learning in parkinson's disease: limitations and potential for rehabilitation. *Parkinsonism & Related Disorders*, 15:S53–S58.

Nishiyama, M., Hong, K., Mikoshiba, K., Poo, M.-M., and Kato, K. (2000). Calcium stores regulate the polarity and input specificity of synaptic modification. *Nature*, 408(6812):584–588.

Niv, Y., Duff, M. O., and Dayan, P. (2005). Dopamine, uncertainty and td learning. *Behavioral and brain functions : BBF*, 1:6–6.

Noori, H. R. (2011). The impact of the glial spatial buffering on the k+ nernst potential. *Cogn Neurodyn*.

Oakley II, B., Katz, B. J., Xu, Z., and Zheng, J. (1992). Spatial buffering of extracellular potassium by müller (glial) cells in the toad retina. *Experimental Eye Research*, 55(4):539–550.

Obeso, J. A., Marin, C., Rodriguez-Oroz, C., Blesa, J., Benitez-Temiño, B., Mena-Segovia, J., Rodríguez, M., and Olanow, C. W. (2008). The basal ganglia in parkinson's disease: Current concepts and unexplained observations. *Annals of Neurology*, 64(S2):S30–S46.

Odekerken, V. J., Boel, J. A., Schmand, B. A., de Haan, R. J., Figee, M., van den Munckhof, P., Schuurman, P. R., de Bie, R. M., de Bie, R., Bour, L., et al. (2016). Gpi vs stn deep brain stimulation for parkinson disease three-year follow-up. *Neurology*, 86(8):755–761.

Okuma, Y. and Yanagisawa, N. (2008). The clinical spectrum of freezing of gait in parkinson's disease. *Movement Disorders*, 23(S2):S426–S430.

Oliveira, R. F., Kim, M., and Blackwell, K. T. (2012). Subcellular Location of PKA Controls Striatal Plasticity: Stochastic Simulations in Spiny Dendrites. *PLoS computational Biology*.

Olsen, M. L., Higashimori, H., Campbell, S. L., Hablitz, J. J., and Sontheimer, H. (2006). Functional expression of kir4.1 channels in spinal cord astrocytes. *Glia*.

Oorschot, D. E. (1996). Total number of neurons in the neostriatal, pallidal, subthalamic, and substantia nigral nuclei of the rat basal ganglia: A stereological study using the cavalieri and optical disector methods. *The Journal of Comparative Neurology*, 366(4):580–599.

Oswald, A.-M. M., Doiron, B., Rinzel, J., and Reyes, A. D. (2009). Spatial profile and differential recruitment of gabab modulate oscillatory activity in auditory cortex. *Journal of Neuroscience*, 29(33):10321–10334.

Overton, P. G. and Clark, D. (1997). Burst firing in midbrain dopaminergic neurons. *Brain Research Reviews*, 25(3):312–334.

Owen, J. A., Ernest, B., and Cressman, J. R. (2013). Controlling seizure-like events by perturbing ion concentration dynamics with periodic stimulation. *PLoS ONE*.

Packard, M. G., Hirsh, R., and White, N. M. (1989). Differential effects of fornix and caudate nucleus lesions on two radial maze tasks: evidence for multiple memory systems. *Journal of Neuroscience*, 9(5):1465–1472.

Paille, V., Fino, E., Du, K., Morera-Herreras, T., Perez, S., Kotaleski, J. H., and Venance, L. (2013). Gabaergic circuits control spike-timing-dependent plasticity. *J Neurosci*, 33(22):9353–63.

Parent, A. and Hazrati, L.-N. (1993). Anatomical aspects of information processing in primate basal ganglia. *Trends in neurosciences*, 16(3):111–116.

Parent, A., Sato, F., Wu, Y., Gauthier, J., Lévesque, M., and Parent, M. (2000). Organization of the basal ganglia: the importance of axonal collateralization. *Trends in Neurosciences*, 23, Supplement 1:S20–S27.

Parent, M., Lévesque, M., and Parent, A. (1999). The pallidofugal projection system in primates: evidence for neurons branching ipsilaterally and contralaterally to the thalamus and brainstem. *Journal of Chemical Neuroanatomy*, 16(3):153–165.

Park, M., Falls, W., and Kitai, S. (1982). An intracellular hrp study of the rat globus pallidus. i. responses and light microscopic analysis. *Journal of Comparative Neurology*, 211(3):284–294.

Pasupathy, A. and Miller, E. K. (2005). Different time courses of learning-related activity in the prefrontal cortex and striatum. *Nature*, 433(7028):873.

Paulsen, J. S. (2011). Cognitive impairment in huntington disease: Diagnosis and treatment. *Current neurology and neuroscience reports*, 11(5):474–483.

Paulsen, J. S. and Long, J. D. (2014). Onset of huntington disease: Can it be purely cognitive? *Movement disorders : official journal of the Movement Disorder Society*, 29(11):1342–1350.

Pavlides, A., Hogan, S. J., and Bogacz, R. (2015). Computational models describing possible mechanisms for generation of excessive beta oscillations in parkinson's disease. *PLoS Computational Biology*, 11(12):e1004609.

Pawlak, V. and Kerr, J. N. (2008). Dopamine receptor activation is required for corticostriatal spike-timing-dependent plasticity. *The Journal of Neuroscience*, pages 2435–2446.

Perea, G., Navarrete, M., and Araque, A. (2009). Tripartite synapses: astrocytes process and control synaptic information. *Trends in neurosciences*, 32(8):421–431.

Phillips, P. E., Stuber, G. D., Heien, M. L., Wightman, R. M., and Carelli, R. M. (2003). Subsecond dopamine release promotes cocaine seeking. *Nature*, 422(6932):614–618.

Pi, H. J. and Lisman, J. E. (2008). Coupled phosphatase and kinase switches produce the tristability required for long-term potentiation and long-term depression. *Journal of Neuroscience*, 28(49):13132–13138.

Plotkin, J. L. and Surmeier, D. J. (2015). Corticostriatal synaptic adaptations in huntington's disease. *Current opinion in neurobiology*, 33:53–62.

Poirazi, P., Brannon, T., and Mel, B. W. (2003). Arithmetic of subthreshold synaptic summation in a model ca1 pyramidal cell. *Neuron*, 37(6):977–987.

Posturna, R. B. and Lang, A. E. (2003). Hemiballism: revisiting a classic disorder. *The Lancet Neurology*, 2(11):661–668.

Proulx, C. D., Hikosaka, O., and Malinow, R. (2014). Reward processing by the lateral habenula in normal and depressive behaviors. *nature neuroscience*, 17(9):1–7.

Quilodran, R., Rothe, M., and Procyk, E. (2008). Behavioral shifts and action valuation in the anterior cingulate cortex. *Neuron*, 57(2):314–325.

Rachmuth, G., Shouval, H. Z., Bear, M. F., and Poon, C.-S. (2011). A biophysically-based neuromorphic model of spike rate-and timing-dependent plasticity. *Proceedings of the National Academy of Sciences*, 108(49):E1266–E1274.

Ransom, C. and H, S. (1995). Biophysical and pharmacological characterization of inwardly rectifying k+ currents in rat spinal cord astrocytes. *J Neurophysiol*.

Redgrave, P. (2007). Basal ganglia. *Scholarpedia*, 2(6):1825.

Redgrave, P. and Gurney, K. (2006). The short-latency dopamine signal: a role in discovering novel actions? *Nat Rev Neurosci*, 7(12):967–975.

Redgrave, P., Rodriguez, M., Smith, Y., Rodriguez-Oroz, M. C., Lehericy, S., Bergman, H., Agid, Y., DeLong, M. R., and Obeso, J. A. (2010). Goal-directed and habitual control in the basal ganglia: implications for parkinson's disease. *Nature reviews. Neuroscience*, 11(11):760–772.

Requarth, T. and Sawtell, N. B. (2011). Neural mechanisms for filtering self-generated sensory signals in cerebellum-like circuits. *Current opinion in neurobiology*, 21(4):602–608.

Rodriguez-Oroz, M. C., Jahanshahi, M., Krack, P., Litvan, I., Macias, R., Bezard, E., and Obeso, J. A. (2009). Initial clinical manifestations of parkinson's disease: features and pathophysiological mechanisms. *The Lancet Neurology*, 8(12):1128–1139.

Rodriguez-Oroz, M. C., Rodriguez, M., Guridi, J., Mewes, K., Chockkman, V., Vitek, J., DeLong, M. R., and Obeso, J. A. (2001). The subthalamic nucleus in parkinson's disease: somatotopic organization and physiological characteristics. *Brain*, 124(9):1777–1790.

Roiser, J. P., Levy, J., Fromm, S. J., Nugent, A. C., Talagala, S. L., Hasler, G., Henn, F. A., Sahakian, B. J., and Drevets, W. C. (2009). The effects of tryptophan depletion on neural responses to emotional words in remitted depression. *Biological Psychiatry*, 66(5):441–450.

Rosas, H., Goodman, J., Chen, Y., Jenkins, B., Kennedy, D., Makris, N., Patti, M., Seidman, L., Beal, M., and Koroshetz, W. (2001). Striatal volume loss in hd as measured by mri and the influence of cag repeat. *Neurology*.

Rosenmund, C., Feltz, A., and Westbrook, G. L. (1995). Calcium-dependent inactivation of synaptic nmda receptors in hippocampal neurons. *Journal of neurophysiology*, 73(1):427–430.

Ruan, H., Saur, T., and Yao, W.-D. (2014). Dopamine-enabled anti-hebbian timing-dependent plasticity in prefrontal circuitry. *Frontiers in neural circuits*, 8:38.

Rubin, J. E., Gerkin, R. C., Bi, G.-Q., and Chow, C. C. (2005). Calcium time course as a signal for spike-timing–dependent plasticity. *Journal of neurophysiology*, 93(5):2600–2613.

Rubin, J. E., McIntyre, C. C., Turner, R. S., and Wichmann, T. (2012). Basal ganglia activity patterns in parkinsonism and computational modeling of their downstream effects. *The European Journal of Neuroscience*, 36(2):2213–2228.

Sakmann, B. and Trube, G. (1984). Conductance properties of single inwardly rectifying potassium channels in ventricular cells from guinea-pig heart. *The Journal of Physiology*, 347:641–657.

Sartorius, A., Kiening, K. L., Kirsch, P., von Gall, C. C., Haberkorn, U., Unterberg, A. W., Henn, F. A., and Meyer-Lindenberg, A. (2010). Remission of major depression under deep brain stimulation of the lateral habenula in a therapy-refractory patient. *Biological Psychiatry*, 67(2):e9–e11.

Saudargiene, A., Cobb, S., and Graham, B. P. (2015). A computational study on plasticity during theta cycles at schaffer collateral synapses on ca1 pyramidal cells in the hippocampus. *Hippocampus*, 25(2):208–218.

Saudargiene, A., Porr, B., and Wörgötter, F. (2004). How the shape of pre-and postsynaptic signals can influence stdp: a biophysical model. *Neural Computation*, 16(3):595–625.

Schultz, W. (1998). Predictive reward signal of dopamine neurons. *J Neurophysiol*, pages 1–27.

Schultz, W. (2002). Getting formal with dopamine and reward. *Neuron*, 36(2):241–263.

Schultz, W. (2015). Neuronal reward and decision signals: From theories to data. *Physiological Reviews*, 95(3):853.

Schultz, W., Dayan, P., and Montague, P. R. (1997). A neural substrate of prediction and reward. *Science*, 275(5306):1593–1599.

Schultz, W., Tremblay, L., and Hollerman, J. R. (2003). Changes in behavior-related neuronal activity in the striatum during learning. *Trends in neurosciences*, 26(6):321–328.

Schulz, J. M., Redgrave, P., and Reynolds, J. N. (2010). Cortico-striatal spike-timing dependent plasticity after activation of subcortical pathways. *Frontiers in synaptic neuroscience*, 2.

Schwartz, J. H. and Javitch, J. A. (2013). *Neurotransmitters*. McGraw-Hill Education.

Seamans, J. (2007). Dopamine anatomy. *Scholarpedia*, 2(6):3737.

Seamans, J. and Durstewitz, D. (2008). Dopamine modulation. *Scholarpedia*, 3(4):2711.

Seol, G. H., Ziburkus, J., Huang, S., Song, L., Kim, I. T., Takamiya, K., Huganir, R. L., Lee, H.-K., and Kirkwood, A. (2007). Neuromodulators control the polarity of spike-timing-dependent synaptic plasticity. *Neuron*, 55(6):919–29.

Shabel, S. J., Proulx, C. D., Trias, A., Murphy, R. T., and Malinow, R. (2012). Input to the lateral habenula from the basal ganglia is excitatory, aversive, and suppressed by serotonin. *Neuron*, 74(3):475–481.

Shen, K.-Z. and Johnson, S. W. (2006). Subthalamic stimulation evokes complex epscs in the rat substantia nigra pars reticulata in vitro. *The Journal of physiology*, 573(3):697–709.

Shen, W., Flajolet, M., Greengard, P., and Surmeier, D. J. (2008). Dichotomous dopaminergic control of striatal synaptic plasticity. *Science*, 321(5890):848–851.

Shen, W., Plotkin, J. L., Francardo, V., Ko, W. K. D., Xie, Z., Li, Q., Fieblinger, T., Wess, J., Neubig, R. R., Lindsley, C. W., et al. (2015). M4 muscarinic receptor signaling ameliorates striatal plasticity deficits in models of l-dopa-induced dyskinesia. *Neuron*, 88(4):762–773.

Shen, X., Ruan, X., and Zhao, H. (2012). Stimulation of midbrain dopaminergic structures modifies firing rates of rat lateral habenula neurons. *PLoS ONE*, 7(4):e34323.

Shoblock, J. R., Sullivan, E. B., Maisonneuve, I. M., and Glick, S. D. (2003). Neurochemical and behavioral differences between d-methamphetamine and d-amphetamine in rats. *Psychopharmacology*, 165(4):359–369.

Shouval, H. Z., Bear, M. F., and Cooper, L. N. (2002). A unified model of nmda receptor-dependent bidirectional synaptic plasticity. *Proceedings of the National Academy of Sciences*, 99(16):10831–10836.

Shouval, H. Z. and Kalantzis, G. (2005). Stochastic properties of synaptic transmission affect the shape of spike time–dependent plasticity curves. *Journal of neurophysiology*, 93(2):1069–1073.

Shumake, J., Edwards, E., and Gonzalez-Lima, F. (2003). Opposite metabolic changes in the habenula and ventral tegmental area of a genetic model of helpless behavior. *Brain Research*, 963(1–2):274–281.

Sibille, J., Dao Duc, K., Holcman, D., and Rouach, N. (2015). The neuroglial potassium cycle during neurotransmission: Role of kir4.1 channels. *PLoS Computational Biology*, 11(3):e1004137.

Sidhu, A. and Kimura, K. (1997). A novel regulation of expression of the α-subunit of the g stimulatory protein by dopamine via d1 dopamine receptors. *Journal of neurochemistry*, 68(1):187–194.

Siegenbeek, v. H. J. (1994). The role of the potassium inward rectifier in defining cell membrane potentials in low potassium media, analzed by computer simulation. *BiophysicalChemistry*.

Simola, N., Morelli, M., and Carta, A. R. (2007). The 6-hydroxydopamine model of parkinson's disease. *Neurotoxicity research*, 11(3-4):151–167.

Singh-Bains, M. K., Waldvogel, H. J., and Faull, R. L. M. (2016). The role of the human globus pallidus in huntington's disease. *Brain Pathology*, 26(6):741–751.

Sizemore, R. J., Seeger-Armbruster, S., Hughes, S. M., and Parr-Brownlie, L. C. (2016). Viral vector-based tools advance knowledge of basal ganglia anatomy and physiology. *Journal of Neurophysiology*, 115(4):2124.

Sjöström, P. J., Turrigiano, G. G., and Nelson, S. B. (2001). Rate, timing, and cooperativity jointly determine cortical synaptic plasticity. *Neuron*, 32(6):1149 – 1164.

Sjöström, P. J., Turrigiano, G. G., and Nelson, S. B. (2003). Neocortical ltd via coincident activation of presynaptic nmda and cannabinoid receptors. *Neuron*, 39(4):641–654.

Smith, Y., Bevan, M. D., Shink, E., and Bolam, J. P. (1998). Microcircuitry of the direct and indirect pathways of the basal ganglia. *Neuroscience*, 86(2):353–387.

Somjen, G. G., Kager, H., and Wadman, W. J. (2008). Computer simulations of neuron-glia interactions mediated by ion flux. *Journal of Computational Neuroscience*, 25(2):349–365.

Stamatakis, A. M., Jennings, Joshua H.and Ung, R. L., Blair, G. A., Weinberg, R. J., Neve, R. L., Boyce, F., Mattis, Joanna Ramakrishnan, C., Deisseroth, K., and Stuber, G. D. (2013). A unique population of ventral tegmental area neurons inhibits the lateral habenula to promote reward. *Neuron*.

Standage, D., Trappenberg, T., and Blohm, G. (2014). Calcium-dependent calcium decay explains stdp in a dynamic model of hippocampal synapses. *PloS one*, 9(1):e86248.

Standley, C., Norris, T., Ramsey, R., and Usherwood, P. (1993). Gating kinetics of the quisqualate-sensitive glutamate receptor of locust muscle studied using agonist concentration jumps and computer simulations. *Biophysical journal*, 65(4):1379–1386.

Stuart, G. J. and Häusser, M. (2001). Dendritic coincidence detection of epsps and action potentials. *Nature neuroscience*, 4(1):63.

Sulzer, D. (2005). The complex regulation of dopamine output: A review of current themes. *Clinical Neuroscience Research*, 5(2–4):117–121.

Surmeier, D. J., Ding, J., Day, M., Wang, Z., and Shen, W. (2007). {D1} and {D2} dopamine-receptor modulation of striatal glutamatergic signaling in striatal medium spiny neurons. *Trends in Neurosciences*, 30(5):228 – 235. Fifty years of dopamine research.

Tabrizi, S. J., Scahill, R. I., Owen, G., Durr, A., Leavitt, B. R., Roos, R. A., Borowsky, B., Landwehrmeyer, B., Frost, C., Johnson, H., Craufurd, D., Reilmann, R., Stout, J. C., and Langbehn, D. R. (2013). Predictors of phenotypic progression and disease onset in premanifest and early-stage huntington's disease in the track-hd study: analysis of 36-month observational data. *The Lancet Neurology*, 12(7):637–649.

Tachibana, Y., Iwamuro, H., Kita, H., Takada, M., and Nambu, A. (2011). Subthalamo-pallidal interactions underlying parkinsonian neuronal oscillations in the primate basal ganglia. *European Journal of Neuroscience*, 34(9):1470–1484.

Tagluk, M. E. and Tekin, R. (2014). The influence of ion concentrations on the dynamic behavior of the hodgkin–huxley model-based cortical network. *Cogn Neurodyn*.

Takada, M., Inoue, K.-I., Koketsu, D., Kato, S., Kobayashi, K., and Nambu, A. (2013). Elucidating information processing in primate basal ganglia circuitry: a novel technique for pathway-selective ablation mediated by immunotoxin. *Frontiers in neural circuits*, 7:1–7.

Takumi, T., Ishii, T., Horio, Y., Morishige, K.-I., Takahashi, N., Yamada, M., Yamashita, T., Kiyama, H., Sohmiya, K., Nakanishi, S., and Kurachi, Y. (1995). A novel atp-dependent inward rectifier potassium channel expressed predominantly in glial cells. *Journal of Biological Chemistry*, 270(27):16339–16346.

Tan, K. R., Yvon, C., Turiault, M., Mirzabekov, J. J., Doehner, J., Labouèbe, G., Deisseroth, K., Tye, K. M., and Lüscher, C. (2012). Gaba neurons of the vta drive conditioned place aversion. *Neuron*, 73(6):1173–1183.

Tecuapetla, F., Jin, X., Lima, S. Q., and Costa, R. M. (2016). Complementary contributions of striatal projection pathways to action initiation and execution. *Cell*, 166(3):703–715.

Terman, D., Rubin, J. E., Yew, A. C., and Wilson, C. J. (2002). Activity patterns in a model for the subthalamopallidal network of the basal ganglia. *The Journal of Neuroscience*, 22(7):2963.

Tigaret, C. M., Olivo, V., Sadowski, J. H., Ashby, M. C., and Mellor, J. R. (2016). Coordinated activation of distinct ca 2+ sources and metabotropic glutamate receptors encodes hebbian synaptic plasticity. *Nature communications*, 7:10289.

Tippett, L. J., Waldvogel, H. J., Thomas, S. J., Hogg, V. M., Roon-Mom, W. v., Synek, B. J., Graybiel, A. M., and Faull, R. L. M. (2007). Striosomes and mood dysfunction in huntington's disease. *Brain*, 130(1):206–221.

Tobler, P. N., Fiorillo, C. D., and Schultz, W. (2005). Adaptive coding of reward value by dopamine neurons. *Science*, 307(5715):1642.

Tong, G., Shepherd, D., and Jahr, C. E. (1995). Synaptic desensitization of nmda receptors by calcineurin. *Science*, 267(5203):1510–1512.

Tong, X., Ao, Y., Faas, G. C., Nwaobi, S. E., Xu, J., Haustein, M. D., Anderson, M. A., Mody, I., Olsen, M. L., Sofroniew, M. V., and Khakh, B. S. (2014). Astrocyte kir4.1 ion channel deficits contribute to neuronal dysfunction in huntington's disease model mice. *Nature Neuroscience*.

Turner, R. S. and Desmurget, M. (2010). Basal ganglia contributions to motor control: a vigorous tutor. *Current Opinion in Neurobiology*, 20(6):704–716.

Tzounopoulos, T., Kim, Y., Oertel, D., and Trussell, L. O. (2004). Cell-specific, spike timing-dependent plasticities in the dorsal cochlear nucleus. *Nature neuroscience*, 7(7).

Tzounopoulos, T., Rubio, M. E., Keen, J. E., and Trussell, L. O. (2007). Coactivation of pre-and postsynaptic signaling mechanisms determines cell-specific spike-timing-dependent plasticity. *Neuron*, 54(2):291–301.

Ullah, G., Cressman, J. R., Barreto, E., and Schiff, S. J. (2009). The influence of sodium and potassium dynamics on excitability, seizures, and the stability of persistent states: Ii. network and glial dynamics. *J. Comput Neurosci.*

Vadalà, M., Vallelunga, A., Palmieri, L., Palmieri, B., Morales-Medina, J. C., and Iannitti, T. (2015). Mechanisms and therapeutic applications of electromagnetic therapy in parkinson's disease. *Behavioral and Brain Functions : BBF*, 11:26.

Valtcheva, S., Paille, V., Dembitskaya, Y., Perez, S., Gangarossa, G., Fino, E., and Venance, L. (2017). Developmental control of spike-timing-dependent plasticity by tonic gabaergic signaling in striatum. *Neuropharmacology*.

Valtcheva, S. and Venance, L. (2016). Astrocytes gate hebbian synaptic plasticity in the striatum. *Nature communications*, 7:13845.

van Albada, S. J., Gray, R. T., Drysdale, P. M., and Robinson, P. A. (2009). Mean-field modeling of the basal ganglia-thalamocortical system. ii: Dynamics of parkinsonian oscillations. *Journal of Theoretical Biology*, 257(4):664–688.

van Albada, S. J. and Robinson, P. A. (2009). Mean-field modeling of the basal ganglia-thalamocortical system. i: Firing rates in healthy and parkinsonian states. *Journal of Theoretical Biology*, 257(4):642–663.

Vijayaraghavan, L., Krishnamoorthy, E. S., Brown, R. G., and Trimble, M. R. (2002). Abulia: A delphi survey of british neurologists and psychiatrists. *Movement Disorders*, 17(5):1052–1057.

Villalba, R. M., Mathai, A., and Smith, Y. (2015). Morphological changes of glutamatergic synapses in animal models of parkinson's disease. *Frontiers in Neuroanatomy*, 9:117.

Volkmann, J. and Deuschl, G. (2007). *Deep brain stimulation*, volume 84(3). Aminoff, Michael J. and Boller, François and Swaab, Dick F.

Wang, H.-Y., Kuo, Z.-C., Fu, Y.-S., Chen, R.-F., Min, M.-Y., and Yang, H.-W. (2015). Gabab receptor-mediated tonic inhibition regulates the spontaneous firing of locus coeruleus neurons in developing rats and in citalopram-treated rats. *The Journal of Physiology*, 593(1):161–180.

Wang, X., Zhong, P., Gu, Z., and Yan, Z. (2003). Regulation of nmda receptors by dopamine d4 signaling in prefrontal cortex. *Journal of Neuroscience*, 23(30):9852–9861.

Watanabe, H., Watanabe, M., Aihara, K., and Kondo, S. (2002). The change of memory formation according to stdp in a continuous-time neural network model. *IEICE transactions on information and systems*, 85(3):603.

Wei, W., Rubin, J. E., and Wang, X.-J. (2015). Role of the indirect pathway of the basal ganglia in perceptual decision making. *The Journal of Neuroscience*, 35(9):4052–4064.

Weiss, T. and Veh, R. W. (2011). Morphological and electrophysiological characteristics of neurons within identified subnuclei of the lateral habenula in rat brain slices. *Neuroscience*, 172:74–93.

Wichmann, T. and DeLong, M. R. (2013). *The basal ganglia*. McGraw-Hill Education.

Wichmann, T. and Soares, J. (2006). Neuronal firing before and after burst discharges in the monkey basal ganglia is predictably patterned in the normal state and altered in parkinsonism. *Journal of Neurophysiology*, 95(4):2120.

Wilson, C. J. and Callaway, J. C. (2000). Coupled oscillator model of the dopaminergic neuron of the substantia nigra. *Journal of Neurophysiology*, 83(5):3084–3100.

Wilson, R. I. and Nicoll, R. A. (2002). Endocannabinoid signaling in the brain. *Science*, 296(5568):678–682.

Winter, C., Vollmayr, B., Djodari-Irani, A., Klein, J., and Sartorius, A. (2011). Pharmacological inhibition of the lateral habenula improves depressive-like behavior in an animal model of treatment resistant depression. *Behavioural Brain Research*, 216(1):463–465.

Wittenberg, G. M. and Wang, S. S.-H. (2006). Malleability of spike-timing-dependent plasticity at the ca3–ca1 synapse. *Journal of Neuroscience*, 26(24):6610–6617.

Woergoetter, F. and Porr, B. (2008). Reinforcement learning. *Scholarpedia*, 3:1448.

Wu, T., Chan, P., and Hallett, M. (2010). Automatic movements in pd patients effective connectivity of neural networks in automatic movements in parkinson's disease. *NeuroImage*, 49(3):2581.

Xiong, Z.-Q. and Stringer, J. L. (2000). Sodium pump activity, not glial spatial buffering, clears potassium after epileptiform activity induced in the dentate gyrus. *Journal of Neurophysiology*, 83(3):1443–1451.

Xu, T.-X. and Yao, W.-D. (2010). D1 and d2 dopamine receptors in separate circuits cooperate to drive associative long-term potentiation in the prefrontal cortex. *Proc Natl Acad Sci U S A*, 107(37):16366–71.

Yagishita, S., Hayashi-Takagi, A., Ellis-Davies, G. C., Urakubo, H., Ishii, S., and Kasai, H. (2014). A critical time window for dopamine actions on the structural plasticity of dendritic spines. *Science*, 345(6204):1616–1620.

Yang, C. R. and Seamans, J. K. (1996). Dopamine d1 receptor actions in layers v-vi rat prefrontal cortex neurons in vitro: modulation of dendritic-somatic signal integration. *Journal of Neuroscience*, 16(5):1922–1935.

Yang, K. and Dani, J. A. (2014). Dopamine d1 and d5 receptors modulate spike timing-dependent plasticity at medial perforant path to dentate granule cell synapses. *J. Neuroscience*, 34(48):15888–15897.

Yang, L.-M., Hu, B., Xia, Y.-H., Zhang, B.-L., and Zhao, H. (2008). Lateral habenula lesions improve the behavioral response in depressed rats via increasing the serotonin level in dorsal raphe nucleus. *Behavioural Brain Research*, 188(1):84–90.

Yang, L.-M., Yu, L., Jin, H.-J., and Zhao, H. (2014). Substance p receptor antagonist in lateral habenula improves rat depression-like behavior. *Brain Research Bulletin*, 100:22–28.

Yin, H. H., Knowlton, B. J., and Balleine, B. W. (2004). Lesions of dorsolateral striatum preserve outcome expectancy but disrupt habit formation in instrumental learning. *European Journal of Neuroscience*, 19(1):181–189.

Yin, H. H., Knowlton, B. J., and Balleine, B. W. (2005a). Blockade of nmda receptors in the dorsomedial striatum prevents action–outcome learning in instrumental conditioning. *European Journal of Neuroscience*, 22(2):505–512.

Yin, H. H., Knowlton, B. J., and Balleine, B. W. (2006). Inactivation of dorsolateral striatum enhances sensitivity to changes in the action–outcome contingency in instrumental conditioning. *Behavioural Brain Research*, 166(2):189–196.

Yin, H. H., Ostlund, S. B., Knowlton, B. J., and Balleine, B. W. (2005b). The role of the dorsomedial striatum in instrumental conditioning. *European Journal of Neuroscience*, 22(2):513–523.

Yu, N., Morris, C. E., Joos, B., and Longtin, A. (2012). Spontaneous excitation patterns computed for axons with injury-like impairments of sodium channels and na/k pumps. *PLoS Comput Biol*.

Zhanga, J.-C., Laua, P.-M., and Bi, G.-Q. (2009). Gain in sensitivity and loss in temporal contrast of stdp by dopaminergic modulation at gain in sensitivity and loss in temporal contrast of stdp by dopaminergic modulation at hippocampal synapses. *PNAS*.

Zhao, Y. and Tzounopoulos, T. (2011). Physiological activation of cholinergic inputs controls associative synaptic plasticity via modulation of endocannabinoid signaling. *Journal of Neuroscience*, 31(9):3158–3168.

Zheng, T. and Wilson, C. J. (2002). Corticostriatal combinatorics: The implications of corticostriatal axonal arborizations. *Journal of Neurophysiology*, 87(2):1007.

Zhuang, X., Belluscio, L., and Hen, R. (2000). G-olf-alpha mediates dopamine d1 receptor signaling. *The Journal of Neuroscience*.

Zucker, R. S. and Regehr, W. G. (2002). Short-term synaptic plasticity. *Annual Review of Physiology*, 64(1):355–405. PMID: 11826273.

FOLIO ADMINISTRATIF

THESE DE L'UNIVERSITE DE LYON OPEREE AU SEIN DE L'INSA LYON

NOM : Foncelle
(avec précision du nom de jeune fille, le cas échéant)

DATE de SOUTENANCE : 05/04/2018

Prénoms : Alexandre

TITRE : Modeling the signaling pathway implicated in spike-timing-dependent plasticity: the role of endocannabinoid and dopamine signaling.

NATURE : Doctorat

Numéro d'ordre : 2018LYSEI028

Ecole doctorale : InfoMaths

Spécialité : Informatique et applications

RESUME : In the brain, the high connectivity level makes it difficult to set up experiments with an appropriate level of control. To address that issue, mathematical models are used to represent the brain in a more comprehensive way. Easier than experiments to test hypotheses, mathematical models can extend them closer to reality and aim to extract the studied principle essence, by simplifying it. Computational modelling is a specific branch of mathematical modelling allowing to solve large numerical calculations. In this thesis, I used computational modelling to study brain parts through different approaches, all in collaboration with neurobiologists and applied to experimental data. A common framework is given by the goal of contributing to a picture of the action of the neuromodulator dopamine. I studied the diversity of dopamine's action at three different scales: the brain region, the cellular level and the molecular level. Dopamine has a large impact on the brain and it is mainly known for its rewarding dimension, it is, indeed, the molecule associated with reward prediction and punishment. Few regions in the brain produce dopamine and these regions are impaired in Parkinson's disease or disrupted in major depressive disorders. Concerning Parkinson's disease, I designed a firing-rate model to fit experimental basal ganglia neural activity, which disclosed significant changes of the neural response between control and Parkinsonian condition. Furthermore, with a Hodgkin-Huxley model accounting for the dynamics of the potassium ion, I could support the hypothesis that the brain region called lateral habenula hyper-activates and induces major depressive disorders because of unbalanced potassium concentration due to astrocyte dysfunction (Kir4.1 channels overexpression). Dopamine is also involved in synaptic plasticity, a phenomenon at the basis of memory that I explored with a third model accounting for several experimental results pertaining to spike-timing-dependent plasticity and its modulation.

MOTS-CLÉS : Computational modeling, neurosciences, synaptic plasticity, Parkinson's disease, Major depressive disorder

Laboratoire (s) de recherche : LIRIS/INRIA

Directeur de thèse: BERRY, Hugues

Président de jury :

Composition du jury :
Tsaneva-Atanasova, Krasimira Professor University of Exeter Rapporteure
Faure, Philippe Directeur de recherche Université Pierre et Marie Curie Rapporteur
Soula, Hédi Professeur Université Pierre et Marie Curie Examinateur
Beslon, Guillaume Professeur INRIA Examinateur
Berry, Hugues Directeur de recherche INRIA Directeur de thèse